UNIVERSITY OF SOUTHAMPTON

OXYNITRIDE SYSTEMS AS POTENTIAL INORGANIC PIGMENTS

A thesis submitted for the Degree of Doctor of Philosophy

by

JOANNA CLAIRE ROOKE

SCHOOL OF CHEMISTRY
FACULTY OF SCIENCE, ENGINEERING AND MATHEMATICS

March 2004

UNIVERSITY OF SOUTHAMPTON

ABSTRACT

FACULTY OF SCIENCE, ENGINEERING AND MATHEMATICS
SCHOOL OF CHEMISTRY

Doctor of Philosophy

OXYNITRIDE SYSTEMS AS POTENTIAL INORGANIC PIGMENTS

By Joanna Claire Rooke

Inorganic oxynitride materials, with potential applications as pigments, have been synthesised and characterised in terms of their crystal structure, band gap energies and physical properties using powder X-ray and powder neutron diffraction (PXD,PND), solid state UV-Visible spectroscopy, $L^*a^*b^*$ colour measurements, scanning electron microscopy (SEM), energy dispersive analysis of X-rays and thermal analysis.

Oxynitride perovskites, $A^{II,III}B^{V}(O,N)_3$, where A is a group 2 or lanthanide metal and B an early transition metal have been synthesised by the direct ammonolysis of stoichiometric metal oxides and carbonates at high temperatures, typically 850 °C, with the inclusion of group 1 and 2 metal halide salts acting as mineralisers. Powder X-ray diffraction studies show the synthesised perovskites to have primarily an orthorhombic distortion, crystallising in the space group *Pnma*, similar to $CaTaO_2N$. Exceptions include compounds crystallising in a rhombohedral system, $Ca_{0.77}Eu_{0.23}TaO_{1.77}N_{1.23}$ or in a monoclinic system, $LaTaON_2$. PXD profiles have highlighted the presence of a competing pyrochlore phase, which becomes more prevalent as the radius of the divalent and trivalent cations decreases such that perovskite phases for smaller lanthanides do not form.

Neutron diffraction studies show that the oxygen to nitrogen ratio in the orthorhombic perovskite is $Ca_{0.5}Nd_{0.5}TaO_{1.5}N_{1.5}$ and there is a slight ordering of O/N over the two anionic sites. In the octahedra forming the framework, the axial positions have greater nitrogen occupancy, whereas the equatorial positions favour oxygen. In contrast to this, the group 2 substitutions onto the lanthanide position in $LaTaON_2$ yielding $A_{(1-x)}La_xTaO_{(2-x)}N_{(1+x)}$, have shown a random distribution of oxygen and nitrogen over both positions.

UV-Visible spectroscopy of these oxynitrides reveal broad reflectance bands and a steep absorption edge, which is directly related to the band gap energy of the compound. By varying the doping levels on the B site with transition elements other than Ta such as Nb, Ti, W and Zr, the colour of the compound can be seen to visibly alter. This can be attributed to a modification in the band gap energies, a direct result of fine-tuning the electronegativity difference between cations and anions. Narrowing of this band gap is achieved by the incorporation of more nitrogen (concurrent substitution of A^{2+} by Ln^{3+} and thus O^{2-} by N^{3-}), or by the replacement of Ta by a more electronegative cation such as Nb.

Thermogravimetric analyses in air show the initial retention of nitrogen (as nitride), until around 450 °C where the nitrogen is replaced by oxygen resulting in white oxide products. This is consistent with variable temperature PXD data that shows a steady increase in lattice parameter size until the original perovskite structure is lost at 450 °C and above.

Solution methods, such as co-precipitation techniques, have been employed to deposit oxide precursors onto mica flakes, which are then fired under flowing ammonia to target thin films of oxynitride pigment on mica to produce interference effects. SEM has shown the presence of two separate morphologies, mica and pigment, thus resulting in unsuccessful depositions. Although the pearlescent nature of mica remains after heat treatment with ammonia, solution methods do not yield the same intense colours seen by the solid state route. This necessitates the use of halide salts to target pigments with high quality hues but this destroys the pearlescent effects seen in mica.

"Every attempt to employ mathematical methods in the study of chemical questions must be considered profoundly irrational and contrary to the spirit of chemistry.... if mathematical analysis should ever hold a prominent place in chemistry -- an aberration which is happily almost impossible -- it would occasion a rapid and widespread degeneration of that science."

Auguste Comte (1798-1857)

PREFACE

TABLE OF CONTENTS

CHAPTER THREE:

CHAPTER FOUR:

CHAPTER FIVE:

CHAPTER SIX:

CHAPTER SEVEN:

ACKNOWLEDGEMENTS

Foremost I am very grateful to my supervisor, Professor Mark Weller, for his continual encouragement and support. His academic guidance throughout this project has been most appreciated.

In addition, I would like to thank Rod Riddle and Lilia Heider for their expert advice and helpful assistance over the past three years in the art of pigment synthesis and characterisation. I would also like to thank Merck for their financial support and the entertaining annual CASE conferences that they host.

I would also like to express thanks to the EPSRC for their contribution to the funding of my PhD and the conferences I have attended.

A special mention must go to the resident experts, Dr. Paul Henry and Dr. Chris Knee, and also Dr. Andrew Hector, for practical advice and above all for passing on their invaluable GSAS knowledge.

I also must thank Lee (and his willingness to see the mighty Saints), Rayne, Jenny, Jon, Nicola, Bob (all things technical), Craig, Marianne, Vince, Tom, Stuart, Seth (at least sane people live in Ipswich too), Humanzee, Rina, Northerner and everyone else who has worked within the Weller group during the past three years. The sense of team spirit and camaraderie shown by all, both in and out of the department has been impressive, especially during those times of sleep depravation at Daresbury, ILL and RAL.

Special thanks go to Dr. Chris Knee, Dr. Jenny Armstrong and Stuart Henderson, who each scoured various chapters of this work for typos and grammatical errors.

Finally I'd like to thank Nayan, Colin (a fellow pink Rhubarb), Robin and Bav for being great friends and pseudo Weller socialites when the call arose, usually around 5pm every Friday when the group adjourns to the bar.

ABBREVIATIONS

Some commonly used abbreviations in this work:

PXD	Powder X-ray Diffraction
VT-PXD	Variable Temperature Powder X-ray Diffraction
PND	Powder Neutron Diffraction
TOF	Time of Flight
TGA	Thermogravimetric Analysis
DTA	Differential Thermal Analysis
UV-Vis	Ultraviolet-Visible
EDAX	Energy Dispersive Analysis of X-rays
SEM	Scanning Electron Microscopy
FWHM	Full Width at Half Maximum
JCPDS	Joint Committee on Powder Diffraction Standards
GSAS	General Structure Analysis System
esd	Estimated Standard Deviation
OCD	Observed Calculated Difference

CHAPTER ONE

INTRODUCTION

1 INTRODUCTION

1.1 INORGANIC PIGMENTS

1.1.1 OVERVIEW OF PIGMENTS

The word *pigment* has been associated with materials that colour matter for centuries but the modern meaning of the word originated in the twentieth century. In accordance with approved standards, a pigment is a substance that consists of finely ground powders with small particle size, which is practically insoluble in the applied medium. It is used on account of its colouring, protective, or magnetic properties.[1] Materials used for their colouring abilities can encompass both dyes and pigments. The characteristic that demarcates pigments from soluble organic dyestuffs is the low solubility they have in binders and solvents.

There are a multitude of inorganic pigments, some are derived from coloured transition metal oxides *i.e.* α-Fe_2O_3 (red to violet), Cr_2O_3 (green) and $CoAl_2O_4$ (blue), others are based on charge transfer compounds such as cadmium sulfide. There has been growing concern over the last decade about the utilisation of heavy metals such as cadmium, chromium and lead in materials. This has resulted in tighter health and safety regulations and hence an increased effort to industrially synthesise inorganic pigments with less toxic elements.[2]

1.1.2 APPLICATIONS

Around 96% of all pigments synthesised world-wide are inorganic pigments, hence they form a fundamental class of pigments with widespread applications. They are most frequently utilised in plastics, paints and varnishes, printing inks, rubber, cosmetics, ceramic glazes and enamels.

1.1.3 DEFINITION OF A PIGMENT

'A pigment is a coloured, black, white or fluorescent particulate organic or inorganic solid, which is usually insoluble in and essentially physically and chemically unaffected by, the vehicle or substrate into which it is incorporated. A pigment will alter appearance by selective absorption and / or scattering of light. The pigment is usually dispersed in a vehicle for application in, for example, the manufacture of paints, plastics or other polymeric materials and inks. The pigment will retain its own unique crystalline or particulate structure throughout the incorporation period.'[1]

1.1.4 CLASSIFICATION OF PIGMENTS

As there are a wide variety of pigments available they tend to be classified into five sub-categories, which are summarised below in *Table 1.1*

Table 1.1: Classification of inorganic pigments.[1]

Term	Definition
White Pigments:	Optical effect is caused by non-selective light scattering, (*e.g.* ZnO).
Coloured Pigments:	Optical effect is caused by selective light absorption and selective light scattering, (*e.g.* iron oxide red, chrome yellow, Ultramarine pigments).
Black Pigments:	Optical effect is caused by non-selective light absorption, (*e.g.* carbon black).
Lustre Pigments:	Optical effect is caused by regular reflection or interference, including:
Metal Effect Pigments	Regular reflection takes place on mainly flat and parallel metallic pigment particles, (*e.g.* aluminium flakes).
Nacreous Pigments	Regular reflection takes place on highly refractive parallel pigment platelets, (*e.g.* TiO_2 on mica).
Interference Pigments	The optical effect of coloured lustre pigments is caused wholly or mainly by the phenomenon of interference, (*e.g.* iron oxide on mica).
Luminescent Pigments:	Optical effect is caused by the capacity to absorb radiation and to emit it as light of a longer wavelength, including:
Fluorescent Pigments	Light of longer wavelength is emitted after excitation without a delay, *ca.* nanoseconds, (*e.g.* Ag doped ZnS).
Phosphorescent Pigments	Light of longer wavelength is emitted within milliseconds after excitation, (e.g. Cu doped ZnS).

1.1.5 TOXICITY OF PIGMENTS

Many inorganic pigments have been known for centuries and their usage is most evident in artwork. Pigments stand the test of time for they are usually resistant to degradation brought about by external effects such as light, weather and pollution. They are generally safe to handle even though many pigment systems contain toxic metals such as cadmium, lead and chromium. However, in recent years there have been increased efforts to find replacements for pigments such as cadmium selenide, chromium oxide and lead chromate, which can be manufactured on an industrial scale. International directives that encourage restrictions on the use of toxic metals, in particular those mentioned above, have now been introduced. Work is

being carried out in several areas of interest to develop new pigments. For instance, transition metal pigments based on cerium compounds have recently begun commercial production.[3]

Other ideas include the synthesis of an inert colourless framework structure that has a chromophore encapsulated within the channels or cages of the structure. One way to achieve this is by trapping the species responsible for the colour *in situ*, in other words whilst the framework is synthesised. The most familiar pigment of this type is Ultramarine blue, $Na_7[AlSiO_4]_6(S_3)$ (which is a synthetic form of the mineral *lapis lazuli*). The chromophore, comprising of S_3^- ions trapped in a sodalite cage, produces an intense blue colour.

Another radical approach is to have a mixed anion compound such as an oxynitride or an oxysulfide. The introduction of different anions alters the band gap (see *Section 1.6*), which in turn allows absorption in the visible region of the electromagnetic spectrum giving rise to coloured compounds as in Cd(S,Se). Work in this project has focussed on oxynitrides as suitable replacements to cadmium and chromium based pigments as several systems have proved to be red through to yellow in colour. These colours have previously been difficult to achieve using less toxic elements. Recently Jansen *et al.* found that $CaTaO_2N$ (yellow) and $LaTaON_2$ (red) were mutually soluble[4] thus leading to a series of solid solutions of formal composition $Ca_{(1-x)}La_xTaO_{(2-x)}N_{(1+x)}$. By varying the cation composition and retaining the perovskite structure, the anionic stoichiometry will also alter. This enables fine-tuning of the band gap to vary the pigment colour from yellow to red.

1.2 TYPES OF COLOURED PIGMENTS

1.2.1 MIXED METAL OXIDE PIGMENTS

A mixed metal oxide pigment is one that has crystallised in a stable oxide lattice. The colour often arises due to the incorporation of coloured *d*-block cations within the structure. Stable oxides renowned for being excellent metal oxide pigments are those with structures such as rutile and spinel, which have high refractive indices, an important optical property, which results in a good hiding power. In other words, the hiding power of a pigment is its ability to mask a substrate, which is governed by how thickly it is applied. Examples of pigments with such structures are $Ti_{0.85}Sb_{0.10}Ni_{0.05}O_2$ (nickel rutile yellow), and $ZnFe_2O_4$ (zinc iron brown) respectively.[1]

Other examples of mixed metal oxide pigments include the primrose yellow bismuth vanadate, ($4BiVO_4 \cdot 3Bi_2MoO_6$). It is essentially dual phase with a tetragonal $BiVO_4$ (scheelite) structure and a metastable, orthorhombic Bi_2MoO_6 (perovskite) structure. By altering the $BiVO_4/Bi_2MoO_6$ ratio the hue can be controlled, for which $BiVO_4$ is responsible for the colour. Increased molybdate content makes this pigment greener. Bismuth vanadate is found in the mineral pucherite. Pure $BiVO_4$ was first synthesised in 1924 by Zintl and was used initially for pharmaceutical purposes.[5] It came to prominence as a pigment in 1976 when it was developed by DuPont.[6-8] This non-toxic green-yellow pigment is used widely in industrial paints especially in automotive finishes. It has excellent weathering properties.

Cobalt blue, another mixed metal oxide, has been understood to date from the sixteenth century though this is not strictly true. Cobalt has been found in ancient glasses and glazes from Persia as early as 2250 BC.[9] It is also known that cobalt pigments have been used in China from as early as the T'ang dynasty, 618-906 AD. In addition, during the 1550's smalt, a potassium silicate glass coloured with cobalt, was in use. Nevertheless it was not until 1777 that Wenzel detailed the effect of alumina on cobalt.[9] However this cobalt aluminate spinel ($CoO \cdot Al_2O_3$) is usually attributed to Thénard who produced it around thirty years after. These cobalt pigments are relatively inert, being resistant to acids, alkalis, oxidation and reduction. They are extremely lightfast and weather resistant; they also have a high thermal stability. The main applications of such pigments are in the plastics and coating industry. They are however a very expensive option as recent years have seen a dramatic increase in the price of elemental cobalt.

1.2.2 IRON PIGMENTS

Iron oxides and hydrates have been used as pigments *i.e.* hematite, ochre, sienna and umber, which produce a diversity of colours depending on basic formula, including other elements such as Mn in umber, α-$(Fe,Mn)_2O_3$, and also crystal structure which is dependant on the origin of the iron ore.[1] Commercially, the second most important class of pigments behind TiO_2 are the iron oxide hydrates, which are red to brown pigments. Their shades are varied by the amount of iron oxide, hydroxide, water and clay present. They are used as wood stains and floor polishes as well as other more common pigment applications due to their cheap synthetic costs, low toxicity and excellent properties such as heat stability and resistance to chemical attack.

1.2.3 CADMIUM PIGMENTS

Cadmium sulfide (CdS) gives a brilliant yellow colour and by replacing the sulfur for selenium, Cd(S,Se), the colour goes from yellow through orange to red. Cadmium pigments typically involve the use of Hg and Zn as well as S and Se and through modifications to the percentage of each element present, can yield shades of light yellow through to orange, red and deep maroon. The colour can be explained by way of band theory, see *Section 1.6.3*. The mineral crystallises hexagonally in the wurtzite lattice (α-form). It exists naturally in the mineral greenockite[1] as recorded by Gay Lussac.

The list of properties these pigments possess makes them good candidates for commercial uses. They not only have a low solubility in water and high durability but also show stability to high temperatures, fade resistance to UV light, good dispersibility and resistance to dilute acids and alkalis. These pigments are the only bright red pigments that can withstand the usual ceramic glaze temperatures of 1010 – 1040 °C. The one major drawback is the toxicity of cadmium metal, which leads to the research into suitable replacements for a cost effective red inorganic pigment with properties equal or better than that of cadmium sulfoselenide.

1.2.4 CHROMATE PIGMENTS

This set of pigments includes lead chromate (chrome yellow) and lead molybdate (molybdate orange and molybdate red).[1] Lead chromate occurs naturally as the red-orange mineral crocoite. Its chemical composition was identified by L N Vauquellin in 1797 and was first synthesised in 1809. The colour of lead chromate coupled with its wide ranging applications and low cost production made it desirable as a pigment. Since the mid seventies however, people have become more aware of the toxicity of lead and thus it now has a much more restricted use.

Making solid solutions of lead chromate with other lead salts such as PbO, $PbMoO_4$ and $PbSO_4$ can diversify the range of lead chromate colours available. The reason for the observed colour in chromate pigments arises from a ligand to metal transfer within the CrO_4^{2-} tetrahedra, see *Section 1.5.1*.

Chromate pigments have many uses in paints, plastics and road markings due to their low costs but certain applications such as children's toys and plastic packaging for foodstuffs are

restricted due to the toxic nature of the comprising elements. They are also not chemically resistant as inks for certain products such as soaps and fertilisers. Chromium is also found in the green pigment, chromium oxide (Cr_2O_3). As chromium is in a lower oxidation state, the electronic transitions and causes of colour have changed. Ultimately, the colour of the chromium ion is different, *d-d* transitions are now possible.

1.2.5 ULTRAMARINE PIGMENTS

During the Middle Ages artists used natural Ultramarine blue, derived from the semiprecious gem lapis lazuli, as a pigment. In 1828, the first synthetic Ultramarine powder pigments were produced by Guimet[10] and Gmelin.[11] Nowadays they are commercially available in blue, violet and pink colours. The pigments are comprised of an aluminosilicate lattice, which has a sodalite structure. Sodium ions and sulfur free radicals are trapped within the lattice and therefore stabilised. Here the colour occurs due to electronic transfers within the sulfur S_3^- and S_2^- units.

Ultramarines have high thermal stabilities, excellent lightfastness and are solvent resistant. They display hydrophilic surface characteristics and are alkali stable although sensitive to acids. More importantly they have low toxicity making them ideal for many applications including make-up, food dyes and children's toys. They are also responsible for some optical brighteners in washing powders giving a blue-whiteness to the powder under ultraviolet light.

1.2.6 BLACK PIGMENTS

The optical quality of black pigments is determined by their light absorption co-efficient and their colour intensity is dependent on the particle size.[1] Iron oxides, mixed metal oxides and carbon black are the most important black pigments. Carbon black is formed by pyrolysis or partial combustion of vapours that contain carbon. This results in a form of highly dispersed elemental carbon, with a very small particle size.

1.2.7 WHITE PIGMENTS

White pigments appear white as a result of their low light absorption and also because they scatter light strongly and in a mainly non-selective fashion.[1] Examples of white pigments include TiO_2, zinc white (ZnO) and lithopone (co-precipitation and calcination of ZnS and $BaSO_4$). Titanium dioxide is the most common inorganic pigment in use. It is important as it is highly stable, non-toxic and has excellent scattering properties.

1.3 LUSTRE PIGMENTS

1.3.1 OVERVIEW OF LUSTRE PIGMENTS

Many pigments have angle-dependent optical effects and consequently have many applications.[12] These effects can have functional purposes; for instance, security printing and optical filters. They also have decorative functions such as car paints and cosmetics.

'In contrast to conventional pigments…effect or lustre pigments show optical properties that are due to specular reflection of light by aligned flaky particles. Their main property is goniochromaticity, *i.e.* the change of lightness and / or colour hue with the viewing angle of the observer.'[13]

Traditional pigments interact with light either by absorption and transmission or diffuse scattering. In contrast to this, lustre pigments tend not to reflect light diffusely but instead by specular reflection, as can be seen in *fig. 1.1* below.

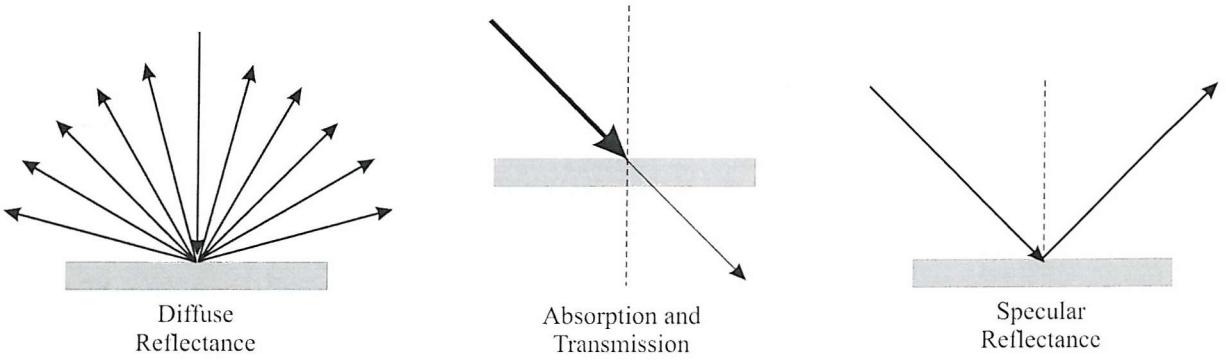

fig. 1.1: *Interaction of light by a pigment; (left) diffuse reflectance from a pigment surface, (middle) selective absorption of white light in a pigment and (right) specular reflectance from a pigment surface.*

Within the category of lustre pigments are nacreous pigments. These simulate the nacreous effect of natural pearls. A synthetic example is TiO_2 deposited on mica. Another sub-section is that of interference pigments. Such pigments consist of alternating transparent layers of materials with differing refractive indices. When other oxide layers are added to TiO_2 on mica, interference effects are achieved due to the optical density differences.

Interference pigments are characterised by selective reflection. A process called refraction happens at each phase boundary such that the multiple reflections of incident light will result in optical interference. This is so because some of the superimposed light waves will now be out of phase and this will result in both constructive and destructive interference. In turn this means certain wavelengths of light will be intensified whereas others are weakened.[14]

1.3.2 METAL PLATELETS

Metal effect pigments consist of small metallic flakes. Tiny platelets of say aluminium or high gloss gold, brass or copper act as tiny mirrors, which are able to almost totally reflect incident light. The optical effect based on mirror reflection of incident light is unidirectional. They tend to be found in the final layers of paint on vehicles.[13]

1.3.3 SINGLE CRYSTAL LUSTROUS PIGMENTS

This category contains non-absorbing pigments such as pearlescent guanine crystals used in the cosmetics industry, nacreous basic lead carbonate (2 $Pb(OH_2)$ x 3 $PbCO_3$) and bismuth oxychloride (BiOCl). Pearlescent guanine crystals or natural pearl essence is found in natural pearls and nacreous shells. In 1656 Jaquin isolated natural pearl essence from fish scales.[15] There is no synthetic process available to replicate this expensive extract and to date fish scales are still used in some cosmetic formulations.

Basic lead carbonate (2 $Pb(OH_2)$ x 3 $PbCO_3$) and other hexagonal lead crystal salts were the first successful synthetic lustre pigment. Basic lead carbonate has an even surface and a high refractive index (2.0) and hence displays a very strong lustre. Though due to the toxic nature of lead, the fragility of the crystals and its low chemically stability, it is not an ideal lustre pigment.

Additions to this group are absorbing pigments such as platelike graphite, laminar phthalocyanines and flaky iron oxides.[13] These flakes are either pure iron oxide or mixed phase pigments that have been crystallised into a hematite lattice and are produced via hydrothermal techniques.

Such lustrous pigments produce high quality pigment surfaces that feel, as well as look, impressive. They also have great mechanical stability. This means they can be dispersed

without damage, even under harsh conditions. The applications of these pigments are, again, in car paint and also in cosmetics.

1.3.4 OXIDE COATED MICA PIGMENTS

Currently metal oxide coated mica forms the most important type of lustre pigment, accounting for greater than eighty five percent of the market.[13] These pigments are in the form of thin films of transparent metal oxide coating a laminar substrate such as mica. Their high refractive indices and the perfection of their coatings determine the gloss of these pigments.

Mica is a natural mineral made of layered aluminium silicate sheets, a common example being muscovite, $KAl_2(OH)_2(Si_3Al)O_{10}$. The potassium ions are rather large and do not fit within the double layers, so are located between them and are co-ordinated to 6 oxygen atoms from each layer producing an ionic bond. These sheets are only weakly bonded together by the potassium ions compared to the bonding within the sheets, this allows for the perfect cleavage in one direction producing thin sheets and flakes of mica.[16] These sheets are quite durable and are often found in sands that have undergone much erosion and transport that would have destroyed most other minerals.

A typical oxide that binds to mica is TiO_2. A fine layer of TiO_2 is deposited onto mica resulting in a transparent silver-white pigment that has a deep shine similar to mother of pearl. If the particle size of the pigment is altered various results can be achieved such as glitter or silky matt effects.[17]

Iron oxide (Fe_2O_3) can also be deposited onto mica yielding a copper red colour with a green interference tinge. If iron oxide is added to the titanium dioxide coatings then a wide range of gold shades can be produced from yellows to reds. This is achieved by varying the thickness of both the TiO_2 and Fe_2O_3 coatings. If chromium oxide (Cr_2O_3) is added to the titania layer then green interference pigments will be produced.[14] Other examples include blue lustre pigments, using cobalt blue[18] and Prussian blue[19] deposited on mica.

Again, these pigments are used within the automotive industry and for cosmetics but can also be used in technical sectors such as plastics and printing. As they contain no environmentally dangerous metals they may also be used in the packaging of foodstuffs.

Other substrates have also been used as well as mica to similar effect such as SiO_2, Al_2O_3 and $BaSO_4$.[12,20,21] Investigations into synthetic mica equivalents have also taken place. Currently there is interest in depositing nanolayers onto silica spheres.[22]

1.3.5 Optical Properties of Coated Mica Pigments

Optical effects of coated mica pigments are due to multiple reflections. TiO_2 is a non-absorbing coating. It has a bright nacreous lustre and on varying the thickness of the coating, pastel interference colours are achievable. The hiding power, a reciprocal of the film thickness, is relatively low in this case. It can be increased for chromatic solids such as Fe_2O_3.[1] This absorbing coating is usually made thicker to allow interference. Also, the thicker coating gives colouristic brilliance and allows two-tone colours to be attained.

Coated mica pigments have multiple layers with differing refractive indices and several phase boundaries. Multiple reflection of light on a thin solid film causes such interference effects in the reflected light and the complementary transmitted light.[23] In *fig. 1.2* the interaction of light upon an iron oxide (Fe_2O_3) coated mica pigment is shown. The sheets of mica have a low refractive index whereas the iron oxide has a high refractive index.

When a beam of white light strikes an interface between two materials with differing refractive indices then the wave will be bent towards the normal if the second material has a greater refractive index, and bent away from the normal if it has a smaller refractive index. This is in accordance with Snell's Law. This physical concept plays a major part in explaining the cause of the lustre effect of coated mica pigments.

Equation 1.1

$$n_1 \sin\theta_i = n_2 \sin\theta_r$$

where n_1 and n_2 are refractive indices of the two media,

θ_i and θ_r are the angles of incident and reflected radiation.

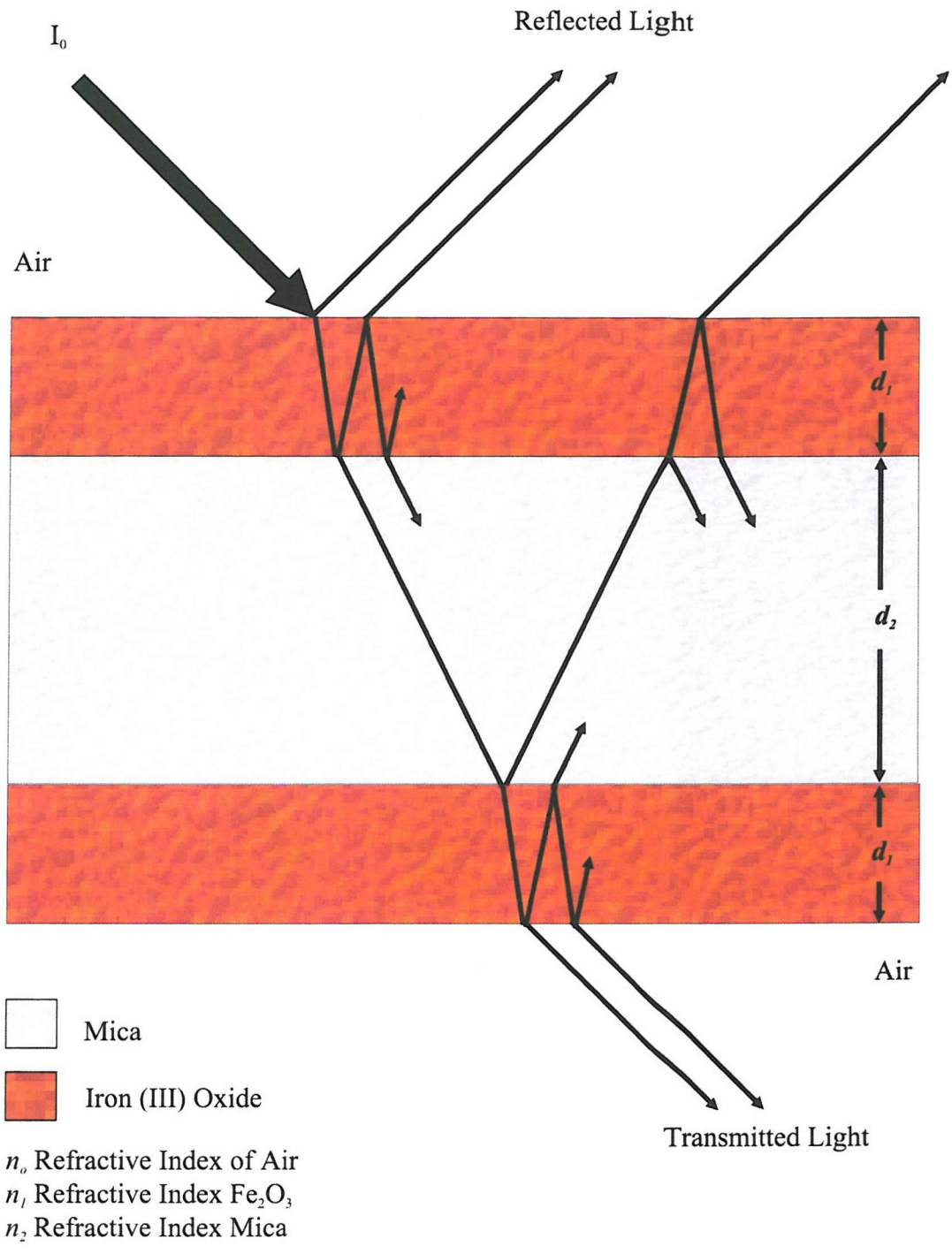

fig. 1.2: *Interference effects of a multilayer thin film pigment consisting of an iron oxide coating (high refractive index) surrounding a mica platelet (low refractive index). Four phase boundaries are shown; air-pigment, pigment-mica, mica-pigment and finally pigment-air.*

When several layers of materials with differing refractive indices are combined, multiple reflections occur due to the various phase boundaries, thus different refractions take place. Subsequently, stronger and more intense interference colours can result. When light strikes the surface of a coated mica pigment part of the incident light is reflected back and in doing so undergoes a 180° phase change. The rest penetrates the pigment layer and is refracted. At the boundary interface between the pigment and the mica layers there is another partial reflection. When this light wave passes through the boundary between pigment and air it is refracted back to the original angle of the first partial reflection and is thus parallel to it. These two components of reflected light will undergo interference effects dependant on the path lengths of the waves, *i.e.* the distances travelled by each wave. The second wave component will be displaced with respect to the first and this distance is governed by the thickness of the pigment film coating. If the waves arrive in phase, they are superimposed and the wave is amplified. If the waves are out of phase then attenuation of the waves occurs accordingly. These pigments never display total extinction of light.[14] This effect occurs at subsequent phase boundaries and the remaining light leaves the pigment at the bottom as a transmission colour that is complementary to the reflected colour. This is a qualitative overview of this effect, a more detailed explanation with the relevant mathematical proof can be found in the literature.[12]

If titanium dioxide is the coating layer on mica, dramatic changes in the colour are observed. When the layer is thin then the pigment appears a silvery white but as the level of TiO_2 coating is increased the interference colour changes and the pigment appears yellow, then red, to blue and finally green with increasing thickness.[1]

1.4 THE ORIGINS AND PROPERTIES OF COLOUR

There is more than one origin of colour and thus it is necessary to understand the cause of colour in a particular pigment system before it can be modified and improved to provide us with the exact colour we require. In other words, it makes sense to only modify parts of a structure that would bring about colour change.

The origin of the blue colour in Egyptian blue ($CaCuSi_4O_{10}$)[24] is from the copper. This is based on the knowledge that a copper Cu^{2+} ion when placed in a square planar environment

often brings about blue colouration. Whereas in the cobalt aluminate spinel ($CoAl_2O_4$) it is the tetrahedrally co-ordinated Co^{2+} ions that impart the blue colour.

If a photon enters a material containing a pigment it can either be absorbed or scattered by the pigment particle, alternatively it could pass straight through. If scattering is much higher in comparison to absorption, the pigment is white. If the opposite is true, then the pigment is black. In the case of coloured pigments, absorption and scattering are selective; they are dependent on the wavelength of incident light.

Inorganic solids can appear coloured if the material is in some way susceptible to visible light. Usually the coloured system absorbs certain wavelengths of light and reflects the rest back into the eye. This produces the observed colour. If the energy of the incident light is the same energy as an electronic transition of the material then absorption is possible. Only certain transitions are allowed within a given structure due to the fact that energy levels are quantised. Knowledge of both electronic transitions and the effect that a perturbation in a structure can have on such transitions yields us some control over compound colour.

Colour is often apparent due to the presence of elements with a number of varying oxidation states such as transition metals. Hence, by cation doping within a structure one may be able to fine tune the colour of the compound to give desirable results.

1.5 ELECTRONIC TRANSITIONS

1.5.1 CHARGE TRANSFER MECHANISM

A transition metal complex can absorb light as a result of charge transfer mechanisms. This can happen in one of several ways. Firstly, an intervalence transfer occurs when the electron redistribution happens between two cations, *i.e.* electron transfer from one cation to another. Secondly, cations can donate electrons to surrounding non-metal atoms in a cation to ligand fashion or vice versa accept electrons in a ligand to cation process. This is known as metal to ligand charge transfer (MLCT) and ligand to metal charge transfer (LMCT) respectively.

Finally, the electron redistribution could involve charge transfer between localised orbitals in different areas of the same molecule or complex. In order for this to be classified as a charge

transfer mechanism the electron-donating group and the electron-accepting group must be quite distinct from each other. These types of transitions are often described as π-π^* and n-π^* transitions as they promote a π electron from a bonding π orbital to an antibonding π^* orbital. They occur mainly in organic conjugated systems and consequently are of no direct relevance to this work.

In the first instance, intervalence or cation-cation transitions, intense colours arise from the transfer of an electron from one cation to another within a mixture of metal ions as in complex metal oxides. In order for this to occur the cations must be capable of adopting two different valence states *i.e.* transitions occur between cations in different oxidation states. Furthermore a transition will not transpire if either cations are widely separated or the anion geometry surrounding one cation differs vastly from the other.

A classic example of such charge transfer mechanisms is with materials containing both Fe^{2+} and Fe^{3+} ions, where an electron is transferred from an Fe^{2+} species to an Fe^{3+} species. An example of a mixed valence iron compound is Prussian blue ($KFe[Fe(CN)_6]$).[25] This is a dark blue pigment used in inks and is prepared by the mixing of two virtually colourless solutions, namely an aqueous solution of pale yellow $K_4[Fe^{2+}(CN)_6]$ and a pale yellow-green solution of any Fe^{3+} salt. To a certain extent, the process of changing the oxidation state of the iron cations alters the lattice energy of the compound. For such a transition to produce colour some energy must be absorbed thus explaining the change in lattice energy.

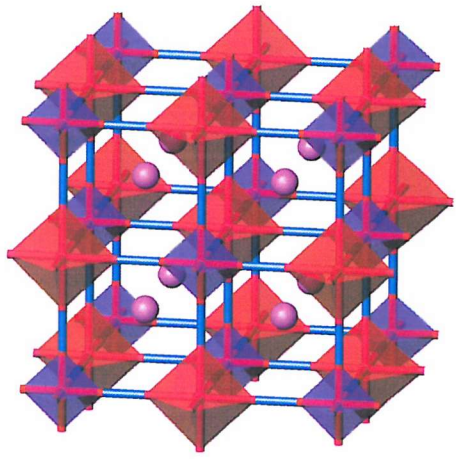

fig. 1.3: *Structure of Prussian blue whereby the Fe(II)C_6 and Fe(III)N_6 octahedra are shown in blue and red respectively and the potassium ions in purple.*

In Prussian blue an iron species is bonded to the carbon atom of the CN^- ligand and the adjacent iron species is linked to the nitrogen atom of the same ligand. This creates a three dimensional network of alternating FeC_6 and FeN_6 octahedra as seen in *fig. 1.3*.

The colour of this pigment is accredited to a minimal amount of a charge transfer state mixing with the ground state wavefunction of a ligand. The delocalisation and mixing of ground and charge transfer states is most favourable for small energy differences between ground and excited states. Also the Fe (II) and Fe (III) sites must be either adjacent and overlap strongly or be bridged by the covalent CN^- ligand. The intensity of colour depends on the concentration of ions present. The light blue colour of aquamarine arises from the same transitions present in Prussian blue. However aquamarine is a form of beryl containing only trace amounts of iron as an impurity.

Another example occurs when there is a slight reduction of a transition metal oxide, a good case being TiO_2. This normally white pigment becomes an intense blue-black when very slightly reduced to $TiO_{2-\delta}$. The valency of some titanium cations will change in order for the compound to remain electrostatically neutral after the loss of several oxygen atoms. This facilitates cation to cation charge transfer effects between Ti^{4+} and Ti^{3+}.

Chromate pigments, such as chrome yellow ($PbCrO_4$), are an example of charge transfer processes. The strong yellow colour arises from an electron being transferred from an oxygen atom to a chromium atom in a tetrahedral environment, this is known as ligand to metal charge transfer (LMCT). For this to occur the metal is usually in a high oxidation state and the ligand has a low ionisation energy. Other such examples of LMCT include potassium permanganate ($KMnO_4$) and potassium dichromate ($K_2Cr_2O_7$). In both cases the colour comes from the complex cations MnO_4^- and $Cr_2O_7^{2-}$ respectively as K^+ ions never display colour in solution. As both the transition metals have lost all the *d*-block electrons yielding formal charges of Mn^{7+} and Cr^{6+}, colour will not arise from crystal field effects but from anion to cation, that is ligand to metal, processes.

Conversely metal to ligand charge transfer (MLCT) occurs in the red material tris(bipyridyl)-iron (II).[26] This transfer happens when a metal is in a low oxidation state and the ligand tends to have vacant π^* orbitals (π acceptor orbitals).

Intra-anion charge transfer is the final process to mention here, as this mechanism gives Ultramarine its colour. As mentioned earlier in *Section 1.2.5* the colour of Ultramarine is due to the presence of polysulfide anions trapped within an aluminosilicate framework. These anions have the approximate formula S_3^-, a triangular arrangement of three sulfur atoms with an additional electron. The molecular orbitals of this polyanion are not fully occupied and thus a transition between filled and vacant levels within one S_3^- unit produces a strong absorption band in the visible region of the spectrum. Hence this is an intra, rather than inter, anion charge transfer process.

1.5.2 d-d TRANSITIONS

When a transition metal ion has *d* electrons, electronic transitions can take place between its *d*-orbitals. Hence *d-d* electronic transitions are responsible for intensely coloured compounds such as $[Ti(OH_2)_6]^{3+}$, an octahedral complex.[27] A key element involves the electron distribution in the *d* orbitals, *fig. 1.4*. The first set of orbitals are collectively known as the t_{2g} or t_2 set whereas the second group are known as the e_g or e set depending on whether they are in an octahedral or tetrahedral environment respectively.

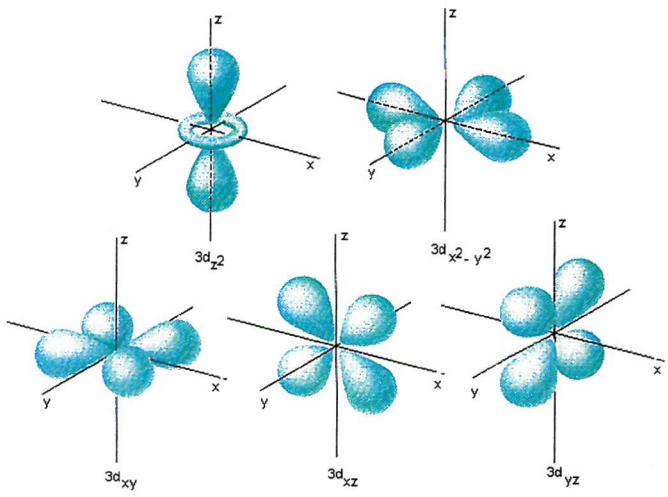

fig. 1.4: *Schematic showing the boundary surfaces and thus the shapes of the five d-orbitals.*[28]

A transition metal atom or ion in isolation possesses degenerate *d* orbitals. The *d* orbital energies increase when located in a crystal due to increased repulsions exerted on the *d* electrons by the electron clouds of surrounding ligands. As the central metal ion is not

spherical but has clearly defined regions of electron density the surrounding electrons are not evenly distributed and some *d* orbitals are higher in energy than others thus generating an energy gap known as Δ_{oct}. This is known as crystal field splitting. This splitting is small and allows for $e_g \leftarrow t_{2g}$ transitions that usually correspond to absorptions within the visible region of the spectrum.

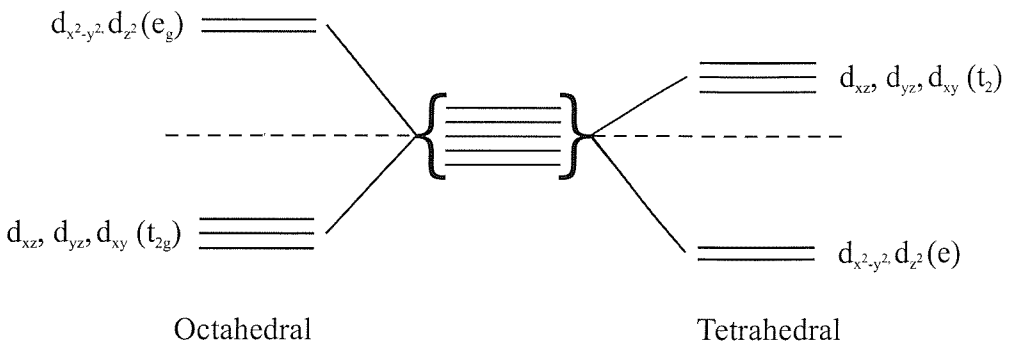

fig. 1.5: *Crystal field splitting effects of d-orbitals in octahedral and tetrahedral complexes.*

The magnitude of the splitting is seen in *fig. 1.5*. For complexes in different symmetry environments, *i.e.* tetrahedral $[Ni(CO)_4]$ and square planar $(NH_4)_2CuCl_4$,[29] interactions between ligands and *d*-orbitals change. Thus the *d*-orbitals are split in different ways according to geometry. The splitting in a tetrahedral environment, Δ_{tet}, is much smaller compared to Δ_{oct}. This is because there are only four negative ions as opposed to six and they are further away from the central metal ion. In fact:

Equation 1.2

$$\Delta_{tet} = \frac{4}{9}\Delta_{oct}$$

For instance, transitions in tetrahedral complexes (no centre of symmetry) are Laporte allowed and correspondingly are more intense than octahedral transitions.

1.5.3 SELECTION RULES

The intensity of observed absorptions are governed by a few selection rules, which are defined as follows:

Spin selection rule:	Transitions may occur only between energy states with the same spin multiplicity, *i.e.* $\Delta S = 0$.
Laporte selection rule:	$\Delta L = \pm 1$ and if the molecule is centrosymmetric, $g \leftrightarrow u$.
Symmetry selection rule:	Product of symmetry of ground and excited states corresponds to x, y and z in the character tables.

The spin selection rule suggests that *d-d* transitions are spin allowed (excluding d^5 high spin) but from Laporte's rule[26] these are formally forbidden in centrosymmetric environments such as octahedral complexes. They can arise either by a vibration or distortion that removes the centre of symmetry. No longer a perfect octahedron, the Laporte selection rule is momentarily by-passed. In the tetrahedral environment there is no centre of symmetry, thus these *d-d* transitions are allowed and therefore are more intense, tending to dominate a spectrum with respect to transitions within the octahedral environment. Examples of transitions with regards to their intensities are given in *Table 1.2*.

Table 1.2: Typical intensities of electronic transitions.

Band Type	Absorption Intensity	Transition Type
Spin Forbidden	$\varepsilon < 1$	*d-d* (Mn^{2+}, d^5)
Laporte Forbidden	$\varepsilon = 20 - 100$	*d-d* (O_h)
Laporte Allowed	$\varepsilon = ca.250$	*d-d* (T_d)
Fully Symmetry Allowed	$\varepsilon = 1000 - 5000$	Charge Transfer

where ε is the extinction co-efficient.

The values in this table for the extinction co-efficient are based on solution UV-Vis data and are therefore estimates. As for solid state data, it is harder to quantify the concentrations of samples accurately and thus gain any numerical values but simple qualitative analysis can be carried out to assign general transition types to solid state UV-Vis. data.

1.5.4 COLOUR FROM LANTHANIDE IONS

The valence electrons of elements belonging to the lanthanide series, also known as rare earth metals, are located in partly filled 4*f* orbitals. The colours of many lanthanides arise due to electron transitions involving these 4*f* orbitals.

There is a significant variation between lanthanide ions and 3*d* transition metal ions. Electrons within the 4*f* orbitals in lanthanides are shielded very well beneath an outer electron configuration ($5s^2\ 5p^6\ 6s^2$) and therefore the crystal surroundings will have little effect unlike *d*-block metal ions. Consequently, important magnetic and optical properties accredited to the 4*f* electrons on a lanthanide ion are normally unvarying and thus do not significantly depend upon the host structure they are contained within. These rare earth elements often lend their use to phosphors and lasers. In such cases a host lattice can be selected with regard to processing conditions without altering the desirable colour properties of the metal ion. Some typical lanthanide ion colours are listed in *Table 1.3*.

Table 1.3: Characteristic colours of some lanthanide ions.[30]

Ion	*f* Electron Configuration	Characteristic Colour
Ce^{3+}	$4f^1$	Yellow
Pr^{3+}	$4f^2$	Green
Nd^{3+}	$4f^3$	Lilac-Violet
Pm^{3+}	$4f^4$	Pink
Sm^{3+}	$4f^5$	Pale Yellow
Sm^{2+}	$4f^6$	Red/Green
Eu^{3+}	$4f^6$	Pink
Eu^{2+}	$4f^7$	Brown
Tb^{3+}	$4f^8$	Pink
Dy^{3+}	$4f^9$	Pale Yellow
Dy^{2+}	$4f^{10}$	Brown
Ho^{3+}	$4f^{10}$	Yellow
Er^{3+}	$4f^{11}$	Pink
Tm^{3+}	$4f^{12}$	Green

The colours of lanthanide ions tend to be quite pale as like *d-d* transitions, *f-f* transitions are forbidden and give very weak absorption bands. However unlike *d-d* transitions, crystal field

effects are virtually insignificant for *f-f* transitions due to the shielding of the 4*f* orbitals from the external charge, thus there is little vibronic broadening of the peaks. In contrast to this 4*f* to 5*d* transitions are formally allowed and give intense broad bands. LMCT on the *f* orbital of the metal usually occurs in the ultraviolet and thus has little effect on colour.

1.6 BAND THEORY

1.6.1 OVERVIEW OF BAND THEORY

Band theory is used to understand the way in which electrons are held in metals, semiconductors and insulators whereby the electron energy levels are broadened into energy bands. It is derived from molecular orbital theory and the bonding within an infinitely large molecule, *i.e.* a solid.

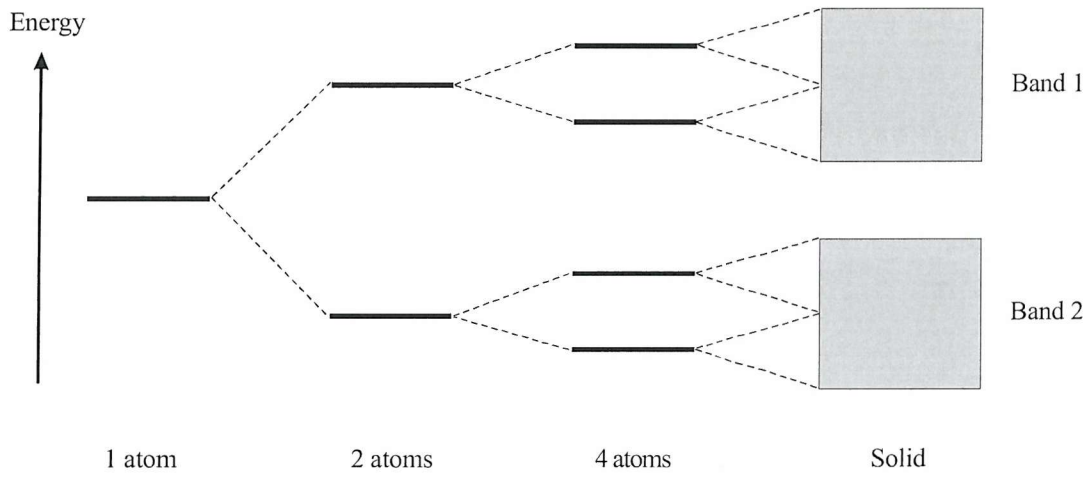

fig. 1.6: *The formation of energy bands within a solid from the constituent atomic orbitals.*

In an isolated atom electrons occupy discrete energy levels. Those highest in energy are the furthest away from the nucleus. Let us consider the outermost energy level of the isolated atom. If another atom approaches the first atom then the outer electron clouds will overlap and interact. The result of this is the splitting of a single energy level into two non-degenerate levels, *i.e.* one at lower energy than the other, *viz.* bonding and anti-bonding orbitals. If the electron clouds of these two atoms were then to interact with a further two atoms four energy levels would ensue; two of higher energy and two of lower energy. This process of splitting energy levels can be continued indefinitely such that the number of energy levels is equal to the number

of atoms within the cluster. As each atom is added the number of energy levels in both the high energy group and the low energy group increases. Concurrently the spacing between energy levels in each group decreases. Ultimately, when a large number of atoms are present such as in a solid, the energy levels are very close together within each group, giving continuous bands of energy. These are referred to as *energy bands* and are represented by the boxes in *fig. 1.6.*

Both the geometry of a structure and the degree of interaction of the energy levels determine the true band structure of a crystal. If the interaction is large, as is the case for the outer orbitals of closely packed large atoms, then the bands are broad. If the interaction is less, then the width of the bands is narrower, which happens to the inner orbitals on atoms further apart. The electrons within the solids fill these bands in much the same way as they fill atomic orbitals, from the lowest energy to the highest energy. The nature of the bands determines the electronic properties of the solid. If these materials are coloured, it is due to electronic transitions within and between the bands.

1.6.2 METALS, INSULATORS AND SEMICONDUCTORS

As mentioned in the previous section, two bands are formed when atoms pack together in a solid. The uppermost band, the higher energy band, is called the conduction band. Conversely the lower energy band is named the valence band. A term known as the *band gap* is applied to the energy difference between the top of the valence band and the bottom of the conduction band. In each crystal orbital it is possible to have two electrons in opposing spin directions. In a completely filled band the net motion of electrons is zero and the conductivity is therefore also zero. This is the case for insulators where the conduction band contains no electrons and the valence band is completely filled. The energy gap for an insulator is typically large, > 12 eV for some ionic solids.

Intrinsic semiconductors have a similar band structure to insulators with one exception. In this case the separation of the empty and filled energy bands, the band gap, is smaller, around 0.1-3 eV. By definition this means it is possible for some electrons of sufficient energy, gained through thermal excitation *etc.*, to transfer from the top of the valence band to the bottom of the conduction band at room temperature leaving behind a vacancy in the valence band. These vacancies behave as positively charged particles and are labelled as positive *holes*. Hence with each transition two mobile charge carriers are created, an electron and a hole.

Metals are materials in which the valence band is full and the conduction band partially filled. The highest energy attained by the electrons in the conduction band is known as the *Fermi level*. When an electric field is applied, the electrons at the top of the valence band can move into other orbitals, resulting in a net movement of charge within the solid, hence metals are conducting solids.

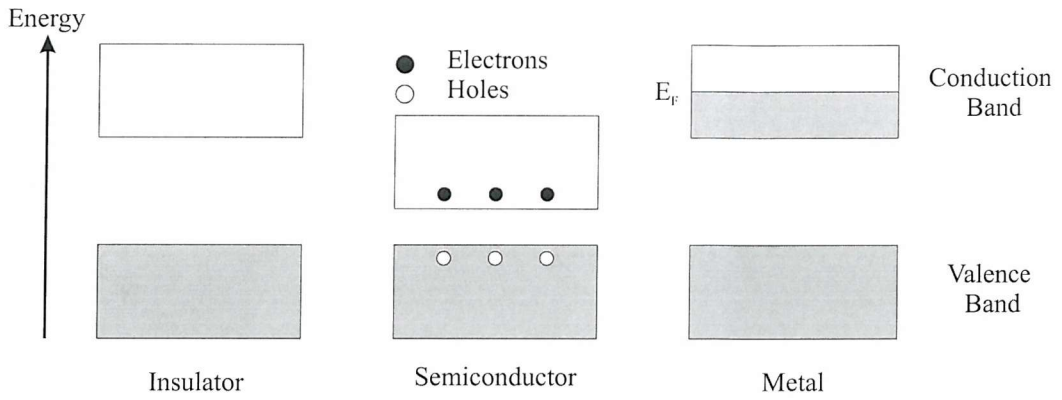

fig. 1.7: *Schematic illustration of the energy bands in (left) an insulator, (middle) a semiconductor and (right) a metal, where E_F represents the Fermi level.*

1.6.3 SEMICONDUCTORS AND COLOUR

The colour of a solid is governed by the energy gap that separates the valence and conduction bands *i.e.* the band gap. In order for a transition to take place an electron must be excited across this band gap and be promoted into the conduction band from the valence band. If the band gap is relatively large then visible light photons are not energetically sufficient to excite electrons into the conduction band. The material then appears transparent to these wavelengths. Such an example is the white pigment TiO_2, which is an excellent insulator. If the minimum energy is much smaller, lying in the infra-red region of the spectrum, the solid will absorb (and reflect) all of the visible spectrum and will appear metallic in nature, such is the case of graphite, which is semi-metallic and dark grey / black in colour. If however the band gap falls in the visible region the solid will absorb all photons with an energy greater than the band gap but not those with a smaller energy. This causes the material to be intensely coloured. There is essentially little difference between semiconductors and insulators apart from the band gap energies and indeed some insulators can appear coloured whereas some semiconductors have very small band gaps and appear black.

This theory can be used to reason the colours of some pigments. For instance vermilion, manufactured from the mineral cinnabar or mercuric sulfide (HgS), has a band gap energy of 3.2×10^{-19} J (2.0 eV)[30] This corresponds to the red-orange end of the visible region. Photons of a shorter wavelength than this, thus more energetic, will be absorbed. The perceived colour of the pigment is due to the photons that have not been absorbed, *viz.* red and orange. Another example is cadmium yellow or cadmium sulfide (CdS). This pigment has a band gap of 4.16×10^{-19} J (2.6 eV),[30] which corresponds to the green-blue part of the visible spectrum. Photons of a lower energy, red, orange, yellow and some green, will not be absorbed whilst the higher energy greens, blue, indigo and violet will be absorbed. The net result of this is that the material appears yellow.

By making solid solutions of semiconductors these band gaps can be finely tuned. This can be exemplified with cadmium sulfide (CdS) and cadmium selenide (CdSe). Both these compounds adopt the wurtzite crystal structure (a form of ZnS). CdSe has a small band gap, 2.56×10^{-19} J (1.6 eV). It absorbs all wavelengths of visible light and hence appears black. As sulfur and selenium are of similar sizes, substitution can occur readily such that a solid solution can be synthesised of general formula, $CdS_{1-x}Se_x$. When $x = 0$, the band gap is appropriate to that of CdS and as x increases the band gap value tends towards that of CdSe. Likewise the perceived colour changes from the yellow of CdS to orange to red and finally to the black of CdSe. By means of proof the material $CdS_{0.25}Se_{0.75}$ is the pigment cadmium orange.

1.7 PERCEPTION OF COLOUR

1.7.1 HOW THE EYE DISTINGUISHES COLOUR

It is difficult to define what exactly colour is. It refers to a physiological response of the brain invoked by light waves falling upon the light sensitive retina, the inner surface of the eye. There are two types of light receptor within the retina, cone cells and rod cells. In order to perceive colour we utilise cones in the retina of the eye. There are three types of cones, each sensitive to different wavelengths of light, which approximately correspond to red, blue and green lights. Together with information from rod cells, which are sensitive to changes in light and dark, the cone information is encoded. This information is sent along the optic nerve to higher brain centres. The encoding is known as opponent process theory.[31] It comprises

three opponent channels which are: red-green, blue-yellow and black-white. As these signals are opposing it is not possible to perceive green shades of red nor is it possible to perceive yellow shades of blue. Nevertheless you can see red and green shades of blue and yellow.

1.7.2 COLOUR PARAMETERS

The *Commission Internationale de l'Eclairages* (CIE) has defined the following terms to be applied to human colour descriptions.

BRIGHTNESS:

'*The attribute of visual sensation according to which an area appears to exhibit more or less light. (An image may be blurred or enhanced by modification of this attribute.)*'

The lightness or brightness value describes the intensity of the colour by the number of photons reaching the eye.

HUE:

'*The attribute of a visual sensation according to which an area appears to be similar to one, or to proportions of two, of the perceived colours red, yellow, green and blue.*'

The hue corresponds to the wavelength of the radiation and hence is given a colour name such as red or blue.

SATURATION:

'*The attribute of visual sensation according to which an area appears to exhibit more or less of its hue. (Sky blue is transformed to a deep blue by changing this attribute.)*'

Saturation, also known as chroma or indeed *colourfulness,* corresponds to the amount of white light mixed in with the hue. Hence this allows pastel colours to be described.

On average a human eye is able to distinguish more than a million different colours. All are as a result of colour mixing, which can be either additive or subtractive. The colours of the spectrum are termed chromatic colours whereas those that do not appear in the spectrum, such as brown, are termed non-chromatic.

1.8 QUANTIFICATION OF COLOUR

1.8.1 ADDITIVE COLOURATION

Colours can be conveniently represented by a three-dimensional co-ordinate system. Typically it is represented as a cylinder where the hue is arranged around the periphery of the cylinder, the saturation the radius and the lightness the central axis. This is commonly known as the Munsell colour cylinder. When two or more beams of different coloured light are combined, additive colour mixing occurs. Therefore mixing of three additive primary colours; red, green and blue can produce the majority of colours. Hence the components of a particular colour are known as its tristimulus values; *r*, *g* and *b*. This is known as the RGB colour model and can be represented in a chromaticity diagram. This is a triangle that has red, green and blue at each of the vertices and white in the centre as equal mixing of the three primary colours produces white. Hence co-ordinates can be given to locate a colour in terms of *r*, *g* and *b*. It represents hue and saturation but not lightness. An example of additive colour mixing is to be found in television screens that comprise small dots of three different phosphors, each shining with one of the primary colours when an electron beam falls onto it.

1.8.2 SUBTRACTIVE COLOURATION

Subtractive colour mixing is a result of absorption and selective reflection or transmission of light. Colour due to absorption is caused by certain wavelengths of incident radiation being more strongly attenuated than others. Examples include stained glass or colour filters whereby a red colour filter absorbs all colours except red light, which it transmits.

The three subtractive primary colours are cyan, magenta and yellow. Cyan absorbs red light but transmits blue and green. Magenta absorbs green light but transmits red and blue. Finally yellow absorbs blue light and transmits red and green. If these three subtractive colours are mixed then we obtain black as selectively all colours are removed by absorption. This is known as the CMYK colour model. If only a small wavelength range of light is absorbed then the remaining colour is said to be its complementary colour. For example, when blue light is absorbed the resulting complementary colour is yellow.

1.8.3 COLOUR SPACES

The ability to quantify colour is important in the pigment industry such that comparisons can be made. The colour of a pigment can be influenced by the medium it is colouring and as such

different colour measurements for the same pigment with identical particle size can be taken. There are various systems for representing, creating and visualising colour and these are known as colour spaces. In effect a colour space is like a mathematical representation of perception.

There are several different colour spaces on account of the fact that some lend themselves better to certain situations than others. The RGB colour space lends itself to computer monitors and television sets whereas the CMYK colour space is used in printing. The primary colours used by artists, cyan, magenta and yellow, are different to the primaries of computer devices because they are concerned with mixing pigments rather than lights or dyes.

The CIE recommended a pair of three dimensional colour spaces in 1976.[32] The CIE 1976 $L^*u^*v^*$ or CIELUV colour space is a linear transform of the x, y chromaticity co-ordinates and is often used in additive colour mixing applications such as television. The CIE 1976 $L^*a^*b^*$ or CIELAB system, like CIELUV, is suitable for expressing differences in colour as it is designed to provide approximate perceptual uniformity. It is employed when dealing with subtractive colourant mixtures such as those found in the textile, plastic, paint, and printing industries. Hue and chroma attributes can be easily derived from a^*, b^* by converting the rectangular a^*, b^* axes into polar co-ordinates. See experimental techniques (*Chapter 2*) for further information on colour measurements.

1.9 MIXED ANION OXYNITRIDE SYSTEMS

1.9.1 METAL OXYNITRIDES

In this research, mixed anion systems are being synthesised in order that they may be combined with mica to form lustre pigments of various hues. The systems that have been targeted in this study are oxynitride systems.

The synthesis of solid solutions of the perovskite systems $CaTaO_2N$ and $LaTaON_2$ have been investigated by Jansen[33,34] with a view to replacing cadmium based red and yellow pigments. These are promising candidates for properties such as brilliance, tinting strength, opacity, dispersability, light-fastness and heat stability rival those of cadmium pigments. Within the $Ca_{(1-x)}La_xTaO_{(2-x)}N_{(1+x)}$ system, the colour of a compound can be tuned from bright yellow to deep red depending on the O to N ratio.[33] Other systems under investigation as

potential pigment candidates include $Ta_{(3-x)}Zr_xN_{(5-x)}O_x$[35] and rare earth tungsten oxynitrides.[36]

As mentioned earlier the colour of a solid arises from selective absorption of light. This occurs due to an electronic interband transition, which leads to a steep absorption edge in the visible spectrum. The extent to which valence orbitals overlap governs the width of the band gap, the distance between conduction and valence bands. This width also alters according to the differences in electronegativity of the cations and anions involved. Using these factors an idea has been deduced that allows *a priori* design of the band gaps within semiconductors. It was the notion of Jansen *et al.* to adopt such ideas in order to develop novel inorganic pigments.[33] They have concentrated on widening or narrowing the band gap by increasing or decreasing the electronegativity difference between cationic and anionic elements respectively. In order to fine tune the band gap they focussed on materials with different non-metals, as the shift in electronegativity is far greater compared to that of metals.

The vast majority of metal oxides have very wide band gaps, too wide to permit absorption in the visible region of the electromagnetic spectrum. Hence compounds such as Ta_2O_5 are white. By introducing nitrogen into the anionic framework the band gap energy can be reduced as nitrogen has a lower electronegativity than oxygen. This reduction can be up to *ca.*1 eV. The energy of the 2*p* orbitals on oxygen and nitrogen, the valence orbitals, have been calculated and given the values $E_{2p}(O) = -14.8$ eV and $E_{2p}(N) = -13.4$ eV. [37,38]

1.9.2 THEORETICAL CONSIDERATIONS

Covalent or non-polar character increases either with an increase in anion size or with an increase in anionic charge such as the replacement of an oxygen anion (O^{2-}) for a nitrogen anion (N^{3-}). The electrons in anions of greater charge or greater size are more loosely held making them more easily polarised by cations thus the degree of covalency increases.[39] Whereas metal oxides are generally deemed to be ionic solids it is assumed that oxynitrides have what is referred to as ionocovalent character,[40] the ionic character is more significant than the covalent character as the metal elements associated with nitrogen become more electropositive.

There are two ways of maintaining electroneutrality within the compound. It is possible either to replace three oxygen atoms with two nitrogen atoms and a vacancy:

$$2N^{3-} + 1\square \equiv 3O^{2-}$$

This does not alter the cationic framework. It is most favourable in crystal structures with enough flexibility to withstand defects and anionic vacancies.[41] Such examples are the rare earth and tungsten oxynitrides with fluorite type structures.[36,42]

The second method does so by introducing a cation in a higher oxidation state to compensate for the extra charge in the anionic framework from the trivalent nitrogen. This process is formally known as the cross-substitution principle, hence:

$$N^{3-} + M^{(n+1)+} = O^{2-} + M^{n+}$$

This allows the same structure type to remain after nitrogen substitution into an oxide lattice. In this case a known oxide system is targeted, such as the perovskite $Ca^{2+}Ti^{4+}O_3$. In order to accommodate nitrogen into the framework one or more of the cations must be replaced. In other words substituting the titanium for tantalum yields $Ca^{2+}Ta^{5+}O_2N$ whereas substituting both Ca and Ti for La and Ta respectively allows for more nitrogen incorporation producing $La^{3+}Ta^{5+}ON_2$. In both cases the perovskite structure remains intact. Substitutions can result in significant modification to the physical and chemical properties of the compounds, such as a dramatic change in colour or its dielectric properties.[35,43-45]

1.9.3 NITRIDE PERSPECTIVE

Combining nitrogen with less electronegative elements results in nitrides[46-51] where the nitrogen adopts a trivalent state with a formal charge of –3. However, nitrides are far less common than oxides because of the large triple bond energy of N_2 equalling 941 kJ mol^{-1} *cf.* 500 kJ mol^{-1} for the O_2 double bond.[52] Compared with metal oxides, work on metal nitrides is still in its infancy. Interest is high due to the high polarisability of the nitride ion N^{3-}. This is understood to explain changes in structure and bonding *cf.* parent oxides and thus the modification of properties.[46]

Lanthanides have a great affinity for nitrogen as they are quite electropositive (1.1 to 1.5 on Pauling's electronegativity scale) hence a stable class of nitrides is that of the rare earth nitrides. Transition metal nitrides are essentially metallic in character and can be thought of

as insertion compounds where nitrogen is inserted into the metal network. Iono-covalent nitrides can have more or less significant ionic or covalent character depending on the elements present within the system. For example, in Ln-M-N ternary nitrides it is the M element that defines the nature of the bonding.[53] If M represents the electropositive lithium the bonding is essentially ionic, whilst replacing with silicon lends to more covalent bonding. As N lies directly between oxygen and carbon its compounds can have similarities to either metal carbides (metallic) or metal oxides (ionic). This helps explain the two different classifications of nitrides.

To synthesise nitrides directly with N_2 requires high temperatures and an absence of oxygen. An inert atmosphere prevents the preferential oxidation or the attack of any forming nitride by O_2.[47] Nitrogen is always released in its elemental form N_2, no other species such as NO and NO_x have ever been detected.[54]

$$\text{NITRIDE} + O_2 \rightarrow \text{OXIDE} + \uparrow N_2$$

Ammonia gas is often used to target nitrides and oxynitrides. At temperatures greater than 823 K NH_3 decomposes into active species that are able to nitride and reduce the starting materials to form oxynitrides and nitrides, hence reaction temperatures in excess of 550 °C should provide a reactive atmosphere to ammonolysise oxide mixtures.[36] Ammonia therefore plays two roles in this reaction, nitridation and reduction.

There are no well established rules as to why a nitride or oxynitride forms, rather each system responds differently to the intrinsic (reaction components) or extrinsic (flow rate, temperature, sintering time *etc.*) parameters applied during the reaction.[41] The flow rate of ammonia can be critical, too little and an oxide will form and too much a nitride will form. Often it is linked to the temperature at which the reaction is to be carried out. As a rule the higher the temperature the higher the rate, thus minimising the dissociation of NH_3 into N_2 and H_2 before reaching the product.

1.9.4 OTHER ANION SYSTEMS

Other such species which, after appropriate substitution into the perovskite oxygen anion position, can be formed are bromides, chlorides, fluorides hydrides and sulfides.[55] Such

examples include $KMgF_3$,[56] $LiEuH_3$,[57] $BaZrS_3$,[58] $CsHgBr_3$ and $CsGeCl_3$.[59] The nitrides and carbides are known to form antiperovskites where the anion is located on the site of the B cation and concurrently the B cation replaces the anions yielding materials such as $GaCo_3C$ and $AgMn_3N$.[60] It is thus feasible that mixed anion systems which incorporate another anion as well as oxygen within the perovskite can be targeted such as oxyhalides and oxysulfides. An atom such as sulfur can also be incorporated into more complex structures yielding oxysulfides that are of interest as safer pigments.[61] There are already known sulfides based on γ-Ce_2S_3 and fluorosulfide (LnSF) pigment systems, on the market today as alternatives to cadmium red.

1.10 CRYSTAL STRUCTURES

Most complex oxynitrides consist of multi-dimensional units constructed from metal-anion polyhedra. The linked MO_xN_y polyhedra are able to form extended structures. There are several structure types that exist with oxynitride anionic networks as outlined in several papers and reviews by Marchand *et al.* Examples include the perovskite, scheelite or pyrochlore structures.[41, 53, 62]

1.10.1 PEROVSKITE STRUCTURE

Perovskites are a large family of crystalline ceramics that derive their name from the mineral $CaTiO_3$, known as perovskite after the Russian mineralogist who identified it, L A Perovski. Perovskite is a very abundant mineral on Earth and is of great interest to geologists, as it holds many clues to this planet's history. The structure is adopted by the majority of ternary phases. Interest in the perovskite structure escalated after the discovery of ferroelectricity in $BaTiO_3$[63] and numerous perovskite phases were found to exhibit similar properties.

The principal structure of a perovskite is a face centred cubic (*fcc*) lattice of the generalised form ABO_3 where typically the A atoms represent large electropositive cations, *i.e.* Ca^{2+} and La^{3+} and the B atoms represent small transition metal cations, *i.e.* Ti^{4+} and Ru^{4+}. The A cations occupy the corners and are co-ordinated to 12 oxygens, the O anions the faces and finally the B cations are in the centre of the unit cell and are each co-ordinated to 6 oxygens. They occupy the interstitial sites found at the centre of the octahedra created by the spheres of the atoms in the adjacent close packed layers.

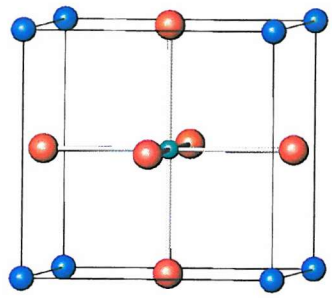

fig. 1.8: *B-centred cation arrangement of a perovskite, where the red spheres are oxygen anions, the blue spheres the A cations and the green sphere a B cation.*

It is also possible to show the 12 co-ordinate geometry of the A cations via an A-centred cation arrangement, *vide infra*. The extended structure may be described as a framework of corner-sharing BO_6 octahedra containing 12 co-ordination A cations, *fig. 1.9* also displays the 3D framework of a perovskite.

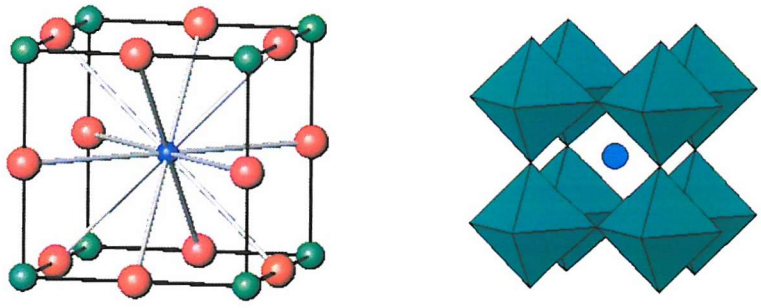

fig. 1.9: *(Left) A-centred cation arrangement of a perovskite, where the red spheres are oxygen anions, the blue sphere an A cation and the green spheres the B cations. (Right) The 3D network of the perovskite structure where the green polyhedra are BO_6 octahedra and the blue sphere an interstitial A cation.*

The perovskite structure is highly stable and can vary in several ways. Typically a distortion from ideal geometry towards a rhombohedral or orthorhombic geometry may be observed. In fact at ambient temperature very few perovskite materials adopt a cubic system, the original mineral $CaTiO_3$ itself has since been found to be orthorhombic.[64] The orthorhombic distortion within the perovskite structure was first determined for $GdFeO_3$[65] and so such distorted perovskites can be referred to as the $GdFeO_3$ structure. Other variations result from defects or vacancies in the structure where oxygen anions are missing and perovskites are

often considered to have an anionic stoichiometry of $3\text{-}\delta$ for correctness. The structural distortions to lower symmetries can be explained by way of strain. Perovskites are often under considerable strain, which is in part due to ionic sizes that are incompatible with ideal cubic geometry.

Both the sizes of the ions and the co-ordination sphere must be considered when assessing whether a ternary phase can adopt a perovskite structure. Obviously it is necessary for the A, B and O ions to be in contact in order for bonding to occur, thus considering the radius ratio rules, $r_A + r_O$ should ideally equal $\sqrt{2}(r_B + r_O)$, where r is the ionic radius. Goldschmidt deduced a tolerance factor for perovskite systems enabling a measure of compatibility between any two cations.[66]

Equation 1.3

$$r_A + r_O = t\sqrt{2}(r_B + r_O)$$

where r_A is the radius of cation A,
r_B is the radius of cation B,
r_O is the radius of anion O,
t is the tolerance factor.

For an ideal cubic close packed perovskite structure, $t = 1$. Deviations from this value indicate an increase in strain within the structure. Goldschmidt showed that the perovskite form was stable for $0.85 < t < 1.06$. The internal bond strain displayed within a structure can be overcome through distortions to lower symmetry, like the tilting of the BO_6 octahedra within the orthorhombic $GdFeO_3$ unit cell.

Studies by Galasso revealed that on occasion the A and B sites are occupied by two or more ions in varying oxidation states,[67] thus allowing the modification of properties to create new materials for use as thermistors,[68] semi-conductors[69] and more recently high temperature superconductors.[70,71]

Substitution of nitrogen for oxygen into the anionic network and thus concurrent replacement of a cation of lower valency for one of higher valency has led to novel perovskite-type oxynitrides.[34,72-80] Introducing nitrogen into the network yields interesting coloured materials due to the differences in electronegativities of oxygen and nitrogen.

Most oxynitride perovskites can be derived from the much studied compound $BaTiO_3$ via cross substitutions on one or more of the cation sites. Differences arise however in crystal systems and symmetries due to distortions within the structure. It is even possible to have the same element stoichiometry but different structural distortions for a compound depending on the intrinsic and extrinsic parameters altered. As an example, $SrTaO_2N$ has been reported as a cubic perovskite with a = 4.033(1) Å by Marchand[77] but when the reaction temperature was brought down to 850 °C and halide salt mineralisers incorporated into the starting materials a tetragonally distorted perovskite was reported, crystallising in the space group *I4/mcm*, a,b = 5.7049(3) Å and c = 8.0499(5) Å.[34] The group two metals can be exchanged for lanthanides leading to the inclusion of more nitrogen into the structure yielding $Ln^{III}B^{V}ON_2$. Again, various deformations have been reported. When firing at a higher temperature an orthorhombic perovskite $SmTaON_2$ is formed, of the type $GdFeO_3$.[76] In contrast to this $LaTaON_2$, when synthesised with mineralisers, adopts a monoclinic structure in the space group *C2/m*.[34] The slight deformation and thus loss of symmetry from ideal cubic geometry, as is the case for $GdFeO_3$ type perovskites, leads to an (8+4) co-ordination for the A site cations as opposed to the usual 12. It is also possible to synthesise perovskites with other transition metals such as the orthorhombic $NdTiO_2N$[73, 76] and $LaZrO_2N$[73] and the cubic $SrWO_2N$[72] and $BaNbO_2N$,[79] thus proving the versatile nature of the perovskite structure. Applications of such materials include use as dielectric materials as well as pigments.[43-45] Modifications to the properties of the parent oxides are best explained using the example of $LaTiO_2N$ and $NdTiO_2N$. They both contain titanium in the IV oxidation state and crystallise with a unit cell similar to $RTiO_3$ (R= Rare Earth). $LaTiO_3$ is metallic at T > –170°C[41] and $NdTiO_3$ a room temperature semiconductor, however both $LaTiO_2N$ and $NdTiO_2N$ present an insulating behaviour.

1.10.2 PYROCHLORE STRUCTURE

Materials adopting the pyrochlore structure belong to a family of ternary oxides, all isostructural to $(NaCa)(NbTa)O_6F/(OH)$,[81] the mineral pyrochlore. The generalised formula of a pyrochlore is $A_2B_2O_7$, but is also expressed as $A_2B_2O_6O'$ to distinguish the crystallographically non-equivalent anionic sites. The ideal pyrochlore structure crystallises within the cubic space group, *Fd-3m*.

Like the perovskite structure there are two different types of cation co-ordination environment. The A cation typically has a radius ~1 Å and is co-ordinated to 8 oxygen atoms

forming scalenohedra (distorted cubes) in a distorted (6+2) arrangement. The B cations are smaller, ~0.6 Å. They are co-ordinated to six, equidistant oxygen atoms resulting in trigonal anti-prisms within the 3D network. The arrangements of B cations are often regarded as BO_6 octahedra, though this is not technically correct with respect to the space group symmetry requirements.

The 3D network can be perceived as corner linked BO_6 octahedra with the interstices filled by A cations.[82] Due to the (6+2) surrounding oxygen arrangement, the eight co-ordinated A cation lies at the centre of a puckered hexagonal ring. By neglecting the A-O interaction, the structure can be regarded as interpenetrating networks of B_2O_6 and A_2O' units, as the A-O' bond distance is shorter than the A-O distance. The A_2O' linkages form zigzag chains and two such chains intersect at O'. Each unit cell contains 8 formula units (8 x $A_2B_2O_7$) and is displayed in *fig. 1.10.*

Similarities are drawn between the pyrochlore and perovskite structures as both can exist with different charge combinations, distortions, defects and vacancies. For example, the pyrochlore structure can feasibly exist without the A cations or a seventh oxygen anion and the pyrochlore structure too can be distorted from a cubic geometry.

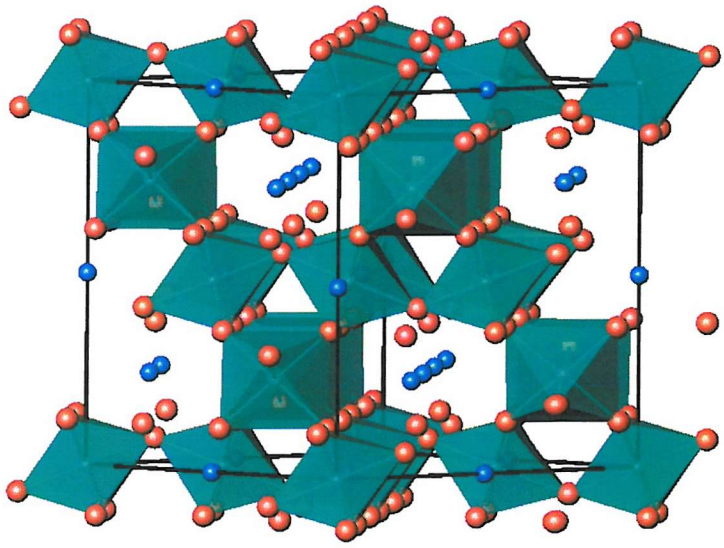

fig. 1.10: *Structure of the pyrochlore unit cell, $A_2B_2O_7$, showing the linked BO_6 octahedra (green), the A cations (blue) and the oxygen anions, including the non polyhedral anions (red).*

As with the perovskite structure, nitrogen can be substituted for oxygen leading to oxynitrides of the form $A_2^{III}B_2^{V}O_5N_2$ for instance.[83] These tend to provide a competing phase with the perovskite phase when synthesising oxynitrides from rare earth elements.[76] Pyrochlore type oxynitrides, of general formula $R_2Ta_2O_5N_2$, can be formed by ammonolysis of $RTaO_4$ (R = Nd→Yb, Y) precursors.[83] The stability of the pyrochlore phase increases with decreasing lanthanide R^{3+} radius. For lanthanum only the perovskite phase is known. For R = Nd→Dy the pyrochlore phase co-exists with a nitrogen rich perovskite. For Er→Yb and Y there is less competition and single phase pyrochlores can be isolated.[41] In $R_2Ta_2O_5N_2$ oxynitrides the distortions are greatest for the larger rare earth cations, the trigonal antiprisim around the tantalum atoms tends towards an octahedron. Smaller R cations are likely to adopt a defect fluorite structure.

Finally the cubic pyrochlore $Sm_2Mo_2O_{3.83}N_{3.17}$ (a = 10.4975(5) Å) has been synthesised by heating the oxide pyrochlore $Sm_2Mo_2O_7$ under NH_3 at milder temperatures (625 °C).[84] This highlights the nitriding or oxidising role of ammonia over its reducing role as the formal oxidation state on molybdenum increases from +4 to *ca.* +5.6.

1.10.3 Rutile Structure

Rutile is the mineral form of TiO_2 and has a hexagonally close packed anionic lattice. The cations occupy half of the octahedral holes which results in a tetragonal structure. This reflects the tendency of titanium to adopt an octahedral co-ordination. The structure consists of TiO_6 octahedra, which have oxide ions that are shared by neighbouring titanium ions. Each oxygen being surrounded by three Ti^{4+} ions and each Ti^{4+} cation surrounded by 6 O^{2-} anions.

TiO_2 is widely used as a white pigment and is often bound to mica to produce a pearlescent pigment with a nacreous lustre. F. Hund[85] highlighted that when titanium is partially substituted for other transition metal ions, it is possible to obtain coloured pigments.

1.10.4 Scheelite Structure

Another structure that can be adopted by oxynitrides is that of the scheelite-type structure. This is common amongst some tungsten oxynitrides, namely $LnWO_3N$ where Ln is a lanthanide.[86] This is based on the mineral scheelite, $CaWO_4$, where Ca is exchanged for a

cation in a higher oxidation state to compensate for the introduction of nitrogen into the framework.

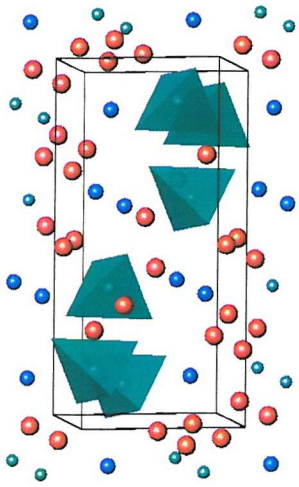

fig. 1.11: *Schematic of the scheelite type structure unit cell where the green polyhedra represent isolated WO_4 tetrahedra, the green spheres tungsten cations, the blue spheres calcium cations and the red spheres oxygen anions.*

It has been written that it is possible to stabilise high oxidation states within an oxynitride system such as W(VI)[86] in $LnWO_3N$ and Os(VIII)[87] in $RbOsO_3N$. Both are scheelite type structures where the central metal atom is in a tetrahedral environment. The O^{2-} ligand has a great ability to stabilise tetrahedral cations in high oxidation states, such as Cr(VI) in $(CrO_4)^{2-}$ and Mn (VII) in $(MnO_4)^-$.

The $LnWO_3N$ system is isostructural with $CaWO_4$ after cross substitution of Ca for a lanthanide, typically Nd, Sm, Gd or Dy. The structure is tetragonal ($I4_1/a$) with isolated tetrahedra $(WO_3N)^{3-}$ linked via Ln^{3+} cations of co-ordination number 8. Again there is competition from a more stable perovskite phase, which is favoured at higher temperatures and longer sintering times.[41] There are however two details which are *a priori* unfavourable in keeping tungsten in this high oxidation state. Firstly the reducing nature of ammonia and secondly tungsten is surrounded by nitrogen atoms and no corresponding tungsten nitrogen binary system exists such as WN_2. Only WN and W_2N are known.[53]

1.10.5 MISCELLANEOUS OXYNITRIDE STRUCTURES

There are many silicate oxynitride glasses and ceramics but these are not particularly relevant to this work. There is much in-depth study on compounds such as *sialons* (Si, Al, O and N). These are of interest in high temperature engineering applications owing to their excellent mechanical properties amongst others.[88-92]

Another phase adopted by oxynitrides is that of K_2NiF_4,[93-95] see *fig. 1.11*. Closely related to the perovskite family, several series have been published. Most notably there has been the determination of the R_2AlO_3N (R = La, Ce, Pr, Nd, Sm) series[96, 97] and also of M_2TaO_3N (M = Ca, Sr, Ba).[93] More recently the first example of a first transition series pseudotetrahedral oxynitride anion comes in the form of the grey-green Ba_2VO_3N.[98]

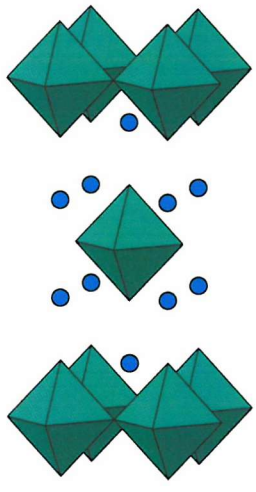

fig. 1.12: Schematic of K_2NiF_4-type unit cell where the green polyhedra represent NiF_6 octahedra, and the blue spheres K^+ cations.

Further structures to mention include the fluorite type which is adopted for some tungsten oxynitrides, *viz.* $R_{2.67}W_{1.33}(O,N,\square)_8$.[36,42] This is of significance as the fluorite structure is flexible and can accept vacancies without collapse. This is represented by the square in the anionic position. Also the bixbyite and fluorite zirconium titanium oxynitride[99] are of note, where the Zr is not sufficiently electropositive to stabilise Ti(IV) but can suppress the complete reduction to Ti(III).

1.11 SCOPE OF THIS WORK

Work in the area of inorganic pigments is of interest commercially as firstly current pigment systems can be costly, on account of the price of the metal ore starting materials. Secondly and more importantly several pigments on the market today contain toxic metals. Due to the desired characteristics of a pigment, *i.e.* stability, most of these pigments are quite safe but over time the risk of degradation and thus possible residues of heavy metals contaminating the environment is of worrying concern. Hence, laws have been introduced to restrict their use and the search for suitable alternatives initiated.

The hardest task to date has been to find bright red pigments and there has been nothing of worth that can rival both the properties and hue of cadmium red. Over recent years there has been a shift to organic based pigments to replace cadmium based pigments. This is not ideal as their production can cost up to 25-30 % more than inorganic pigments. Also yields of less than 80% are not uncommon for some organic pigments[100] *cf.* >90% for most inorganic systems. Another problem is that the thermal stability of an organic pigment is not sufficient for use in ceramic glazes and thermoplastics.

The aims of this study are to investigate coloured oxynitride systems with a view to obtaining a wider range of materials suitable for use as new pigments. Identification of suitable phases makes use of techniques such as powder X-ray diffraction, powder neutron diffraction, thermogravimetric analysis, UV-Vis. spectroscopy and colour measurements. *Chapters 3-6* detail the systematic optimisation of the perovskite system to target promising candidates for pigment applications. As the emphasis is with colour as opposed to the complete structural investigation only a proportion of the numerous samples generated are fully characterised. Attempts are also made to deposit candidate phases onto muscovite mica to extend the available colour range of lustre pigments. These materials were analysed with the help of electron microscopy imaging, as well as the techniques used for the oxynitride phases alone. The results of this study are summarised in *Chapter 7*.

1.12 REFERENCES

[1] Buxbaum G.; *Industrial Inorganic Pigments*, Wiley-VCH (Germany), Second Edition (1998)

[2] European Economic Community Guideline No. 91 / 338 / EWG (1991)

[3] Vilmin G.; *Chemistry & Industry*, "Green Process Gives Rare Earth Reds", **19**, 761 (1997)

[4] Jansen M., Letschert H. P.; *Oxynitride-based coloured pigments and process for their preparation*, European Patent No. 0697373 (1995)

[5] Zintl V.; German Patent 4, 22, 947 (1924)

[6] Du Pont; US Patent 40, 26, 722 (1976)

[7] Du Pont; US Patent 40, 63, 956 (1976)

[8] Du Pont; US Patent 41, 15, 141/2 (1976)

[9] Young R. S.; *Cobalt: Its Chemistry, Metallurgy and Uses*, Reinhold (USA), First Edition (1960)

[10] Guimet J.; *Bull. Soc. Enc. Ind. Nat.*, **27**, 346 (1828)

[11] Gmelin C.; *Bull. Soc. Enc. Ind. Nat.*, **27**, 216 (1828)

[12] Pfaff G., Reynders P.; *Chem. Rev.*, **99**, 1963 (1999)

[13] Ostertag W., Norbert M.; *Macromol. Symp.*, **100**, 163 (1995)

[14] Cramer W. R.; *Color Res. Appl.*, **27**, 276 (2002)

[15] Taylor H. F.; *Drugs, Oils, Paints*, **3**, 106 (1937)

[16] Budworth D. W.; *An Introduction to Ceramic Science*, Pergamon Press (UK), First Edition (1970)

[17] Merck KgaA; *Plastic Additives & Compounding*, "Pearl Lustre Pigments Give Plastics an Edge", 30 (2000)

[18] Junru T., Yunfang H., Wenxiang H., Xiuzeng C., Xiansong F.; *Dyes Pigments*, **52**, 215 (2002)

[19] Junru T., Xiansong F., Wenxiang H., Xiuzeng C., Li W.; *Dyes Pigments*, **56**, 93 (2003)

[20] Teaney S., Pfaff G., Nitta K.; *Eur. Coat. J.*, **4**, 90 (1999)

[21] Ohtsu K., Sato N. (Sakai Kagaku Kogyo KK); World Patent Application 97 / 40118 (1997)

[22] Anselmann R.; *J. Nanopart. Res.*, **3**, 329 (2001)

[23] Pfaff G.; *Anorg. Chem. In Unserer Zeit.*, **31**, 6 (1997)

[24] Pabst A.; *Acta Crystallogr.*, **12**, 733 (1959)

[25] Williams A.; *A Theoretical Approach to Inorganic Chemistry*, Springer-Verlag (Germany), First Edition (1979)

[26] Shriver D. F., Atkins P. W., Langford C. H.; *Inorganic Chemistry*, Oxford Science Publications (UK), Second Edition (1994)

[27] Atkins P. W.; *Physical Chemistry*, Oxford Science Publications (UK), Fourth Edition (1992)

[28] http://chemed.chem.purdue.edu/genchem/topicreview/bp/ch6/atom_emrframe.html

[29] Greenwood N. N., Earnshaw A.; *Chemistry of the Elements*, Pergamon Press (UK), First Edition (1984)

[30] Tilley R.; *Colour and the Optical Properties of Materials*, Wiley (UK), First Edition (2000)

[31] Hurvich L. M., Jameson D.; *J. Opt. Soc. Am*, **45**, 602 (1955)

[32] Commission Internationale de l'Eclairage; *CIE Technical Report*, **116** (1995)

[33] Jansen M., Letschert H.; *Nature*, **404**, 980 (2000)

[34] Günther E., Hagenmayer R., Jansen M.; *Z. Anorg. Allg. Chem.*, **626**, 1519 (2000)

[35] Günther E., Jansen M.; *Mat. Res. Bull.*, **36**, 1399 (2001)

[36] Diot N., Larcher O., Marchand R., Kempf J. Y., Macaudière P.; *J. Alloy. Compd.*, **323-324**, 45 (2001)

[37] Marchand R., Tessier F., Le Sauze A., Diot N.; *Int. J. Inorg. Mater.*, **3**, 1143 (2001)

[38] Hoffmann R.; *J. Chem. Phys.*, **39**, 1397 (1963)

[39] Douglas B., McDaniel D., Alexander J.; *Concepts and Models of Inorganic Chemistry*, Wiley (USA), Third Edition (1994)

[40] Marchand R.; *C.R. Acad. Sci.II C*, **2 (11-13)**, 669 (1999)

[41] Tessier F., Marchand R.; *J. Solid State Chem.*, **171**, 143 (2003)

[42] Marchand R., Antoine P., Laurent Y; *J. Solid State Chem.*, **107**, 34 (1993)

[43] Marchand R., Pors F., Laurent Y., Regreny O., Lostec J., Haussonne J. M.; *J. Phys.-Paris*, **47 (C-1)**, 901 (1986)

[44] Marchand R., Gervais F.; *Solid State Commun.*, **93**, 857 (1995)

[45] Fang C. M., de Wijs G. A., Orhan E., de With G., de Groot R. A., Hintzen H. T., Marchand R.; *J Phys. Chem. Solids*, **64**, 281 (2003)

[46] Kniep R.; *Pure Appl. Chem.*, **69**, 185 (1997)

[47] DiSalvo F. J.; *Mater. Sci. Forum.*, **325-326**, 3 (2000)

[48] King R. B.; *Can. J. Chem.*, **73**, 963 (1995)

[49] Brese N. E., O'Keefe M.; *Struct. Bonding (Berlin)*, **79**, 307 (1992)

[50] Gregory D. H.; *J. Chem. Soc., Dalton Trans.*, **3**, 259 (1999)

[51] Niewa R., DiSalvo F. J.; *Chem. Mater.*, **10**, 2733 (1998)

[52] DiSalvo F. J., Clarke S. J.; *Curr. Opin. Solid. St. Mat. Sci.*, **1(2)**, 241 (1996)

[53] Marchand R.; *Handbook on the Physics and Chemistry of Rare Earths*, Chapter 166: "Ternary and Higher Order Nitride Materials", **25**, 51 (1998)

[54] Le Gendre L., Marchand R., Laurent Y.; *J. Eur. Ceram. Soc.*, **17**, 1813 (1991)

[55] Galasso F. S.; *Perovskites and High T_c Superconductors*, Gordon and Breach (USA), First Edition (1990)

[56] Ludekens W. L. W., Welch A. J. E.; *Acta. Crystallogr.*, **5**, 841 (1952)

[57] Messer C. E., Hardcastle K.; *Inorg. Chem.*, **3**, 1327 (1964)

[58] Clearfield A.; *Acta Crystallogr.*, **16**, 134 (1963)

[59] Naray-Szabo I.; *Mulgyet Zoylemen*, **1**, 30 (1947)

[60] Nowtony H., Ettmayer P.; *J. Inst. Met.*, **97**, 180 (1996)

[61] Hernández-Alonso M. D., Gómez-Herrero A., Landa-Cánovas A. R., Durán A., Fernández-Martínez F., Otero-Diáz L. C.; *J. Alloy. Compd.*, **344**, 199 (2002)

[62] Marchand R., Laurent Y., Guyader J., L'Haridon P., Verdier P.; *J. Eur. Ceram. Soc.*, **8**, 197 (1991)

[63] Von Hippel A.; *RPTPB* 4660 (1994).

[64] Subramanian M. A., Calabrase J. C., Torardi C. C., Gopalakristashan J., Askew T. R., Flippen F. R., Morrisey K. J., Chowdry U., Sleight A. W.; *Nature*, **332**, 440 (1988)

[65] Geller S., Wood A. E.; *Acta Crystallogr.*, **9**, 563 (1956)

[66] Goldschmidt V. M.; *Skr. Nor. Vidensk. Akad. Kl 1: Mat. Naturvidensh. Kl* (1926)

[67] Galasso F. S., Katz L., Ward R.; *J. Am. Chem. Soc.*, **81**, 820 (1959)

[68] General Ceramics, *Oxide Thermoelectric Materials Final Rpt.*, Contract NOBS-78414 (1961)

[69] Galasso F. S., Derby W.; *Inorg. Chem.*, **1**, 71 (1965)

[70] Cava R. J., Batlogg B., Kajewski J. J., Favrovo R., Rupp L. W., White A. E., Short K., Pecks W. F., Komelan T.; *Nature*, **332**, 814 (1988)

[71] Chu C. W., Hor P. H., Meng R. L., Gao L., Huang Z. L.; *Science*, **235**, 567 (1988)

[72] Fawcett I. D., Ramanujachary K. V., Greenblatt M.; *Mat. Res. Bull.*, **32(11)**, 1565 (1997)

[73] Clarke S. J., Guinot B. P., Michie C. W., Calmont M. J. C., Rosseinsky M. J.; *Chem. Mater.*, **14**, 288 (2002)

[74] Weller M. T., Skinner S. J.; *Int. J. Inorg. Mater.*, **2**, 463 (2000)

[75] Grins J., Svensson G.; *Mat. Res. Bull.*, **29(7)**, 801 (1994)

[76] Marchand R., Pors F., Laurent Y.; *Ann. Chim. Fr.*, **16**, 553 (1991)

[77] Marchand R., Pors F., Laurent Y.; *Rev. Int. Hautes Tempér. Réfract. Fr.*, **23**, 11 (1986)

[78] Hellwig A., Hendry A.; *J. Mat. Sci.*, **29**, 4686 (1994)

[79] Pors F., Marchand R., Laurent Y.; *Mat. Res. Bull.*, **23**, 1447 (1988)

[80] Bacher P., Antoine P., Marchand R., L'Haridon P., Laurent Y., Roult G.; *J. Solid State Chem.*, **77**, 67 (1988)

[81] von Gaertner H. R.; *N. Jahr. Fuer Mineral. Geol. Pal.*, **61**, 1 (1930)

[82] Byström A.; *Ark. Kemi min. Geol.*, **18A**, 1 (1945)

[83] Pors F., Marchand R., Laurent Y.; *J. Solid State Chem.*, **107**, 39 (1993)

[84] Veith G. M., Greenblatt M., Croft M., Goodenough J. B.; *Mat. Res. Bull.*, **36**, 1521 (2001)

[85] Hund F.; Bayer, US Patent 30, 22, 186 (1959)

[86] Antoine P., Marchand R., Laurent Y.; *Rev. Int. Hautes Tempér. Réfract. Fr.*, **24**, 43 (1987)

[87] L'Haridon P., Pastuszak R., Laurent Y.; *J. Solid State Chem.*, **43**, 29 (1982)

[88] Hampshire S.; *Key Eng. Mat.*, **237**, 239 (2003)

[89] Hampshire S.; *Key Eng. Mat.*, **247**, 155 (2003)

[90] Hampshire S.; *J. Non-Cryst. Solids*, **316(1)**, 64 (2003)

[91] Das T.; *B. Mater. Sci.*, **23(6)**, 499 (2000)

[92] Navarro J. M. F.; *Glastech. Ber.-Glass*, **71(9)**, 263 (1998)

[93] Pors F., Marchand R., Laurent Y.; *Ann. Chim. Fr.*, **16**, 547 (1991)

[94] Assabaa-Boultif R., Marchand R., Laurent Y., Videau J-J.; *Mat. Res. Bull.*, **29**, 667 (1994)

[95] Diot N., Marchand R., Haines J., Léger J. M., Macaudière P., Hull S.; *J. Solid State Chem.*, **146**, 390 (1999)

[96] Marchand R.; *C.R. Acad. Sc. Paris*, **282C**, 329 (1976)

[97] Marchand R., Pastuszak R., Laurent Y.; *Rev. Chim. Miner.*, **19**, 684 (1982)

[98] Clarke S. J., Chalker P. R., Holman J., Michie C. W., Puyet M., Rosseinsky M. J.; *J. Am. Chem. Soc.*, **124**, 3337 (2002)

[99] Clarke S. J., Michie C. W., Rosseinsky M. J.; *Chem. Mater.*, **12**, 863 (2000)

[100] Novotny J.; *RSC Inorganic Pigments Conference*, London (1994)

CHAPTER TWO

EXPERIMENTAL TECHNIQUES

2 EXPERIMENTAL TECHNIQUES

2.1 POWDER X-RAY DIFFRACTION

2.1.1 X-RAY DIFFRACTION

Electromagnetic radiation can interact with a compound by being scattered from its original direction of propagation. If the energy is unchanged during this process it is deemed to be elastic scattering but if the frequency alters, thus altering the energy, scattering is inelastic. A very useful application of elastic scattering is X-ray diffraction. This technique arises from X-rays that are scattered by individual atoms within a crystalline sample. Interference can occur between these scattered X-rays, giving rise to a characteristic pattern of diffraction intensity.

There are certain requirements for X-ray diffraction, which are as follows:

i) The material must contain a periodic distribution of scattering matter, with repeating lattice spacings on a scale similar to X-ray wavelengths.

ii) The wavelength of the incident radiation is of a similar order of magnitude to the periodic repeat distances of scattering matter.

iii) The scattering is elastic and coherent.

Max von Laue[1] identified that, due to the similarity of the magnitude of the interatomic spacings within a crystal and the wavelength of X-rays (*ca.* 10^{-10} m), crystals can act as diffraction gratings for X-rays.

2.1.2 X-RAY RADIATION

X-rays are electromagnetic radiation with wavelengths of around 100 pm that are usually produced by bombarding a metal target with high energy electrons. The electrons decelerate as they enter the metal and generate radiation with a continuous range of wavelengths called *Bremsstrahlung*.[2] Superimposed on the continuum are several sharp discrete peaks of high intensity. These lines have arisen from collisions of the incoming electrons with the electrons in the inner shells of the atoms, *i.e.* core electrons; typically the atoms are of a high atomic number, to yield high energy photons in the X-ray region. A collision results in an electron being ejected from a core orbital within a metal atom and an electron in a higher energy

orbital decaying into this vacancy. The excess energy is emitted as an X-ray photon. These X-rays are quantised and are given symbols to represent the transition that is occurring.

2.1.3 POWDER X-RAY DIFFRACTION THEORY

Powder X-ray diffraction (PXD) is a technique developed by Peter Debye and Paul Scherrer[3] that uses a crystalline powdered sample and monochromatic radiation. It is a non-destructive technique that can be used to determine lattice parameters, locations of atoms within a unit cell, sample purity and defects within a crystal structure. It can also identify different phases of a compound if it exists as polymorphs.

Table 2.1: Expressions for d_{hkl} values in the different crystal systems.[4]

Crystal System	Expression for d_{hkl}
Cubic	$\frac{1}{d_{hkl}^2} = \frac{h^2 + k^2 + l^2}{a^2}$
Tetragonal	$\frac{1}{d_{hkl}^2} = \frac{h^2 + k^2}{a^2} + \frac{l^2}{c^2}$
Orthorhombic	$\frac{1}{d_{hkl}^2} = \frac{h^2}{a^2} + \frac{k^2}{b^2} + \frac{l^2}{c^2}$
Hexagonal	$\frac{1}{d_{hkl}^2} = \frac{4}{3}\left(\frac{h^2 + hk + k^2}{a^2}\right) + \frac{l^2}{c^2}$
Monoclinic	$\frac{1}{d_{hkl}^2} = \frac{1}{\sin^2\beta}\left(\frac{h^2}{a^2} + \frac{k^2\sin^2\beta}{b^2} + \frac{l^2}{c^2} - \frac{2hl\cos\beta}{ac}\right)$
Triclinic	A more complex expression due to the low symmetry of the crystal system.

A crystal is comprised of an infinite set of parallel planes that pass through lattice points. These planes can be described by the Miller indices, h, k and l whereby each hkl represents a set of planes separated by a perpendicular distance, d_{hkl}. They are defined by the reciprocal values of the positions where a plane intersects the a, b and c axes within a unit cell respectively. The Miller notation avoids the use of ∞ and fractions in illustrating the distance at which a plane would intersect the a, b and c axes by taking the reciprocal of the labels. Hence, h, k and l are integers that are positive, negative or zero. The relationship between d_{hkl}

and the lattice parameters of a unit cell is dependent upon the crystal system and can be determined via geometry. These relationships are summarised in *Table 2.1.*

The wavelengths of X-rays are comparable to the separations of the lattice planes and will therefore diffract when passed through a crystal in accordance with the Bragg Law, which is:

Equation 2.1

$$n\lambda = 2d\sin\theta$$

where n is an integer, 1,2,3…

λ is the wavelength of incident X-rays,

d is the separation of lattice planes,

θ is the glancing angle of the X-rays.

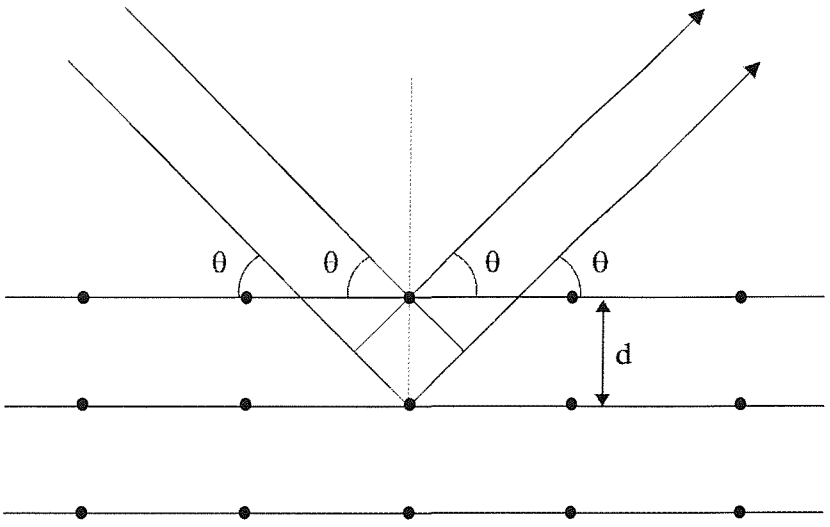

fig. 2.1: *Schematic representing diffraction from individual point scatterers aligned in parallel planes.*

If a radiation beam hits a sample with an incidence angle of θ and is scattered by atoms lying in planes separated by a distance d, then constructive interference and thus a diffraction maximum would occur if the pathlength difference is an integral number of wavelengths. The d-spacings in the crystal can be calculated via measuring the diffraction maxima. In general only the first order maxima, where $n = 1$, are visible in a PXD pattern. At angles other than the Bragg angle destructive interference occurs. This arises as the diffracted beams are out of phase and therefore can cancel each other out.

The powders used contain crystallites of random orientations. Therefore, there are some crystallites with the correct orientation such that their planes can give rise to a diffracted intensity at a particular glancing angle. These crystallites lie in all possible angles around the incident radiation beam. Hence, the diffracted beam lies on a cone around the incident beam of half angle 2θ. Each set of (*hkl*) planes leads to a separate diffraction cone which results in a diffraction maxima or *reflection peak* in the diffraction pattern.

In theory, a crystal should display diffraction from all lattice planes. However, intensity is not always observable for every plane as a result of defects and systematic absences within the lattice.

2.1.4 INSTRUMENTATION FOR POWDER X-RAY DIFFRACTION

The powder patterns were measured on one of two machines, a Siemens D5000 and a Bruker D8. These diffractometers, see *fig. 2.2*, use the copper $K_{\alpha 1}$ radiation emission, λ=1.5406 Å, with a primary germanium single crystal monochromator to filter out $K_{\alpha 2}$ radiation. The two emissions arise from the differing energy states of the *p* electrons *i.e.* they are not quite degenerate. Cu-$K_{\alpha 1}$, refers to the source of the X-rays.

In the copper target vacant 1*s* orbitals are generated, the symbol K denotes the filling of vacant orbitals from shells described by the principle quantum number 1, *i.e.* 1*s*. In copper atoms this is achievable by decay from the 3*p* or 2*p* levels. The X-rays generated by L electrons descending into K shells, 1*s*←2*p* transitions, are termed K_{α}. Those generated by M electrons descending into K shells, 1*s*←3*p* transitions, are termed K_{β}. The numeric subscript term arises from the spin alignments in the *np* level. A transition that fills a shell described by the principal quantum number 2, *i.e.* 2*s* and 2*p* shells, is given the symbol L and so on through the alphabet.

A monochromator is employed in order that a single wavelength can be harnessed for use in a powder diffraction experiment. A single crystal or a metal foil filter can be used for this purpose. This radiation is collimated by aperture slits as shown in *fig. 2.2*.

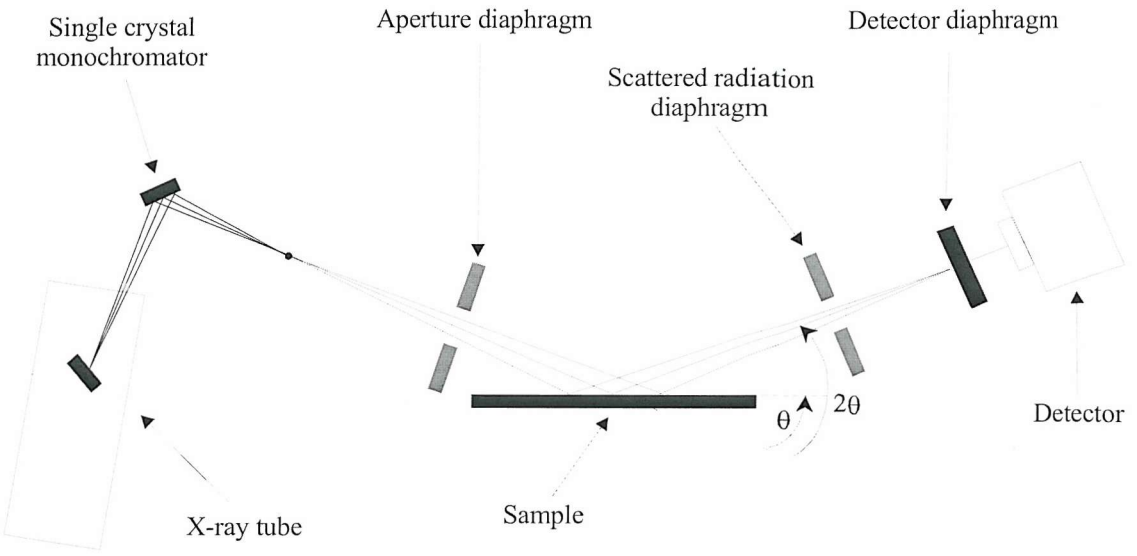

fig. 2.2: *Schematic diagram of the powder X-ray diffractometer, where the lines represent the path of the X-ray beam.*

In order to carry out a diffraction experiment the powder is mounted into a recess within an aluminium or plastic sample holder and is packed down such that it is flush with the edge of the holder leaving a flat level surface for analysis. This is placed inside the diffractometer and is rotated at constant angular velocity as the measurements are taken. The scintillation detector is rotated at twice that velocity between pre-set values; in other words, it moves as a function of 2θ, thus the incident beam, sample and detector are arranged according to the Bragg Brentano geometry.

The data were captured and manipulated using a personal computer. Initial characterisation was performed by recording PXD patterns, typically over the 2θ range 10 - 60° with a step size of 0.02° for 10 minutes. These measurements were used for phase identification and indexing performed using the software Diffrac^{plus} evaluation program[5] (*EVA*) and *CELREF*[6] respectively, see *Section 2.3.2*.

To obtain a more accurate idea of lattice parameters slower scans over wider 2θ ranges (typically 10-110°) were used. Further structural analysis from these data sets involved using the Rietveld method, as discussed in *Section 2.3.3*.

2.1.5 *VARIABLE TEMPERATURE POWDER X-RAY DIFFRACTION*

PXD equipment may be combined with either a cryostat or a furnace in order to obtain variable temperature PXD data. In this work data sets were collected over the temperature range 100-1200 °C on the Bruker D8 diffractometer fitted with an Anton Paar high temperature camera 1200 (HTK 1200) furnace stage to analyse the evolution of structural and phase changes with increasing temperature. It is also possible to carry out data collections under an atmosphere other than air, such as N_2 or under vacuum.

The sample was mounted in an alumina holder and placed in a sealed chamber, which was the heating environment. The incident and diffracted X-rays entered and exited this chamber through the Kapton windows as seen in the schematic below.

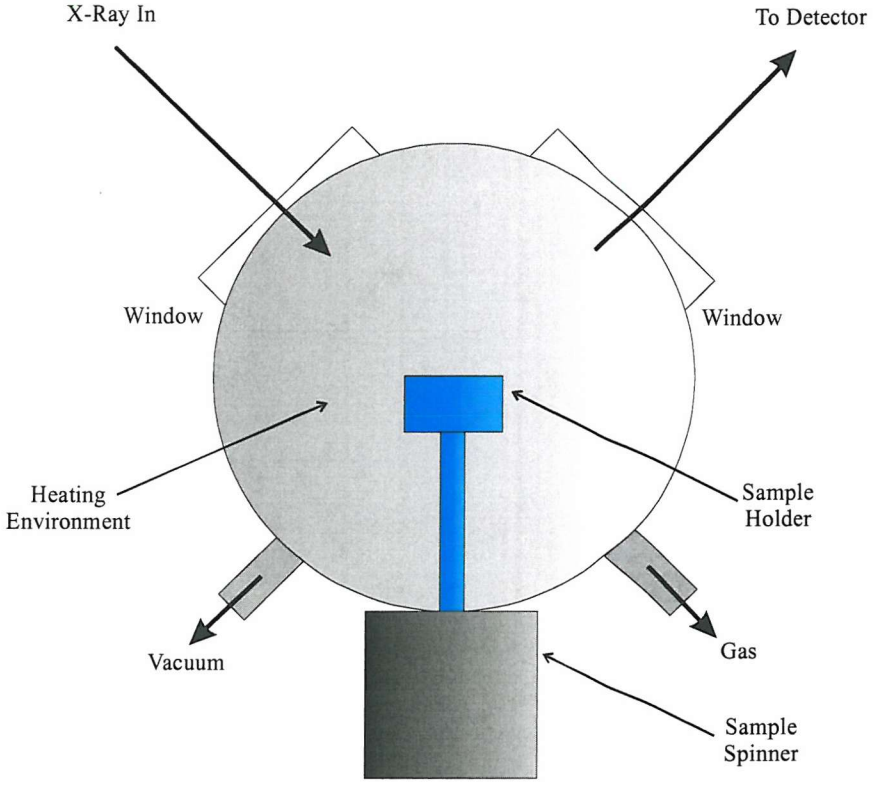

fig. 2.3: *Schematic of the Anton Paar HTK 1200 furnace stage used in conjunction with a Bruker D8.*

When collecting data using the HTK sample stage a different detector is required. Instead of a scintillation counter, a position sensitive detector (PSD) is employed.

2.1.6 PARTICLE SIZE ESTIMATION

The polycrystalline samples generated in this work often give rise to broad peaks in their PXD profiles. This peak broadening is related to decreasing crystallite size in accordance with the Scherrer formula.

Equation 2.2

$$t = \frac{0.9\lambda}{\sqrt{B_M^2 - B_S^2}\cos\theta}$$

where t is the crystallite thickness,

λ is the X-ray wavelength,

θ is the Bragg angle which is half the measured diffraction angle,

B_M is the width in radians of a diffraction peak of the sample at half height,

B_S is the width in radians of a diffraction peak of a standard at half height.

This method does tend to underestimate the true particle size as it is essential to have a highly crystalline standard as a reference but nevertheless provides useful measurements for comparisons.

2.2 POWDER NEUTRON DIFFRACTION

2.2.1 POWDER NEUTRON DIFFRACTION THEORY

It was recognised in 1936 that wave mechanics could be applied to describe the motion of neutrons. This idea heralded the first neutron diffraction experiments.

Powder neutron diffraction (PND) is similar to X-ray diffraction and arises as the wavelength of a neutron beam, dependent to some degree on temperature, is similar to that of atomic spacings. The crystal structure is obtained via ascertaining the position of the nuclei. The neutrons scatter from materials via the interaction of the radiation with the nuclei as opposed to the electron cloud, as with X-rays. Hence the scattering power of an atom is only weakly related to the atomic number. The converse is true for X-ray radiation where the scattering power increases as the number of electrons increases.[7]

The scattering power of an atom is related to a combination of factors. Firstly, potential scattering, which itself is dependent upon the number and the size of particles within the nucleus. Secondly, it is associated with resonance scattering, a consequence of a bound state temporarily formed by the neutron with the nucleus.

Neutron diffraction is advantageous for locating hydrogen and other light elements in solids containing heavier elements, such as oxygen in metal oxides, though samples containing hydrogen require deuterating due to the incoherent scattering of the ^{1}H isotope. The incoherent scattering cross section is much larger than that of other elements and can be reduced when hydrogen is exchanged for deuterium, which in turn makes it easier to differentiate reflections from the background profile. It is also good for distinguishing silicon and aluminium and other pairs of elements with similar atomic number, such as oxygen and nitrogen, as neighbouring elements can have different scattering cross sections.

PND probes the bulk of the solid, for the interaction between a neutron and an atomic nucleus is weak, as a neutron carries no charge. It is also a non-destructive technique.

2.2.2 TIME OF FLIGHT POWDER NEUTRON DIFFRACTION

PND was carried out at the ISIS facility at the Rutherford Appleton Laboratory (RAL). This is a neutron spallation source, meaning that neutrons are generated by bombarding a metal target, such as tantalum, with high energy protons from an accelerator. This produces a pulsed source of neutrons, which can be used for diffraction on account of the wave-particle duality theory stated by de Broglie.

Equation 2.3

$$\lambda = \frac{h}{m_n v_n}$$

where λ is the wavelength,

h is Planck's constant,

m_n is the mass of a neutron,

v_n is the velocity of a neutron.

The mode of operation of a pulsed neutron source diffractometer is fundamentally different to X-ray diffractometers mentioned in the previous section. In the conventional X-ray

diffraction experiment described in *Section 2.1* the variables within the Bragg equation are θ and d, with λ fixed, however in this case d and λ are varied and θ remains fixed. It is necessary therefore to measure the time of flight (TOF) of a neutron over a known flight path, from source to sample to detector, in order to determine λ. A time of flight diffractometer measures the Bragg reflections at fixed scattering angles and records the time of arrival of a neutron after the initial pulse produced at the target.[8] Conventional diffractometers measure the Bragg reflections by scanning a detector over the angle range required for study.

The relationship between d-spacing and TOF can be derived from de Broglie's law stated in *Equation 2.3* and also Bragg's law, *Equation 2.1*.

Equation 2.4

$$\lambda = \frac{h}{m_n v_n} = 2d\sin\theta$$

If one considers a primary flight path, from moderator to sample, to be a distance l_1 and a secondary flight path, from sample to detector, to be a distance l_2, the corresponding flight times would be t_1 and t_2 respectively. Remembering that velocity is distance over time one can substitute for velocity in the following manner:

Equation 2.5

$$\frac{h}{m_n}\left(\frac{t_1 + t_2}{l_1 + l_2}\right) = 2d\sin\theta$$

Hence with a total neutron flight path $l_1 + l_2 = l$ and total time of flight $t_1 + t_2 = t$ then:

Equation 2.6

$$t = 2dl\left(\frac{m_n}{h}\right)\sin\theta$$

This shows that there is a linear relationship between t and d such that $t \propto d$. This means therefore that for a 12 metre instrument such as POLARIS, a 1 Å d-spacing reflection will be detected in a backscattering bank at a TOF of ~5000 μs.

2.2.3 *INSTRUMENTATION FOR POWDER NEUTRON DIFFRACTION*

The instrument used was POLARIS, a medium resolution, high intensity powder diffractometer with the large detector bank and intense neutron flux providing a high counting rate. This diffractometer is ideal for small samples, typically in the range of 1-2 g. Good quality data can be obtained from simple structures in relatively fast time.

A polychromatic or white beam of neutrons is received from an ambient temperature water moderator. The sample is positioned at a distance 12 m away from the moderator and the incident and transmitted neutron flux is monitored via the use of two glass scintillator detectors before and after the sample. The dimensions of the beam can be altered using collimators within the incident beam in order to match the sample size or reduce the background noise produced from the equipment in the sample environment.

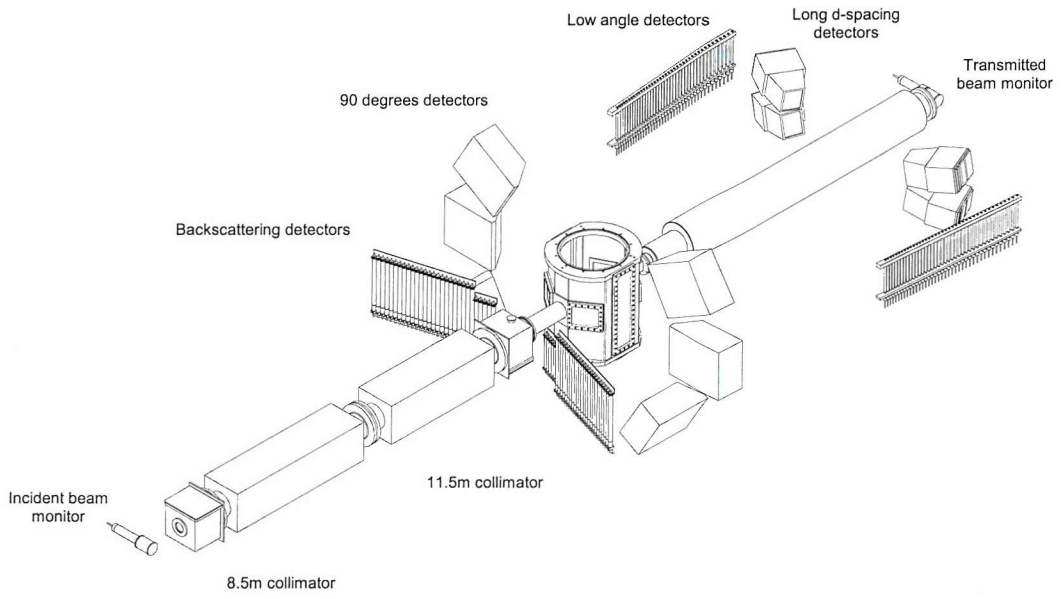

fig. 2.4: *Schematic of powder neutron diffractometer POLARIS at the ISIS facility situated at the Rutherford Appleton Laboratory (RAL).*[8]

Samples to be studied are placed inside vanadium cans within an evacuated sample chamber. Several detectors are employed to record the scattered neutrons, though the backscattering bank (C) yields the highest resolution data over the *d*-spacing range 0.2 - 3.2 Å and is the most commonly used data set in refinements.

2.3 STRUCTURAL REFINEMENT

2.3.1 REFERENCE MATERIALS

In order to index peaks and calculate lattice parameters some kind of reference material is required to compare the positions of diffraction lines and their intensities to recognised standards. This comes from *The Powder Diffraction File* maintained by the Joint Committee on Powder Diffraction Standards (JCPDS).[9]

2.3.2 CELL PARAMETER DETERMINATION

The unit cell is an imaginary fundamental unit of a translationally repeating pattern. From this cell the entire crystal can be constructed solely by the translational displacements. The unit cell chosen to describe a lattice is usually the one with the sides of the shortest length, given the notation a, b and c. The angles between them are denoted α, β and γ. These unit cells are classified into seven different crystal systems depending on the symmetry elements they possess. For example, a cubic lattice has four threefold axes in a tetrahedral array. Other examples include monoclinic, orthorhombic and hexagonal.

The spacing of the lattice points in a crystalline sample were investigated via the use of PXD. Initial lattice parameter values for crystalline materials were determined using *CELREF*,[6] a refinement program for diffraction patterns which uses an iterative least squares refinement method.

Equation 2.7

$$M = \sum_i W_i \left(\sin_i^2 \theta^{obs} - \sin_i^2 \theta^{calc}\right)^2$$

where W_i is a weighting factor,

M is a weighted minimised difference for observed 2θ data.

A raw data file can be read into the program and reflection peaks within the pattern are selected for refinement against theoretical values given for expected reflections. These are based upon starting cell parameters obtained from a model found in the literature for similar compounds. The cell parameters obtained from such a program can only reflect the goodness of fit between the observed peaks and the chosen peaks which have been calculated from the literature data. It provides no indication of sample impurities. For complete structural

determination, a refinement process known as a Rietveld refinement can be performed giving a more accurate analysis of collected data.

2.3.3 THE RIETVELD METHOD

2.3.3.1 OVERVIEW OF RIETVELD METHOD

Typical solid state experimental procedures, high temperature sintering and grinding, result in powders containing small crystallites. This means that the single crystal methodology of structure determination is inappropriate. Instead, structural refinements are often carried out using the Rietveld Method.[10,11] In this thesis the refinements were performed using the computer package *General Structure Analysis System* (GSAS),[12] of Von Dreele and Larson.

GSAS is a structural refinement method as opposed to a structural solution method therefore it is necessary to have a good test model from the literature as a starting point inclusive of lattice parameters, atomic positions and a space group. From this, a theoretical pattern is generated.

A powder diffraction pattern obtained from a crystalline material can be thought of as an array of individual reflection profiles where each one has a peak height, a peak position, peak shape, a breadth, tails which decay gradually with distance from the peak position and an integrated area proportional to the Bragg intensity, I_k, where k represents the miller indices h, k and l.[13] Typically there are many Bragg reflections contributing to the intensity at any given point in the observed profile. This intensity, I_k, is proportional to the square of the absolute value of the structure factor, $|F_k|^2$.

A technique was devised to utilise the full information content at each step, i, of the powder pattern, which allowed structure determination using a method of profile refinement.

In every powder pattern using the Rietveld method the profiles are not fully resolved but partially overlap. A characteristic of this method is that prior to refinement neither the assignment of observed intensity to a particular Bragg reflection nor resolving the overlapping reflections is necessary. As a consequence a fairly good starting model is required.[13]

The Rietveld method is a procedure that compares an experimental diffraction pattern with a theoretical model by refining and varying a number of structural / positional parameters *viz.* lattice parameters, atomic co-ordinates, site occupancies *etc.* and also profile parameters *viz.* peak shape, asymmetry, instrumental factors such as the diffractometer zero point *etc.* A least squares refinement is carried out to minimise the difference between observed data and calculated profile and hence obtain the best fit between the entire observed pattern and the entire calculated pattern based on simultaneously refined models for the structural and profile parameters.

2.3.3.2 THEORETICAL CONSIDERATIONS

It can be shown that the structure factor, F, is the sum of the contributions of the scattering amplitudes, f, and the phases, ϕ, of each atom[11] for any regular array of stationary atoms. This leads to the expression:

Equation 2.8

$$F = \sum_{j=1}^{N} f_j \exp[i\phi_j]$$

The total phase shift of an atom, j, in a unit cell at a point (x_j, y_j, z_j) from the origin, is the sum of the phase shifts in each direction. When the phase shift is evaluated, the structure factor for one unit cell becomes:

Equation 2.9

$$F_{hkl} = \sum_{j=1}^{N} f_j \exp\left[2\pi i\left(hx_j + ky_j + lz_j\right)\right]$$

where h, k and l represent Miller indices defining the plane from which the reflection occurs.

It is possible to show that the intensity of the scattered beam, for very small crystals, is proportional to the square of the structure factor.

Equation 2.10

$$I_{hkl} = kL^2|F_{hkl}|^2$$

where k is the scaling constant,

L is the Lorentz factor, a geometric function of the method of data collection and hence the instrument used.

The scattered intensity is modified by imperfections in the lattice structure of real crystals. Defects and substitutional disorder, particularly in non-stoichiometric materials, can cause local structural irregularities. Furthermore, thermal motion diminishes the scattered intensity, a consequence of time dependent vibrations of the atoms about their mean positions. The atoms in a plane *hkl* are displaced randomly from their ideal in plane positions. This disrupts the in-plane behaviour of their combined scattering. The correction to the structure factor, reflected by a plane *hkl*, is shown in *Equation 2.11*.[14]

Equation 2.11

$$T_{hkl} = \exp\left[-B_{hkl}\frac{\sin^2\theta}{\lambda^2}\right]$$

where T_{hkl} represents the thermal motion correction,

B is equal to $8\pi^2U$, where U is the root mean square thermal displacement.

So that for a unit cell the structure factor becomes:

Equation 2.12

$$F_{hkl} = \sum_{j=1}^{N} f_j n_j \exp\left[-B_j\frac{\sin^2\theta}{\lambda^2}\right]\exp\left[2\pi i(hx_j + ky_j + lz_j)\right]$$

where n_j is the occupation factor of the j^{th} atom, equal to one in a structure free from defects.

However, one must assume that the displacements attributed to thermal motion are isotropic. This is rarely the case, with the exception of some highly symmetric special positions of the cubic space groups. A more rigorous analysis[10] would describe the anisotropy of thermal motion in the form of an ellipsoid, thus superseding *Equation 2.11* by *Equation 2.13*:

Equation 2.13

$$T_{hkl} = \exp\left[-\tfrac{1}{4}\left(B_{11}h^2a^{*2} + B_{22}k^2b^{*2} + B_{33}l^2c^{*2} + 2B_{12}hka^*b^* + 2B_{23}klb^*c^* + 2B_{13}hla^*c^*\right)\right]$$

At a given point, the intensity of the scattered beam is also dependent on the multiplicity of the particular *hkl* reflection. Consequently, in a particular crystal symmetry class for a specific *hkl* reflection, there can be a series of equivalent planes diffracting at the same angle resulting in an increased intensity.

2.3.3.3 DATA REFINEMENT

It is widely recognised that the Rietveld method is an invaluable approach for the structural analyses of most classes of crystalline materials that cannot be synthesised as single crystals. There is a myriad of parameters one can vary when undertaking a refinement though all are not necessary for every refinement. The procedure outlined below for analysing powder diffraction data includes some of the fundamental variables that can be refined during the process.

i) Determination of an approximate structural model; which is achieved through the comparison of experimental data with other known structures and their diffraction patterns.

ii) Refinement of the overall scale factor and background parameters.

iii) Refinement of lattice parameters, zero point error and possible sample displacement correction so that the Bragg reflections may be precisely located. At this stage a preliminary refinement of the peak shape parameters is usually carried out.

iv) Location of atomic positions within a unit cell by allowing the positions to vary from the model data. This alters the peak intensities and thus allows improvement of the peak shape.

v) Variation of fractional occupancies yields information as to the distribution and percentage of each atom on shared sites within the unit cell.

vi) Refinement of the isotropic temperature factors to define thermal motion follows when the atomic positions are known.

vii) Full refinement of peak shape parameters, in addition to any asymmetry or preferred orientation parameters which might be necessary.

viii) Variation of the anisotropic temperature factors may potentially be refined if required. This can often lead to a significant improvement in the fit, though the refinement of these factors is usually only feasible with neutron data.

The Rietveld refinement was used in this study for both single wavelength PXD and TOF neutron data. Although there are differences between the two data sources, which results in variations to the refineable parameters, the method itself is the same. In all cases, the *best-fit* between theoretical and experimental data is sought, *i.e.* the best least squares fit to all the intensities at each step. Let the quantity minimised in the least squares refinement be the residual M, thus M is the sum over all the data points:

Equation 2.14

$$M = \sum_i w_i (y_i^{obs} - y_i^{calc})^2$$

where w_i is a weighting factor given by $1/y_i^{obs}$,

y_i^{obs} is the observed intensity at each step / point i ($2\theta_i$ for PXD),

y_i^{calc} is the calculated intensity at each step.

For PXD data, the calculated intensities (y_i^{calc}) are determined from the structural model by summing the calculated contributions from neighbouring Bragg reflections (k) plus the background b_i:

Equation 2.15

$$y_i^{calc} = s\sum_k L_k |F_k|^2 \phi(2\theta_i - 2\theta_k) P_k A + y_{bi}$$

where s is the scale factor,

L_k contains Lorentz, polarisation and multiplicity factors,

ϕ is the reflection profile function,

F_k is the structure factor for the k^{th} Bragg reflection,

P_k is the preferred orientation function,

A is an absorption factor,

y_{bi} is the background intensity at the i^{th} step.

Preferred orientation is the tendency for crystallites, due to their morphology, to be ordered in a particular way or set of ways. Systematic distortions of the reflection intensities are an outcome of preferred orientation. Mathematical corrections can be made for this phenomenon and is defined by the expression:

Equation 2.16

$$P_k = \left\{G_2 + (1 - G_2)\exp\left[-G_1\alpha_k^2\right]\right\}$$

where G_1 and G_2 are refineable parameters,

α_k is the angle between the presumed cylindrical symmetry axis and the preferred orientation axis direction.

The background intensity at angle $2\theta_i$ is obtained from a specified refineable background function, [b_i]. In the absence of a better function the following fifth order polynomial is used:

Equation 2.17

$$y_{bi} = \sum_{m=0}^{5} B_m \left(\frac{2\theta_i}{BKPOS} - 1 \right)^m$$

where *BKPOS* is the background position, user-specified in the input control file.

Major developments in methodology have led to choices in background functions. More sophisticated expressions such as cosine fourier series and various power series can be adopted and replace *Equation 2.17*. Their selection is based on the optimisation of the fit.

A comparison of intensities is performed at every point, subsequently it is fundamental for the construction of the calculated profile to accurately describe the shape of the Bragg reflections, *viz.* peak shape. The instrument employed generally dictates the peak shape. For the Siemens D5000 and Bruker D8 the peak shape is pseudo-Voigt and can be described by the equation:

Equation 2.18

$$\eta L + (1 - \eta) G$$

where L and G are the Lorentzian and Gaussian contributions to the peak shape,

η is the mixing parameter which can be refined as a linear function of 2θ.

η is defined as:

Equation 2.19

$$\eta = N_A + N_B (2\theta)$$

where N_A and N_B are refineable parameters.

The Gaussian (G) and Lorentzian (L) contributions to the peak shape are represented by the equations:

Equation 2.20

$$G = \frac{(4 \ln 2)^{1/2}}{H_k \sqrt{\pi}} \exp\left[\frac{-4 \ln 2 (2\theta_i - 2\theta_k)^2}{H_k^2} \right]$$

Equation 2.21

$$L = \frac{2}{\pi H_k \left[1 + 4 \frac{(2\theta_i - 2\theta_k)^2}{H_k^2} \right]}$$

where $2\theta_k$ is the calculated position for the k^{th} Bragg peak corrected for the counter zeropoint,

H_k is the full-width-at-half-maximum (FWHM) of the k^{th} Bragg reflection.

The FWHM, H_k, of a peak has been shown to alter with the scattering angle $2\theta_k$ and for constant wavelength neutron diffraction data is modelled as:

Equation 2.22

$$H_k^2 = U \tan^2 \theta + V \tan \theta + W$$

where U, V and W are refineable parameters and are both instrument and sample dependent.

Consequently, this equation can construe the peak broadening effects that arise as result of particle size. More complex expressions[15] apply to other data depending on experimental set up.

Due to the detector and sample heights, the peak shape displays marked asymmetry at low scattering angles. This leads to a shift of the peak maximum to a slightly lower angle whilst the integrated intensity remains unchanged. Accordingly, a semi-empirical correction factor can be applied to modify for this:

Equation 2.23

$$1 - \frac{sP(2\theta_i - 2\theta_k)^2}{\tan \theta_k}$$

where P is the asymmetry parameter,

s = +1, 0, -1 when $(2\theta_i - 2\theta_k)^2$ is positive, zero or negative.

For each least squares refinement the refineable parameters fall into two distinct categories. The first defines the structural parameters. These describe the contents of the unit cell and include the overall temperature factors, atomic co-ordinates and fractional occupancies of each site. The second contains the profile parameters. These describe the position, shape and

FWHM of each peak. They consist of the profile scale factor, unit cell parameters, *U*, *V*, *W*, zeropoint, asymmetry and preferred orientation correction.

There are however drawbacks to using the GSAS program depending on the adequacy of the structural model used. It can yield false structural refinements whereby a local minimum as opposed to a global minimum has been achieved. In order to ascertain whether the minimisation has occurred successfully there are criteria of fit that one observes to visualise the progress of the refinement. These are collectively known as reliability factors. Reliability factors, or R-factors, are employed to make a quantitative assessment of the agreement between the observed and calculated profiles. These are labelled as $R_{profile}$ (R_p), $R_{expected}$ (R_{exp}), $R_{weighted\ profile}$ (R_{wp}) and are given by:

Equation 2.24

$$R_{profile} = R_p = 100\left[\frac{\sum_i \left|y_i^{obs} - y_i^{calc}\right|}{\sum_i y_i^{obs}}\right]$$

Equation 2.25

$$R_{expected} = R_{exp} = 100\left[\frac{(N-P+C)}{\sum_i w_i (y_i^{obs})^2}\right]^{\frac{1}{2}}$$

where R_{exp} is defined from the statistics of the refinement,

N is the number of observations,

P is the number of refineable parameters,

C the number of constraints.

From a mathematical point, $R_{weighted\ profile}$ (R_{wp}) is the most significant of the R-factors. This is so because the residual that is being minimised is the numerator. For identical reasoning it is the factor which best reflects the progress of a refinement and is given by:

Equation 2.26

$$R_{wp} = 100\left[\frac{\sum_i w_i \left(y_i^{obs} - y_i^{calc}\right)^2}{\sum_i w_i \left(y_i^{obs}\right)^2}\right]^{\frac{1}{2}}$$

Another criterion that measures the *goodness of fit* is the chi-squared test (χ^2). This criterion ideally should tend to one meaning perfect correlation between the model and the data has been achieved. This is defined as:

Equation 2.27

$$\chi^2 = \left(\frac{R_{wp}}{R_{exp}} \right)^2$$

For a good fit, the R_{wp} should approach the statistically expected R-factor, R_{exp}. As a visual key, the goodness of fit can be observed by examining a plot of the profile fit. The difference line between calculated and observed patterns should be as flat as possible for a good fit.

2.3.3.4 NEUTRON DIFFRACTION DATA REFINEMENT

The refinement of PND data has several notable advantages over the X-ray method. The scattering length of a particular atom is related to the size of the nucleus as opposed to the number of electrons it possesses, as discussed earlier. Neutron diffraction experiments are not affected by a form factor. Consequently, data may be collected over a larger angular range thus yielding a greater number of reflection points to be included in the refinement. Furthermore, preferred orientation effects are reduced as a consequence of sample mounting *cf.* PXD. The sample is inside a vanadium can rather than in a recessed holder to which the sample must lie flush.

The TOF data from POLARIS was refined using the GSAS package and the Rietveld technique as for X-ray data. In these cases, 2θ data is replaced by TOF data. This is facilely converted to *d*-spacing values using *Equations 2.4-6*. For TOF data refined by this method, a *d*-spacing dependent absorption correction is applied. In addition, the peak shape is more complex and is often fitted in terms of Gaussian, Lorentzian and exponential expressions rather than the mainly Gaussian expression used for single wavelength neutron data.

2.4 SOLID STATE ULTRAVIOLET - VISIBLE SPECTROSCOPY

Ultraviolet-Visible (UV-Vis.) spectroscopy was performed using a Perkin Elmer UV-Vis. lambda 35 spectrometer set up in diffuse reflectance mode. Spectra were collected in the visible range of 380 – 780 nm.

There are two radiation sources, a halogen lamp and a deuterium lamp, which cover the working range of the spectrometer. A holographic concave grating is employed as a monochromator with 1053 lines / mm in the centre. When collecting data over the visible region, radiation from the halogen lamp is reflected by mirror 1 (M1) towards mirror 2 (M2) whilst M1 also blocks radiation from the deuterium lamp. It continues along the optical pathway illustrated in *fig. 2.5* and finally passes through a convex lens onto the photodiode detector.

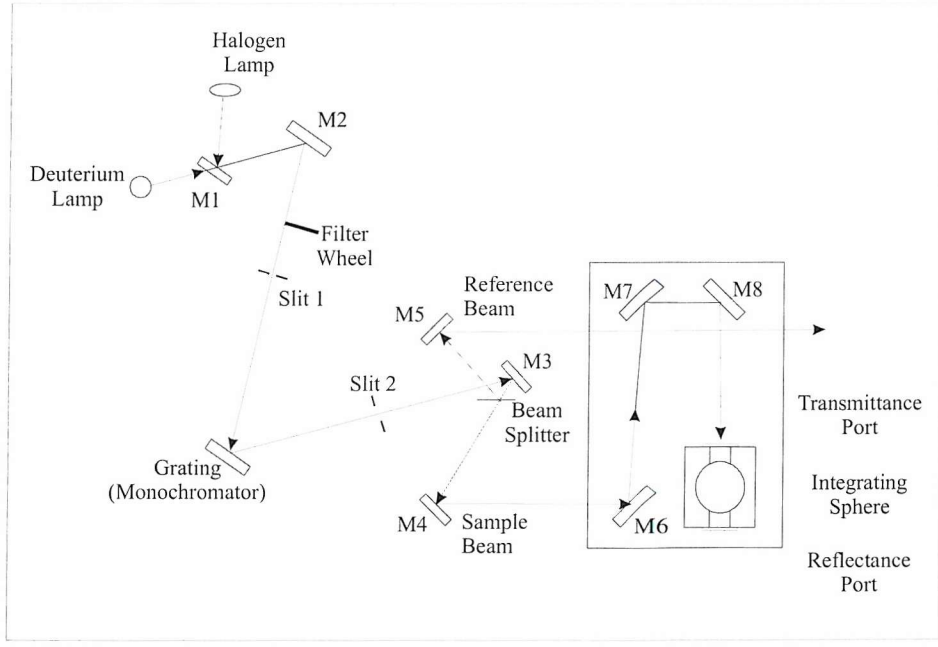

fig. 2.5: *Optical path for a Lambda 35 spectrometer, where M1, M2 and M5 are plane mirrors, M2 a toroidal mirror and M3 a spherical mirror.*

A barium sulphate plate was used as a reference to obtain a background correction before commencing data collection. The powder samples were mounted into either a recessed plastic holder or quartz fronted aluminium holder and pressed into a cake, then the data collected. Colour measurements can be obtained from UV-Vis. data and this is detailed in *Section 2.5*.

2.5 COLOUR MEASUREMENTS

2.5.1 STANDARDISATION OF COLOUR MEASUREMENTS

Different colours arise from observing different wavelengths of visible light. Visible light is defined as the region between 380 and 780 nm in the electromagnetic spectrum. Pigments and coatings can be unambiguously characterised by their spectral reflectance curves, $\rho(\lambda)$, which are measured over this range.

The colour of an object will depend primarily on three things. Firstly, the spectral reflectance (if opaque) or spectral transmittance (if translucent) of the material. Secondly, the spectral composition of light present when viewing the object and finally the spectral sensitivity of the eye of the observer.

The human eye is sensitive to three different fundamental colour components. These are named the primary colours of light *i.e.* red, green and blue. The eye observes these colour components and transmits this information to the brain to compute and evaluate the perceived colour of the object. As colour is a psychological response to light stimuli it cannot be measured, hence the technique of colourimetry has been developed. This provides for the measurement of physical phenomena that can equate to perceived colour.

Each colour can be simulated by additively mixing the three primary colours (red, green and blue)[16] or *colour stimuli* in the correct ratios. Hence, to define any colour it must be possible to give a set of three values. This is known as the trichromatic principle where the three reference stimuli are pre-defined and allows a three-dimensional colour space to be constructed where the colour co-ordinates or *tristimulus values* are interpreted as components of a vector based on the *Commision Internationale de l'Eclairage* (CIE) system.[17]

In colourimetry, a sample would be illuminated with three separate light sources, red, green and blue, in order to ascertain colour measurements. For uncoloured illumination, *i.e.* UV-Vis. spectroscopic data, it is also possible to elucidate some colour measurements. These are useful to ascertain as they enable the determination of the colour of the sample and thus its suitability as a pigment.

For uncoloured illumination, the tristimulus values are dependent on the spectral reflectance as follows:

Equation 2.28

$$X = \int \bar{x}(\lambda)\rho(\lambda)\cdot d\lambda$$

Equation 2.29

$$Y = \int \bar{y}(\lambda)\rho(\lambda)\cdot d\lambda$$

Equation 2.30

$$Z = \int \bar{z}(\lambda)\rho(\lambda)\cdot d\lambda$$

where $x(\lambda)$, $y(\lambda)$ and $z(\lambda)$ are the CIE spectral tristimulus values.

However this does not allow for pigment testing between the sample and a reference, *i.e.* colour differences, hence an absolute colour space is required. Here the three co-ordinates are denoted by L^*, a^*, b^*. The L^* value represents the lightness of an object where the range is from zero (black) to a hundred (white) or the lightness axis. The a^* value represents a measure of redness (positive a^*) or a measure of greenness (negative a^*), the red-green axis. Finally the b^* value represents a measure of yellowness (positive b^*) and blueness (negative b^*), the yellow-blue axis. L^*, a^* and b^* can be considered to be analogous to the z, x and y axes in the Cartesian co-ordinate system respectively. Any colour can therefore be described by its unique $L^*a^*b^*$ values and is located within the 3-dimensional space delineated by these axes. Computer software calculates the values based on *Equations 2.31-33*.

Equation 2.31

$$L^* = 116\left(\frac{Y}{Y_0}\right)^{1/3} - 16$$

Equation 2.32

$$a^* = 500\left[\left(\frac{X}{X_0}\right)^{1/3} - \left(\frac{Y}{Y_0}\right)^{1/3}\right]$$

Equation 2.33

$$b^* = 200\left[\left(\frac{Y}{Y_0}\right)^{1/3} - \left(\frac{Z}{Z_0}\right)^{1/3}\right]$$

where X, Y, Z are tristimulus values,

X_0, Y_0, Z_0 are illuminant values (standard/reference).

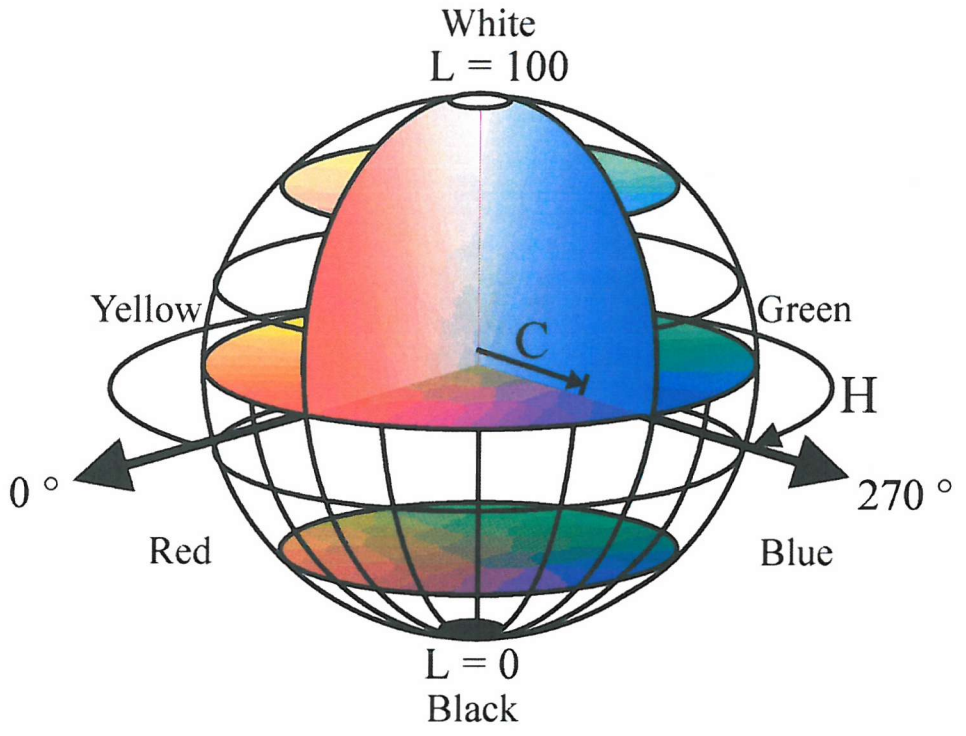

fig. 2.6: *CIELCH colour space diagram, where lightness is represented as the axis of the sphere.*

This rectangular system can be replaced with an alternative system, see *fig. 2.6*, which is based on polar co-ordinates. The H and C axes correspond to the hue angle and chroma (intensity). The L value represents lightness as in the CIELAB system.

2.5.2 Particle Size and Colour Measurements

Particle size has a great influence upon the colour of a given system. The scattering and absorption properties of larger particles differ from smaller particles. Hence in order to compare colour measurements of different pigments the particle sizes must ideally be identical or at the very least, similar. Overall, the larger the particle size the more intense or brighter the colour becomes.

2.5.3 Kubelka-Munk Theory

Two constants; the absorption co-efficient (K) and the scattering co-efficient (S), can define the optical properties of a film that absorbs and scatters light. In an overview to the Kubelka-Munk theory[18,19] let a single beam, L^+, be the flux of diffuse incident light and a beam, L^-, be the flux of light scattered in the opposite direction. Each beam is attenuated by absorption

and scattering losses but is reinforced by scattering losses of the respective opposite beam. These losses are determined quantitatively by two linked differential equations using the two co-efficients K and S. These equations may be integrated for the valid boundary conditions at the incident light side and also the opposite side. Solutions for the transmittance τ and the reflectance ρ are obtained from these integrals as a function of the absorption co-efficient K, the scattering co-efficient S and the film thickness h. The most significant quantity, which is derived from the Kubelka-Munk theory, is the reflectance of an infinitely thick opaque film:

Equation 2.34

$$K/S = (1-\rho_\infty)^2/(2\rho_\infty)$$

From this Kubelka-Munk function and within the range of validity of the theory the reflectance, ρ, depends only upon the ratio of the absorption to scattering co-efficients and not on their individual values.

2.5.4 *MULTIPLE SCATTERING*

The absorption co-efficient, K, obeys the Beer-Lambert law[20] even at high pigment concentrations, σ. Thus K is proportional to σ. The relationship between scattering co-efficient S and concentration σ is more complex. As concentration increases the distance between particles inevitably decreases and consequently there is an interaction and impedance between the light scattered by individual particles and thus their scattering power usually falls. The scattering co-efficient, whilst following Beer's Law at low concentrations, deviates substantially from linearity at higher concentrations. Empirical formulae can be used to quantitatively represent this concentration dependence. For example, there is a linear relationship between S/σ and $\sigma^{2/3}$.

2.5.5 *MIE'S THEORY*

Mie applied Maxwell's equations to a model in which a plane wave front meets an optically isotropic sphere with refractive index n and absorption index κ.[21] Integration gives rise to values for the absorption cross-section Q_A and scattering cross-section Q_S. These dimensionless numbers relate the proportion of absorption and scattering to the geometric diameter of the particle. Thus this theory has provided an awareness of the effect of particle size on the colour properties of pigments and thereby the following conclusions can be drawn:

i) For very small particles, the absorption is independent of the particle size so a further reduction in particle size will not result in additional absorption. This necessitates an optimised particle size in order to achieve the highest absorption for a given system.

ii) With increasing absorption index κ, the absorption of very small particles increases.

iii) Absorption values for large particles are *ca.* equal for all relative refractive indices n and absorption indices κ, and decrease hyperbolically.

As a final note on particle size, the smaller the particle size the greater the density of particles, thus the greater the scattering and the lighter in appearance the object appears.

2.6 THERMOGRAVIMETRIC ANALYSIS

A Polymer Laboratories PL-STA 1500 simultaneous thermal analysis machine was employed to study the thermal characteristics of the pigments synthesised. This permits both thermogravimetric analysis (TGA) and differential thermal analysis (DTA) to be carried out concurrently.

TGA is used to analyse solid state materials by measuring the mass of a compound as a function of temperature or time. The sample is heated at a rate of between 1 and 50 °C per minute under a controlled atmosphere using cylinder gases and the mass loss measured. The data collected can yield vital information about the water content of a material and the temperature of dehydration. If the sample is reduced down to the component metals, the oxygen content of a compound can be obtained from the weight loss. It can also give the temperature at which a material decomposes.

DTA is a technique that compares the temperature of the sample to that of an inert reference material, in this case alumina. The information obtained is plotted real time against furnace temperature. The temperature of both the reference material and sample will be identical until a thermal event occurs, such as melting, dehydration, or structural change. When thermal events occur they can be either exothermic, if the sample temperature increases faster than the reference material, or endothermic, if this rate is slower than the reference.

As all thermal events are recorded during differential thermal analysis, the data obtained yields a more complete record of thermal characteristics of a sample. In contrast to this thermogravimetric analysis can only supply information when a mass loss occurs. By studying both techniques together, the temperatures at which changes to a sample occur can be classified into those that involve a change in mass and those that do not.

It is also possible to study the thermal changes that occur as a sample cools such that they can be divided into reversible and non-reversible events.

In a typical experiment about 15 mg of sample is heated from room temperature to 1000 °C at a constant heating rate of 10 °C per minute in air at 1 atm. Data points are collected every 4 seconds and displayed in real time. From the data collected, it is possible to ascertain the temperatures at which the nitrogen content begins to diminish and thus the temperature at which the colour rapidly fades.

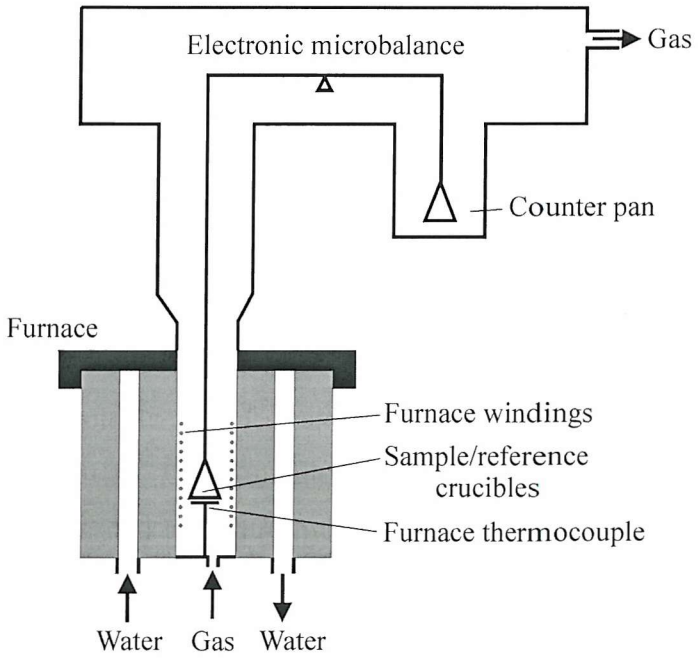

fig. 2.7: Schematic representation of a simultaneous thermal analysis machine.

2.7 ELECTRON MICROSCOPY

Electron microscopy is a versatile technique with several applications, namely electron diffraction and imaging. The imaging facility has been used in this work for two principal reasons; examining the morphology of samples and for identifying whether pigments have been successfully deposited onto mica. Energy Dispersive Analysis of X-rays (EDAX) was employed to obtain elemental analyses of individual crystallites of various samples.

In many ways electron optics is identical to light optics as light can be considered as both a wave and a particle. Visible light can therefore be conceived as photons or as radiation of wavelength 380-780 nm whilst electrons may be considered as radiation with wavelengths typically between 0.001 and 0.01 nm.

Electrons are generated from thermionic emission and then accelerated through a potential in order to obtain a monochromatic beam.[22] This alters the wavelength of the electron beam according to *Equation 2.35*.

Equation 2.35

$$\lambda = \left[\frac{1.5}{(V + 10^{-6} V^2)} \right]^{1/2}$$

where λ is the wavelength in nm,

V is the potential difference.

2.7.1 ELECTRON-SAMPLE INTERACTIONS

Electrons can interact with samples via either elastic or inelastic scattering.

Elastic Scattering occurs when there is no detectable change in the energy of the primary electrons even if the direction of propagation of the electron does change.

Inelastic Scattering occurs in many processes and is a general term referring to any process that causes the primary electrons to lose energy. Inelastic scattering brings about the generation of X-rays and secondary electrons that are used in imaging and the acquisition of analysis data.

2.7.2 *TYPES OF ELECTRONS*

Electron sample interactions can produce three types of electrons which are defined as secondary effects caused by the primary beam.

i) *Secondary electrons* are electrons that escape from a sample with energies below *ca.* 50 eV. The yield of such electrons per primary electron can be more than one and hence they are abundant and are most commonly used for imaging signals in scanning electron microscopy (SEM).

ii) *Backscattered electrons* are primary electrons that leave the surface before relinquishing all their energy. They are most likely to still possess a large fraction of their incident energy so are generally high-energy electrons. These are also used in imaging as well as diffraction and SEM analysis.

iii) *Auger electrons* are expelled as a result of the absorption of energy by an atom from the primary beam. This atom will relax and in doing so emit energy in the form of a characteristic X-ray or a characteristic electron (Auger Electron). These emissions are characteristic of a particular atomic species and can be used for quantitative elemental analysis of a sample.

2.7.3 *SCANNING ELECTRON MICROSCOPY TECHNIQUE*

Scanning electron microscopy (SEM) was performed using a Philips XL30ESEM machine. The microscope consists of an electron gun that generates an electron beam via thermionic emission from a heated tungsten filament. The tungsten filament acts as a cathode and is heated to *ca.* 2800 K by the passage of a current while held at a high negative potential with respect to the anode and the rest of the microscope. The electrons are accelerated to an energy typically in the region of 1-30 keV. The beam of electrons travels through an evacuated optical path (*approx.* pressure $< 10^{-10}$ Pa) as electrons are strongly scattered by gases unlike light.

The electron beam travels down the SEM and before hitting the sample is demagnified by two electromagnetic condenser lenses. This controls the convergence angle and diameter of the beam (2-10 nm). Below the condenser lenses lie four or five electromagnetic objective lenses. These lenses form the first intermediate image and diffraction pattern, which can be enlarged by the subsequent projector lenses and then displayed on screen. These projection lenses determine the overall magnification of the final image.

Scan coils are used to scan the beam across the sample and a scintillator-photomultiplier system is employed as a detector to count the number of low energy secondary electrons or other radiation emitted from each region of the sample.

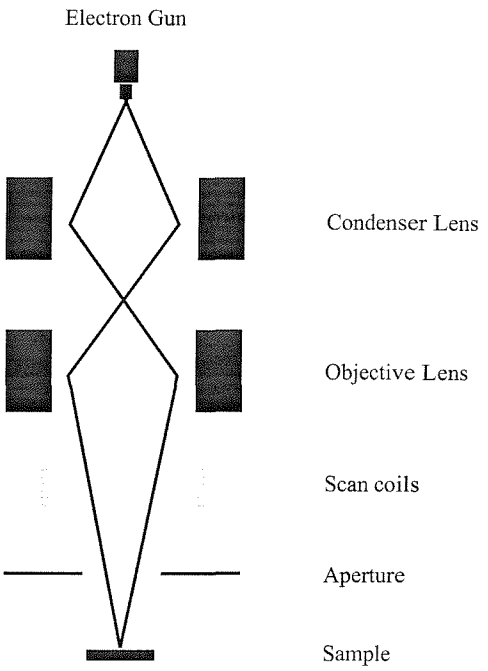

fig. 2.8: *Schematic diagram of the scanning electron microscope, where the solid line represents the path of the electron beam.*

2.7.4 ENERGY DISPERSIVE ANALYSIS OF X-RAYS

The detector used for EDAX normally comprises a small piece of semi-conducting silicon or germanium. This is held in a position where as many X-rays as possible, emitted from the sample, fall upon it. Each incoming X-ray excites a number of electrons into the conductance band of the silicon. This leaves an equal number of positively charged holes in the outer electron shells. The energy required for one excitation is only 3.8 eV, thus the number of electron-hole pairs generated is proportional to the energy of the X-ray photon being detected.

A spectrum can be obtained from the results consisting of several broad bands, the height of the peak being dependent on the number of counts received at that energy. As each element produces its own characteristic X-rays, every peak can be attributed to a certain element. For elements lighter than tin (Z=50), the most intense lines are $K_{\alpha 1}$ and $K_{\alpha 2}$ in the K series of

lines. As the elements get heavier, more energy than provided by the beam current is required to knock electrons out of the K shell so the L and M series are used instead. A computer is employed to interpret the data. From a database it is able to assign an element to each line in the spectrum and from the number of counts calculate the percentage of each element within the sample.

There are some limitations to EDAX. Firstly, elements lighter than sodium are impossible to detect accurately with a standard detector. Secondly, the energy resolution of the detector is poor. Each X-ray line is not seen as a sharp line but a broad peak, making it difficult to resolve closely spaced lines. Finally, spurious peaks in the spectrum may be produced as the result of two identical photons arriving at the detector simultaneously. A detector will interpret this as a single photon of twice the energy and produce what is known as a *sum peak*.

2.8 REFERENCES

[1] Woolfson M. M.; *An Introduction to X-ray Crystallography,* Cambridge University Press (UK), First Edition (1970)

[2] Young H. D., Freedman R. A.; *University Physics*, Addison Wesley (USA), Ninth Edition (1996)

[3] West A. R.; *Solid State Chemistry and its Applications*, Wiley (UK), First Edition (1984)

[4] Weller M. T.; *Inorganic Materials Chemsitry*, Oxford University Press (UK), First Edition (1994)

[5] Bruker Advanced X-Ray Solutions; *EVA*, **V 6.0** (2000)

[6] Laugier J., Bochu B.; *CELREF*, Laboratoire des Matériaux et du Génie Physique, Ecole Nationale Supérieure de Physique de Grenoble INPG (France) (2000)

[7] Bacon G. E.; *Neutron Diffraction*, Oxford University Press (UK), Third Edition (1975)

[8] http://www.isis.rl.ac.uk

[9] International Centre for Diffraction Data; 12 Campus Boulevard, Newton Square, Pennsylvania, 19073-3273 (USA)

[10] Rietveld H. M.; *Acta Crystallogr.*, **22**, 151 (1967)

[11] Rietveld H. M.; *J. Appl. Crystallogr.*, **2**, 65 (1969)

[12] Larson A. C., Von Dreele R. B.; *General Structure Analysis System*, MS-H805, Los Alamos National Laboratory, (USA) N M 87545 (1990)

[13] Young R. A.; *The Rietveld Method*, International Union of Crystallography, Oxford University Press (USA), First Edition (1993)

[14] Buerger M. J.; *Contemporary Crystallography,* McGraw-Hill (USA), First Edition (1970)

[15] Caglioti G., Paoletti A., Ricci F. P.; *Nucl. Instrum. Methods*, **35**, 223 (1958)

[16] Tilley R.; *Colour and the Optical Properties of Materials*, Wiley (UK), First Edition (2000)

[17] Commission International de l'Eclairage; *CIE Technical Report,* **116** (1995)

[18] Kubelka P., Munk F.; *Z. Tech. Phys.*, **12,** 539 (1931)

[19] Kubelka P.; *J. Opt. Soc. Am.*, **38,** 448 (1948)

[20] Atkins P. W.; *Physical Chemistry*, Oxford University Press (UK), Fifth Edition (1995)

[21] Mie G.; *Ann. Phys.*, **25**, 377 (1908)

[22] Goodhew P., Humphreys J., Beanland R.; *Electron Microscopy and Analysis*, Taylor & Francis (UK), Third Edition (2001)

CHAPTER THREE

SYNTHESIS AND CHARACTERISATION OF $Ca_{(1-x)}Ln_xTaO_{(2-x)}N_{(1+x)}$ AND $Ln_2Ta_2O_5N_2$ (Ln = Sc, Y, La, Ce-Lu EXCLUDING Pm)

3 LANTHANIDE SUBSTITUTIONS IN $Ln_2Ta_2O_5N_2$ AND $Ca_{0.5}Ln_{0.5}TaO_{1.5}N_{1.5}$

3.1 INTRODUCTION

Substituting one non-metal for another within a crystal system can result in a significant shift in the electronegativity difference. This change will alter the band gap of a compound and therefore alter the energy at which an electronic interband transition occurs. In turn this may modify the colour of a compound. Most metal oxides are white, as they possess large band gaps, whereas many oxynitrides are coloured. Nitrogen has a lower electronegativity than oxygen thus the band gap is reduced. This decrease in the energy gap between valence and conduction bands is partly accounted for by the difference in the energy levels of the 2*p* orbitals where $E_{2p}(O) = -14.8$ eV and $E_{2p}(N) = -13.4$ eV (top of the valence band).[1] This can be represented in terms of a molecular orbital diagram whereby the difference in energy between metal and oxygen orbitals is greater than the difference between the metal and nitrogen orbitals, see *fig. 3.1*.

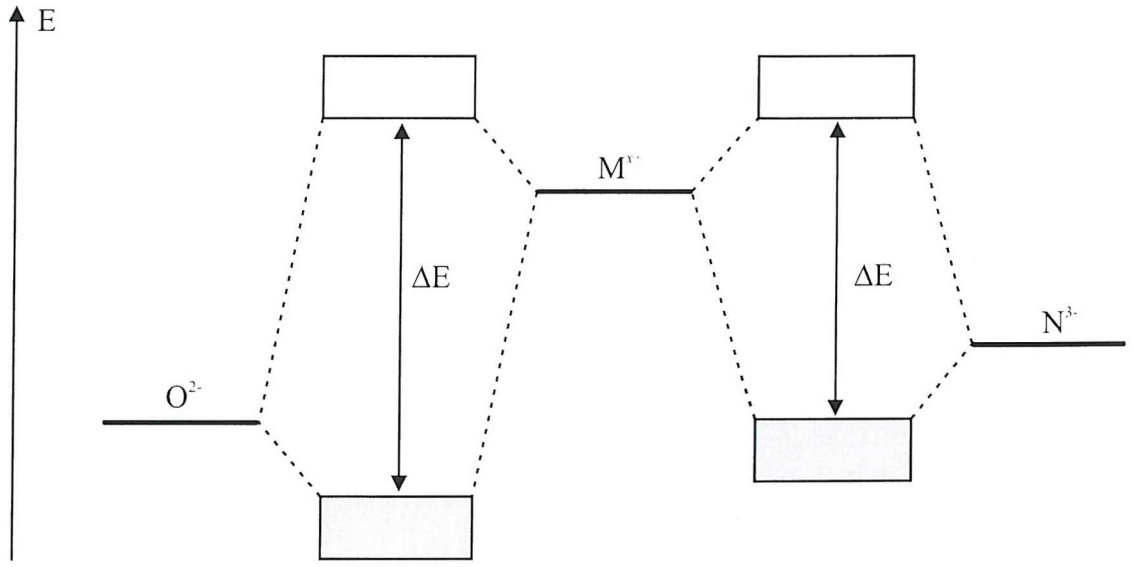

fig. 3.1: *Combination of atomic orbitals forming band structure in oxides (left) and nitrides (right), where ΔE represents the band gap.*

However, it is not simply a case of replacing oxygen with nitrogen to obtain a desirable pigment substitute; high chemical and physical stabilities are also required alongside properties such as the material's hue and lightness. As tantalum, alkaline earth metals and rare earth metals form the most stable polar nitrides[2,3] they prove to be a good starting place

to systematically target oxynitride systems via substitutions of cations and variations in stoichiometries. The perovskite system was chosen as not only is it versatile and produces durable solids but also previous work has been carried out on several compounds namely, $CaTaO_2N$[4,5] and $LaTaON_2$,[4,6] providing an ideal basis on which adaptations can be made.

Trivalent cations including group IIIb Sc-La, lanthanides from across the series, Ce-Lu (excluding Pm) and In were substituted onto the A site of an oxynitride perovskite type structure, $AB(O,N)_3$. Both the fully substituted lanthanide end members of the series, $LnTaON_2$ and also the stoichiometrically equal calcium lanthanide $Ca_{0.5}Ln_{0.5}TaO_{1.5}N_{1.5}$ series were targeted. As the pyrochlore $Ln_2Ta_2O_5N_2$ provides a competing phase, especially for smaller Ln^{3+}, it too was studied in terms of colour and basic structural analysis.

In substituting the cations the band gap will alter only slightly compared with changing the anion as little difference exists between the electropositivities of the cations. Hence the electronic interband transitions will remain within the visible region and the overall colour can be fine-tuned in order to determine the best candidates for pigment applications.

3.2 SYNTHESIS

Samples were synthesised by treating simple metal oxides and carbonates with gaseous ammonia at elevated temperatures, a route used extensively in previous work.[7-10] In the syntheses highlighted here, stoichiometric amounts of Ta_2O_5 (Aldrich, 99%), $CaCO_3$ (99%) and Ln_2O_3 (Ln = trivalent lanthanide, Sc, Y or In), CeO_2, Pr_6O_{11} or Tb_4O_7 (source dependent on lanthanide, see *Appendix I*), were intimately ground in an inert acetone media with *ca.* 50% wt. ratio of halide salts (NaCl, KCl, $CaCl_2$) employed as mineralisers. The presence of solvent creates a slurry, which can aid particle dispersion and thus provide a better degree of mixing between reagents.

These mixtures were then fired at 800-1000 °C under dry flowing ammonia (Air Products, Electronic Grade) for 20 hours at a flow rate of *ca.* 7 dm^3 hr^{-1}. If necessary the products were ground and fired again for further 20 hour intervals. The mineralisers were leached from the fired materials using excess de-ionised water.

The rate determining step of a traditional ceramic route is the diffusion of reactants. Diffusion pathways are driven by the crystallisation of a thermodynamically stable phase and furthermore by the differences in vacancy concentrations. The halide salts used have lower melting points than the reactants and the reaction temperature. As a result, upon melting, the mineralisers act as a flux aiding the ionic transport.

The compounds synthesised were analysed using a variety of techniques, namely UV-Vis. spectroscopy, colour measurements and powder X-ray diffraction. In the case of $Ca_{0.5}Nd_{0.5}TaO_{1.5}N_{1.5}$ powder neutron diffraction was employed.

3.3 POWDER X-RAY DIFFRACTION DATA

Initial phase identification of the compounds synthesised was carried out via powder X-ray diffraction (PXD). For the crystalline phases, overnight data sets were collected on a Siemens D5000 using Cu $K_{\alpha 1}$ radiation (λ=1.5406 Å).

3.3.1 PHASE IDENTIFICATION AND CHARACTERISATION OF $LnTaON_2$ AND $Ln_2Ta_2O_5N_2$

Primary phase identification was carried out using *EVA*[11] and the PXD data were collated in *Table 3.1*. Several of the PXD data sets are illustrated in *fig. 3.2* and represent a general overview of the lanthanide substitutions in $LnTaON_2$, though more commonly the pyrochlore phase, $Ln_2Ta_2O_5N_2$, is formed.

Table 3.1: Phase identification for target phase $LnTaON_2$ where Ln is Y, Sc, La or an *f*-block lanthanide excluding Pm.

Sample	Phase Identification
Scandium	Perovskite with Ta_3N_5 and Sc_2O_3 impurities.
Yttrium	Multiphase: Pyrochlore, Y_3TaO_7, Ta_3N_5 and Y_2O_3. Substantial peak splitting.
Lanthanum	Perovskite.
Cerium	Perovskite and Pyrochlore, further heating more amorphous.
Praseodymium	Pyrochlore.
Neodymium	Perovskite and Pyrochlore.
Samarium	Perovskite and Pyrochlore.
Europium	Pyrochlore with minor Perovskite phase.
Gadolinium	Pyrochlore and Perovskite phase; peak splitting.
Terbium	Pyrochlore.
Dysprosium	Pyrochlore.
Holmium	Pyrochlore, potential Ta_3N_5 impurity.
Erbium	Pyrochlore with minor Perovskite phase, Ta_3N_5; substantial peak splitting.
Thulium	Pyrochlore and Ta_3N_5.
Ytterbium	Pyrochlore.
Lutetium	Pyrochlore with minor Perovskite phase, Ta_3N_5; substantial peak splitting.

The competition of the pyrochlore structure over the perovskite structure is best illustrated here at 100% doping. The smaller lanthanides predominantly adopt a pyrochlore structure and the bigger lanthanides form perovskites, compare Yb^{3+} and La^{3+}. Another noticeable tendency is the formation of a Ta_3N_5 impurity phase for smaller radii lanthanide substitutions (Sc, Dy-Lu excluding Yb).

La is the only sample to form a single phase perovskite and the PXD pattern is in agreement with the monoclinic model described in the literature.[4] This sample was synthesised in order to carry out a comparative study on the variance of colour across the series.

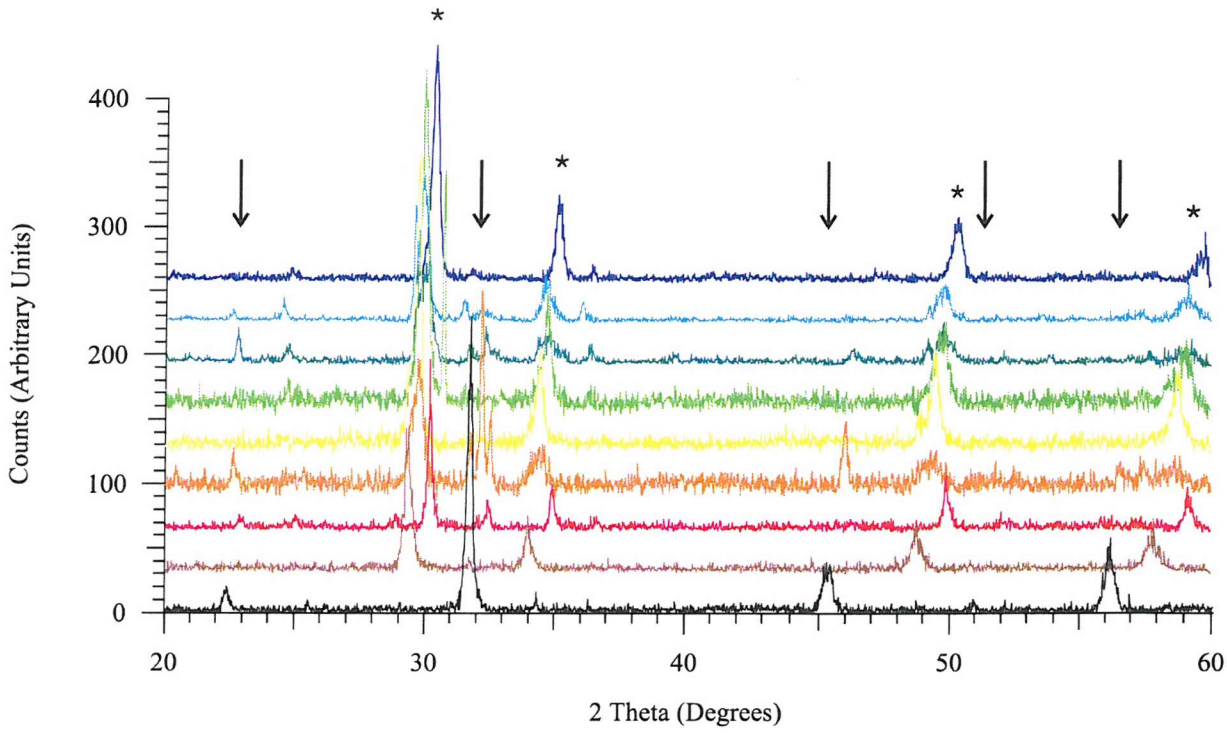

fig. 3.2: *Powder X-ray diffraction data for $LnTaON_2$ target phases, where an arrow represents a reflection due to a perovskite structure ($LaTaON_2$) and * indicates a reflection due to a pyrochlore structure ($Ln_2Ta_2O_5N_2$). From the lowest pattern upwards Ln is La, Pr, Eu, Gd, Tb, Dy, Er, Tm and Yb respectively.*

Indexing the peaks of the pyrochlore phase within the PXD data was performed using *CELREF*[12] employing the model for $Ln_2Ta_2O_5N_2$ described in the literature for cubic pyrochlores crystallising in the space group *Fd-3m* where Ln = Y, Sm and Yb.[13] The lattice parameters obtained are displayed in *Table 3.2*. From the lattice parameters average cell volumes were calculated.

The cell size can be seen to be getting smaller as the size of the cationic radius decreases. This is in accordance with literature data from Marchand,[13] though pyrochlores have not previously been reported for Pr, Eu, Tb and Tm. In this work single phase pyrochlore-type structures are formed from the mixed valence oxides of terbium and praseodymium but for Eu, a competing perovskite phase and for Tm, a Ta_3N_5 impurity phase are also formed.

Table 3.2: Estimated lattice parameters in Å for the $Ln_2Ta_2O_5N_2$ series.

Ln^{3+}	a [Å]	V [Å^3]
Pr*	10.557 (2)	1176.6 (7)
Eu	10.325 (5)	1100.7 (16)
Tb*	10.417 (5)	1130.4 (16)
Dy*	10.355 (5)	1110.3 (16)
Tm	10.331 (3)	1102.6 (10)
Yb*	10.246 (6)	1075.6 (19)

where (*) represents a sample containing only a pyrochlore-type phase.

These data sets serve merely as a guideline as the samples synthesised here were not highly crystalline (see *fig. 3.2*) after multiple firings. In some cases, after further heating at higher temperatures (950 °C), the amount of pyrochlore phase diminishes and there is concurrent augmentation of the corresponding competing perovskite phase, *i.e.* $EuTaON_2$ or indeed the onset of perovskite formation when at lower temperatures only the pyrochlore phase forms, *i.e.* $Pr_2Ta_2O_5N_2$ and $PrTaON_2$.

3.3.2 PHASE IDENTIFICATION AND CHARACTERISATION OF $Ca_{(1-x)}Ln_xTaO_{(2-x)}N_{(1+x)}$, $x = 0.5$

Primary phase identification was carried out using *EVA*[11] and the PXD data was collated in *Table 3.3.*

This overview highlights the formation of the competing pyrochlore phase ($Ln_2Ta_2O_5N_2$) that is present with various lanthanide substitutions, a phenomenon previously reported by Marchand *et al.*[6] It is unclear whether exchange occurs on the lanthanide site for calcium in this structure as well. This trend becomes more apparent on moving from left to right across the lanthanide group. For lanthanide oxides following the form Ln_2O_3, the Ln^{3+} radii decrease across the series in accordance with the lanthanide contraction. As the cation size decreases the amount of competing pyrochlore phase increases.

Table 3.3: Phase identification for $Ca_{(1-x)}Ln_xTaO_{(2-x)}N_{(1+x)}$, where Ln is Sc, Y, La or an *f*-block lanthanide excluding Pm, with target phase of $x = 0.5$.

Sample	Phase Identification
Scandium	Perovskite with Ta_3N_5 and Sc_2O_3 impurities.
Yttrium	Perovskite and Pyrochlore.
Lanthanum	Perovskite with minor Pyrochlore phase.
Cerium	Pyrochlore.
Praseodymium	Pyrochlore.
Neodymium	Perovskite.
Samarium	Perovskite and Pyrochlore.
Europium	Perovskite.
Gadolinium	Perovskite with minor Pyrochlore phase.
Terbium	Pyrochlore.
Dysprosium	Perovskite.
Holmium	Perovskite with minor Pyrochlore phase.
Erbium	Perovskite and Pyrochlore.
Thulium	Perovskite and Pyrochlore.
Ytterbium	Perovskite and Pyrochlore.
Lutetium	Perovskite, Pyrochlore and Lu_2O_3.

The inclusion of the larger Ca^{2+} ion may aid the formation of a perovskite structure with smaller lanthanide ions but more probable is a calcium rich perovskite tending towards $CaTaO_2N$ and a lanthanide rich pyrochlore tending towards $Ln_2Ta_2O_5N_2$. Indeed, for the latter lanthanides a co-ordination number of 12 is not stable and thus substitution onto the A site of a perovskite is not expected. Instead a pyrochlore phase is formed whereby the lanthanide ions adopt a co-ordination number of 8. The change in co-ordination sphere as the Ln^{3+} radius decreases is illustrated in the case of Ln_2O_3. For the early lanthanide sesquioxides, Ln = La-Sm, an *A*-M_2O_3 structure is adopted where the metal atom is 7 co-ordinate. As the radius decreases the lanthanide adopts a *C*-M_2O_3 structure with a co-ordination number of 6.[14]

The reaction with ammonia is slower for lanthanides to the right of the series. Due to the high charge density and thus greater forces of attraction and repulsion, smaller Ln^{3+} ions diffuse more slowly than either larger Ln^{3+} species or ions in a lower valency. This may also account for a competing reaction being favoured and hence more pyrochlore phase is formed. By

altering the reaction conditions, such as temperature and gas flow, one may be able to favour a certain reaction over the other.[6] For example, the mixed phase (perovskite and pyrochlore), calcium ytterbium sample was fired again at 950 °C under N_2. This results in an increase in the competing pyrochlore phase to an extent that both phases command equal intensities in the PXD pattern.

For higher oxidation state lanthanide reagents, *i.e.* CeO_2 (IV), Pr_6O_{11} (III/IV) and Tb_4O_7 (III/IV), the pyrochlore phase was favoured although it is likely that these lanthanides reduce to Ln^{3+} in the presence of a gaseous ammonia atmosphere.

Selected PXD patterns for the calcium lanthanide oxynitrides are displayed in *fig. 3.3* with the reflections attributed to the perovskite and the pyrochlore structures clearly identified.

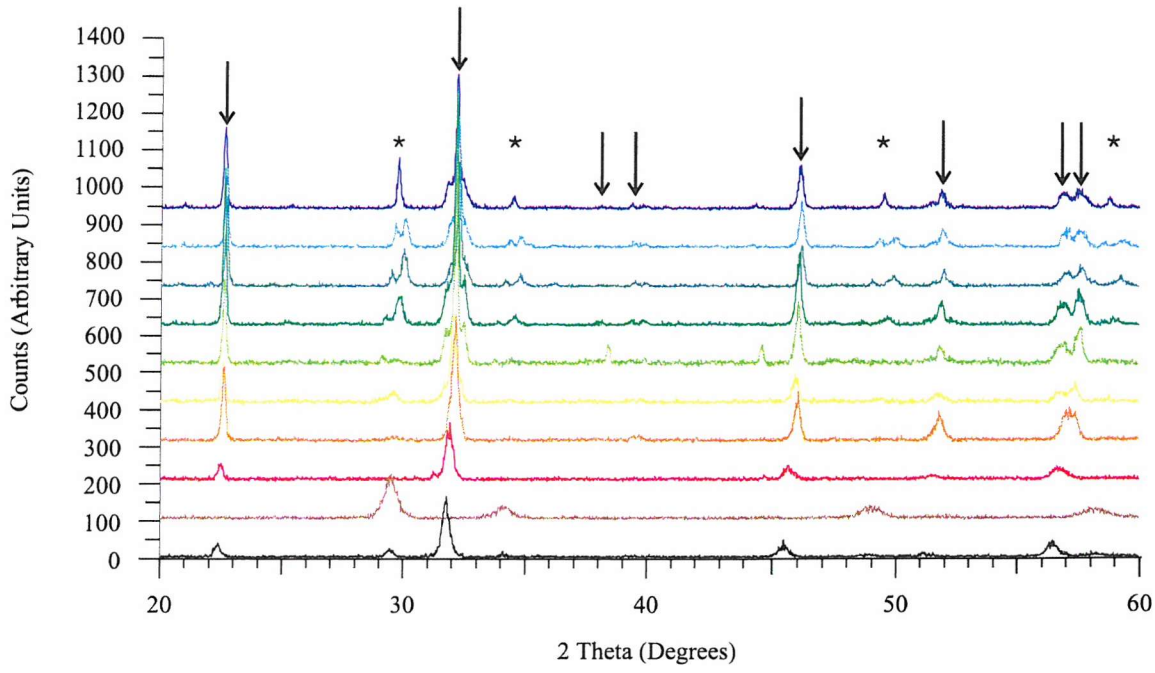

fig. 3.3: *Powder X-ray diffraction data for $Ca_{(1-x)}Ln_xTaO_{(2-x)}N_{(1+x)}$ target phases (x = 0.5), where an arrow represents a reflection due to a perovskite structure ($CaTaO_2N$) and * indicates a reflection due to a pyrochlore structure ($Ln_2Ta_2O_5N_2$). From the lowest pattern upwards Ln is La, Pr, Nd, Eu, Gd, Dy, Ho, Er, Tm and Yb respectively.*

These data sets display a high degree of peak splitting within the traces, revealing more distorted structures and a lowering of symmetry from cubic geometry to rhombohedral and orthorhombic perovskite structures. This increases when moving across the lanthanide group and is especially apparent for lanthanides lying to the right of dysprosium. These compounds also have a high proportion of both perovskite and pyrochlore phases. One factor that may accentuate peak splitting is the different crystal symmetries of $LaTaO_2N$ and $CaTaO_2N$. Both compounds have reflections in their respective PXD patterns at similar 2θ values. Due to the peak broadening effect of oxynitrides these peaks could overlap yielding the shoulders on each peak.

The FWHM of the peaks is large and hence the expected particle size is small in accordance with *Equation 2.2*. The broadening of the peaks increases as the size of the lanthanide ion decreases, *i.e.* the upper patterns in *fig. 3.3* have the broadest peaks and thus the smallest crystallite size.

Based on tolerance factors for the perovskite structure and also co-ordination geometries of various ions, both scandium and indium are too small to reside on the A site. The PXD data however shows the presence of a perovskite type structure, albeit of poor crystallinity in the case of scandium. There are two possible explanations for this outcome. Firstly it could suggest that the *s*-block metals present in the mineralisers occupy this site in favour of Sc^{3+} and In^{3+}. Secondly it is feasible that this structure can tolerate vacancies within the cationic network.

The results obtained from the indium study could lend themselves to support either argument. Firstly the target compound $Ca_{0.5}In_{0.5}TaO_{1.5}N_{1.5}$ results in a bright yellow compound, but when the In_2O_3 is omitted in order to synthesise $Ca_{0.5}\square_{0.5}Ta(O,N,\square)_3$ (where $\square$ represents a vacancy) the compound is a dull orange. As $CaTaO_2N$ is known to be yellow when synthesised under identical conditions this could suggest that some calcium present in the $CaCl_2$ mineraliser is indeed incorporated into the structure during the reaction. A PXD plot comparing $Ca_{0.5}In_{0.5}TaO_{1.5}N_{1.5}$ to $CaTaO_2N$ can be found in *Appendix II*. This highlights the formation of a crystalline perovskite phase isostructural to $CaTaO_2N$. An EDAX study was carried out and the sample is found to contain less than 1% In and a cation deficient A site.

Rietveld analysis revealed A site fractional occupancies of 0.992 (4) Ca and 0.008 (4) In thus confirming EDAX results.

Indexing the peaks of the perovskite phase within the PXD data was performed using *CELREF*[12] and a model for $CaTaO_2N$ described in the literature.[4] The lattice parameters obtained are displayed in *Table 3.4* with the later lanthanides omitted. As the radii of the late lanthanide cations are too small to adopt a co-ordination number of 12 the perovskite phase could be attributed to a calcium deficient $Ca_{(1-x)}TaO_{(2-x)}N$ phase, as the perovskite structure itself is stable even with vacancies in the anionic and cationic sub-networks. Also excluded are samples with the lanthanides Pr, Ce and Tb as they do not form perovskite phases. Finally Eu is also omitted as it is a rhombohedrally distorted perovskite, further details on this compound are reported in *Section 3.4*.

From the lattice parameters, estimated cell volumes were calculated, *vide infra*. These can be seen to be decreasing on descending the table corresponding to the decreasing cation radius.

Table 3.4: Estimated lattice parameters in Å for the $Ca_{0.5}Ln_{0.5}TaO_{1.5}N_{1.5}$ series.

Ln^{3+}	*a* [Å]	*b* [Å]	*c* [Å]	*V* [Å^3]
La	5.642 (9)	7.87 (5)	5.621 (1)	249.6
Nd	5.612 (6)	7.95 (4)	5.630 (2)	251.2
Sm	5.645 (3)	7.90 (3)	5.581 (2)	248.9
Gd	5.560 (4)	8.03 (3)	5.539 (7)	247.3
Dy	5.611 (5)	7.94 (2)	5.521 (6)	246.0
Ho	5.609 (5)	7.92 (2)	5.516 (6)	245.0

These data can only stand as a guideline as in most cases a single phase perovskite has not formed and thus these measurements should not be directly compared as their stoichiometries, the calcium to lanthanide ratios, are not known. For the four samples that formed single phase perovskites, long scan PXD data were acquired and structural analyses completed. These are discussed in *Section 3.4*.

3.4 STRUCTURAL ANALYSIS

PXD data sets of $Ca_{0.5}Ln_{0.5}TaO_{1.5}N_{1.5}$ where Ln is Nd, Dy or Eu were collected from 2θ =10-110° for 15 hours on a Siemens D5000. These samples are single phase perovskites but crystallise in different space groups.

Although $LaTaON_2$ and $CaTaO_2N$ are both perovskites, they crystallise in different space groups. $LaTaON_2$ is monoclinic, crystallising in the space group *C2/m* whereas $CaTaO_2N$ displays an orthorhombic symmetry adopting the space group *Pnma*.[4] For each analysis refinements were undertaken using different space groups, *viz. C2/m* and *Pnma*. Each space group has characteristic reflections seen in the PXD patterns. In fact $CaTaO_2N$ has some weak intensity peaks at around 2θ = 39 °. These peaks are present in the samples of La, Nd and Dy, and it was found that employing a starting model based on orthorhombic $CaTaO_2N$ yields the most stable fit.

In contrast to this, the Eu sample could not be satisfactorily refined in either *C2/m* or *Pnma* as the quality of the data is not sufficient to resolve any information about peak splitting for weak intensities, hence a space group of higher symmetry was employed. As the literature model for $EuTa(O,N)_3$,[6] crystallising in the cubic space group *Pm3m* did not adequately model the pattern, this sample was refined in a rhombohedral space group. This is based on starting models for $AgTaO_3$ and $LaNiO_3$ found in the JCPDS database,[15,16] where the structure is referred to the hexagonal axes. Structures that belong to a trigonal system can crystallise in a hexagonal or a rhombohedral lattice. Both types of lattices can be referred to either hexagonal or rhombohedral axes. The unit cell becomes non-primitive when a rhombohedral lattice is referred to hexagonal axes or vice versa.

Refinements were performed using the *GSAS* suite of programs[17] employing the Rietveld method.[18-20] Lattice parameters and atomic positions for these refinements are summarised in *Tables 3.5 - 3.10* and the final profile fit achieved for the X-ray data sets are shown in *figs. 3.4-3.6*. The $U_{(iso)}$ values for oxygen and nitrogen are fixed at 0.0250 $Å^2$ as temperature factors are unreliable for such light elements. The oxygen to nitrogen ratio on each site is linked to the A cation stoichiometries to maintain charge balance.

Table 3.5: Crystallographic data for $Ca_{0.5}Nd_{0.5}TaO_{1.5}N_{1.5}$.

Compound	$Ca_{0.5}Nd_{0.5}TaO_{1.5}N_{1.5}$
Crystal System	Orthorhombic
Space Group	*Pnma* (no. 62)
Cell Parameters	a = 5.6404 (10) Å
	b = 7.9435 (16) Å
	c = 5.5885 (12) Å
Cell Volume	250.40 (7) Å^3
χ^2	0.2287
R_{wp}	0.1314

Table 3.6: Refined atomic positions for $Ca_{0.5}Nd_{0.5}TaO_{1.5}N_{1.5}$. E.s.ds are given in parentheses.

Atom	x	y	z	Occupancy	$U_{(iso)}$ [Å^2]
Ca / Nd	0.018 (3)	0.25	0.021 (3)	0.5 / 0.5	0.034 (3)
Ta	0.5	0	0	1.0	0.0146 (8)
O / N (1)	0.462 (2)	0.25	0.050 (2)	0.5 / 0.5	0.0250
O / N (2)	0.337 (8)	0.009 (2)	0.750 (9)	0.5 / 0.5	0.0250

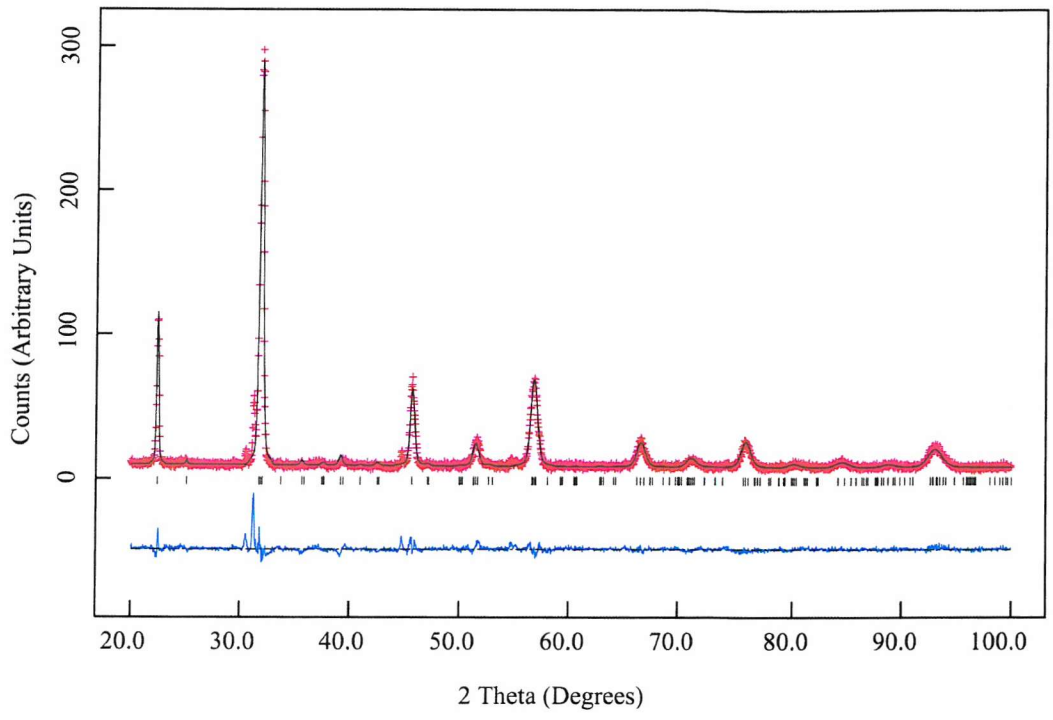

fig. 3.4: *Rietveld refinement fit for $Ca_{0.5}Nd_{0.5}TaO_{1.5}N_{1.5}$; obtained from PXD data collected on a Siemens D5000. The cross marks are the observed intensities, the upper trace the calculated profile, the black tick marks the calculated peak positions and the lower line the difference.*

Table 3.7: Crystallographic data for $Ca_{0.77}Eu_{0.23}TaO_{1.77}N_{1.23}$.

Compound	$Ca_{0.77}Eu_{0.23}TaO_{1.77}N_{1.23}$
Crystal System	Rhombohedral
Space Group	*R –3c* (No. 167)
Cell Parameters	a = 5.5946 (4) Å
	c = 13.606 (2) Å
Cell Volume	368.81 (6) Å^3
χ^2	2.126
R_{wp}	0.1353

Table 3.8: **Refined atomic positions for $Ca_{0.77}Eu_{0.23}TaO_{1.77}N_{1.23}$. E.s.ds are given in parentheses.**

Atom	*x*	*y*	*z*	Occupancy	$U_{(iso)}$ [Å^2]
Ca	0	0	0.25	0.773 (8)	0.0422 (23)
Eu	0	0	0.25	0.227 (8)	0.0422 (23)
Ta	0	0	0	1.0	0.0024 (6)
O / N	0.564 (3)	0	0.25	0.59 / 0.41	0.0250

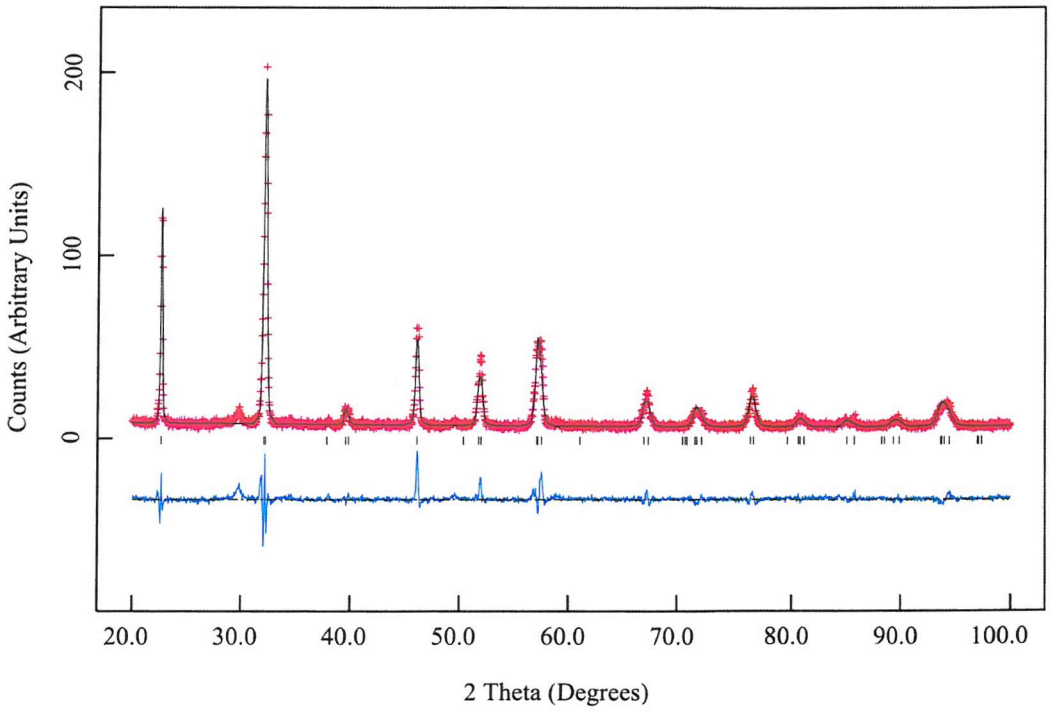

fig. 3.5: *Rietveld refinement fit for $Ca_{0.77}Eu_{0.23}TaO_{1.77}N_{1.23}$; obtained from PXD data collected on a Siemens D5000. The cross marks are the observed intensities, the upper trace the calculated profile, the black tick marks the calculated peak positions and the lower line the difference.*

Table 3.9: Crystallographic data for $Ca_{0.57}Dy_{0.43}TaO_{1.57}N_{1.43}$.

Compound	$Ca_{0.57}Dy_{0.43}TaO_{1.57}N_{1.43}$
Crystal System	Orthorhombic
Space Group	*Pnma* (no. 62)
Cell Parameters	a = 5.6426 (3) Å
	b = 7.8815 (5) Å
	c = 5.5213 (3) Å
Cell Volume	245.54 (3) Å^3
χ^2	0.1740
R_{wp}	0.1012

Table 3.10: Refined atomic positions for $Ca_{0.57}Dy_{0.43}TaO_{1.57}N_{1.43}$. E.s.ds are given in parentheses.

Atom	x	y	z	Occupancy	$U_{(iso)}$ [Å^2]
Ca	0.0505 (8)	0.25	-0.019 (2)	0.573 (8)	0.006 (2)
Dy	0.0505 (8)	0.25	-0.019 (2)	0.427 (8)	0.006 (2)
Ta	0.5	0	0	1.0	0.0095 (8)
O / N (1)	0.602 (7)	0.25	0.142 (7)	0.523 / 0.477	0.0250
O / N (2)	0.247 (10)	-0.048 (3)	0.755 (11)	0.523 / 0.477	0.0250

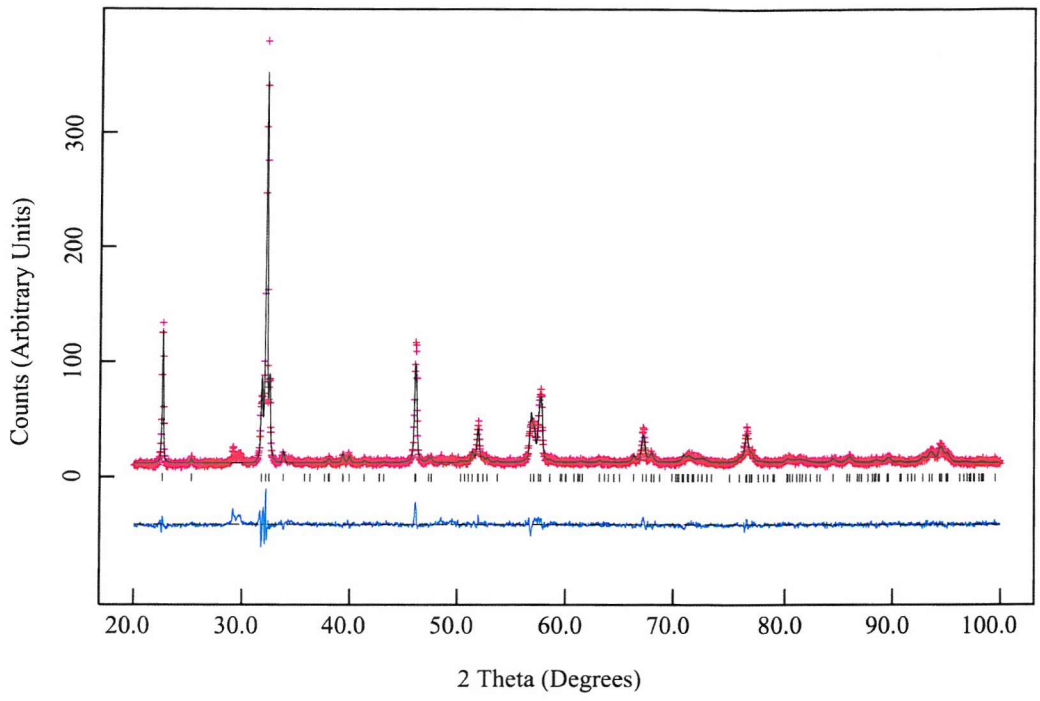

fig. 3.6: *Rietveld refinement fit for $Ca_{0.57}Dy_{0.43}TaO_{1.57}N_{1.43}$; obtained from PXD data collected on a Siemens D5000. The cross marks are the observed intensities, the upper trace the calculated profile, the black tick marks the calculated peak positions and the lower line the difference.*

Full details for the lanthanum sample are reported in *Chapter 4*, a comparison study of alkaline earth substitutions. This perovskite crystallises in the orthorhombic space group *Pnma*. A combined refinement of the powder neutron and X-ray diffraction data sets yields a stoichiometry of $Ca_{0.61}La_{0.39}TaO_{1.61}N_{1.39}$ and lattice parameters a = 5.665 (1) Å, b = 7.980 (1) Å and c = 5.666 (1) Å, with an overall cell volume of 256.12 (8) Å^3.

For both the neodymium and the dysprosium samples the data obtained follows that of the orthorhombically distorted $CaTaO_2N$[4] therefore suggesting both elements can be successfully substituted onto the A site within the perovskite structure with less distortions than the lanthanide end member $LaTaON_2$, which crystallises in a monoclinic space group.[4] The atomic positions shift away from the starting model x, y and z values within the unit cell when a cation is substituted for one of a different size.

The values obtained from PXD for the anionic positions typically yield large esd values and therefore are not reliable. The anionic temperature factors are difficult to determine, thus

have been set at their default values and have consequently not been refined. As oxygen and nitrogen are isoelectronic their sites cannot be distinguished from each other using PXD data alone hence when there are two anionic positions it is assumed the anions randomly occupy both sites alike. Another consequence of this is that the oxygen and nitrogen ratios are fixed to be identical over both anionic positions for the Nd and Dy samples.

The overall cell size can be seen to be decreasing as the lanthanide radius decreases, *i.e.* the cell volume of the La sample is greater than that of Nd, which in turn is greater than the Dy cell volume. In this comparison however the amount of lanthanide present must be taken into account. The amount of lanthanide doping and thus calcium doping on the A-site does vary with 39% La, 50% Nd and 42% Dy on the A-site in each compound respectively. Although the sizes of Ca^{2+} and La^{3+} are similar the radii of the lanthanides decrease across the series. Hence, the presence of more calcium in the Eu and Dy samples causes an increase in the expected cell sizes, based on target stoichiometry.

One refinement factor that could be confirmed analytically is one of metal ion stoichiometry. By carrying out atomic absorption spectroscopy, one could ascertain accurate ratios of cations to confirm the site occupancies from the refinement. In the absence of other analytical techniques, it could be assumed that the non-idealised stoichiometries, *i.e.* different from initial reagent stoichiometry, is a result of the formation of competing phases or mixed metal halides that were removed as the sample was washed.

In the case of europium, the symmetry of the unit cell is rhombohedral, this can be seen in the PXD pattern as the peaks are less split than for an orthorhombic perovskite. Therefore the distortion is less and the symmetry greater. According to the refined data there is also a preference for calcium on the A site over europium which may be linked to the change in symmetry.

Considering europium, it is assumed that it takes oxidation state (III) but under the reducing synthetic conditions this oxidation state is not as stable as it is for other trivalent lanthanides. Hence the europium oxynitride compounds targeted could, at least in part, contain Eu (II). The presence of divalent europium within an oxynitride system has been reported by Marchand,[6] hence the targeted compound $EuTaON_2$ is formally written $EuTa(O,N)_3$. The major observation is the difference in colour, the europium sample is black compared with

the brown and yellow colours reported for other samples. A colour change is noted in this study too, $Ca_{0.77}Eu_{0.23}TaO_{1.77}N_{1.23}$ is an olive green colour compared to the orange and yellow powders obtained from other syntheses.

3.5 POWDER NEUTRON DIFFRACTION DATA

Powder neutron diffraction (PND) studies were carried out on the $Ca_{0.5}Nd_{0.5}TaO_{1.5}N_{1.5}$ sample. This is beneficial as the site occupancy of oxygen and nitrogen can be determined as they have different coherent scattering lengths, N = 9.36 fm and O = 5.803 fm.[21,22] This is not possible in PXD as both anions have the same number of electrons and thereby have similar scattering factors.

Unfortunately, some lanthanide samples cannot be analysed by neutron diffraction for their absorption co-efficients are too high. Naturally occurring sources of europium and dysprosium contain isotopes that are strong absorbers of neutrons in high abundance[22] thus making it necessary to use specifically pre-selected isotopes which only weakly absorb. Thus it was only possible to collect data on the neodymium sample.

Time of flight data was collected at 298 K at the ISIS facility in the Rutherford Appleton Laboratory (RAL), on *POLARIS*, a medium resolution, high intensity powder diffractometer. The results for the lattice parameters and atomic positions are summarised in *Tables 3.11* and *3.12*.

Table 3.11: Crystallographic data for $Ca_{0.5}Nd_{0.5}TaO_{1.5}N_{1.5}$.

Compound	$Ca_{0.5}Nd_{0.5}TaO_{1.5}N_{1.5}$
Crystal System	Orthorhombic
Space Group	*Pnma* (no. 62)
Cell Parameters	a = 5.653 (1) Å
	b = 7.955 (2) Å
	c = 5.605 (1) Å
Cell Volume	252.05 (10) Å^3
χ^2	1.560
R_{wp}	0.0248

Table 3.12: Refined atomic positions for $Ca_{0.5}Nd_{0.5}TaO_{1.5}N_{1.5}$. E.s.ds are given in parentheses.

Atom	x	y	z	Occupancy	$U_{(iso)}$ [Å^2]
Ca / Nd	0.0360 (7)	0.25	-0.012 (2)	0.5 / 0.5	-0.0067 (8)
Ta	0.5	0	0	1.0	0.0005 (6)
O (1)	0.486 (1)	0.25	0.074 (2)	0.380 (40)	0.0040 (4)
N (1)	0.486 (1)	0.25	0.074 (2)	0.620 (40)	0.0040 (4)
O (2)	0.2917 (9)	0.0429 (6)	0.7064 (9)	0.560 (20)	0.0039 (4)
N (2)	0.2917 (9)	0.0429 (6)	0.7064 (9)	0.440 (20)	0.0039 (4)

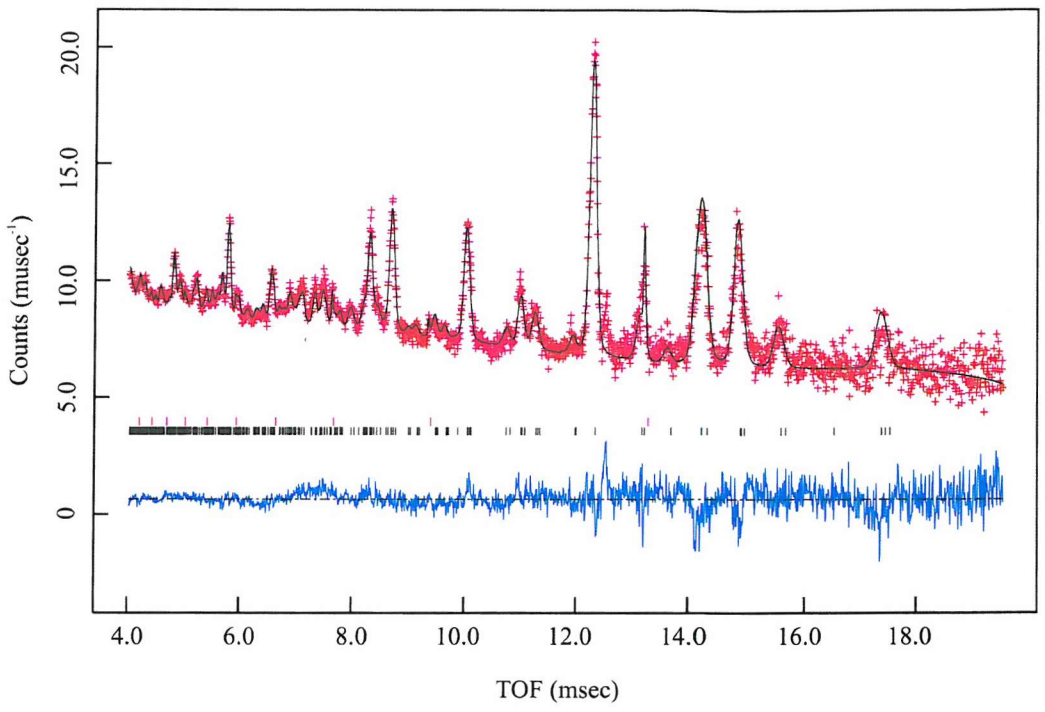

fig. 3.7: *Rietveld refinement fit for $Ca_{0.5}Nd_{0.5}TaO_{1.5}N_{1.5}$; obtained from PND data collected on the POLARIS diffractometer backscattering bank at the Rutherford Appleton Laboratory (UK). The cross marks are the observed intensities, the upper trace the calculated profile, the black tick marks the calculated peak positions of the sample, the red tick marks the calculated positions of the vanadium can and the lower line the difference.*

The refinement data yields important information about the distribution of anions within the structure. It suggests that nitrogen ions have a preference for the first O/N site, the axial anionic position within the octahedral network whereas the oxygen ions have a slightly greater preference for the equatorial O/N (2) site. This is similar to $LaTaON_2$ where the axial positions of the TaO_2N_4 octahedra are occupied by nitrogen.[4]

Without the use of PND or *ab initio* calculations within the density functional theory, it is impossible to say anything about the ordering of the anions within an oxynitride. It must therefore be assumed that the distribution of oxygen and nitrogen is random until further analysis proves otherwise.

PND studies on four perovskites, $LaTaON_2$, $CaTaO_2N$, $SrTaO_2N$[4] and $BaTaO_2N$[23,24] give some indication as to the distribution of anions. Jansen found the first three compounds to be ordered whereas in the case of $BaTaO_2N$, more detailed studies have centred on both ordered and disordered models.[25] Work has also focussed on local structure and relaxations of symmetry elements[25] as this varies due to the differences in ionic radii and valencies.

3.6 CRYSTAL STRUCTURE AND BOND LENGTHS OF $Ca_{(1-x)}Ln_xTaO_{(2-x)}N_{(1+x)}$

3.6.1 ORTHORHOMBIC CRYSTAL STRUCTURE

The symmetry details and atomic positions obtained from a Rietveld refinement can be interpreted to generate a representation of the crystal structure using polyhedra to identify the TaO_xN_y octahedra. In example, the crystal structure of $Ca_{0.5}Nd_{0.5}TaO_{1.5}N_{1.5}$ is represented in *fig. 3.8, vide infra.*

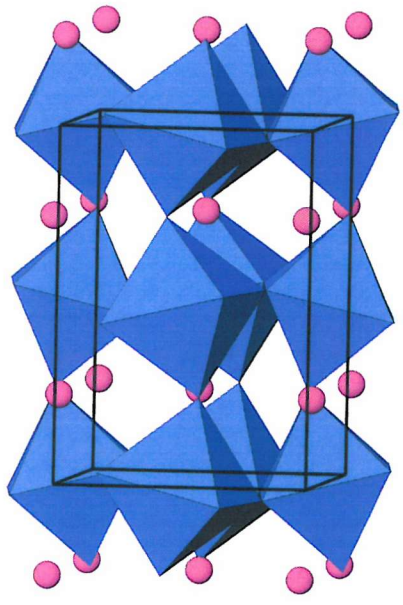

fig. 3.8: *Crystal structure of $Ca_{0.5}Nd_{0.5}TaO_{1.5}N_{1.5}$, where the blue polyhedra represent TaO_3N_3 octahedra and the pink spheres represent calcium and neodymium cations occupying the interstitial A sites.*

This structure plot reveals the distortions within the lattice from cubic symmetry. In a cubic perovskite the apices of the octahedra are vertical. In this example the octahedra are tilted such that the Ta-X-Ta, where X represents an apical anion, bonding follows a zigzag path

throughout the structure. The bond angle for Ta-X-Ta obtained from the Rietveld refinement was 160.0(6)°, as opposed to 180° in a cubic perovskite.

3.6.2 *RHOMBOHEDRAL CRYSTAL STRUCTURE*

In the same manner symmetry details and atomic positions for the refined rhombohedral perovskite, $Ca_{0.77}Eu_{0.23}TaO_{1.77}N_{1.23}$, can be used to generate a crystal structure. Overall the crystal structure is similar to *fig. 3.8* though the tilting of the octahedra is less for a rhombohedral distortion from cubic symmetry than for an orthorhombic distortion. A different orientation of the polyhedra can be viewed down one axis of the unit cell, this is represented in *fig. 3.9*.

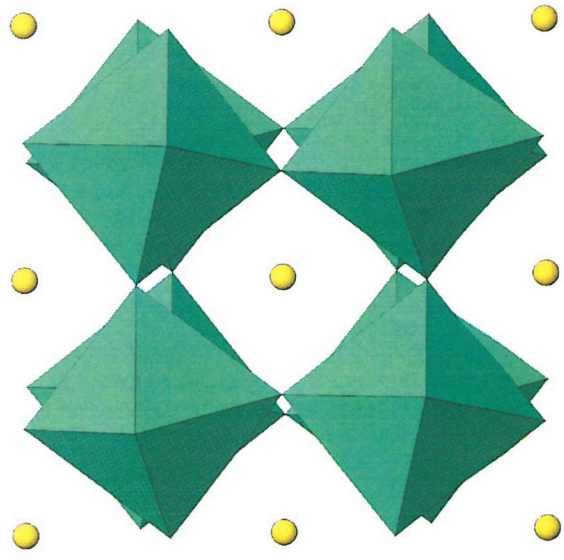

fig. 3.9: *Crystal structure of $Ca_{0.77}Eu_{0.23}TaO_{1.77}N_{1.23}$, where the green polyhedra represent $TaO_{3.54}N_{2.46}$ octahedra and the yellow spheres represent calcium and europium cations occupying the interstitial A sites.*

In a cubic structure only one polyhedra layer would be visible, however due to distortions in $Ca_{0.77}Eu_{0.23}TaO_{1.77}N_{1.23}$ the layer below is not completely obstructed from view as represented in *fig. 3.9*.

3.6.3 *BOND LENGTHS*

The average cation anion bond lengths are generated from a Rietveld refinement and are listed in *Table 3.13*.

Table 3.13: Bond lengths of the A and B cations to anions in $Ca_{(1-x)}Ln_xTaO_{(2-x)}N_{(1+x)}$ where $0 < x \leq 1$ and Ln = Nd, Eu and Dy obtained from PXD.

Compound	B Cation-Anion [Å]		A Cation-Anion [Å]	
$Ca_{0.5}Nd_{0.5}TaO_{1.5}N_{1.5}$	Ta-O/N (1):	2.017 (19) x2	Ca/Nd-O/N (1):	3.14 (9) x1
Orthorhombic, *Pnma*	Ta-O/N (2):	2.357 (31) x2	Ca/Nd-O/N (1):	2.51 (9) x1
	Ta-O/N (2):	1.677 (33) x2	Ca/Nd-O/N (1):	3.21 (1) x1
			Ca/Nd-O/N (1):	2.42 (1) x1
			Ca/Nd-O/N (2):	3.03 (9) x2
			Ca/Nd-O/N (2):	2.55 (1) x2
			Ca/Nd-O/N (2):	3.14 (8) x2
			Ca/Nd-O/N (2)	2.65 (8) x2
$Ca_{0.77}Eu_{0.23}TaO_{1.77}N_{1..23}$	Ta-O/N:	2.0053 (30) x6	Ca/Eu-O/N:	2.441 (17) x3
Rhombohedral, *R-3c*			Ca/Eu-O/N:	3.154 (17) x3
			Ca/Eu-O/N:	2.8068 (21) x6
$Ca_{0.57}Dy_{0.43}TaO_{1.57}N_{1.43}$	Ta-O/N (1):	2.198 (18) x2	Ca/Dy-O/N (1):	2.68 (4) x1
Orthorhombic, *Pnma*	Ta-O/N (2):	2.00 (6) x2	Ca/Dy-O/N (1):	2.10 (4) x1
	Ta-O/N (2):	2.02 (6) x2	Ca/Dy-O/N (1):	3.46 (4) x1
			Ca/Dy-O/N (1):	3.24 (4) x1
			Ca/Dy-O/N (2):	2.88 (5) x2
			Ca/Dy-O/N (2):	2.47 (5) x2
			Ca/Dy-O/N (2):	2.73 (5) x2
			Ca/Dy-O/N (2):	3.19 (4) x2

The Ta-O/N bond lengths in the neodymium sample are on average shorter than the literature values for $CaTaO_2N$, used as a starting model in the refinement.[4] This is due to the abnormally short bond length (1.677 Å) bringing down the average value. The A site-anion bond lengths are, in contrast, slightly longer (by 0.023 Å on average) than literature values for $CaTaO_2N$. This could be due to increased tilting of the TaX_6 octahedra. The average bond lengths in the dysprosium sample are longer than those calculated from literature values. As these correspond to long A site cation to anion bond lengths it is feasible that they cannot be met due to the small radius of the dysprosium cation compared to calcium and thus the reduction in preferred co-ordination number. Therefore this could result in only a weak interaction between Dy and O/N as bond strength is inversely proportional to bond length.

On the other hand calcium and neodymium are comparable in size, with crystal radii of 1.48 and 1.41 Å respectively.

3.7 UV-VISIBLE SPECTROSCOPY

UV-Vis. spectroscopy was carried out on a Perkin Elmer UV/Vis/Lambda 35 in the range of 200 nm to 800 nm with $BaSO_4$ used as a reference. Spectra for some lanthanide substitutions, regardless of crystallinity, can be found in *figs. 3.10* and *3.11*. These spectra highlight differences in the absorption bands in the region of 450 – 650 nm for these compounds.

The colour of a solid is dependent on the selective absorption of light. This in turn is related to an electronic interband transition which leads to a steep absorption edge in the visible region. The spectrometer measures % reflection as opposed to absorption so thus as the sum of % reflection and % absorption is equal to one these spectra could be inverted to give the absorption edge, a physical concept used by Jansen to assess spectroscopic data.[10]

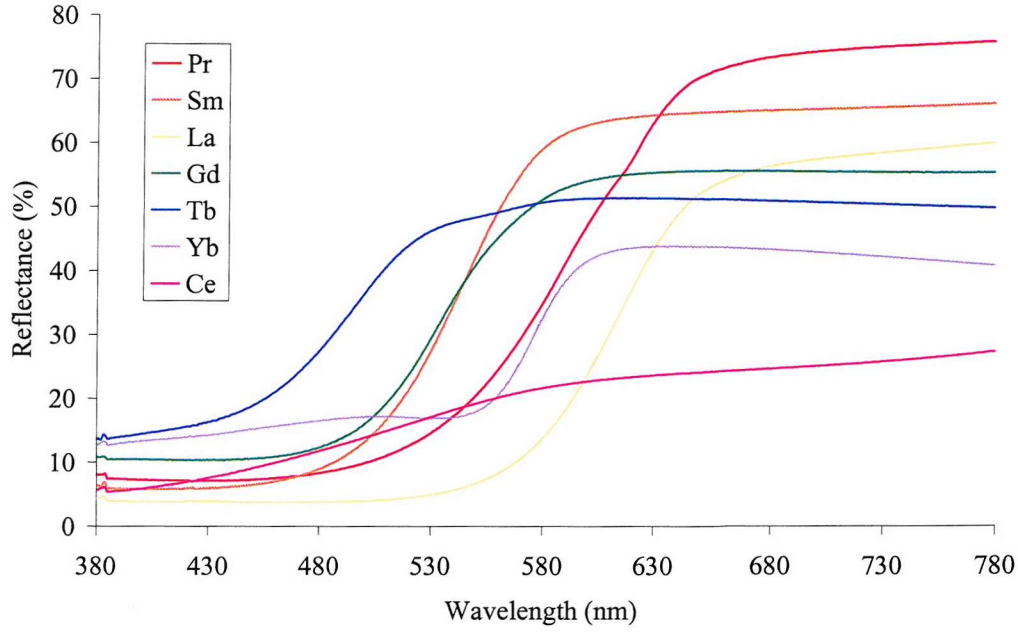

fig. 3.10: *UV-Visible spectra of $LaTaON_2$ and $Ln_2Ta_2O_5N_2$ where Ln = La, Ce, Pr, Sm, Gd, Tb, and Yb, arranged in order of percentage reflectance (see legend).*

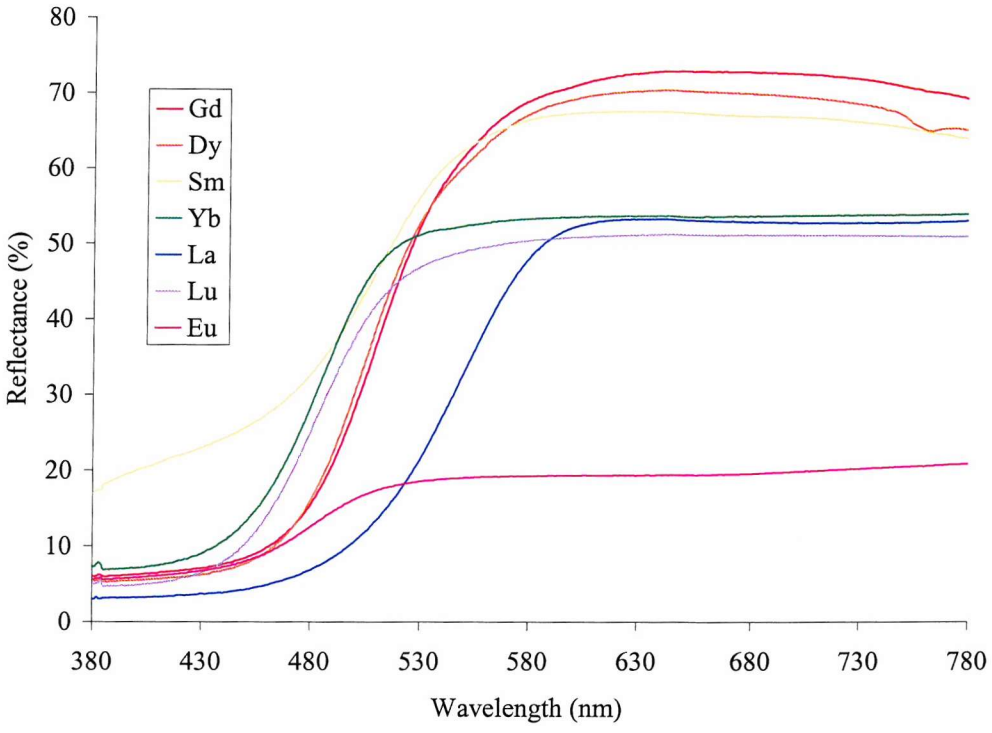

fig. 3.11: *UV-Visible spectra of $Ca_{(1-x)}Ln_xTaO_{(2-x)}N_{(1+x)}$, where x = 0.5 (target phase) and Ln = La, Sm, Eu, Gd, Dy, Yb and Lu, arranged in order of percentage reflectance (see legend).*

Most of the spectra display broad reflectance bands with a steep edge. These bands correspond to the absorption of radiation and thus promotion of electrons across the band gap of the semiconductor materials. The width of this band gap determines the energy required to promote an electron. For oxynitride materials this is usually in the visible region and hence intensely coloured compounds are a result.

Light of longer wavelengths is being reflected corresponding to the red end of the electromagnetic spectrum whilst the samples absorb wavelengths of light from the blue end, which is expected based on the colours of these pigments (green-red). The terbium sample in *fig. 3.10* reflects more light of shorter wavelengths than any other sample, which is responsible for its green hue. Both the cerium sample in *fig. 3.10* and the europium sample in *fig. 3.11* have low reflectance over the visible region. This corresponds to the dark colours (olive green) of the samples and consequently results in lower lightness values compared with the brighter coloured pigments.

From this data the better pigments are, in the 50% doping case; Gd and Dy and in the 100% doping; La, Pr and Sm. These pigments display the steepest edges in their spectra. This is a sign of colour purity. It also happens that all five samples have the higher percentage reflectance values at long wavelengths yielding a more intense colour.

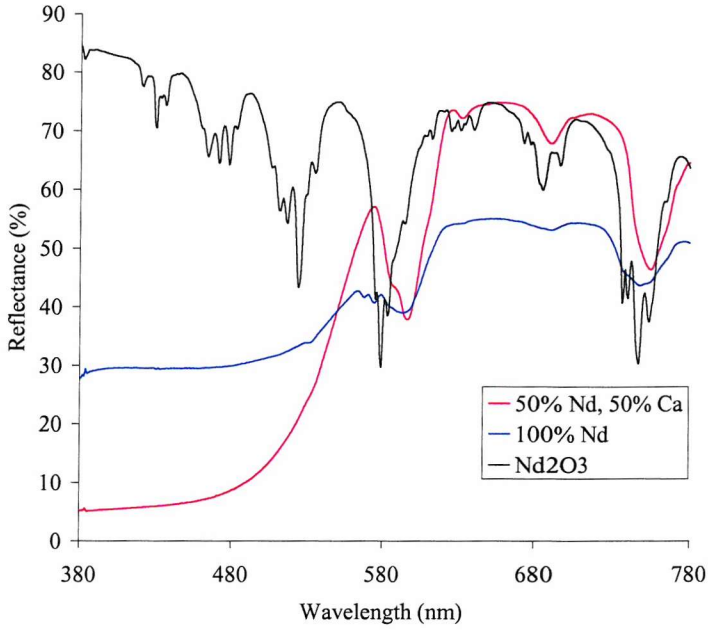

fig. 3.12: *UV-Visible spectra of $Ca_{0.5}Nd_{0.5}TaO_{1.5}N_{1.5}$ (blue), $NdTaON_2$ / $Nd_2Ta_2O_5N_2$ mixed phase (red) and Nd_2O_3 (black).*

Interesting results are obtained from both neodymium samples. Several electronic transition bands can clearly be seen in *fig 3.12*. These transitions can be seen to match those displayed in the spectrum of Nd_2O_3. These arise due to transitions from the 4*f* orbitals to the empty 5*d* orbitals in neodymium and are therefore present in samples containing neodymium.

For the lanthanide substitutions made onto the A site of the perovskite and pyrochlore structures, there are many variations in the observed product colour. These differences support the idea that the band gap of an oxynitride can be fine tuned in order to alter the colour of the compound. The substitution of different lanthanides within both structures adjusts the electronegativity difference between cation and anion, based on the electropositivity value of each lanthanide. This in turn modifies the band gap slightly, thus changing the energy at which the characteristic interband transition takes place thereby altering the colour. Altering the cation ratios within each system directly alters the uptake of

nitrogen, such that electroneutrality is maintained, hence this too can affect the band gap energies.

For the single phase products it is possible to estimate the band gap energies from the absorption edges within the UV-Vis. spectra. This is performed using *Equations 3.1 – 3.4.*

Equation 3.1

$$c = f\lambda$$

where c is the speed of light in a vacuum, 3×10^8 m s^{-1},

f is the frequency of incident radiation in hertz,

λ is the wavelength of incident radiation in metres.

Equation 3.2

$$E_J = hf$$

where E_J is the energy of incident radiation in joules,

h is Planck's constant, 6.63×10^{-34} m^2 kg s^{-1} (or J s).

Equation 3.3

$$E_{eV} = qV$$

where E_{eV} is the work done on a charge in electronvolts,

q is the charge in coulombs,

V is the potential difference of the electric field in volts.

As the charge on an electron is 1.6×10^{-19} C (coulombs), 1 electronvolt is the energy given to an electron accelerated through a potential difference of 1 volt. Thus;

Equation 3.4

$$1 \text{ eV} = 1.6 \times 10^{-19} \text{ J}$$

Band gap calculations have been summarised in *Table 3.14.* Meaningful numbers may only be ascertained for single phase materials as the band gap is particular to the compound. Where a competing phase exists the UV-Vis. spectrum includes reflectance from both phases, *i.e.* it does not discriminate between each compound, thus the absorption edge varies. The wavelength for the absorption edge is taken midway between the start and finish of the range

at which the change from absorption to reflection takes place, *i.e.* at the point of inflection, hence this is easier to estimate when the gradient is steeper.

Table 3.14: Band gap calculations of various lanthanide substitutions.

Target Sample	Colour	Estimated Wavelength [nm]	Band Gap Energy [eV]
$LaTaON_2$	Brick Red	610	2.04
$CaPrTa_2(O,N)_7$	Yellow Green	480	2.59
$Pr_2Ta_2O_5N_2$	Orange	580	2.14
$Ca_{0.5}Eu_{0.5}TaO_{1.5}N_{1.5}$	Olive Green	490	2.54
$Tb_2Ta_2O_5N_2$	Lime Green	470	2.64
$Dy_2Ta_2O_5N_2$	Brick Red	590	2.11
$Ca_{0.5}Dy_{0.5}TaO_{1.5}N_{1.5}$	Bright Yellow	540	2.30
$Yb_2Ta_2O_5N_2$	Coral	585	2.13

Band gap calculations could not be obtained for $Ca_{0.5}Nd_{0.5}TaO_{1.5}N_{1.5}$ as this spectrum did not have the same broad absorption bands that the other spectra displayed, see *fig. 3.12*. Although the onset of the absorption edge can be seen at around 480 nm, the end of the edge is masked by a *f-d* transition.

The values of these band gap energies are in direct relation to the observed colour. Those with larger band gaps have absorption edges towards shorter λ and thus electronic transitions occur at higher energies making the pigments green rather than yellow or red.

There appears to be neither a correlation between the lanthanide series nor the structure, *i.e.* perovskite or pyrochlore with the colour of the compound. Red and orange colour pigments are found for small and big radii alike and for perovskite and pyrochlore structures. There is however a reported link between composition and band gap value, based on the amount of nitrogen present. Jansen and Letschert found that the position of the band gap energy varied linearly, from 2.00 to 2.75 eV, with x for the system, $Ca_{(1-x)}La_xTaO_{(2-x)}N_{(1+x)}$.[10] The results obtained in this study are of similar values, hence the estimations are a good approximation to the true values.

More information about the colour and brightness of the pigments is obtained from $L^*a^*b^*$ measurements in the next section.

3.8 COLOUR MEASUREMENTS

From the UV-Vis. spectroscopy data, colour measurements have been ascertained and collated in *Table 3.15*. Alongside this is a description of the colour to aid interpretation of the $L^*a^*b^*$ numbers.

The colour measurements were carried out 2 years after synthesis and in some cases the colours had faded slightly though some of the pigments originally took pastel shades compared with the intense colours of $LaTaON_2$ and $CaTaO_2N$, see *Chapter 7*. The amount of ammonolysis time affected the intensity of colour, with the colour deepening after each firing, therefore suggesting more nitrogen substitution had taken place.

Various end members of the series, $LnTaON_2$ where Ln = lanthanide, have been synthesised previously by Marchand *et al.* and are stated to be brown in colour with the exception of $GdTaON_2$ (bright yellow) and $EuTa(O,N)_3$ (black).[6] This is due to the differences in synthetic technique. Marchand's approach is via an intermediate phase $LnTaO_4$, synthesised from the parent oxides at 1400-1500 °C. Several heating cycles with intermediate grinding is required to complete the reaction. The product is then fired under ammonia for 24 hours at 950 °C. Although a successful approach, a much lower reaction temperature can be achieved with the use of halide salt mineralisers.[4,10] Low temperature routes are ideal in this work as the end goal is to deposit the best phases onto mica to create lustre pigments.

In interpreting the $L^*a^*b^*$ colour measurements the following definitions should be recognised:

L^* is a measure of lightness (of an object) and takes a value between 0 (black) to 100 (white).
a^* is a measure of redness (positive a^*) or greenness (negative a^*)
b^* is a measure of yellowness (positive b^*) or blueness (negative b^*)

Table 3.15: Colour measurements of $Ca_{(1-x)}Ln_xTaO_{(2-x)}N_{(1+x)}$ where $0 < x \leq 1$ and Ln a lanthanide excluding Pm.

Target Sample	Colour	*L**	*a**	*b**
$ScTaON_2$	Dark Orange	53.14	29.45	40.63
$YTaON_2$	Orange Red	51.61	31.67	30.02
$LaTaON_2$*	Brick Red	41.39	39.10	31.47
$CeTaON_2$	Olive Green	50.24	3.41	23.27
$PrTaON_2$*	Orange	58.24	32.89	43.19
$NdTaON_2$	Dusty Pink	68.35	8.78	12.13
$SmTaON_2$	Bright Orange	69.66	20.01	64.22
$EuTaON_2$*	Mid Brown	35.07	5.75	13.00
$GdTaON_2$*	Golden Yellow	67.81	14.55	48.15
$TbTaON_2$*	Lime Green	73.16	-2.95	35.29
$DyTaON_2$*	Brick Red	51.03	21.08	22.39
$HoTaON_2$	Brown	55.92	1.82	5.13
$ErTaON_2$	Orange Red	54.42	27.66	28.62
$TmTaON_2$	Orange Brown	51.42	26.23	26.21
$YbTaON_2$	Coral	56.86	22.17	18.83
$LuTaON_2$	Brick Red	51.41	32.29	27.03
$Ca_{0.5}Sc_{0.5}TaO_{1.5}N_{1.5}$	Camel	60.23	17.76	37.97
$Ca_{0.5}Y_{0.5}TaO_{1.5}N_{1.5}$	Camel	68.14	11.37	37.75
$Ca_{0.5}La_{0.5}TaO_{1.5}N_{1.5}$*	Golden Orange	63.60	19.89	63.72
$Ca_{0.5}Ce_{0.5}TaO_{1.5}N_{1.5}$	White	N/A	N/A	N/A
$Ca_{0.5}Pr_{0.5}TaO_{1.5}N_{1.5}$*	Yellow Green	66.19	0.05	25.94
$Ca_{0.5}Nd_{0.5}TaO_{1.5}N_{1.5}$*	Golden Orange	66.77	20.72	59.98
$Ca_{0.5}Sm_{0.5}TaO_{1.5}N_{1.5}$	Light Yellow	80.51	1.02	37.02
$Ca_{0.5}Eu_{0.5}TaO_{1.5}N_{1.5}$*	Olive Green	49.45	-4.49	23.57
$Ca_{0.5}Gd_{0.5}TaO_{1.5}N_{1.5}$*	Bright Yellow	79.02	4.72	69.34
$Ca_{0.5}Tb_{0.5}TaO_{1.5}N_{1.5}$*	White	N/A	N/A	N/A
$Ca_{0.5}Dy_{0.5}TaO_{1.5}N_{1.5}$*	Bright Yellow	78.65	2.60	69.97
$Ca_{0.5}Ho_{0.5}TaO_{1.5}N_{1.5}$*	Yellow Orange	77.79	1.96	63.88
$Ca_{0.5}Er_{0.5}TaO_{1.5}N_{1.5}$	Medium Yellow	63.11	2.56	44.11
$Ca_{0.5}Tm_{0.5}TaO_{1.5}N_{1.5}$	Golden Yellow	69.23	1.19	46.03
$Ca_{0.5}Yb_{0.5}TaO_{1.5}N_{1.5}$*	Pale Yellow	75.31	-8.46	47.87
$Ca_{0.5}Lu_{0.5}TaO_{1.5}N_{1.5}$	Bright Yellow	73.08	-7.16	50.89

Samples marked (*) are single phase or single phase with minimal competing phase.

All target compounds were screened as colour intensity is more important than crystallinity, although the presence of certain impurities drastically alters the results. For instance Ta_3N_5, which is vermillion,[26] makes a sample browner and darker reducing L^*, whereas the presence of a white metal oxide makes the pigment brighter, increasing L^*.

The colour of the compound synthesised has been affected by the presence of mineralisers. This was highlighted in the synthesis of $Ca_{0.61}La_{0.39}TaO_{1.61}N_{1.39}$, see *Chapter 4*. Using the mineraliser route this compound is a bright golden orange but when they are omitted the compound, synthesised under identical conditions, is light terracotta.

With the exception of the a few samples, there appears to be a good similarity in the hues of the compounds. Most range from yellow to brick red, which corresponds to interband transitions at the lower energy end of the visible spectrum. It is assumed that more nitrogen is present when the wavelength causing such transitions is longer. The substitution of oxygen for nitrogen results in a narrowing of the band gap and thus a lowering of the energy at which these transitions occur, pushing the transitions towards the red wavelengths of light. This phenomenon is visibly observed in the cases of $LaTaON_2$ and $CaTaO_2N$. The former sample has the higher nitrogen content and is brick red *cf.* the bright yellow $CaTaO_2N$.

From these $L^*a^*b^*$ values the best pigments are those that have high $+a^*$ (red pigments) or high $+b^*$ (yellow pigments) or high values for both (orange pigments). These were usually the perovskite phases, La, Nd, Gd or Dy, with calcium substituted onto the A site as well. The better yellow pigments (Gd and Dy) have an a^* value close to zero, as is the case for gadolinium and dysprosium. However the $+b^*$ values, the yellowness numbers are not as high as cadmium yellow ($+b^* = 99.12$), the pigment they are designed to replace. In the same respect the red and orange pigments synthesised here do not match the values of the cadmium reds and oranges. With further manipulation of stoichiometry as well as lanthanide cation the values of the commercial pigments could be met.

When a compound is white, such as the 50 % attempted doping of terbium on the A-site, there is little to no nitrogen substitution and the band gap has been shifted into the ultraviolet. In fact it is possible that the pyrochlore $Ca_2Ta_2O_7$ has formed with an amorphous terbium oxide phase undetected by PXD. Although terbium is not usually in the oxidation state typical of most lanthanides, the atmosphere of ammonia may cause a reduction from the

mixed valence state in Tb_4O_7 to Tb (III), thus explaining the lime green pyrochlore that forms when terbium oxide and tantalum pentoxide are reacted together.

3.9 DISCUSSION AND CONCLUSIONS

The major difficulty in the production of oxynitride perovskites and pyrochlores via concurrent substitution is one of valency. Oxynitrides that are rich in divalent cations tend to form more readily than those that have undergone concurrent substitution, M^{2+} for Ln^{3+} together with O^{2-} for N^{3-}. The trivalent ions have slower mobilities within the solid state compared with that of the divalent ions. As the diffusion of ions across the crystal faces of the reactants is key to the formation of new mixed metal compounds it would follow that an increase in charge density could decrease the rate of diffusion. Charge density increases on increasing valency and decreasing ionic radius hence by reasoning the lanthanides to the right of the series have slower ionic mobilities than the alkaline earth cations they replace. This means that samples containing only lanthanide on the A site, often require two overnight heat treatments at 850 °C followed by 8 hours at 950 °C with intermediate re-grindings.

The samples generated in this work show a varying range of colours from green through to yellow and red. By altering the compositions of the mutually soluble $CaTaO_2N$ and $LaTaON_2$, Jansen *et al.*[10] have been able to fine tune the properties, in particular the oxygen to nitrogen ratio. In the same way, it is possible to substitute into this structure various cations, which in turn alters the hue of the pigment synthesised. There are in fact many permutations possible, not only in the type of substituted cations but also in stoichiometric composition including more than two different A site cations or a mixed B site. From an industrial point of view a combinatorial approach could be employed to target the best candidates for pigment synthesis. In this way reaction conditions can also be varied to optimise the synthesis without the need for hundreds of experiments.

Optimisation of synthetic conditions is important as there appears to be a discrepancy in the colour of a compound depending upon the conditions used. In a preliminary study that trials the experimental method an orange, single phase, crystalline sample of $LaTaON_2$ is readily obtained from firing the appropriate reactants at 850 °C overnight. After intimate grinding and re-firing at this temperature, the same orange colour is retained. However, subsequent

firing at 950 °C for a further 8 hours turns the compound brick red. The colour change has meant a shift of the band gap towards lower energy and thus an increase in nitrogen within the unit cell. This is most likely as a direct result of how fast the reactive gas flows through the furnace, a variable that proved difficult to control. The use of a gas flow meter appeared to hinder the reaction and was discarded in favour of judging by eye the volume of effluent gases in a paraffin bubbler.

It is beneficial to reduce the temperature and the use of reactive gas as this brings down the cost of pigment manufacture. The temperature reduction is an essential step when considering the applications of these pigments. The scope of this work is to synthesise new lustre pigments which involves coating mica flakes with the oxynitride phases synthesised. Mica is only thermally stable up to *ca.* 850 °C after which it decomposes hence it is critical that any reaction must be carried out below this temperature.

It has proved difficult to synthesise either a pure lanthanide single phase perovskite or pyrochlore as both phases co-exist for certain ionic radii magnitudes. These have been synthesised previously without the use of mineralisers and at higher temperatures via a $LnTaO_4$ precursor.[6] The crystal structure of the pyrochlore is dependant on the radius of Ln^{3+}, whereby the smaller ions tend towards a defect fluorite structure and the bigger cations cause the distortion of the trigonal antiprism around tantalum towards an octahedron.[27]

The colour of the europium sample with no calcium present is brown. It has been suggested by Marchand[6] that europium is reduced to Eu^{2+}. This is due to the instability of the +3 oxidation state of europium compared with other lanthanides when treated with the reducing ammonia gas. The reduction in positive charge on europium alters the band gap and thus the colour accordingly. Added to this, the colour of the Eu^{2+} ion in solution is brown. Hence there is this difference between the europium samples and the intense colours of the majority of the other samples.

3.10 REFERENCES

[1] Hoffmann R.; *J. Chem. Phys.*, **39**, 1397 (1963)

[2] Niewa R., DiSalvo F. J.; *Chem. Mater.*, **10**, 2733 (1998)

[3] Marchand R.; *Handbook on the Physics and Chemistry of Rare Earths*, Chapter 166: "Ternary and Higher Order Nitride Materials", **25**, 51 (1998)

[4] Günther E., Hagenmayer R., Jansen M.; *Z. Anorg. Allg. Chem.*, **626**, 1519 (2000)

[5] Marchand R., Pors F., Laurent Y.; *Rev. Int. Hautes Tempér. Réfract. Fr.*, **23**, 11 (1986)

[6] Marchand R., Pors F., Laurent Y.; *Ann. Chim. Fr.*, **16**, 553 (1991)

[7] Diot N., Larcher O., Marchand R., Kempf J. Y., Macaudière P.; *J. Alloy. Compd.*, **323-324**, 45 (2001)

[8] Marchand R., Laurent Y., Guyader J., L'Haridon P., Verdier P.; *J. Eur. Ceram. Soc.*, **8**, 197 (1991)

[9] Diot N., Marchand R., Haines J., Léger J. M., Macaudière P., Hull S; *J. Solid State Chem.*, **146**, 390 (1999)

[10] Jansen M., Letschert H.; *Nature*, **404**, 980 (2000)

[11] Bruker Advanced X-Ray Solutions; *EVA*, **V 6.0** (2000)

[12] Laugier J., Bochu B.; *CELREF*, Laboratoire des Matériaux et du Génie Physique, Ecole Nationale Supérieure de Physique de Grenoble INPG (France) (2000)

[13] Pors F., Marchand R., Laurent Y.; *J. Solid State Chem.*, **107**, 39 (1993)

[14] Wells A. F.; *Structural Inorganic Chemistry*, Oxford University Press (UK), Third Edition (1962)

[15] Wolcyrz M., Lukaszewski M.; *Z. Kristallogr. Kristallgeom., Kristallphys., Kristallchem.*, **177**, 53 (1986)

[16] García- Muñoz J. L., Rodríguez-Carvajal J., Lacorre P., Torrance J. B.; *Phys. Rev. B*, **46**, 4414 (1992)

[17] Larson A. C., Von Dreele R. B.; *General Structure Analysis System*, MS-H805, Los Alamos National Laboratory, (USA) N M 87545 (1990)

[18] Rietveld H. M.; *Acta Crystallogr.*, **22**, 151 (1967)

[19] Rietveld H. M.; *J. Appl. Crystallogr.*, **2**, 65 (1969)

[20] McCusker L. B., Von Dreele R. B., Cox D. E., Louër D., Scardi P.; *J. Appl. Crystallogr.*, **32**, 36 (1999)

[21] Weller M. T., Skinner S. J.; *Int. J. Inorg. Mater.*, **2**, 463 (2000)

[22] http://www.ncnr.nist.gov/resources/n-lengths/

[23] Marchand R., Pors F., Laurent Y., Regreny O., Lostec J., Haussonne J. M.; *J. Phys.-Paris*, **47 (C-1)**, 901 (1986)

[24] Pors F., Marchand R., Laurent Y.; *Mat. Res. Bull.*, **23**, 1447 (1988)

[25] Fang C. M., de Wijs G. A., Orhan E., de With G., de Groot R. A., Hintzen H. T., Marchand R.; *J Phys. Chem. Solids*, **64**, 281 (2003)

[26] Brese N. E., O'Keefe M.; *Struct. Bonding (Berlin)*, **79**, 307 (1992)

[27] Tessier F., Marchand R.; *J. Solid State Chem.*, **171**, 143 (2003)

CHAPTER FOUR

SYNTHESIS AND CHARACTERISATION OF $A_{(1-x)}La_xTaO_{(2-x)}N_{(1+x)}$ (A = Mg-Ba)

4 ALKALINE EARTH SUBSTITUTIONS IN $A_{0.5}La_{0.5}TaO_{1.5}N_{1.5}$, A = Mg-Ba

4.1 INTRODUCTION

Tantalum oxynitride systems have been of interest to pigment chemists since Jansen *et al.* reported that properties such as brilliance, tinting strength, opacity, dispersability, light-fastness and heat stability rival those of cadmium pigments.[1] Suitable replacements for cadmium based pigments are required due to tougher restrictions on the use of heavy metals. To date there has been little success in finding materials with both suitable properties and the same vibrant red colour that Cd(S,Se) possesses, so the use of more expensive and less stable organic alternatives has been prolific.

This chapter advances the work of the lanthanum substitutions of the previous chapter by interchanging various alkaline earth metals onto the A site of a perovskite-type tantalum oxynitride system, $A_{(1-x)}La_xTaO_{(2-x)}N_{(1+x)}$, with target stoichiometry x = 0.5. The Group 2 metals investigated were magnesium, calcium, strontium and barium. The compounds synthesised were analysed using a variety of techniques. Both X-ray and neutron powder diffraction methods were employed to gain structural details of the compounds synthesised. Thermogravimetric analysis and variable temperature powder X-ray diffraction were used to monitor temperature specific changes such as the loss of nitrogen and the expansion of the unit cell. UV-Vis. spectroscopy and $L^*a^*b^*$ measurements were undertaken to assess the materials' colour properties and thus capabilities of replacing existing yellow, orange and red pigments currently on the market today. Finally, energy dispersive analysis of X-rays (EDAX) was carried out to calculate atomic stoichiometries within the magnesium substituted sample.

4.2 SYNTHESIS

Gas transformation reactions with ammonia at elevated temperatures are a route to oxynitrides used extensively in previous work.[2-4] Samples were synthesised by treating simple metal oxides and carbonates with gaseous ammonia at high temperatures. In the syntheses highlighted here, the target compound for each alkaline earth metal substitution was a perovskite-type structure of stoichiometry $A_{0.5}La_{0.5}TaO_{1.5}N_{1.5}$. For each reaction

stoichiometric amounts of Ta_2O_5 (Aldrich, 99%), ACO_3 where A is Mg-Ba (99%) and La_2O_3 (99.99%) were intimately ground in an inert acetone media with *ca.* 50% wt. ratio of halide salts employed as mineralisers. The mineralisers employed were $CaCl_2$, NaCl and KCl, used in equimolar proportions. The samples were fired at 800 - 1000 °C under dry flowing ammonia (Air Products, Electronic Grade) for 20 hours at a flow rate of ~ 7 dm^3 hr^{-1}. If necessary the products were ground and fired again for a further 20 hours. The mineralisers were leached from the fired materials by washing thoroughly with excess de-ionised water.

Halide salts have lower melting points than the reactants and the reaction temperature. Consequently, upon melting mineralisers act as a flux aiding the ionic transport. The mechanisms by which mineralisers work is poorly understood but their presence as catalysts is to aid the formation of an extremely stable crystal structure and to bring down the temperature of the reaction.

4.3 POWDER DIFFRACTION DATA

Powder X-ray diffraction (PXD) data sets were collected on a Siemens D5000 using Cu $K_{\alpha 1}$ radiation (λ=1.5406 Å). Powder neutron diffraction (PND) studies were carried out at the ISIS facility at the Rutherford Appleton Laboratory. Time of flight (TOF) data sets were collected at 298 K on *POLARIS*, a medium resolution, high intensity powder diffractometer. PND allows the oxygen and nitrogen sites to be readily distinguished as they have different scattering lengths. It is not possible to differentiate these sites in PXD, as both anions are isoelectronic.

Both X-ray and neutron powder diffraction data sets were collected on all the synthesised samples, $A_{(1-x)}La_xTaO_{(2-x)}N_{(1+x)}$, where A = Mg, Ca, Sr or Ba (target stoichiometry of $x = 0.5$). In each case a combined Rietveld refinement of both data sets was performed in order that structural data for each compound synthesised could be obtained. Joint refinements were carried out as the use of complementary radiation sources gives an accurate description of the anionic as well as the cationic frameworks. As mentioned in the previous chapter, due to the different coherent scattering lengths of oxygen and nitrogen, PND data facilitates the refinement of anionic occupancy. In contrast to this PXD data sets are beneficial when considering the distribution of cations on the mixed A site, this is particularly relevant for

elements with similar coherent scattering lengths. For example strontium (Z = 38) and lanthanum (Z = 57). The coherent scattering lengths for these elements are 7.02 fm and 8.24 fm respectively.[5] These cations are not isoelectronic and as La^{3+} has more electrons it has the greater scattering power of X-rays *cf.* Sr^{2+}. Consequently, a joint refinement yields more information over two separate refinements.

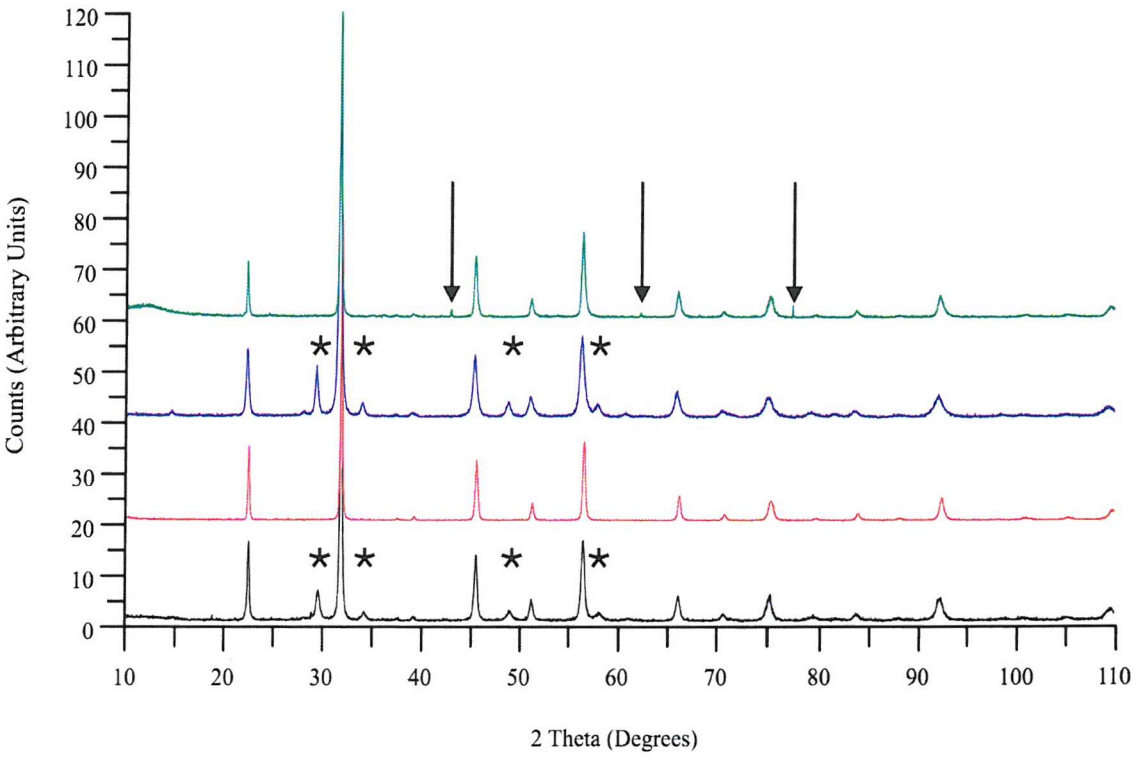

fig. 4.1: *Powder X-ray data for $A_{(1-x)}La_xTaO_{(2-x)}N_{(1+x)}$, where A is Mg (green), Ca (blue), Sr (red) or Ba (black). The asterisk indicates the competing pyrochlore phase and the arrows the MgO impurity.*

After preliminary analysis of the PXD data, shown in *fig. 4.1*, several trends became apparent. The strontium doped system results in a single phase product while in systems where barium and calcium formally substitute for lanthanum in $LaTaON_2$, *i.e.* $Ca,Ba_{(1-x)}Ln_xTaO_{(2-x)}N_{(1+x)}$, a competing pyrochlore phase is formed for some x. This phenomena has previously been reported by Marchand *et al.*[6] for other perovskite-type oxynitrides. The pyrochlore phase detectable in the powder X-ray data is similar to that of $Yb_2Ta_2O_5N_2$ reported in the literature,[7] suggesting that the residual perovskite phase is lanthanide deficient, thus altering the overall stoichiometry of the target phase.

A distorted perovskite is readily obtained for the targeted magnesium substituted compound $Mg_{(1-x)}Ln_xTaO_{(2-x)}N_{(1+x)}$ but later work, primarily PND, showed a small level of MgO impurity.

In some of the X-ray data sets collected the peaks are moderately broad suggesting a small particle size and a lack of coherence, possibly due to compositional inhomogeneity where some regions are predominately oxygen rich whereas others are nitrogen rich.

Several reflections display minor splitting, indicating the distortions from cubic geometry. These distortions are likely to increase as the ionic radius of the A-site cation increases. Goldschmidt deduced a tolerance factor, which measures the compatibility of two cations crystallising in a perovskite structure. From *Equation 1.3*, it can be seen that as the radius of r_A increases so does the tolerance factor t. For an ideal cubic close packed perovskite structure, $t = 1$. Deviations from this value indicate an increase of internal bond strain within the structure. This strain can be reduced through distortions such as the tilting of the TaO_xN_y octahedra within the orthorhombic unit cell.

4.4 STRUCTURAL ANALYSIS

Further structural analysis of these products concentrated on the following idealised composition $A_{0.5}La_{0.5}TaO_{1.5}N_{1.5}$, A = Mg, Ca, Sr, Ba and for each of these materials a powder neutron diffraction data set was collected. In order to define the structures and investigate the stoichiometries of the perovskites, both the powder data sets from X-ray diffraction and from time of flight (TOF) neutron diffraction were analysed simultaneously in a combined refinement using the *GSAS* suite of programs[8] employing the Rietveld method.[9,10] The data sets were refined using a starting model of the orthorhombic $CaTaO_2N$ published in the literature.[11]

The sample $Sr_{0.5}La_{0.5}TaO_{1.5}N_{1.5}$ is a single phase, orthorhombically distorted perovskite with no competing pyrochlore phase or impurities. Structure refinement shows that it crystallises in the space group *Pnma* with cell parameters as displayed in *Table 4.1*.

Table 4.1: Crystallographic data for $Sr_{0.5}La_{0.5}TaO_{1.5}N_{1.5}$.

Compound	$Sr_{0.5}La_{0.5}TaO_{1.5}N_{1.5}$
Crystal System	Orthorhombic
Space Group	*Pnma* (no. 62)
Cell Parameters	a = 5.6543 (3) Å
	b = 7.9666 (4) Å
	c = 5.6479 (3) Å
Cell Volume	254.4 (1) Å^3
χ^2	0.7332
R_{wp}(PXD)	0.1784
R_{wp}(PND)	0.0353

Final refined atomic positions are summarised in *Table 4.2* and the final profile fits achieved for the neutron data and X-ray data are shown in *figs. 4.2a* and *4.2b*. Note that the unit cell size has increased with respect to the literature model for $CaTaO_2N$, (V = 246.32 (3) Å^3). This can be justified due to the increase in size of strontium and lanthanum incorporated into the unit cell.

Table 4.2: Refined atomic positions for $Sr_{0.5}La_{0.5}TaO_{1.5}N_{1.5}$. E.s.ds are given in parentheses.

Atom	x	y	z	$U_{(iso)}$ [Å^2]
Sr/La	0.0056(6)	0.25	0.0019(9)	0.0199(3)
Ta	0.5	0	0	0.0060(2)
O/N (1)	0.4939(8)	0.25	0.0060(2)	0.0128(3)
O/N (2)	0.2726(3)	0.0363 (2)	0.7283(3)	0.0174(4)

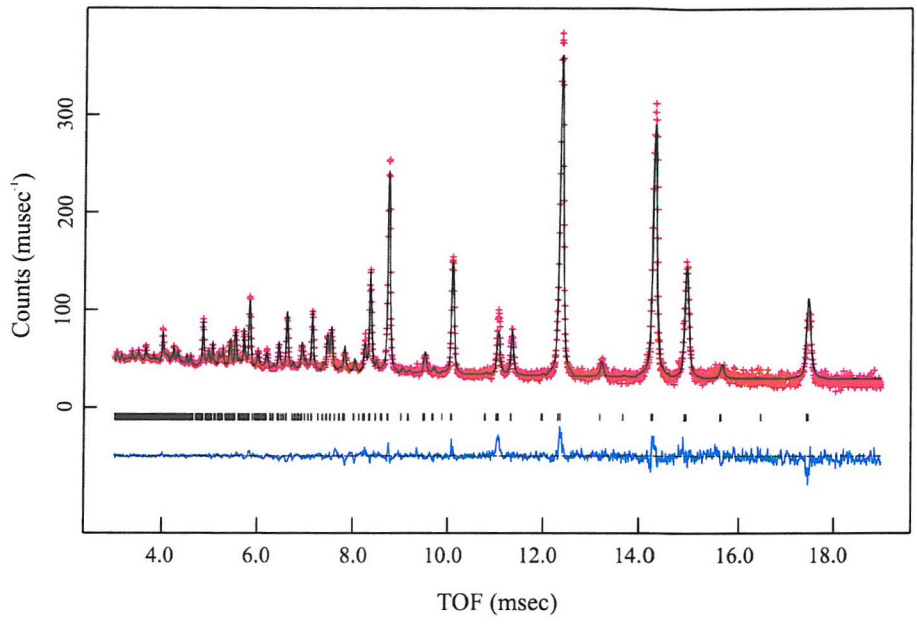

fig. 4.2a: *Rietveld refinement fit for $Sr_{0.5}La_{0.5}TaO_{1.5}N_{1.5}$; obtained from PND data collected on the POLARIS diffractometer backscattering bank at the Rutherford Appleton Laboratory (UK). The cross marks are the observed intensities, the upper trace the calculated profile, the black tick marks the calculated peak positions and the lower line the difference.*

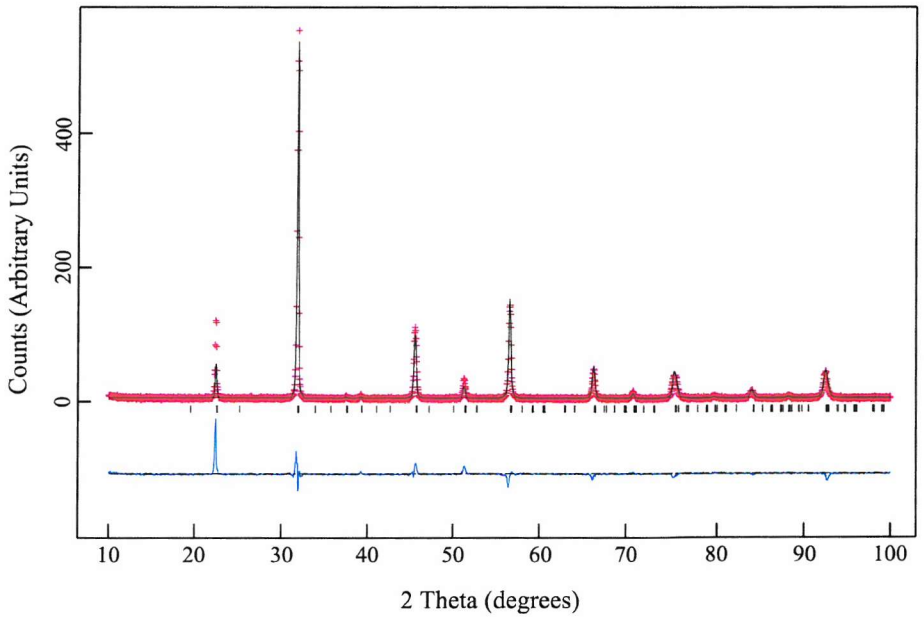

fig. 4.2b: *Rietveld refinement fit for $Sr_{0.5}La_{0.5}TaO_{1.5}N_{1.5}$; obtained from PXD data collected on a Siemens D5000. The cross marks are the observed intensities, the upper trace the calculated profile, the black tick marks the calculated peak positions and the lower line the difference.*

Analysis of the data sets from calcium and barium containing systems is more difficult as inspection of the profiles shows significant levels of a competing pyrochlore impurity phase as described above. Obviously the composition of the perovskite material is dependent on the amount and composition of the competing phases. The diffraction data from both the calcium and barium derivatives is thus modelled using a multiphase technique but with cation stoichiometries linked between phases to the idealised reaction mixture composition and the oxide to nitride ratio constrained to balance overall electroneutrality. For instance the perovskite phase $A_{(1-x)}La_xTaO_{(2-x)}N_{(1+x)}$ where A= barium, a predominance of lanthanum on the cation site is refined necessitating an increase in nitrogen content giving an overall stoichiometry of $Ba_{0.24}La_{0.76}TaO_{1.24}N_{1.76}$. Conversely, when A = calcium, a greater level of calcium on the cation site is found giving a refined stoichiometry of $Ca_{0.61}La_{0.39}TaO_{1.61}N_{1.39}$. Although the reactants ACO_3 and La_2O_3 were mixed in a 1:1 ratio the differences are accountable due to a competing pyrochlore phase such as $Ln_2Ta_2O_5N_2$.[7] This can be assumed to be barium rich for the barium sample but lanthanum rich for the calcium sample, based on the stoichiometries of the main perovskite phase. It is also feasible to have a mixed alkaline earth and lanthanide site in the pyrochlore system yielding $A_xLa_{2-x}Ta_2O_{5+x}N_{2-x}$. In explanation, when x amount of A^{2+} replaces x La^{3+} then the oxygen level must increase and the nitrogen level decrease by x respectively to maintain neutrality within the compound. This therefore could explain the deficiencies in barium in the perovskite phase in comparison to the idealised reaction mixture stoichiometry. Finally it is assumed that there is a full site occupancy on both the cation and anion sites, as it is not possible to devise an accurate constraint allowing for vacancies but maintaining electroneutrality across both phases.

Observed calculated difference (OCD) plots for the calcium sample $Ca_{0.61}La_{0.39}TaO_{1.61}N_{1.39}$ and the barium sample $Ba_{0.24}La_{0.76}TaO_{1.24}N_{1.76}$ are located in *Appendix III.*

Table 4.3: Crystallographic data for $Ca_{0.61}La_{0.39}TaO_{1.61}N_{1.39}$.

Compound	$Ca_{0.61}La_{0.39}TaO_{1.61}N_{1.39}$
Crystal System	Orthorhombic
Space Group	*Pnma* (no. 62)
Cell Parameters	a = 5.665 (1) Å
	b = 7.980 (1) Å
	c = 5.666 (1) Å
Cell Volume	256.12 (8) Å^3
χ^2	0.8809
R_{wp}(PXD)	0.1226
R_{wp}(PND)	0.0277

Table 4.4: Refined atomic positions for $Ca_{0.61}La_{0.39}TaO_{1.61}N_{1.39}$. E.s.ds are given in parentheses.

Atom	x	y	z	Occupancy	$U_{(iso)}$ [Å^2]
Ca	0.003(1)	0.25	0.008(2)	0.608(8)	0.0031(2)
La	0.003(1)	0.25	0.008(2)	0.392(8)	0.0031(2)
Ta	0.5	0	0	1.0	0.0031(2)
O/N (1)	0.490(2)	0.25	0.0754(9)	0.536(3) / 0.464(3)	0.0075(3)
O/N (2)	0.2734(5)	0.0380(4)	0.7287(6)	0.536(3) / 0.464(3)	0.0075(3)

For the calcium sample the competing phase is refined as a cubic pyrochlore in the space group *Fd-3m,* yielding a cell parameter of a = 10.557(3) Å and a cell volume of 1176.7(8) Å^3. In both the calcium and the barium samples further refinements of this competing phase, such as atomic fractions, prove inconclusive as a constraint to maintain the stoichiometry of metal cations between the phases and also to balance the charge of the cation and anion ratios proved difficult to impose. The phase fractions obtained for the perovskite and pyrochlore phases are 15.7(1) and 0.73(3). From this it is calculated that 95.6% of the sample adopts the perovskite phase whilst the remaining 4.4% is attributed to the pyrochlore phase. Thus the emphasis is on the best possible fit of the perovskite phase and less important, the fit of the pyrochlore phase.

Table 4.5: Crystallographic data for $Ba_{0.24}La_{0.76}TaO_{1.24}N_{1.76}$.

Compound	$Ba_{0.24}La_{0.76}TaO_{1.24}N_{1.76}$
Crystal System	Orthorhombic
Space Group	*Pnma* (no. 62)
Cell Parameters	a = 5.6757 (6) Å
	b = 7.9932 (7) Å
	c = 5.6630 (6) Å
Cell Volume	256.92 (4) Å^3
χ^2	0.9526
R_{wp}(PXD)	0.1737
R_{wp}(PND)	0.0370

Table 4.6: Refined atomic positions for $Ba_{0.24}La_{0.76}TaO_{1.24}N_{1.76}$. E.s.ds are given in parentheses.

Atom	x	y	z	Occupancy	$U_{(iso)}$ [Å^2]
Ba	0.0152(6)	0.25	0.005(2)	0.24(3)	0.0052(2)
La	0.0152(6)	0.25	0.005(2)	0.76(2)	0.0052(2)
Ta	0.5	0	0	1.0	0.0052(2)
O/N (1)	0.493(2)	0.25	0.0785(7)	0.414(7) / 0.586(7)	0.0081(2)
O/N (2)	0.2729(4)	0.0377(3)	0.7270(5)	0.414(7) / 0.586(7)	0.0081(2)

From the refinement, the competing barium rich phase is also refined as a cubic pyrochlore in the space group *Fd-3m* with a = 10.567(2) Å and a cell volume of 1180.0(4) Å^3. Considering the low occupancy of barium within the perovskite phase it can be assumed that there is a high proportion of barium on the A site of the $A_xLa_{2-x}Ta_2O_{5+x}N_{2-x}$ pyrochlore. This is reflected in the increase of the pyrochlore unit cell parameter compared to that of the calcium refinement. This is expected as Ba^{2+} is a bigger cation, *i.e.* $Ba^{2+} > La^{3+} > Ca^{2+}$.

The phase fractions obtained for the perovskite and pyrochlore phases are 0.920(7) and 0.038(1). From this it is calculated that 96.04% of the sample adopts the perovskite phase whilst the remaining 3.96% is attributed to the pyrochlore phase. These results mirror the calcium substitution in that there is approximately 4% competing pyrochlore phase for each

sample. This does not fully account for the reduction in barium within the perovskite phase, thus either an amorphous barium phase is present or some barium has been exchanged for metals within the halide salt mineralisers.

In this work crystal radii are quoted from Shannon[12] as they correspond more closely with the actual physical size of ions within solids. The crystal radius of a 12 co-ordinate Ca^{2+} ion (148 pm) is similar to a 12 co-ordinate La^{3+} ion (150 pm).[12] A Ba^{2+} ion has a larger radius (175 pm) and therefore contributes to increased strain within the perovskite structure.[13] From this data tolerance factors can be calculated as given by *Equation 1.3* (see *Chapter 1*).

Table 4.7: Approximate perovskite tolerance factors for ions occupying the A-site.

Ion	Compound	Crystal Radius* [pm]	Tolerance Factor†, *t*
Ca^{2+}	$CaTaO_2N$	148	0.95
Sr^{2+}	$SrTaO_2N$	158	0.98
Ba^{2+}	$BaTaO_2N$	175	1.04
La^{3+}	$LaTaON_2$	150	0.95

* Crystal radii are quoted for ions in twelve co-ordinate geometry. Crystal radius of Ta^{5+} in octahedral geometry is 78 pm and the crystal radii of O^{2-} and N^{3-} are 126 and 132 pm respectively.

† An average value for the anionic crystal radii was calculated based on the ratio of O:N within the compound. Hence for $ATaO_2N$ and $LaTaON_2$ $R_{O/N}$ becomes 128 pm and 130 pm respectively.

For an ideal cubic close packed perovskite structure, $t = 1$. Deviations of the tolerance factor from unity are an indication of increased strain on the perovskite structure suggesting the ions are either too big, $t > 1$, or too small, $t < 1$, to fit on their allotted site.[14] Goldschmidt showed that the perovskite form was stable for $0.85 < t < 1.06$.[13] From the results in *Table 4.7* it can be seen that the co-ordination prerequisites of the two cations are met for each of the compounds with $BaTaO_2N$ being the closest to the limit. These are all known compounds reported in the literature,[11,15] thus consequently are expected to obey the tolerance factors. The results for $BaTaO_2N$ and $LaTaON_2$ highlight the preference for the smaller radius La^{3+}

over Ba^{2+} in $Ba_{0.24}La_{0.76}TaO_{1.24}N_{1.76}$ thus minimising the strain within the structure. The internal bond strain displayed within a structure can be overcome through distortions to lower symmetry. Like the tilting of the FeO_6 octahedra within the orthorhombic $GdFeO_3$ unit cell, this tilting is also displayed in the TaO_xN_y octahedra in perovskite-type oxynitride structures, which can be seen in *fig. 3.8* in the previous chapter. The average cation anion bond lengths are generated from a Rietveld refinement and are listed in *Table 4.8*.

Table 4.8: Bond lengths of the A and B cations to anions in $Ca_{(1-x)}Ln_xTaO_{(2-x)}N_{(1+x)}$ where $0 < x \leq 1$ and Ln = Nd, Eu and Dy.

Compound	B Cation-Anion [Å]		A Cation-Anion [Å]	
$Sr_{0.5}La_{0.5}TaO_{1.5}N_{1.5}$	Ta-O/N (1):	2.0385 (5) x2	Sr/La-O/N (1):	2.924 (6) x1
Orthorhombic, *Pnma*	Ta-O/N (2):	2.0229 (19) x2	Sr/La-O/N (1):	2.793 (6) x1
	Ta-O/N (2):	2.0301 (19) x2	Sr/La-O/N (1):	3.269 (6) x1
			Sr/La-O/N (1):	2.381 (6) x1
Ta-X_{ax}-Ta = 155.37 (13)°			Sr/La-O/N (2):	2.750 (4) x2
Av. Ta-X = 2.031 (2) Å			Sr/La-O/N (2):	2.8999 (31) x2
Av. A-X = 2.835 (4)Å			Sr/La-O/N (2):	3.1621 (32) x2
			Sr/La-O/N (2)	2.515 (4) x2
$Ca_{0.61}La_{0.39}TaO_{1.61}N_{1..39}$	Ta-O/N (1):	2.0409 (11) x2	Ca/La-O/N (1):	2.929 (12) x1
Orthorhombic, *Pnma*	Ta-O/N (2):	2.025 (4) x2	Ca/La-O/N (1):	2.787 (12) x1
	Ta-O/N (2):	2.042 (4) x2	Ca/La-O/N (1):	3.241 (9) x1
			Ca/La-O/N (1):	2.310 (9) x1
Ta-X_{ax}-Ta = 155.65 (28)°			Ca/La-O/N (2):	2.779 (7) x2
Av. Ta-X = 2.036 (3) Å			Ca/La-O/N (2):	2.906 (5) x2
Av. A-X = 2.832 (7) Å			Ca/La-O/N (2):	3.155 (5) x2
			Ca/La-O/N (2):	2.521 (6) x2
$Ba_{0.24}La_{0.76}TaO_{1.24}N_{1.76}$	Ta-O/N (1):	2.0476 (9) x2	Ba/La-O/N (1):	2.994 (7) x1
Orthorhombic, *Pnma*	Ta-O/N (2):	2.0352 (30) x2	Ba/La-O/N (1):	2.742 (7) x1
	Ta-O/N (2):	2.0354 (30) x2	Ba/La-O/N (1):	3.309 (7) x1
			Ba/La-O/N (1):	2.360 (7) x1
Ta-X_{ax}-Ta = 154.80 (21)°			Ba/La-O/N (2):	2.739 (5) x2
Av. Ta-X = 2.039 (2) Å			Ba/La-O/N (2):	2.883 (4) x2
Av. A-X = 2.846 (5) Å			Ba/La-O/N (2):	3.203 (4) x2
			Ba/La-O/N (2):	2.550 (4) x2

The bond lengths of $CaTaO_2N$ reported in the literature,[11] yield an average Ta-Anion distance of 2.029 Å and an average Ca-Anion distance of 2.812 Å. All three compounds reported here have an average A-X bond length greater than the literature value, which increases as the average ionic radius on the A site increases. As the compounds all contain a certain amount of cations bigger than Ca^{2+}, *viz.* Sr^{2+}, Ba^{2+} and La^{3+}, the bond length is expected to increase. The bond angle between two Ta atoms through the apical anion that they share decreases on increasing cation radii. Thus implying that the tilting within the octahedra is increasing as the A cation radii increase, bringing greater disorder.

Finally the substitution of magnesium onto the A-site with target stoichiometry $Mg_{0.5}La_{0.5}TaO_{1.5}N_{1.5}$ was analysed. In this case a perovskite-type compound is readily obtained and there is no competing pyrochlore phase. There are however impurity peaks from MgO, which corresponds with a magnesium deficient A site. Several starting models were discredited in the joint refinement of both data sets. Firstly a refinement that modelled only magnesium and lanthanum occupancies on the A site of the perovskite was carried out. This included a constraint that accounted for the MgO impurity reducing the amount of magnesium present in the perovskite. A stable end point was not easily achieved and it was thought that potentially there is no magnesium present due its small ionic radius. Hence a refinement which allowed for vacancies on the A site was conducted; though this too was inconclusive. Finally EDAX data was collected, reported in *Section 4.5*, which shows the presence of calcium within the sample. This suggests a calcium uptake on the A site from the $CaCl_2$ mineralisers present in the reaction. Thus the percentages obtained from EDAX were used as an ideal starting point in the refinement. This refinement shows that indeed there is a reduction in magnesium due to the MgO phase and the most stable fit is achieved by constraining the divalent cations to the same occupancy.

Crystallographic data obtained from the PND data can be found in *Tables 4.9* and *4.10*. It can be seen that there are almost equal quantities of calcium and magnesium within the molecular formula and that the lanthanum stoichiometry is slightly higher than the target phase, in contradiction to the EDAX results.

Table 4.9: Crystallographic data for $Ca_{0.22}Mg_{0.22}La_{0.55}TaO_{1.5}N_{1.5}$.

Compound	$Ca_{0.22}Mg_{0.22}La_{0.55}TaO_{1.5}N_{1.5}$
Crystal System	Orthorhombic
Space Group	*Pnma* (no. 62)
Cell Parameters	a = 5.6558 (6) Å
	b = 7.9711 (6) Å
	c = 5.6488 (4) Å
Cell Volume	254.67 (4) Å^3
χ^2	1.832
R_{wp}(PXD)	0.1421
R_{wp}(PND)	0.0314

Table 4.10: Refined atomic positions for $Ca_{0.22}Mg_{0.22}La_{0.55}TaO_{1.5}N_{1.5}$. E.s.ds are given in parentheses.

Atom	x	y	z	Occupancy	$U_{(iso)}$ [Å^2]
Mg/Ca	0.0143(6)	0.25	-0.001(2)	0.221(6)	0.0121(4)
La	0.0143(6)	0.25	-0.001(2)	0.549 (11)	0.0121(4)
Ta	0.5	0	0	1	0.0033(2)
O/N (1)	0.4904(7)	0.25	0.0761(6)	0.5 / 0.5	0.0070(4)
O/N (2)	0.2783(4)	0.0369(3)	0.7232(4)	0.5 / 0.5	0.0108(3)

Information on the oxygen to nitrogen ratio was not obtained as varying these site occupancies resulted in instabilities within the refinement. Thus it is suggested that there are in fact deficiencies within the anionic network such that electroneutrality can be maintained. As it stands there is slightly more negative charge than positive (7.5 *cf.* 7.09) thus a reduction in either oxygen, nitrogen or both anions would restore the charge balance.

4.5 ENERGY DISPERSIVE ANALYSIS OF X-RAYS

Energy Dispersive Analysis of X-rays (EDAX) was carried out on the magnesium sample to ascertain what percentage of magnesium and of lanthanum occupies the A-site of the

perovskite thus yielding extra information to aid the powder neutron refinement carried out in *Section 4.4*. Scanning electron microscopy (SEM) was employed to image the sample and as there was no clear distinction between the phases, *i.e.* there was only one morphology visible, it is assumed that the material sampled includes MgO as well as the perovskite phase.

The results show a presence of calcium within the compound. This comes from the mineralisers ($CaCl_2$) and is therefore assumed to replace some of the magnesium on the A-site thus explaining the MgO impurity found in the PND data.

From the atomic percentages the stoichiometry of the compound has been calculated and can be found in *Table 4.11*.

Table 4.11: Percentage analysis of elements present in the magnesium sample.

Element	Weight %	Atomic %	Ratio
Mg	3.81	9.73	0.41
La	8.4	3.75	0.16
Ca	5.17	8	0.34
Ta	69.26	23.74	1
O	7.96	30.86	1.30
N	5.4	23.91	1.01

This yields a compound of stoichiometry $Ca_{0.34}Mg_{0.41}La_{0.16}TaO_{1.3}N_{1.0}$. Such a stoichiometry would give rise to vacancies in both the anionic and cationic sublattices and a compound that is not electroneutral overall. However, errors for a technique such as EDAX are large. Generally for this technique, the true values are expected to be *ca.* 10% above or below the experimental value. These results are therefore interpreted as approximations rather than exact stoichiometries.

These figures were used in the starting model of the Rietveld refinement in order that a closer approximation to the true structure can be found. Several refinements had previously been attempted but the most stable and reliable model gives a stoichiometry of $Ca_{0.22}Mg_{0.22}La_{0.55}TaO_{1.5}N_{1.5}$, allowing for anionic vacancies to maintain charge balance as previously discussed.

There is a slight discrepancy between the two compositions, namely that there appears to be more lanthanum present than the EDAX results show. This value is actually close to the target stoichiometry. The EDAX results show that there is more magnesium than calcium within the material sampled. An amount of that magnesium can be attributed to the MgO phase, as EDAX does not differentiate between the two phases within the area sampled.

The EDAX data and weight percentages of the two phases obtained from the Rietveld refinement can be used in conjunction to see if they correlate to each other. As shown in *Table 4.12*.

Table 4.12: Element amount obtained from Rietveld refinement.

Phase	Weight Fraction (GSAS)	Amount Mg [g]	Amount Ca [g]	Amount La [g]	Amount Ta [g]
MgO	0.054 (5)	3.26	N/A	N/A	N/A
Perovskite	0.946	1.60	2.63	22.8	54.02

Remembering that the errors for a technique such as EDAX are large, this table shows that the amount of each element calculated from the phase fractions of the Rietveld refinement are similar to the EDAX results. The major exception being lanthanum of which there is a threefold difference between the EDAX composition and the Rietveld composition.

4.6 UV-VISIBLE SPECTROSCOPY

UV-Visible spectroscopy was carried out on a Perkin Elmer UV/Vis/Lambda 35 in the range of 200 nm to 800 nm with $BaSO_4$ used as a reference.

For the alkaline earth substitutions made onto the A site of the perovskite structure, namely Mg, Ca, Sr and Ba, variations in product colour are detectable supporting the presence of different levels of nitrogen within each system. UV-Vis. spectroscopy data, *fig. 4.3*, highlights differences in the absorption bands in the region of 200 – 600 nm for these compounds.

Jansen has discussed the electronic structure of certain oxynitride perovskites. The bands in the spectra arise due to the absorption of radiation and thus promotion of electrons across the band gap of the semiconductors. The width of this band gap determines the energy required to promote an electron into the conductance band. By introducing nitrogen this band gap can be reduced, thus the energy required for a transition reduced, bringing these absorption bands into the visible region.

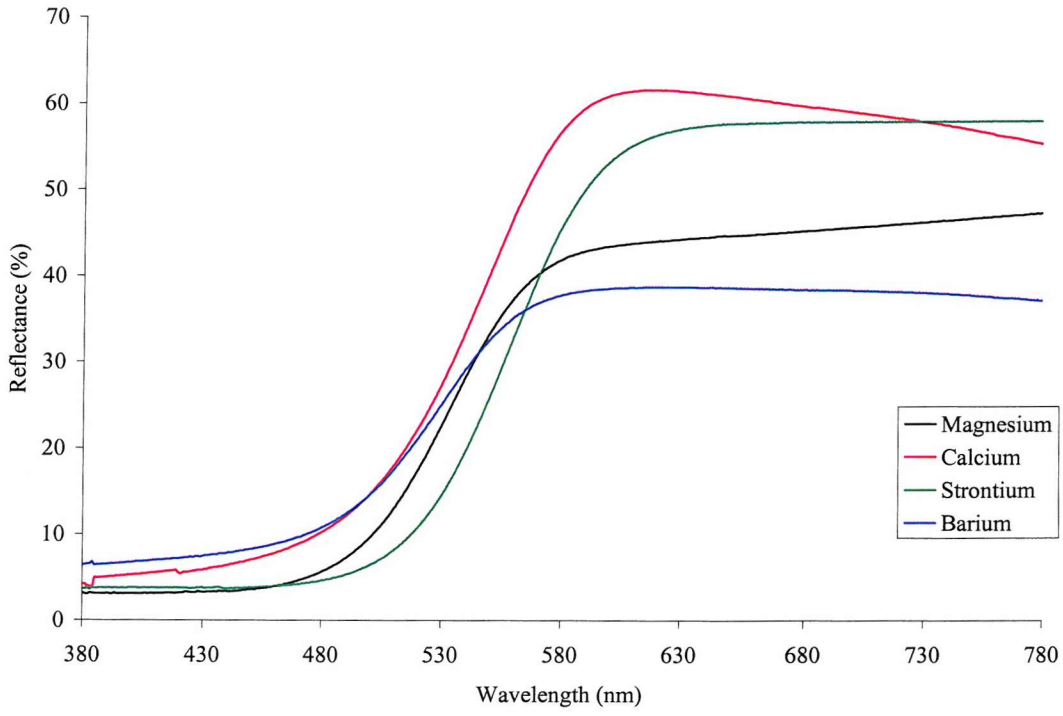

fig. 4.3: *UV-Visible spectra of samples $A_{(1-x)}La_xTaO_{(2-x)}N_{(1+x)}$ where A = Mg-Ba.*

All the spectra display broad reflectance bands with a steep edge. Light of longer wavelengths is being reflected corresponding to the red end of the electromagnetic spectrum whilst the samples absorb wavelengths of light from the blue end, which is expected based on the colours of these pigments (yellow-orange). Barium reflects more green and blue light than the other samples and indeed this compound has an undesirable green tinge making it a much duller yellow. From this data, there is no correlation between the size of the cation included in the perovskite and the location of the absorption edge. There is a shift of the edge towards the longer wavelengths on descending group 2 for Mg, Ca and Sr but the absorption edge of barium occurs in the same region as magnesium. What must also be considered is the presence of two phases within the sample, which give band gap values of similar energies thus masking the true location of the absorption edge of the perovskite material. In the case

of the barium and calcium samples, there is a contribution to the spectra from both perovskite and pyrochlore phases, whereas the strontium sample is a single phase perovskite. Also, as a result, each sample could have different oxygen to nitrogen ratios. This affects the overall band gap and therefore colours of each sample. Interestingly the nitrogen rich, barium perovskite compound has a higher energy band gap than the other compounds. This is contradictory to the belief that the presence of more nitrogen actually reduces the band gap, thus suggesting that there is more than one factor affecting the value of the band gap.

The magnesium sample contains a magnesium oxide impurity. As this is a white powder it also contributes to the spectra by reflecting white light making the compound appear brighter than its true value.

4.7 COLOUR MEASUREMENTS

From the UV-Vis. spectroscopy data colour measurements have been ascertained and collated in *Table 4.13*.

Table 4.13: Colour measurements of $A_{(1-x)}La_xTaO_{(2-x)}N_{(1+x)}$ (where A = Mg-Ba) and of some commercial pigments.[1]

Sample	*L**	*a**	*b**
$Ca_{0.22}Mg_{0.22}La_{0.55}TaO_{1.5}N_{1.5}$	61.31	13.64	63.21
$Ca_{0.61}La_{0.39}TaO_{1.61}N_{1.39}$	68.87	18.63	60.87
$Sr_{0.5}La_{0.5}TaO_{1.5}N_{1.5}$	60.66	29.97	62.68
$Ba_{0.24}La_{0.76}TaO_{1.24}N_{1.76}$	60.94	7.65	43.19
Cadmium Yellow	75.66	-7.90	99.12
Cadmium Orange	64.68	47.70	96.26
Cadmium Red	41.10	65.21	56.84

The *L** values for these four compounds are very similar with only $Ca_{0.61}La_{0.39}TaO_{1.61}N_{1.39}$ being brighter than the others, meaning more light is reflected back into the eye of the observer. However, there are differences in the other values. All compounds exhibit both positive *a** and positive *b** as expected for red, orange and yellow pigments. The barium

sample is the worst candidate for potential pigment applications as it is a dull yellow with a greenish tinge. This is reflected in the low positive a^* values given, much further towards the greenness axes than the other samples. The other three samples are yellow to orange with $Sr_{0.5}La_{0.5}TaO_{1.5}N_{1.5}$ having the highest redness value. From the samples generated by alkaline earth substitutions this proves to be the best orange pigment as it is not only bright but also has a more positive a^* value. In comparison to cadmium pigments the a^* and b^* values are worse but they are better than other non cadmium pigments on the market according to the $L^*a^*b^*$ values found in the literature.[1]

4.8 THERMOGRAVIMETRIC ANALYSIS

Thermogravimetric analysis (TGA) was performed on a Polymer Labs STA 1500 from room temperature to 1000 °C with a constant heating rate of 10 °C min^{-1} in air at 1 atm.

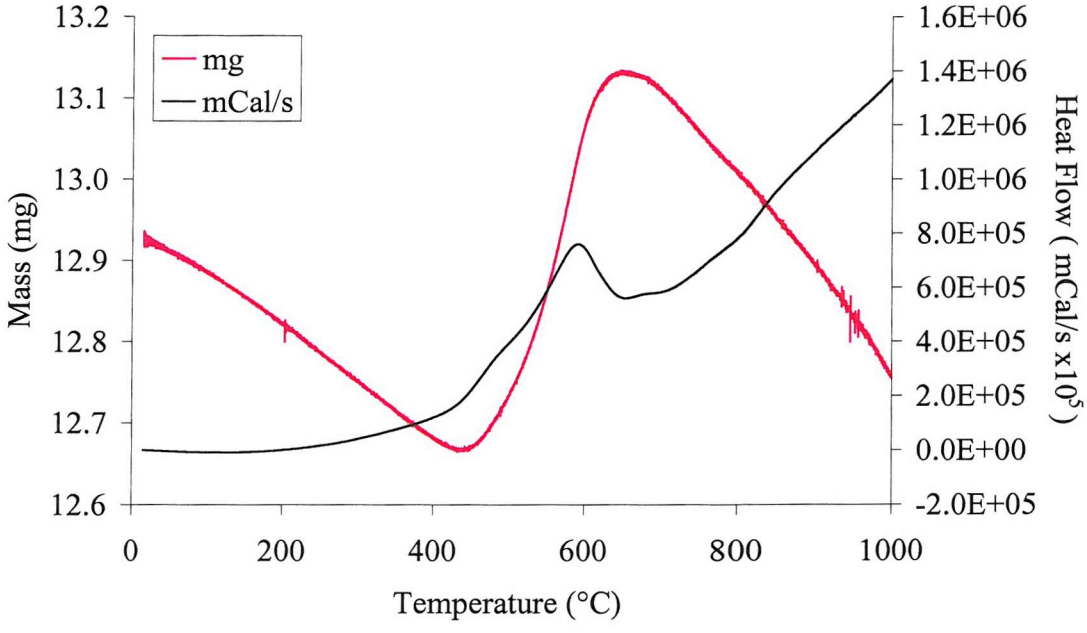

fig. 4.4: *Differential thermal analysis (black) and thermogravimetric analysis (red) of* $Ca_{0.61}La_{0.39}TaO_{1.61}N_{1.39}$.

Thermogravimetric analyses were carried out to ascertain the stability of these compounds when heated under air, see for example *fig. 4.4*. At around 400 °C the samples begin to

decompose. The sharp increase in mass corresponds to an uptake of oxygen to replace the nitrogen within the system (on the required 3 for 2 basis to maintain charge balance). It has been reported that the gain in mass is higher than the expected gain to transform the sample to an oxide and a heavier intermediate is formed suggesting some nitrogen retention.[16] Oxygen adsorption may also occur on the surface of the sample, contributing to the mass increase. The final mass loss is due to the loss of any residual nitrogen present in the intermediate compound. Before heating, the oxynitride samples are either orange or yellow in colour. After heating white oxides are formed. According to the literature, nitrogen is always released as N_2 with no evolution of gaseous NO_x.[16]

4.9 VARIABLE TEMPERATURE X-RAY DIFFRACTION

Variable temperature (VT) studies were carried out on two samples; firstly on $Sr_{0.5}La_{0.5}TaO_{1.5}N_{1.5}$ and secondly on $Ca_{0.61}La_{0.39}TaO_{1.61}N_{1.39}$ with the pyrochlore impurity. The strontium sample was heated and data sets were collected *in-situ* every 50 °C from 100 – 1000 °C. A final set was taken at room temperature after the heating cycle.

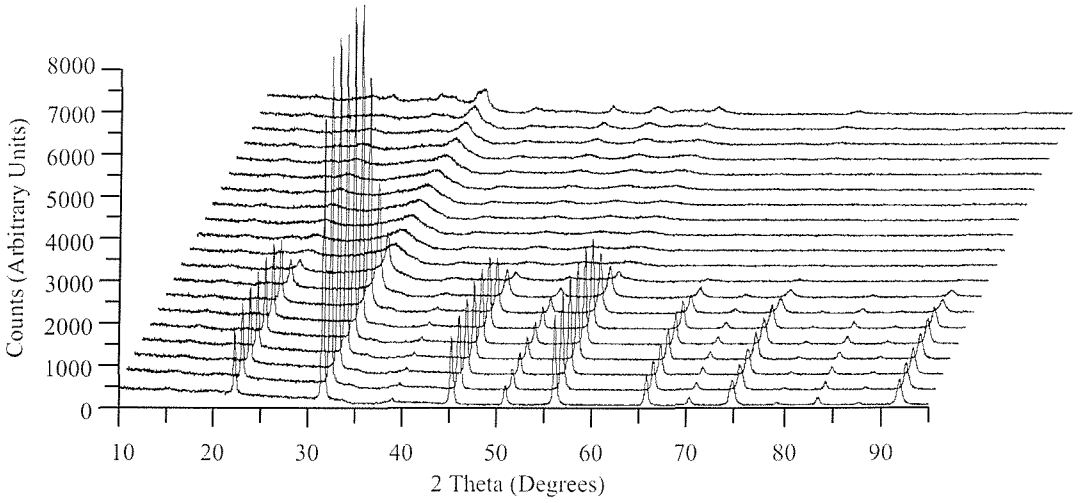

fig. 4.5: *Stack plot of variable temperature powder X-ray diffraction data collected at 50 °C intervals, from 100 °C (lowest pattern), for $Sr_{0.5}La_{0.5}TaO_{1.5}N_{1.5}$.*

In *fig. 4.5* are VT-PXD patterns for $Sr_{0.5}La_{0.5}TaO_{1.5}N_{1.5}$. The perovskite structure is maintained up to 500 °C, above this temperature the structure becomes more amorphous. At

1000 °C small peaks are emerging suggesting an oxide perovskite-type structure is beginning to form. Either higher temperatures or longer firing times may result in the synthesis of the oxide analogue with probable cationic vacancies to maintain electroneutrality.

Nine data sets were refined using the Rietveld method[9,10] and the lattice parameters and unit cell volumes are given for each temperature in *Table 4.14*. The data above 500 °C shows only a few weak, broad reflections making it impossible to obtain reliable structural characterisation.

Table 4.14: Variation in lattice parameters for $Sr_{0.5}La_{0.5}TaO_{1.5}N_{1.5}$ (100-500 °C).

Temp [°C]	*a* [Å]	*b* [Å]	*c* [Å]	*V* [Å^3]
100	5.665 (3)	8.041 (2)	5.673 (2)	258.40 (5)
150	5.665 (3)	8.041 (2)	5.673 (2)	258.40 (5)
200	5.667 (2)	8.045 (2)	5.677 (2)	258.81 (5)
250	5.670 (2)	8.049 (2)	5.680 (2)	259.21 (5)
300	5.673 (2)	8.053 (1)	5.682 (2)	259.6 (1)
350	5.675 (1)	8.061 (2)	5.695 (1)	260.50 (5)
400	5.675 (9)	8.060 (2)	5.695 (10)	260.50 (5)
450	5.666 (3)	8.055 (4)	5.693 (2)	259.81 (9)
500	5.670 (3)	8.022 (4)	5.718 (2)	260.1 (2)

The variations in lattice parameters *a*, *b* and *c* and unit cell volume *V* can be seen more clearly in the graphs shown in *fig. 4.6*. The linear regions show that as the temperature increases the lattice parameters and cell volume increase as expected. At elevated temperatures the thermal motion of the atoms increases thus increasing bond lengths and lattice parameters. Above 400 °C these numbers fluctuate. As this is the point at which nitrogen is lost as determined by thermogravimetric analysis, it is assumed that the original oxynitride compound is no longer present. These values have therefore been omitted from the graph as they do not relate to the expansion of the unit cell of the oxynitride but are values attributed to an intermediate oxidised phase.

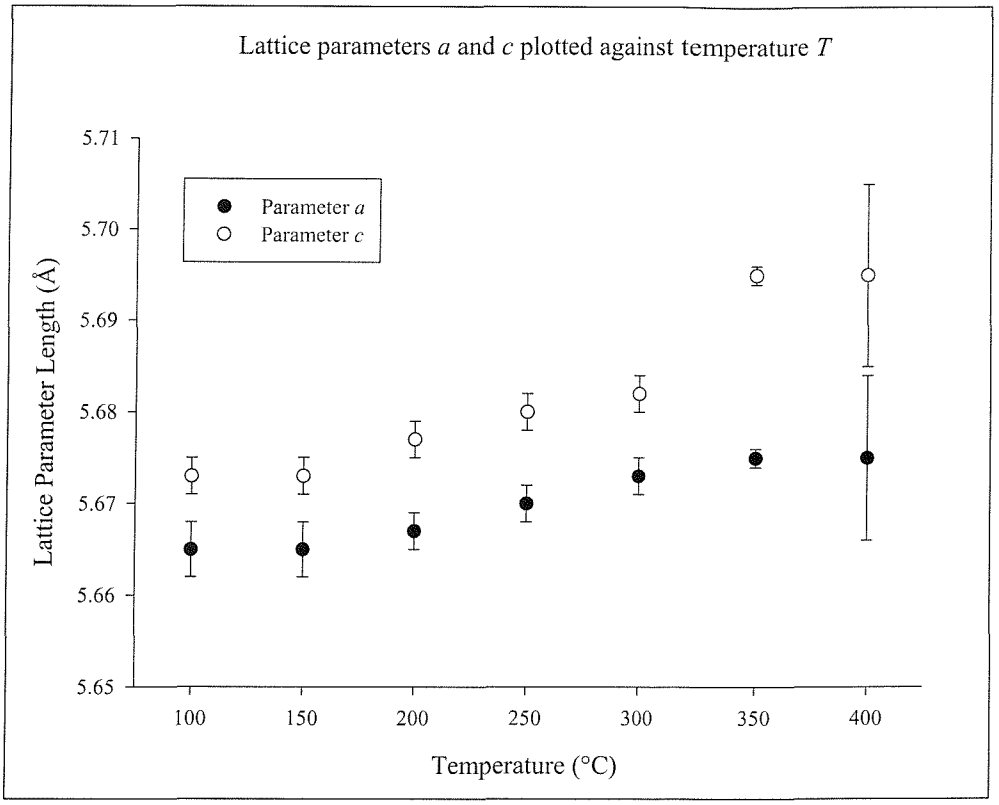

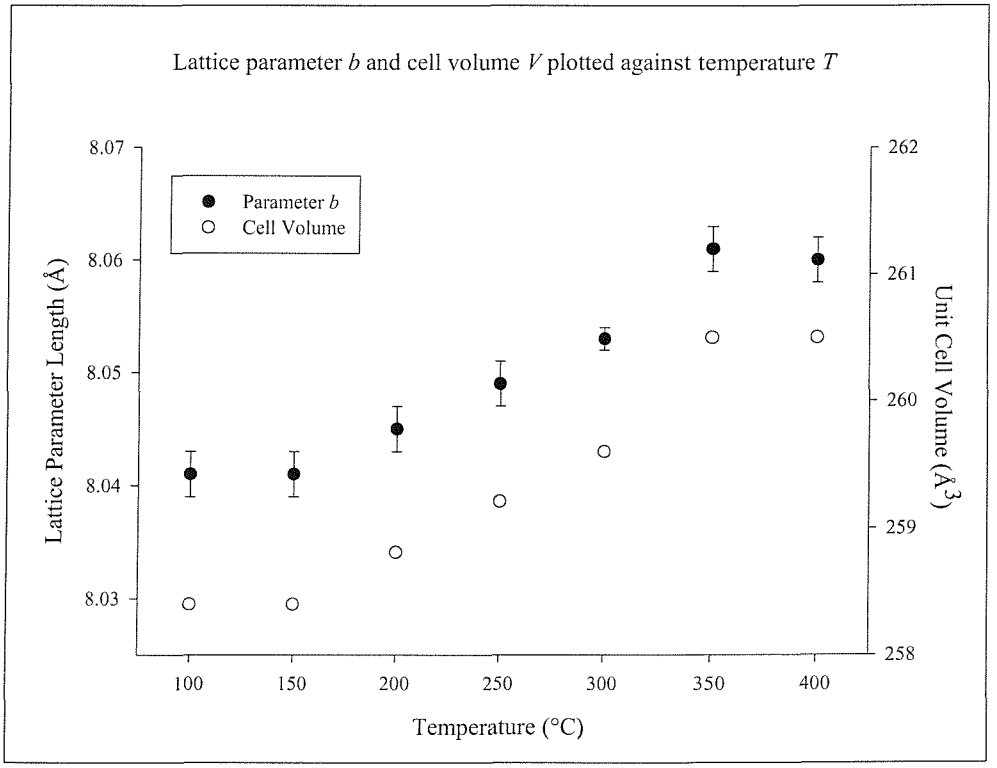

fig. 4.6: *(Upper and Lower) Graphs representing the increase in lattice parameters and unit cell volume with increasing temperature. Error bars are smaller than the markers of the cell volume series and have therefore been omitted.*

VT-PXD data sets were taken every 50 °C starting at 100 °C for the $Ca_{0.61}La_{0.39}TaO_{1.61}N_{1.39}$ sample with the pyrochlore impurity. The last heating run was taken at 650 °C, as this is well above the temperature at which nitrogen is lost. A final data set was collected at room temperature after cooling at the end of the heating cycle. In this instance there is again a detection of a crystalline phase suggesting that after losing nitrogen a pure oxide perovskite phase is formed.

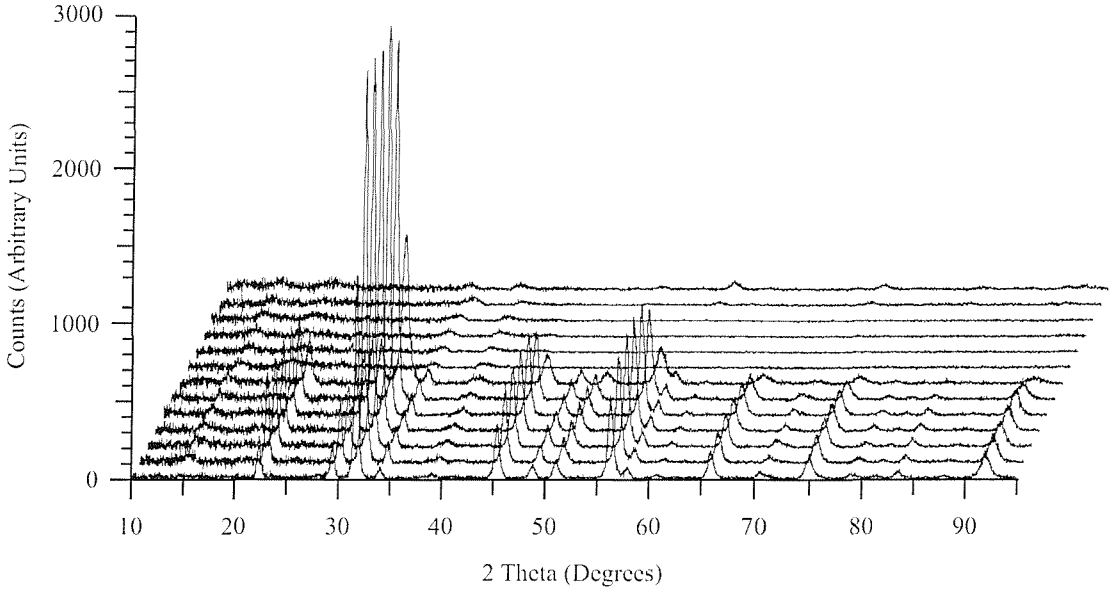

fig. 4.7: *Stack plot of variable temperature powder X-ray diffraction data collected at 50 °C intervals, from 100 °C (lowest pattern), for* $Ca_{0.61}La_{0.39}TaO_{1.61}N_{1.39}$.

Seven data sets were refined using the Rietveld method and the lattice parameters and unit cell volumes are given for each temperature in *Table 4.15*. The data above 400 °C only shows weak, broad reflections, so as with the strontium sample it is impossible to obtain reliable structural characterisation.

Both nitrogen and oxygen anions are isoelectronic and therefore the O/N ratio cannot be determined by PXD as stated earlier. From these data sets it is impossible to deduce by how much the percentage of oxygen within the anionic sublattice is increasing as the temperature increases. From TGA data it can be assumed that above 400 °C the anionic ratio determined by PND is no longer the same and that the compound is predominately oxygen rich.

Table 4.15: Variation in lattice parameters for $Ca_{0.61}La_{0.39}TaO_{1.61}N_{1.39}$ (25-400°C).

Temp [°C]	*a* [Å]	*b* [Å]	*c* [Å]	*V* [Å^3]
100	5.672 (2)	8.034 (3)	5.645 (2)	257.2 (1)
150	5.674 (1)	8.038 (2)	5.648 (1)	257.58 (1)
200	5.679 (1)	8.044 (2)	5.645 (1)	257.86 (6)
250	5.680 (1)	8.048 (2)	5.652 (1)	258.40 (5)
300	5.682 (1)	8.052 (2)	5.658 (1)	258.88 (5)
350	5.690 (1)	8.061 (2)	5.657 (1)	259.50 (6)
400	5.622 (3)	7.953 (3)	5.709 (2)	255.3 (2)

The traces show that both the perovskite phase and the pyrochlore phase are present until 400 °C then both phases are lost. The heating cycle was terminated at 650 °C with the final run at room temperature showing the presence of a poorly crystalline phase, which is likely to be an oxide perovskite.

Again, there is an increase in cell parameters with increasing temperature, which is best displayed with the unit cell volume. The steady increase continues until *ca.* 350 °C after which there is an elongation along the *c* axis and a reduction in *a* and *b* resulting in an overall reduction in *V* as the cell collapses. This corresponds to the loss of nitrogen and the uptake of oxygen as the structure is lost.

The competing pyrochlore phase behaves in a similar fashion to the perovskite phase. It is clearly visible in the stack plot, see *fig. 4.7*, until 400 °C whereby the characteristic reflections become weak as the structure is lost. The cubic cell parameter *a* and the cell volume also increase steadily with increasing temperature until 400 °C at which point the structure is lost and the cell collapses and both *a* and *V* are reduced *cf.* perovskite phase.

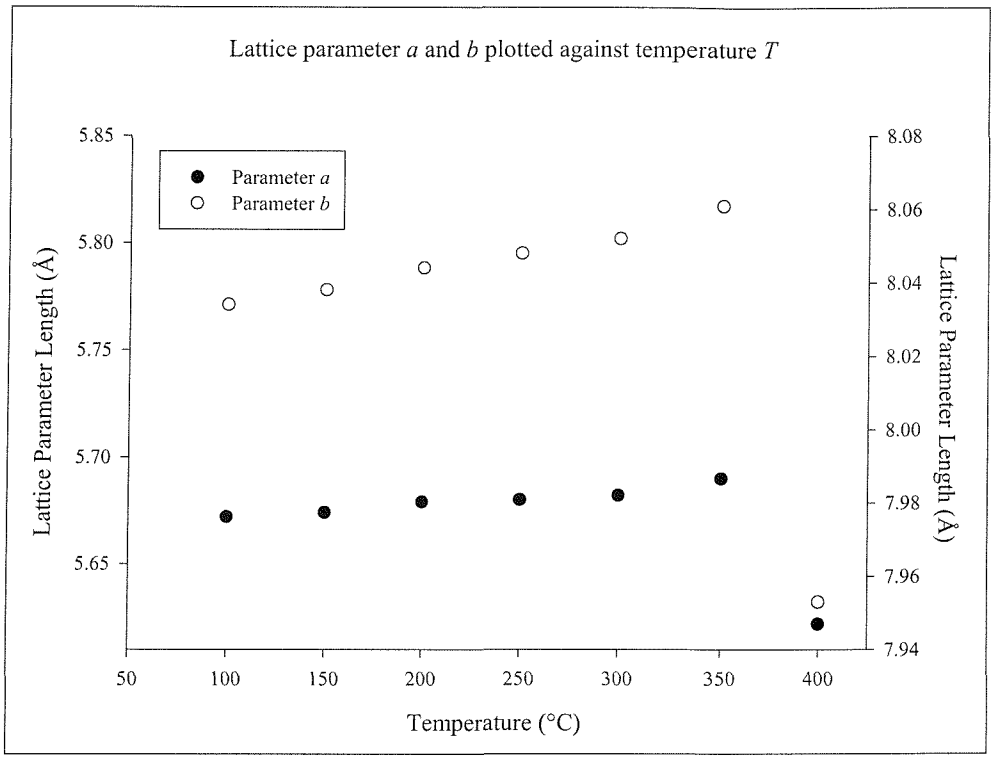

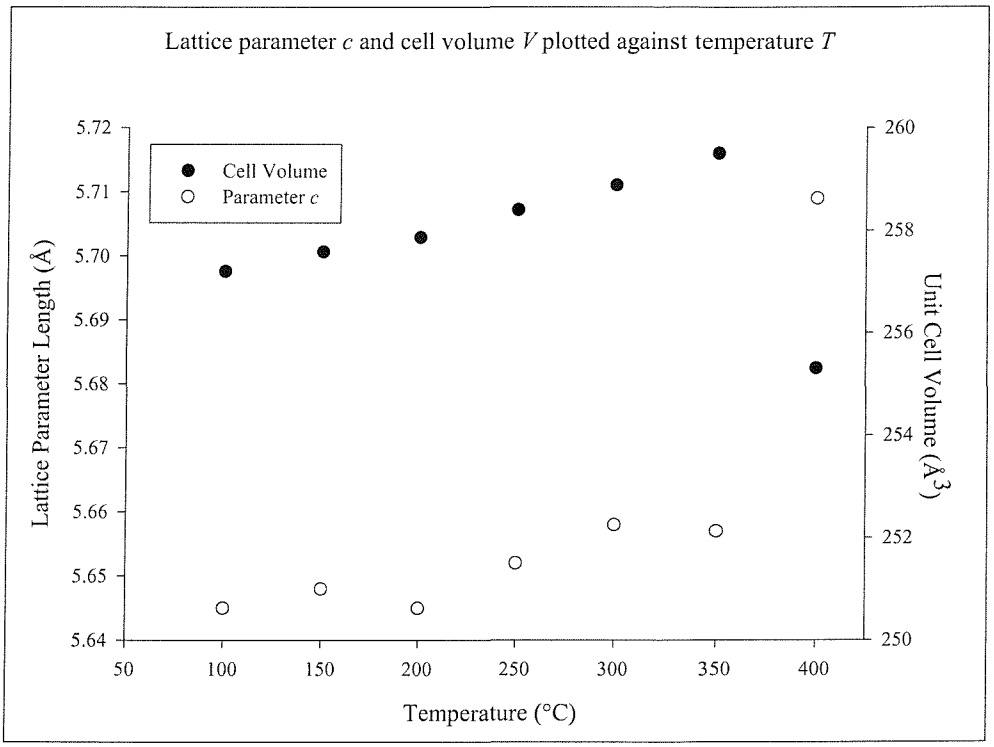

fig. 4.8: *(Upper and Lower) Graphs representing the variation in lattice parameters and unit cell volume with increasing temperature. Error bars are smaller than the markers and have therefore been omitted.*

4.10 DISCUSSION AND CONCLUSIONS

The syntheses of $A_{(1-x)}Ln_xTaO_{(2-x)}N_{(1+x)}$ where A is Mg, Ca, Sr, Ba has been accomplished though the value of x within the perovskite phase varies as a function of A with incorporation of high levels of the smaller cation (excluding Mg) most facile. The perovskite-type compounds reported here are all orthorhombically distorted adopting the space group *Pnma*. For Ca and Ba, competition from a pyrochlore-type phase occurs during synthesis.

The incorporation of magnesium into the unit cell is not as facile as this is too small to be ideally situated on the A-site of the perovskite. Instead some of the magnesium is replaced by calcium, found in the mineralisers and a MgO impurity is present. Synthesis of a magnesium compound could be attempted without metal halides but this would affect the colour of the compound as trial reactions have been completed without mineralisers but the intensity of colour is lost. Ideally $MgCl_2$ could be used as a mineraliser to prevent other cations occupying the A-site but unfortunately the melting point is quite low at 714 °C in comparison to the reaction temperature of 850 °C. Ideally the melting point of the mineralisers is just below the reaction temperature otherwise problems of volatility arise.

Due to the uncertainties in composition of the magnesium compound highlighted through the Rietveld refinements, comparisons with other samples, between compound colour and the energy range of the absorption edge, must not be made.

The refinement of the strontium sample is most stable with a 50 % occupancy of oxygen and 50% occupancy of nitrogen on each anion site. It is therefore assumed that the anions are randomly distributed over both sites, unlike the quaternary phases $SrTaO_2N$ and $LaTaON_2$ which have an ordered anion distribution with nitrogen favouring the apical positions.[11] The distortion within $Sr_{0.5}La_{0.5}TaO_{1.5}N_{1.5}$ is similar to that of the orthorhombic perovskite $CaTaO_2N$ although the cell volume has increased due to the increased ionic radii of Sr^{2+}. In contrast to this $SrTaO_2N$ crystallises in the space group *I4/mcm* and $LaTaON_2$ crystallises in a monoclinic space group *C2/m*. These compounds are of higher and lower symmetry than $Sr_{0.5}La_{0.5}TaO_{1.5}N_{1.5}$ respectively.

Likewise for the calcium and barium perovskites there is no preference of site for oxygen and nitrogen and both refinements give better fits and more reliable temperature factors with an

equal distribution on either site. The increase in size of cation from Ca^{2+} to Ba^{2+} has affected the divalent and trivalent ratios, with the smaller cation favoured over a larger cation. This results in the compositions $Ca_{0.61}La_{0.39}TaO_{1.61}N_{1.39}$ and $Ba_{0.24}La_{0.76}TaO_{1.24}N_{1.76}$. Hence, an increase in divalent cation over lanthanide leads to a decrease in nitride anion and vice versa, meaning the latter compound has more nitrogen. Theoretically this means that the band gap should narrow for the barium compound and the absorption edge in the UV-Vis. spectrum shift to longer wavelengths, however it is not the case. This may be as a result of the pyrochlore phase that also contributes to the spectrum, as this is assumed to be barium rich and thus oxygen rich. This means that the pyrochlore phase is likely to have a band gap that is higher in energy thus altering the absorption edge displayed. In the absence of empirical calculations, values for the band gaps cannot be given.

Nevertheless, the compounds are bright orange and yellow powders making them ideal candidates as pigments to replace some existing cadmium pigments. Spectroscopic data show that these materials have an absorption edge between 480 and 580 nm, similar to cadmium pigments. Although structural analysis is paramount in determining electrical properties of a polar solid it is not the most important factor in pigment chemistry; more important is the hue and the stability of the compound to external conditions. From $L^*a^*b^*$ values it is apparent that the calcium and strontium samples are the better candidates to replace existing orange pigments.

Heating the oxynitrides under air to 1000 °C results in oxidation producing white oxide products with decomposition starting at around 400 °C. As the temperature is raised there is an expansion of the unit cell as the bond lengths increase due to the thermal motion of the atoms. Eventually the cell collapses and the structure is lost, resulting in the diminished patterns in the VT-PXD plots. If the *in-situ* analysis at high temperature, *ca.* 1000 °C, is carried out after a much longer sintering time, it is possible that highly crystalline oxide perovskite phases may form as nitrogen is replaced by oxygen.

4.11 REFERENCES

[1] Jansen M., Letschert H.; *Nature*, **404**, 980 (2000)

[2] Marchand R., Pors F., Laurent Y.; *Rev. Int. Hautes Tempér. Réfract. Fr.*, **23**, 11 (1986)

[3] Clarke S. J., Michie C. W., Rosseinsky M. J.; *Chem. Mater.*, **12**, 863 (2000)

[4] Weller M. T., Skinner S. J.; *Int. J. Inorg. Mater.*, **2**, 463 (2000)

[5] http://www.ncnr.nist.gov/resources/n-lengths/

[6] Marchand R., Pors F., Laurent Y.; *Ann. Chim. Fr.*, **16**, 553 (1991)

[7] Pors F., Marchand R., Laurent Y.; *J. Solid State Chem.*, **107**, 39 (1993)

[8] Larson A. C., Von Dreele R. B.; *General Structure Analysis System*, MS-H805, Los Alamos National Laboratory, (USA) N M 87545 (1990)

[9] Rietveld H. M.; *Acta Crystallogr.*, **22**, 151 (1967)

[10] Rietveld H. M.; *J. Appl. Crystallogr.*, **2**, 65 (1969)

[11] Günther E., Hagenmayer R., Jansen M.; *Z. Anorg. Allg. Chem.*, **626**, 1519 (2000)

[12] Shannon R. D.; *Acta Crystallogr. A.*, **32**, 751 (1976)

[13] Goldschmidt V. M.; *Skr. Nor. Vidensk. Akad. Kl 1: Mat. Naturvidensh. Kl* (1926)

[14] Weller M. T.; *Inorganic Materials Chemsitry*, Oxford University Press (UK), First Edition (1994)

[15] Pors F., Marchand R., Laurent Y.; *Mat. Res. Bull.*, **23**, 1447 (1988)

[16] Le Gendre L., Marchand R., Laurent Y.; *J. Eur. Ceram. Soc.*, **17**, 1813 (1991)

CHAPTER FIVE

SYNTHESIS AND CHARACTERISATION OF $CaNb_xTa_{(1-x)}O_2N$ AND $LaNb_xTa_{(1-x)}ON_2$

5 NIOBIUM DOPING IN OXYNITRIDE PEROVSKITES

5.1 INTRODUCTION

So far this thesis has dealt with the substitutions of cations upon the interstitial A site of a perovskite in order to investigate the effect nitrogen content has upon on resultant compound colour. According to band theory, the energy gap between conductance and valence bands in a solid is related to the difference in the orbital energies of the constituent atoms of the solid. This difference is significantly altered when the anions are substituted. Replacing one non-metal for another results in a large shift in the electronegativity difference ($\Delta\chi$), where the Pauling scale yields values of χ (O) = 3.44 *cf.* χ (N) = 3.04. The shift is generally smaller when the electropositive cations are substituted within an ionic lattice as the differences in electronegativities are less.

Studies by Hellwig and Hendry on the homogenity of oxynitride samples have been based around the fugacity of nitrogen.[1] At temperatures above 550 °C ammonia decomposes *in-situ* into active species which are able to nitride the reactants. Sometimes during ammonolysis the reactants closest to the gas inlet are more coloured than those furthest away suggesting that the reduction of tantalum and the uptake of nitrogen is greater nearest the inlet but still within the hot zone of the furnace. This leads to the problem of sample inhomogenity highlighted by the colour gradient of the product. X-ray photoelectron spectroscopy was employed by Hellwig to deduce the differences in the valence state of tantalum in barium tantalum oxynitrides.[1] From these studies it has been postulated that the red brown colour of $BaTaO_2N$, (high nitrogen content) is a result of the reduction of Ta (V) to Ta (IV) yielding a stoichiometrical composition of $Ba_2Ta_2O_3N_2\square$, whereas the products towards the gas outlet (yellow and white) contain more Ta (V).

In this chapter niobium doping upon the B site of the perovskites $CaTaO_2N$ and $LaTaON_2$ was carried out to see the relative effect of tantalum and niobium contents on sample colour. Tantalum and niobium are often referred to as twin elements as there is little difference between physical data and indeed the metal radii and the ionic radii are the same due to the lanthanide contraction. According to Végards law, lattice parameters of a solid solution series are linearly related to composition.[2] The law assumes implicitly that the variance of lattice parameters with composition is governed by the relative sizes of the ions involved in the

exchange mechanism. However, the substitution of niobium for tantalum should not affect the size of the unit cell as the crystal radii of Nb^{5+} and Ta^{5+} are identical in a 6 co-ordinate environment.

Nevertheless, the colour may be altered due to a slight difference in electronegativity, where the electronegativities for Ta and Nb are 1.5 and 1.6 on the Pauling scale respectively. The increase in electronegativity of niobium would give an overall reduction in electronegativity difference between cations and anions. This in turn could narrow the band gap making the red and yellow compounds of $LaTaON_2$ and $CaTaO_2N$ much darker. A compound that has a small band gap has the ability to absorb more wavelengths of visible light and hence the more light from the visible spectrum that is absorbed the darker the compound becomes. If all visible light is absorbed, then the compound is black.

Another consequence of differences in electronegativity is that niobium is more easily reduced than tantalum as it is more electronegative than tantalum. In other words, the colour of the oxynitrides could vary depending on the oxidation state of niobium.

5.2 SYNTHESIS

Samples were synthesised using the gas transformation method employed in the previous chapters. Stoichiometric amounts of Ta_2O_5 (Aldrich, 99%), Nb_2O_5 (Aldrich, 99.9%), $CaCO_3$ (99%) and La_2O_3 (99%) were intimately ground in an inert acetone media with *ca.* 50% wt. ratio of halide salts employed as mineralisers. The salts used, NaCl, KCl and $CaCl_2$, were in equimolar ratios. The samples were treated with dry flowing gaseous ammonia (Air Products, Electronic Grade) for 20 hours at a flow rate of *ca.* 7 dm^3 hr^{-1} and a reaction temperature of 850 °C. The mineralisers were leached from the fired materials by washing thoroughly with excess de-ionised water. Phase identification of the samples was completed with the aid of powder X-ray diffraction and colour differences were analysed via UV-Visible spectroscopy and $L^*a^*b^*$ measurements.

5.3 POWDER X-RAY DIFFRACTION DATA

Short scan powder X-ray diffraction (PXD) data sets were collected on a Siemens D5000 using Cu $K_{\alpha 1}$ radiation (λ=1.5406 Å). Primary phase identification of the compounds synthesised was carried out using *EVA*,[3] a software package that compares acquired data to literature equivalents in the JCPDS database. Estimate lattice parameters were obtained by indexing the peaks in *CELREF*.[4]

5.3.1 PHASE IDENTIFICATION AND CHARACTERISATION OF $CaNb_xTa_{(1-x)}O_2N$

The PXD data sets are presented in *fig. 5.1* for the niobium doping in $CaTaO_2N$, where the level of niobium doping increases by 10% intervals with the upper pattern representing the targeted quaternary phase, $CaNbO_2N$.

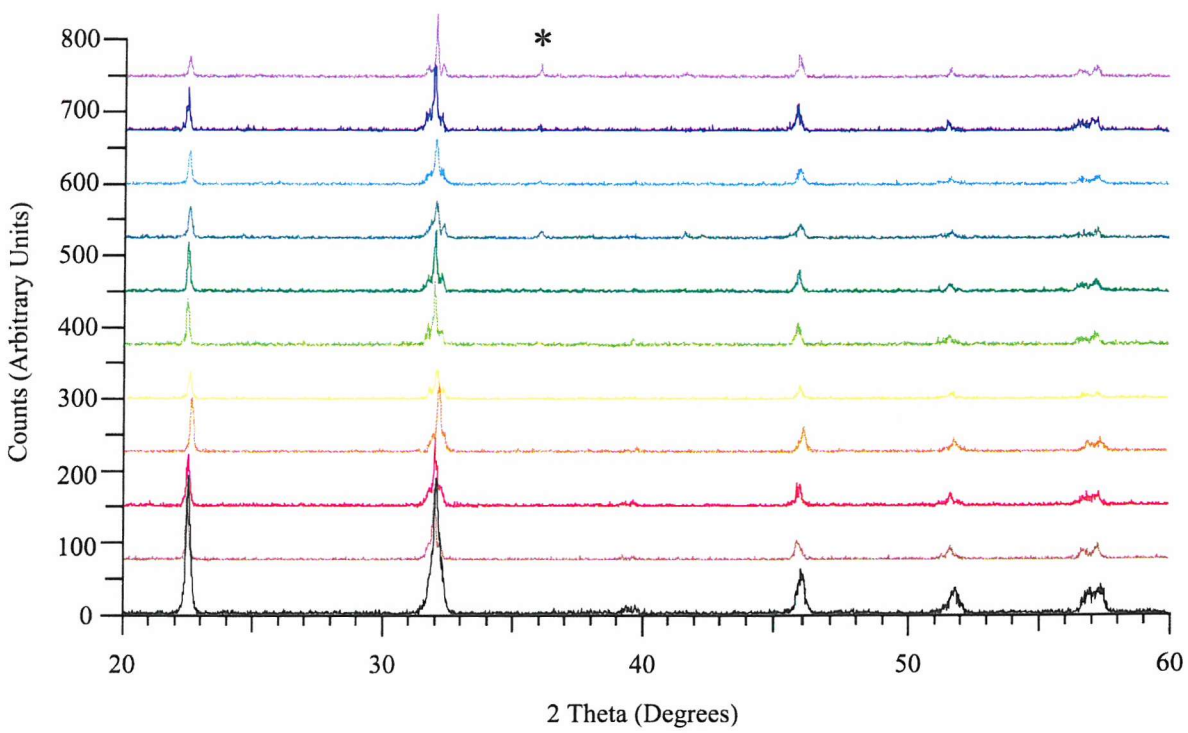

fig. 5.1: *Powder X-ray diffraction data for $CaNb_xTa_{(1-x)}O_2N$ target phases, from the lowest pattern upwards x = 0, 0.1, 0.2, 0.3, 0.4, 0.5, 0.6, 0.7, 0.8, 0.9 and 1. The asterisk (*) represents an impurity phase $NbN_{0.6}O_{0.3}$.*[5]

These data sets show that a perovskite phase is formed for all x, suggesting successful substitution of niobium for tantalum in $CaTaO_2N$. The level of splitting and thus distortion

within the unit cell increases on increasing niobium content and the reflections in these oxynitrides mirror those of $CaNbO_3$.[6] The splitting ($\Delta\theta$) of the 2 0 0 / 0 0 2 reflection, either side of the 1 2 1 reflection at ~ $2\theta = 32°$, where $\Delta\theta \sim 1°$, is as great as the splitting in $CaNbO_3$. This splitting is much less in the quaternary phase $CaTaO_2N$ even though both $CaTaO_2N$ and $CaNbO_3$ crystallise in the orthorhombic space group *Pnma*.

For $x \geq 0.7$ a $NbN_{0.6}O_{0.3}$ impurity phase is observed (see *fig. 5.1*). This implies that the actual amount of niobium present in the series $CaNb_xTa_{(1-x)}O_2N$ is less than the idealised composition. This suggests that 100% doping of niobium on the B site is difficult. $CaNbO_2N$ has recently been reported in the literature,[7] synthesised by ammonolysis of the pyrochlore $Ca_2Nb_2O_7$, with salt additives to minimise NbO_xN_y impurities. It may be possible to target this phase via the ammonolysis of the ternary phase $CaNbO_3$ at high temperature though the oxidation state is likely to remain as Nb (IV). As low temperature routes play a central role in this work, synthesis via mixed metal oxide precursors has not been attempted as this often involves calcination at T > 1000 °C.

The peaks were indexed against the model of $CaTaO_2N$ previously reported in the literature.[8] The lattice parameters obtained are displayed in *Table 5.1*. From the lattice parameters average cell volumes were calculated.

Table 5.1: Lattice parameter data for $CaNb_xTa_{(1-x)}O_2N$, where $0 \leq x \leq 1$.

Target Sample	*a* [Å]	*b* [Å]	*c* [Å]	*V* [Å^3]
$CaTaO_2N$	5.611 (4)	7.856 (5)	5.556 (5)	244.9 (6)
$CaNb_{0.1}Ta_{0.9}O_2N$	5.632 (4)	7.859 (7)	5.566 (5)	246.4 (6)
$CaNb_{0.2}Ta_{0.8}O_2N$	5.627 (3)	7.879 (4)	5.579 (4)	247.3 (4)
$CaNb_{0.3}Ta_{0.7}O_2N$	5.612 (2)	7.865 (3)	5.550 (3)	245.0 (3)
$CaNb_{0.4}Ta_{0.6}O_2N$	5.621 (3)	7.865 (4)	5.563 (4)	245.9 (4)
$CaNb_{0.5}Ta_{0.5}O_2N$	5.639 (5)	7.891 (6)	5.574 (6)	248.0 (7)
$CaNb_{0.6}Ta_{0.4}O_2N$	5.627 (5)	7.875 (6)	5.562 (7)	246.5 (7)
$CaNb_{0.7}Ta_{0.3}O_2N$	5.636 (4)	7.869 (5)	5.566 (5)	246.9 (6)
$CaNb_{0.8}Ta_{0.2}O_2N$	5.632 (6)	7.867 (7)	5.562 (8)	246.4 (8)
$CaNb_{0.9}Ta_{0.1}O_2N$	5.639 (5)	7.884 (6)	5.574 (7)	247.8 (7)
$CaNbO_2N$	5.629 (5)	7.877 (6)	5.562 (7)	246.6 (7)

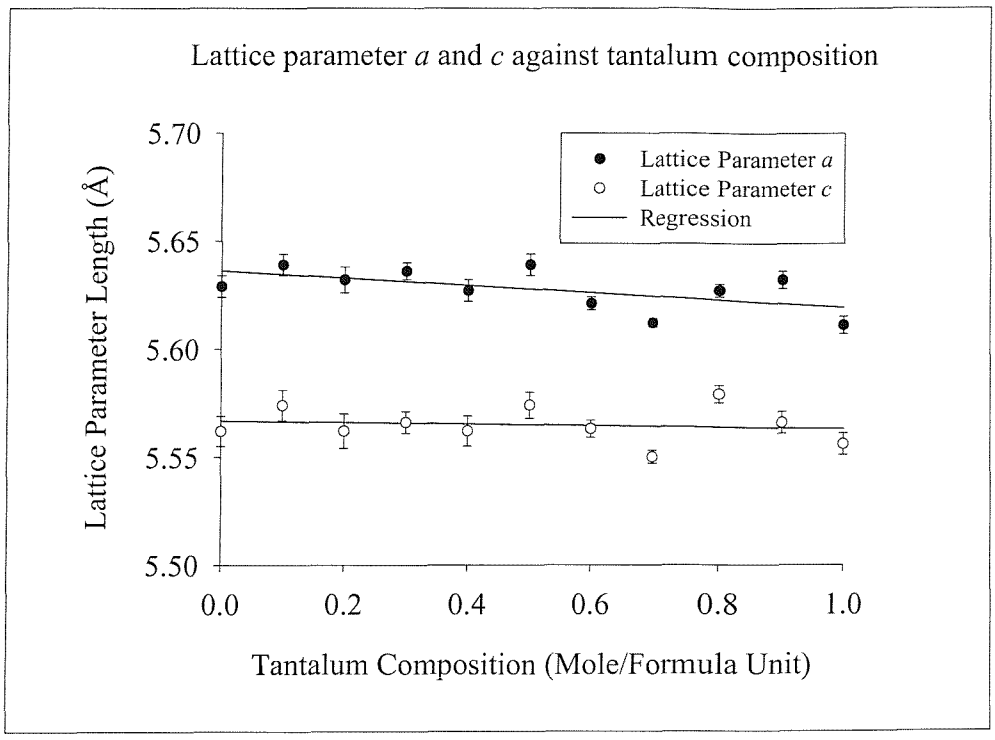

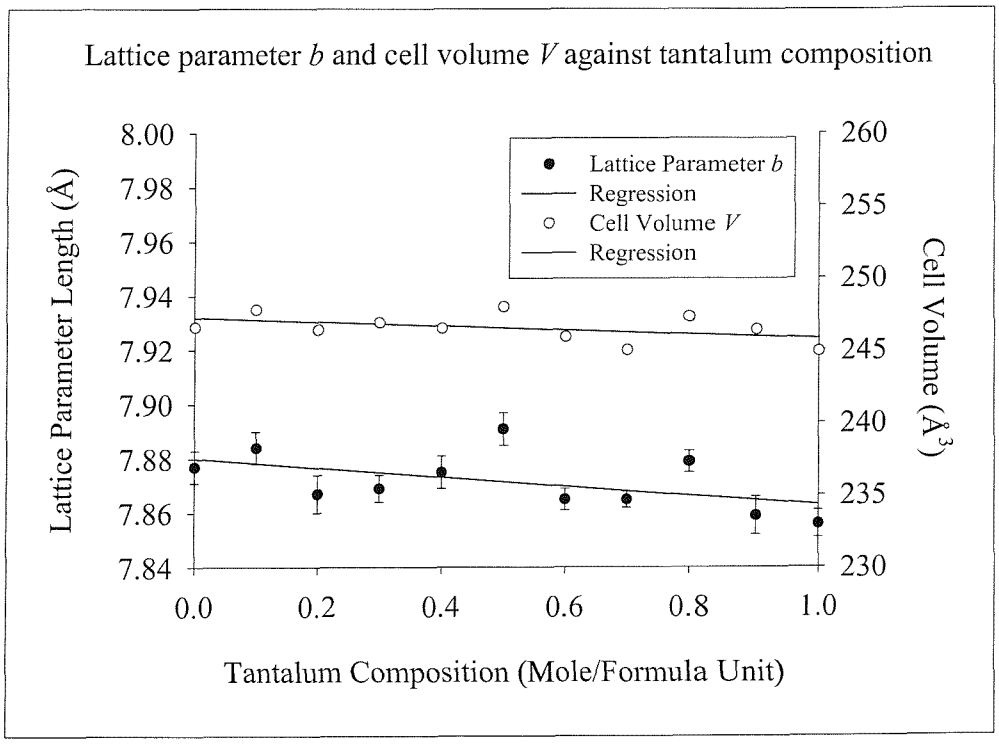

fig. 5.2: *(Upper and Lower) Graphs represent the variation in lattice parameters and unit cell volume of* $CaNb_xTa_{(1-x)}O_2N$ *with increasing tantalum composition.*

Overall no major trend is expected as the crystal radii of both Ta^{V} and Nb^{V} in a 6 co-ordinate sphere is 0.78 Å.[9] These data do show some fluctuation as there is a very slight increase in lattice parameters and cell volumes as x increases. This may be explained by a partial reduction of Nb^{5+} to Nb^{4+}, thus increasing the crystal radius from 0.78 to 0.82 Å in a 6 co-ordinate environment.

5.3.2 *PHASE IDENTIFICATION AND CHARACTERISATION OF $LaNb_xTa_{(1-x)}ON_2$*

The PXD data sets are presented in *fig. 5.3* for the niobium doping in $LaTaON_2$, where the level of niobium doping increases by 10% intervals, with the upper pattern representing the quaternary phase $LaNbON_2$ reported in the literature.[10]

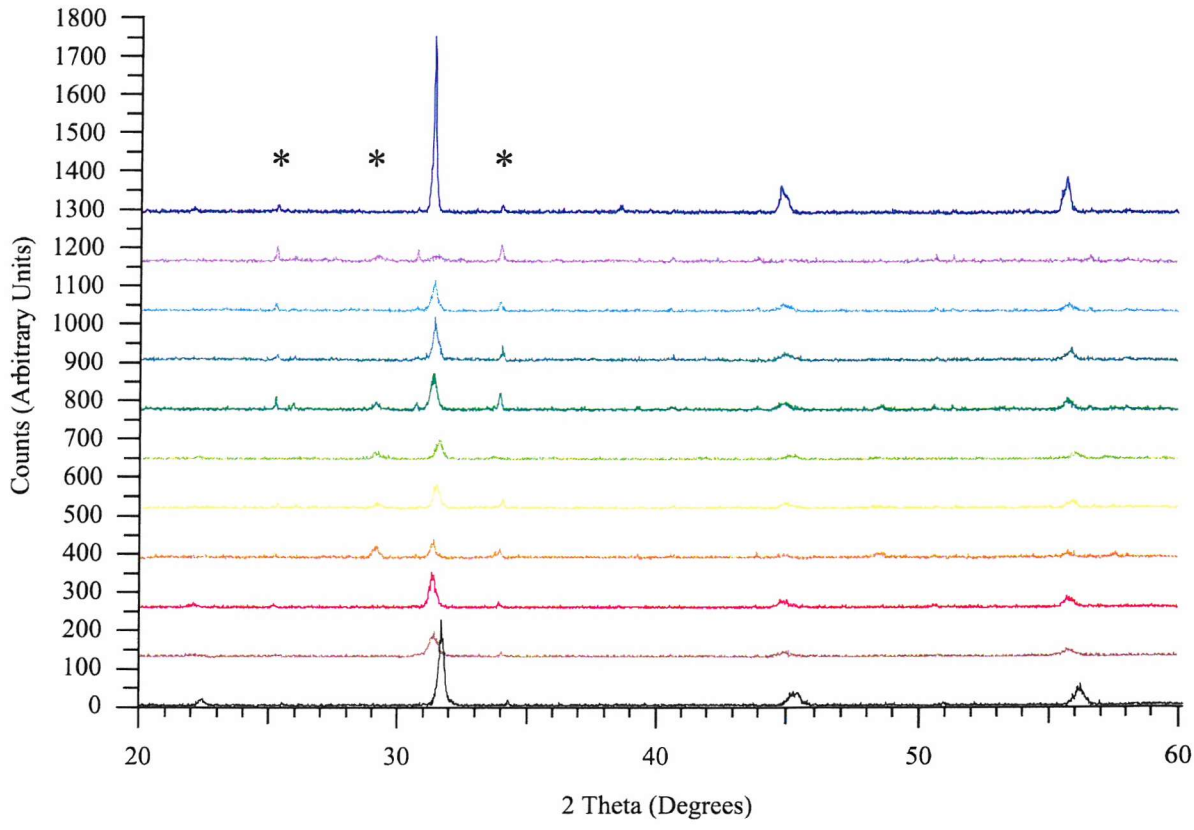

fig. 5.3: *Powder X-ray diffraction data for $LaNb_xTa_{(1-x)}ON_2$ target phases, from the lowest pattern upwards x = 0, 0.1, 0.2, 0.3, 0.4, 0.5, 0.6, 0.7, 0.8, 0.9 and 1. The asterisk (*) represents impurity phases as stated in discussion.*

The formation of single phase perovskites of stoichiometry $LaNb_xTa_{(1-x)}ON_2$ is not as facile as the calcium phases previously discussed. This is due to sintering problems. Within this system there is a threefold increase in the number of trivalent ions compared to the

$CaNb_xTa_{(1-x)}O_2N$ series, causing an increase in the number of species with high charge densities. This in turn has slowed the diffusion process down, making the formation of a stable phase more difficult.

This leads to the formation of several impurity phases, *viz.* NbO_2 and two tantalum (oxy)nitride phases. The peaks seen at $2\theta = 25°$ can be attributed to the 4 0 0 reflection for NbO_2, where niobium is reduced to Nb^{IV} under the ammonia atmosphere. This impurity is present in the target compounds of high niobium content, so in analogy to the calcium samples it is difficult to achieve high levels of niobium doping via this synthetic technique. It must be noted that $LaNbON_2$ is reported in the literature but was synthesised via an intermediate oxide phase, $LaNbO_4$.[10]

The peak at $2\theta = 29°$ is assigned to the 1 1 1 reflection for TaON and the peak at $2\theta = 34°$ is assigned to the 1 1 0 reflection for $TaN_{0.43}$, both of which have previously been reported in the literature.[11,12] As these too are (oxy)nitrides they are likely to affect the overall colour of the compound. For example, TaON is reported as a bright yellow or green powder depending on the level of niobium impurity in the Ta_2O_5 starting material.[13]

The peaks were indexed against an orthorhombic model of $LaNbON_2$ previously reported in the literature,[10] with the exception of $LaTaON_2$ which was modelled against a monoclinic pattern for $LaTaON_2$.[8] The lattice parameters obtained are displayed in *Table 5.2*. From the lattice parameters average cell volumes were calculated.

Table 5.2: Lattice parameter data for $LaNb_xTa_{(1-x)}ON_2$, where $0 \leq x \leq 1$.

Target Sample	*a* [Å]	*b* [Å]	*c* [Å]	*V* [Å^3]	
$LaTaON_2$	8.030 (2)	8.045 (3)	5.662 (5)	365.8 (6)	(258.7)
$LaNb_{0.1}Ta_{0.9}ON_2$	5.79 (1)	5.65 (1)	8.033 (4)	262.8 (1)	
$LaNb_{0.2}Ta_{0.8}ON_2$	5.68 (3)	5.73 (3)	8.092 (4)	263.4 (3)	
$LaNbON_2$	5.717 (3)	5.726 (4)	8.064 (2)	264.0 (4)	

For a monoclinic distortion the angle between *a* and *c* (β) is no longer 90° thus β in $LaTaON_2$ is equal to 134.8°. Dividing the cell volume of $LaTaON_2$ by $\sqrt{2}$ allows comparisons to be made, with the niobium doped samples.

The other samples all contain impurities, thus the tantalum and niobium contents of the perovskites are unknown. No cell parameters have been ascertained, as comparisons between these phases are meaningless. It is expected that the cell parameters of different compositions have similar values. There has been no increase in the radii of the cations adopting the perovskite structure thus only a small change in the unit cell is expected, similar to the solid solution series $CaNb_xTa_{(1-x)}O_2N$. In analogy with the calcium series there is a slight increase in unit cell volume with decreasing tantalum composition, but with only three orthorhombic data points there is not sufficient evidence to state this as fact.

From these PXD data sets it is inconclusive as to which crystal system a compound has adopted. These profiles could either be similar to those of $LaNbON_2$ (orthorhombic)[10] or $LaTaON_2$ (monoclinic).[8] The peaks that differentiate the two perovskite phases are of low intensity and cannot be readily distinguished from the background. At low angles, peaks attributed to both monoclinic distortions and orthorhombic distortions can overlap, whereas at high angles they are more easily resolved. If the data range is extended to higher 2θ it should be easier to distinguish the crystal symmetry of a compound. Although again these peaks are likely to be of low intensity so to pick them out from the background radiation, longer scan times and good quality data are required.

If both $LaTaON_2$ and $LaNbON_2$ are mutually soluble then both distortions could be found in the sample, especially if homogeneity of the reactants is a problem.

5.4 UV-VISIBLE SPECTROSCOPY

UV-Vis. spectroscopy was carried out on a Perkin Elmer UV/Vis/Lambda 35 in the range of 200 nm to 800 nm with $BaSO_4$ used as a reference. Spectra for the niobium doped target samples $CaNb_xTa_{(1-x)}O_2N$ and $LaNb_xTa_{(1-x)}ON_2$, can be found in *figs. 5.4* and *5.5* respectively.

The spectra display the characteristic broad reflectance bands with steep edges, a property they share with other oxynitride materials reported in previous chapters. A clear shift of absorption edge to lower energies is visible in the $CaNb_xTa_{(1-x)}O_2N$ series upon increasing niobium content. This trend is more ambiguous with the lanthanum samples. The majority of

samples have impurity phases, as discussed earlier, which affects the data. Each phase contributes to the sample spectra; the technique does not differentiate between separate phases.

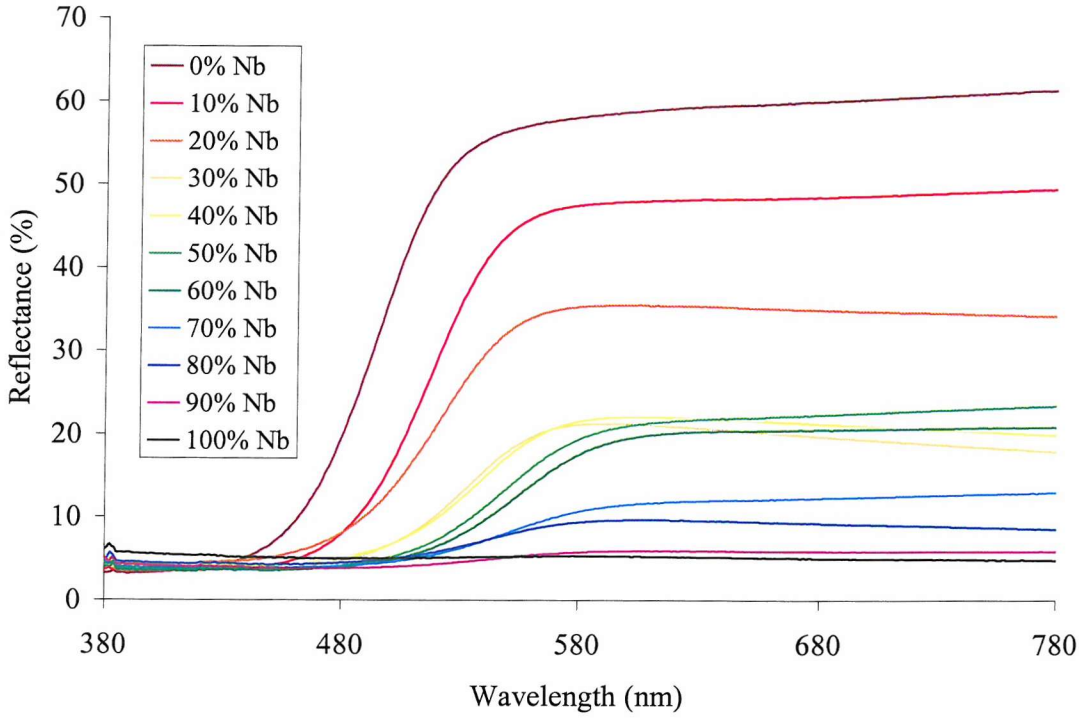

fig. 5.4: *UV-Visible spectra of $CaNb_xTa_{(1-x)}O_2N$, where $0 \leq x \leq 1$ starting from 0% Nb doping ($CaTaO_2N$) downwards to 100 % Nb doping ($CaNbO_2N$).*

The level of reflectance decreases on increasing niobium content, meaning the amount of light that is absorbed by the samples increases on increasing niobium content. This explains the loss of colour from yellow through brown to black for the calcium samples and red through brown to black for the lanthanum samples. (*N.B.* A powder that absorbs all wavelengths of visible light appears black whereas a powder reflecting all wavelengths of visible light appears white.)

The samples with higher tantalum content have steeper absorption edges than those of high niobium content. The steepness of an edge is related to colour purity. For this reason, coupled with the amount of light that is reflected by each of the samples, the best pigments are those with high tantalum content. This could suggest a link between the oxidation state of tantalum and the colour of the sample as previously hypothesised by Hellwig *et al.*[1]

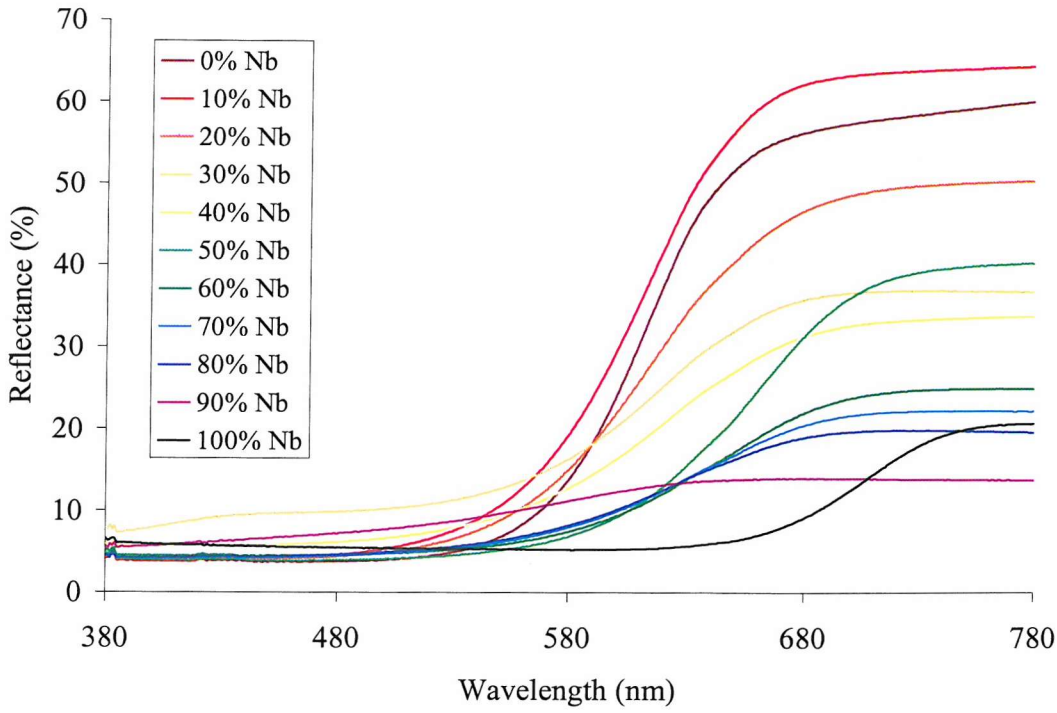

fig. 5.5: *UV-Visible spectra of $LaNb_xTa_{(1-x)}ON_2$, where $0 \leq x \leq 1$ starting from 0% Nb doping ($LaTaON_2$) downwards to 100 % Nb doping ($LaNbON_2$).*

These spectra highlight differences in the position of absorption bands, in the region of 410 – 620 nm (calcium samples) and 500 – 760 nm (lanthanum samples), for these compounds. The absorption edge is at lower energies when greater nitrogen incorporation occurs; thus the edge is located at longer wavelengths for the lanthanum samples compared to the calcium samples. As a less electronegative element replaces oxygen within the unit cell there is a reduction in the band gap as previously discussed. This corresponds to the energy at which an interband transition occurs, thus the oxygen rich $CaTaO_2N$ is yellow whilst the nitrogen rich $LaTaON_2$ is red. It is possible to estimate the band gap energies from the absorption edges within the UV-Vis. spectra. This is performed using *Equations 3.1 – 3.4*.

Band gap calculations have been summarised in *Table 5.3*. Meaningful numbers may only be ascertained for single phase products as the band gap is particular to the compound. Where a competing phase exists the UV-Vis. spectrum includes reflectance from both phases, *i.e.* it does not discriminate between each compound, thus the absorption edge varies. The wavelength for the absorption edge is taken midway between the start and finish of the range at which the change from absorption to reflection takes place, hence this is easier to estimate when the gradient is steeper.

Table 5.3: Band gap calculations for various levels of niobium doping in the perovskites $CaNb_xTa_{(1-x)}O_2N$ and $LaNb_xTa_{(1-x)}ON_2$, where $0 \leq x \leq 1$.

Target Sample	Estimated Wavelength [nm]	Band Gap Energy [eV]
$CaTaO_2N$	480	2.59
$CaNb_{0.1}Ta_{0.9}O_2N$	500	2.49
$CaNb_{0.2}Ta_{0.8}O_2N$	510	2.44
$CaNb_{0.3}Ta_{0.7}O_2N$	520	2.39
$CaNb_{0.4}Ta_{0.6}O_2N$	530	2.35
$CaNb_{0.5}Ta_{0.5}O_2N$	545	2.28
$CaNb_{0.6}Ta_{0.4}O_2N$	555	2.24
$LaTaON_2$	600	2.07
$LaNb_{0.1}Ta_{0.9}ON_2$	585	2.13
$LaNb_{0.2}Ta_{0.8}ON_2$	605	2.05
$LaNbON_2$	695	1.79

The values of these band gap energies are in direct relation to the observed colour. Those with larger band gaps have absorption edges towards shorter λ and thus electronic transitions occur at higher energy making the pigments more yellow than red.

For $CaNb_xTa_{(1-x)}O_2N$, the band gap decreases on increasing niobium content as niobium is more electronegative than tantalum. Thus, the sample colour goes from yellow through brown to black on increasing x. This can be explained by way of electronegativities. Niobium is slightly more electronegative than tantalum (1.6 *cf.* 1.5 on the Pauling scale) thus the difference in electronegativity between cations and anions is reduced on increasing niobium content. There may also be greater amounts of nitrogen incorporated into the unit cell. Both of these events result in a reduction in the band gap energy. If this reduction is large, it can allow more visible light to be absorbed making the compounds appear brown or even black.

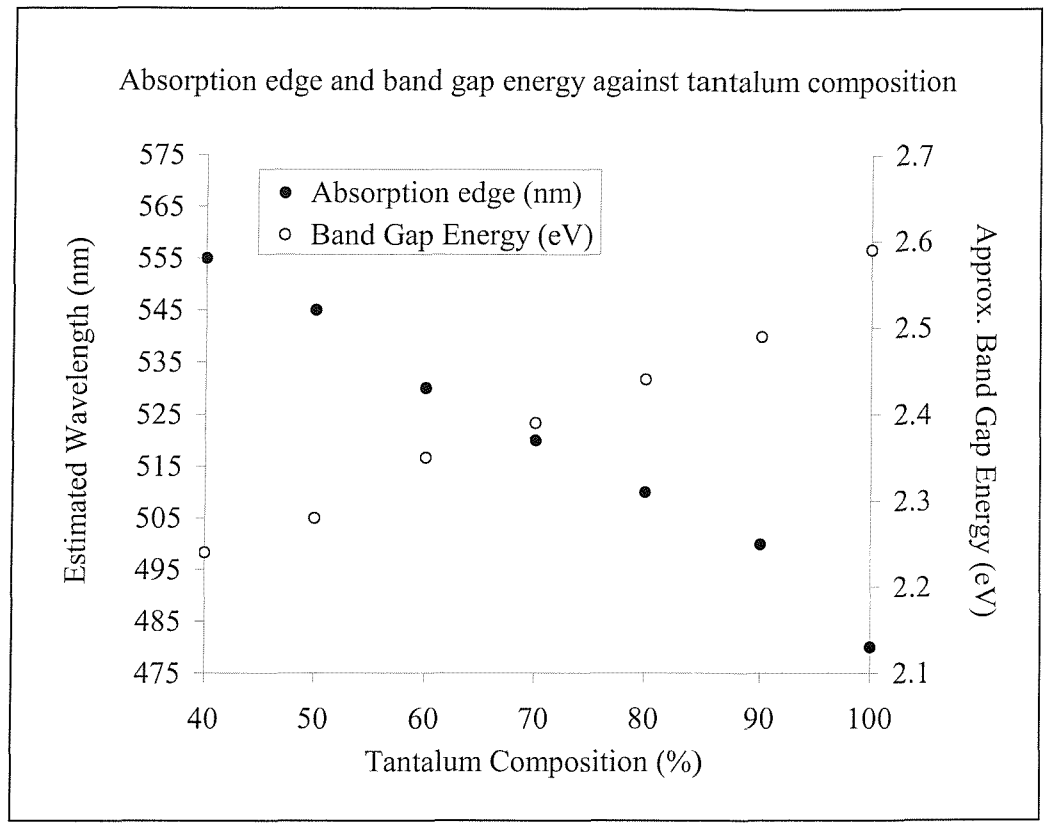

fig. 5.6: *Graph showing variation of wavelength of absorption edge (primary y axis) and band gap energies (secondary y axis) with composition of the solid solution series, $CaNb_xTa_{(1-x)}O_2N$.*

There is also the question of oxidation states. Niobium could be more easily reduced than tantalum thus meaning the presence of Nb^{IV} in the compounds synthesised. This too may darken the colour as NbO_2 (Nb^{IV}) is dark grey / black where as Nb_2O_5 (Nb^{V}) is white. Supporting this theory, one can compare the known nitride systems. Tantalum (V) is stable in the compound Ta_3N_5 but no analogous Nb_3N_5 phase is known, whereas mixed oxidation state Nb(III/IV) nitrides are common, such as Nb_4N_5 and Nb_5N_6.

Thermodynamically both Ta^{IV} and Ta^{V} are more stable to reduction than their niobium counterparts. The ionisation energy $M^{3+} \rightarrow M^{4+}$ is 3200 kJ mol^{-1} for tantalum compared to 3695 kJ mol^{-1} for niobium. Likewise Ta^{V} is more stable than Nb^{V} as $M^{4+} \rightarrow M^{5+}$ for Ta and Nb is 4300 kJ mol^{-1} and 4877 kJ mol^{-1} respectively.[14] With this in mind, stable phases with Nb^{5+}, are less likely to form as niobium is more prone to reduction than tantalum. Alternatively there may be a kinetic reason for this reduction, based on the reactivity of the niobium source compared with that of tantalum. If the source has a smaller particle size

distribution it will be more reactive and therefore likely to reduce easily. The reactivities of these commercially sourced oxides (Ta_2O_5 and Nb_2O_5) are unknown. As particle size is indicative of reactivity it is possible to acquire a PXD profile of the reactants and estimate the particle size using the Scherrer formula (*Equation 2.2*). On observation it would seem that Nb_2O_5 has a smaller particle size than Ta_2O_5 but what must also be considered is the simultaneous intimate grinding of all reactants that is carried out before ammonolysis as this process reduces the particle size distribution.

Similar results are expected for the solid solution series $LaNb_xTa_{(1-x)}ON_2$, with the band gap energy decreasing for increasing niobium content based on the reasoning for the calcium series. In this series, the effect of the niobium reduction is highlighted with the $Nb^{IV}O_2$ impurity phase. This has made determination of band gap energies across the lanthanide series difficult. Impurities would contribute to the UV-Vis. spectrum altering the position of the absorption edge thus yielding false band gap estimations.

5.5 COLOUR MEASUREMENTS

From the UV-Vis. spectroscopy data colour measurements have been ascertained and are collated in *Table 5.4*. This quantifies how much the yellowness and redness numbers of the samples decrease with increased niobium content for $CaTaO_2N$ and $LaTaON_2$ respectively.

$L^*a^*b^*$ measurements were ascertained for all target compounds, although the presence of certain impurities drastically alters the results. For instance, the presence of coloured oxynitride phases with the perovskite compound targeted gives rise to false a^* and b^* measurements. The presence of a white or black metal oxide makes the pigment brighter or duller respectively, thus altering the lightness value (L^*), such is the case with NbO_2 impurities which are dark grey.

These measurements highlight several trends. Primarily the lightness value, corresponding to the amount of light that is reflected, drops on increasing x. This data backs up the observed colour change towards black powders as an L^* value of 0 corresponds to 100% absorption of visible light and thus is associated with compounds that appear black.

The parameters governing colour can be seen to diminish with increasing niobium content, *e.g.* $CaNb_xTa_{(1-x)}O_2N$ samples have a decreasing yellowness number (positive b^*) upon increasing x and $LaNb_xTa_{(1-x)}ON_2$ samples have a decreasing redness number (positive a^*) upon increasing x. In both cases the samples with high niobium content have very low colour measurements approaching zero as expected for dark grey and black powders.

Table 5.4: Colour measurements of the solid solution series $CaNb_xTa_{(1-x)}O_2N$ and $LaNb_xTa_{(1-x)}ON_2$, where $0 \leq x \leq 1$.

Target Sample	L^*	a^*	b^*
$CaTaO_2N$	90.72	-8.29	58.17
$CaNb_{0.1}Ta_{0.9}O_2N$	67.40	4.31	67.67
$CaNb_{0.2}Ta_{0.8}O_2N$	59.58	4.40	51.70
$CaNb_{0.3}Ta_{0.7}O_2N$	46.42	7.51	38.62
$CaNb_{0.4}Ta_{0.6}O_2N$	46.47	9.84	36.24
$CaNb_{0.5}Ta_{0.5}O_2N$	43.41	15.05	34.31
$CaNb_{0.6}Ta_{0.4}O_2N$	41.36	15.86	31.77
$CaNb_{0.7}Ta_{0.3}O_2N$	34.35	9.42	18.26
$CaNb_{0.8}Ta_{0.2}O_2N$	33.17	5.46	13.95
$CaNb_{0.9}Ta_{0.1}O_2N$	26.98	3.38	6.11
$CaNbO_2N$	27.37	0.45	0.25
$LaTaON_2$	41.39	39.10	31.47
$LaNb_{0.1}Ta_{0.9}ON_2$	46.52	35.59	38.09
$LaNb_{0.2}Ta_{0.8}ON_2$	41.62	29.53	29.73
$LaNb_{0.3}Ta_{0.7}ON_2$	45.20	16.16	14.02
$LaNb_{0.4}Ta_{0.6}ON_2$	39.69	17.79	18.04
$LaNb_{0.5}Ta_{0.5}ON_2$	30.69	18.31	12.40
$LaNb_{0.6}Ta_{0.4}ON_2$	31.52	14.01	10.58
$LaNb_{0.7}Ta_{0.3}ON_2$	32.08	13.65	12.53
$LaNb_{0.8}Ta_{0.2}ON_2$	32.47	12.98	12.46
$LaNb_{0.9}Ta_{0.1}ON_2$	37.67	5.89	11.33
$LaNbON_2$	27.76	1.17	-0.99

5.6 DISCUSSION AND CONCLUSIONS

It has been found that the substitution of tantalum by niobium in the two perovskite series $CaNb_xTa_{(1-x)}O_2N$ and $LaNb_xTa_{(1-x)}ON_2$, where $0 \leq x \leq 1$, is successful for high tantalum content. The level of impurities increases with increasing niobium content. Substitutions are less successful in the lanthanum series, which is a probable result of sintering difficulties arising from the mobility of trivalent lanthanum ions.

The splitting of the reflections in the diffraction profiles of $CaNb_xTa_{(1-x)}O_2N$ are consistent with the oxide analogue $CaNbO_3$.[6] The increased splitting for samples with greater Nb content suggest a slight increase in lattice parameter which may lead to further distortions of the octahedra on account of altering bond lengths. However, the fluctuations in unit cell parameters are minimal, which is expected as there is no difference in the size of the tantalum and niobium radii due to the lanthanide contraction. It could be an indication of the presence of Nb (IV) as the crystal radius of Nb (IV) is greater than Nb (V).

This chapter highlights the important role tantalum plays in achieving a satisfactory pigment. The replacement of tantalum by niobium has resulted in the darkening and eventual blackening of the solid solution series, thus the ideal candidates are those which have a high tantalum content.

Ammonolysis reactions often yield a degree of inhomogeneity within the product. The reason for this comes from the variation of nitrogen fugacity along the length of the furnace, which is greatest at the gas inlet side of the hot zone. A study by Hellwig *et al.*[1] has been conducted on the formation of the cubic perovskite $BaTaO_2N$. They have found that there is a variation in colour dependent upon location within the hot zone, with the powder going from red nearest the gas inlet through yellow to white. They proposed that both nitrogen content and tantalum valency account for the colour variation. X-ray photoelectron spectroscopy (XPS) studies have resulted in the theory that the red powder contains Ta^{4+} ions, reduced from Ta^{5+} by the ammonia, whereas the white powder contains Ta^{5+} ions. This led to the postulation of a correlation between Ta (IV) and intense colours. The problem with inhomogeneity can sometimes be minimised by reversing the flow of ammonia for half of the

reaction time or increasing the flow of ammonia. However, the later often results in the formation of a Ta_3N_5 phase, as complete nitridation takes place.

In this work, the intense colours of the compounds are lost as the tantalum content is reduced, which too suggests a correlation between tantalum and colour. Although whether the tantalum is reduced under the flowing ammonia atmosphere is an unknown parameter. Even though there is little difference in chemistry between niobium and tantalum there is significant difference in colour across the solid solutions.

In the quest for safer non-toxic red pigments, several factors must be acknowledged. This work addresses the need for the physical and chemical properties of a potential oxynitride pigment to meet the specific requirements. For instance, it must be resistant to light, heat and chemical attack. Added to this the colour of any red compound must be matched to those of Cd(S,Se) and HgS, a poor alternative is not an appropriate substitute. An important factor, which has thus far been ignored, is one of cost.

Tantalum is an expensive metal as it has a low abundance, averaging only 2 ppm in the Earth's crust. However it is a versatile and extremely diverse material. Its extremely high melting point, tensile strength and resistivity to acids and fused alkalis advocates its many metallurgic applications. Tantalum compounds achieve the highest capacitance per gram of any known material hence its use in electronic components is widespread. Bearing this in mind, a reduction in the use of the precious metal tantalum is beneficial in reducing the cost of the full scale production of oxynitride pigments. Work in the following chapter concentrates on the partial replacement of tantalum in the perovskite structures by other transition metals.

The substitution of vanadium for tantalum was also carried out for high tantalum content in $CaV_xTa_{(1-x)}O_2N$. The syntheses result in black powders that adopted the perovskite structure though from PXD data sets these compounds are not crystalline; the peaks are broad and split. The radius of the V^{5+} cation is smaller than either Ta (V) or Nb (V) which may account for the difficulties in forming a crystalline phase. Vanadium is more easily reduced than tantalum or niobium and all four oxidation states can be found in a 6 co-ordinate sphere. The lower oxidation states, having a lower charge density thus larger crystal radius, means that it is likely that vanadium is reduced when incorporated into the perovskite cell.

5.7 REFERENCES

[1] Hellwig A., Hendry A.; *J. Mat. Sci.*, **29**, 4686 (1994)

[2] West A. R.; *Solid State Chemistry and its Applications*, Wiley (UK), First Edition (1984)

[3] Bruker Advanced X-Ray Solutions; *EVA*, **V 6.0** (2000)

[4] Laugier J., Bochu B.; *CELREF*, Laboratoire des Matériaux et du Génie Physique, Ecole Nationale Supérieure de Physique de Grenoble INPG (France) (2000)

[5] von Brauer G., Jander J.; *Z. Anorg. Allg. Chem.*, **270**, 160 (1952)

[6] Mitchell R. H., Choi J. B., Hawthorne F. C., McCammon C. A., Burns P. C.; *Can. Mineral.*, **36**, 107 (1998)

[7] Kim Y-I., Woodward P., Baba-Kishi K. Z., Tai C. W.; *Chem. Mater.*, **16**, 1267 (2004)

[8] Günther E., Hagenmayer R., Jansen M.; *Z. Anorg. Allg. Chem.*, **626**, 1519 (2000)

[9] Shannon R. D.; *Acta Crystallogr. A.*, **32**, 751 (1976)

[10] Marchand R., Pors F., Laurent Y.; *Ann. Chim. Fr.*, **16**, 553 (1991)

[11] Brauer G., Weidlein J., Strähle J.; *Z. Anorg. Allg. Chem.*, **348**, 298 (1966)

[12] Conroy L. E., Noerlund Christensen A.; *J. Solid State Chem.*, **20**, 205 (1997)

[13] Orhan E., Tessier F., Marchand R.; *Solid State Sci.*, **4**, 1071 (2002)

[14] Emsley J.; *The Elements*, Oxford University Press (UK), Second Edition (1991)

CHAPTER SIX

SYNTHESIS AND CHARACTERISATION OF TITANIUM, TUNGSTEN AND ZIRCONIUM CONTAINING OXYNITRIDES

6 TITANIUM, TUNGSTEN AND ZIRCONIUM CONTAINING OXYNITRIDES

6.1 INTRODUCTION

Further results on the partial replacement of tantalum within oxynitride systems are discussed in this chapter. Variables such as the type of metal cations (A = Ca, Sr, Ba, B = Ti, W, Zr, *etc.*) and stoichiometry of metal cations ($AB_xB'_{(1-x)}X_3$) were altered within the perovskite structure, ABX_3, to generate numerous target materials. Within the timeframe of this project, it was only possible to focus on certain metal substitutions and compositions.

Previous work has indicated the formation of oxynitride materials containing metal cations such as chromium,[1] molybdenum,[2,3] titanium,[4,5] tungsten,[6-10] vanadium,[11] and zirconium.[12-14] Thus, initial studies targeted oxynitrides containing these metals as well as target phases with metals such as bismuth, hafnium, tin and zinc. In some cases the metal ions can easily be reduced, therefore stable, crystalline phases with metals such as bismuth and tin are difficult to produce. The most facile syntheses involve titanium and to some extent tungsten. From these findings, mixed metal oxynitride compounds were synthesised that contained tantalum, titanium or tungsten plus another metal on the B site, or in a few cases just titanium or tungsten on the B site of the perovskite structure.

The substitutions of metals of different electropositivities allow for fine-tuning of the band gap energy ΔE. This results in a slight shift in the wavelengths of visible light that are absorbed, which in turn permits a range of coloured oxynitride compounds, see *fig. 6.1*. The picture represents the various hues achievable through ammonolysis of metal oxide and carbonate precursors. The red compounds include Ta_3N_5 and $LaTaON_2$, whereas the oranges and golds result from the partial replacement of lanthanum by alkaline earth metals (calcium, strontium and barium) and the yellow represents $SrTaO_2N$. The green and blue powders are a direct result of titanium substitutions with lighter shades of blue achievable via tungsten substitution (not shown). Finally the brown compound is the target compound $EuTa(O,N)_3$ / $Eu_2Ta_2(O,N)_7$ (see *Chapter 3*).

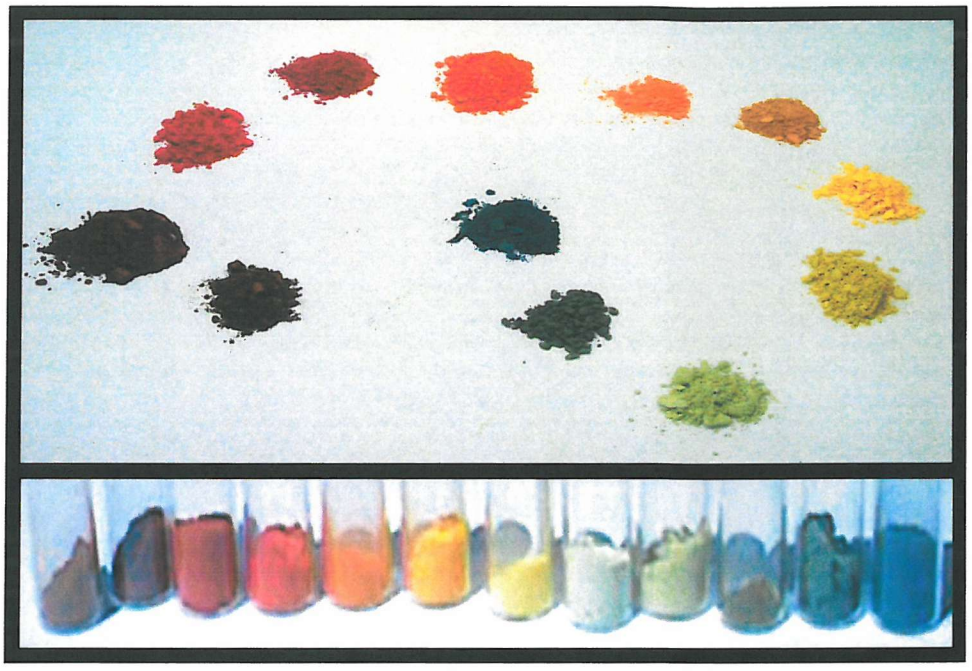

fig. 6.1: Various tantalum and titanium oxynitride systems after gas transformation by ammonia.

This chapter focuses primarily on titanium substitutions sharing the B cation position of a perovskite with tantalum, tungsten and niobium, though mixed tungsten tantalum compounds and a tantalum zirconium compound are also summarised here.

6.2 SYNTHESIS

Samples were synthesised using the gas transformation method,[15,16] employed in the previous chapters, unless otherwise stated. Stoichiometric amounts of the appropriate metal oxides and carbonates were intimately ground in an inert acetone media with *ca.* 50% wt. ratio of halide salts employed as mineralisers. The salts used, NaCl, KCl and $CaCl_2$, were in equimolar ratios. The various reactants used are as follows; TiO_2 (Alfa, 99.8%), Ta_2O_5 (Aldrich, 99%), Nb_2O_5 (Aldrich, 99.9%), ZrO_2 (Aldrich, 99%), WO_3 (Alfa, 99.7%), $CaCO_3$ (Aldrich, 99%), $SrCO_3$ (Aldrich, 99%) and $BaCO_3$ (Aldrich, 99%).

The titanium samples were treated with dry flowing gaseous ammonia (Air Products, Electronic Grade) for 20 hours at a flow rate of *ca.* 7 dm^3 hr^{-1} and a reaction temperature of

850 °C. The mineralisers were leached from the fired materials by washing thoroughly with excess de-ionised water. Where necessary the products were ground and re-fired at a higher temperature (950 °C). Tungsten is easily reduced and therefore milder conditions were adopted for materials containing this element. The first firing was conducted at 650 °C with an increase to 700 or 750 °C for a second heat treatment. The reduction in temperature required different mineralisers to be employed; in such cases $SrBr_2$ was used as this melts at 643 °C, thus generating a flux to aid ionic transport.

Phase identification of the samples was completed by powder X-ray diffraction (PXD). Data sets were collected on a Siemens D5000 or Bruker D8 using Cu $K_{\alpha 1}$ radiation (λ=1.5406 Å). In the case of $BaWON_2$, a powder neutron diffraction (PND) study was also undertaken.

UV-Visible spectroscopy was carried out on a Perkin Elmer UV/Vis/Lambda 35 in the range of 200 nm to 800 nm with $BaSO_4$ used as a reference. From the spectroscopy data $L^*a^*b^*$ measurements were calculated, tabulated and compared.

Thermogravimetric analyses (TGA) were performed by S Henderson using a Mettler Toledo TGA/SDTA851^e with a TSO801RO UNIVERSAL sample robot. Samples were heated under N_2 with a constant heating rate of 10 °C min^{-1}. At 1000 °C the gas was switched to O_2 and the temperature held for 30 minutes before a cooling cycle was initiated.

6.3 TITANIUM

6.3.1 SYNTHESIS AND CHARACTERISATION OF $SrTa_xTi_{(1-x)}O_{(3-x)}N_x$, $0 \leq x \leq 1$

6.3.1.1 DIRECT AMMONOLYSIS

Titanium doping of $SrTaO_2N$, a bright yellow pigment, was achieved by targeting the solid solution series of $SrTa_xTi_{(1-x)}O_{(3-x)}N_x$. The compounds were analysed by PXD. Phase identification is summarised in *Table 6.1* and a stack plot of the profiles is found in *fig. 6.2*.

Table 6.1: Phase identification for solid solution series $SrTa_xTi_{(1-x)}O_{(3-x)}N_x$ where x is between 0 and 1.

Sample	Phase Identification
$SrTaO_2N$	Perovskite, follows $SrTaO_2N$.[17]
$SrTa_{0.9}Ti_{0.1}(O,N)_3$	Perovskite and TaON.
$SrTa_{0.8}Ti_{0.2}(O,N)_3$	Perovskite and TaON.
$SrTa_{0.7}Ti_{0.3}(O,N)_3$	Perovskite (asymmetric peaks).
$SrTa_{0.6}Ti_{0.4}(O,N)_3$	Perovskite and TaON (poor crystallinity).
$SrTa_{0.5}Ti_{0.5}(O,N)_3$	Perovskite.
$SrTa_{0.4}Ti_{0.6}(O,N)_3$	Perovskite, segregation $SrTaO_2N$, $SrTiO_3$ (almost equal).
$SrTa_{0.3}Ti_{0.7}(O,N)_3$	Perovskite, segregation $SrTaO_2N$, $SrTiO_3$ (more $SrTiO_3$).
$SrTa_{0.2}Ti_{0.8}(O,N)_3$	Perovskite, segregation $SrTaO_2N$, $SrTiO_3$ (more $SrTiO_3$), TaON.
$SrTa_{0.1}Ti_{0.9}(O,N)_3$	Perovskite (asymmetric peaks).
$SrTi(O,N)_3$	Perovskite, follows $SrTiO_3$.[18]

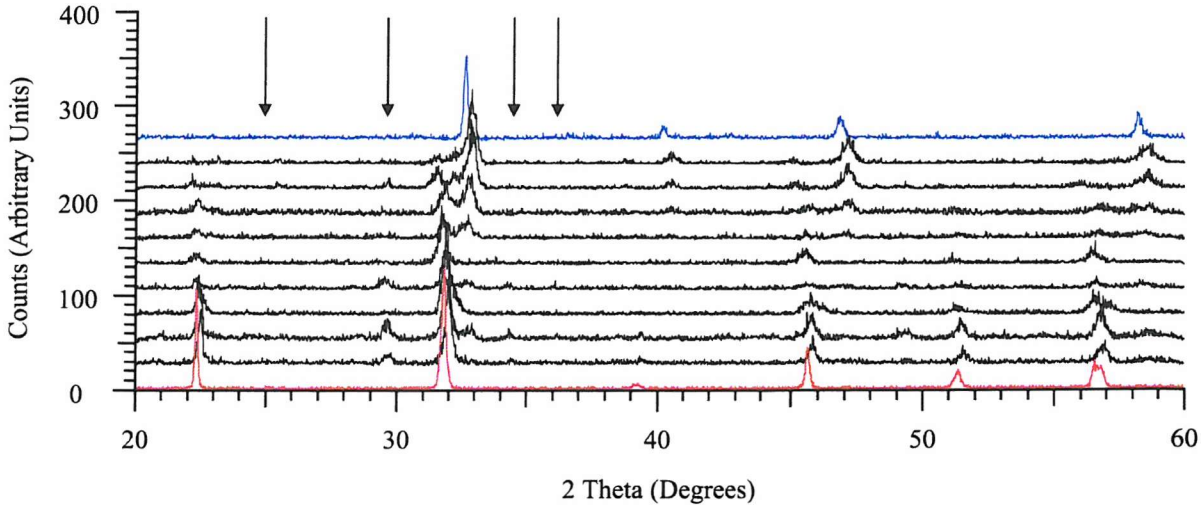

fig. 6.2: Powder X-ray diffraction data for $SrTa_xTi_{(1-x)}O_{(3-x)}N_x$ target phases, from the upper pattern downwards x = 0, 0.1, 0.2, 0.3, 0.4, 0.5, 0.6, 0.7, 0.8, 0.9 and 1.0, where the arrows represent a TaON impurity phase.

A perovskite phase is formed for all x though there are certain differences between compositions across the series. For high tantalum content there is a competing TaON phase, this disappears as the percentage of titanium increases. As the Ti content increases the peaks

become broader with further splitting as a result of decreasing particle size and increasing distortions within the unit cell respectively. Eventually at *ca.* 60% Ti doping, two distinct peaks are resolved for each expected perovskite peak. This suggests two different perovskite structures, with different cell parameters, exist due to inhomogeneity within the sample. There is substantial overlapping of the peaks for high tantalum content, indicating a perovskite phase that is tantalum rich and another that is titanium rich. Alternatively a mutual solubility may exist between a titanium phase and a tantalum phase, with decreasing solubility on increasing titanium stoichiometry. Such compositional variance could also explain the asymmetry displayed in the peaks of $SrTa_{0.7}Ti_{0.3}O_{2.3}N_{0.7}$. Aside from this, asymmetric peaks can be a direct result of the reduction in particle size and thus the broadening of reflections would be evident in the PXD profile.

The positions of the perovskite peaks are an indication of lattice parameter size with a shift to higher 2θ indicating a decrease in dimensions. The replacement of tantalum by titanium could result in a smaller unit cell as the crystal radius of the respective cations is reduced. (Ta^{5+} 78 pm *cf.* Ti^{4+} 74.5 pm). However, around 30-40% Ti doping the peak positions move towards lower 2θ, indicating an increase in cell parameter. This occurrence is likely to be brought about by a variance in anionic composition, such as differences in the oxygen to nitrogen ratio across the series and the possibility of vacancies within this sub-network. Alternatively, due to the TaON impurity in several samples, the actual ratio of titanium and tantalum is unknown, *i.e.* the samples with TaON impurities may have perovskite phases with titanium composition greater than the original reactant stoichiometry. Hence, the profiles may not be stacked in ascending order of titanium content. This could result in the fluctuations of the lattice parameter sizes, represented by the shift in PXD reflections, as observed in *fig. 6.2*.

Thermogravimetric analyses were carried out to try to ascertain the amount of nitrogen within these compounds. Considering the possibility of vacancies, for correctness the series can formally be written as $SrTa_xTi_{(1-x)}(O,N,\square)_{3-\delta}$. Assuming that the metals are in their maximum oxidation states, this molecular formula allows electroneutrality to be maintained, *i.e.* if vacancies are present there will be more N^{3-} present within the structure than in the target stoichiometry $SrTa_xTi_{(1-x)}O_{(3-x)}N_x$.

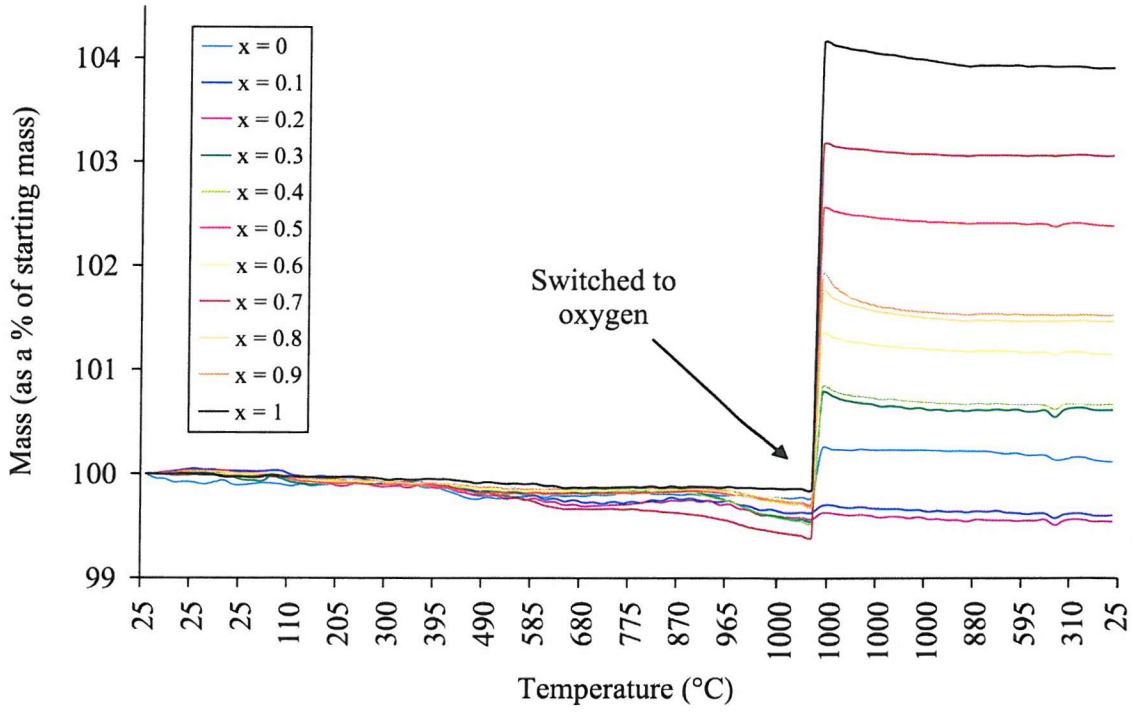

fig. 6.3: *Thermogravimetric analyses of $SrTa_xTi_{(1-x)}O_{(3-x)}N_x$ where x = 1, 0.7, 0.5, 0.9, 0.8, 0.6, 0.4, 0.3, 0.0, 0.1 and 0.2 in descending order.*

The first readings at 25 °C correspond to the machine being flushed with nitrogen prior to heating the samples. At 1000°C the gas supply is switched to oxygen and held at this temperature for 30 minutes. At this point the samples are oxidised and oxygen atoms replace nitrogen within the unit cell. Thus there is a direct relationship between the mass increase and the amount of nitrogen in the compound. The increase in mass is greater for the samples of higher tantalum content, as those compounds contain more nitrogen. The mass increase is a direct result of the replacement of nitrogen atoms by the heavier oxygen atoms. This occurs on the basis of $2\ N^{3-} \equiv 3\ O^{2-}$ to maintain electroneutrality.

$$4\ SrTaO_2N + 3\ O_2 \rightarrow 4\ SrO + 2\ Ta_2O_5 + 2\ N_2$$

The samples, $SrTa_xTi_{(1-x)}O_{(3-x)}N_x$ where x = 0, 0.1 and 0.2, adopting predominately a $SrTiO_3$ perovskite phase, show only minimal increases in their masses suggesting only a minimal occupancy of the anionic sites by nitrogen. As the replacement of tantalum by titanium leads to a reduction in the overall positive charge the nitrogen content should decrease on increasing titanium content.

The trend is not clear cut, correlating the PXD data to the TGA data, the single phase perovskites with no phase segregation correspond to the samples with the highest nitrogen content, *i.e.* $x = 1$, 0.7 and 0.5. There are also a few anomalies at higher titanium doping with 100% and 90% doping having a greater mass increase than 80% Ti doping. This is most likely due to the uptake of oxygen in a defect structure, *i.e.* vacancies are now occupied by oxygen anions.

EDAX analysis was performed on the single phase sample $SrTa_{0.7}Ti_{0.3}O_{2.3}N_{0.7}$ to investigate the actual cation composition compared to the target stoichiometry. The results obtained are displayed in *Table 6.2*.

Table 6.2: EDAX data obtained on the sample $SrTa_{0.7}Ti_{0.3}O_{2.3}N_{0.3}$.

Element	Weight %	Atomic %	Ratio
Ca	8.50	9.94	0.5
Sr	17.7	9.46	0.48
Ta	47.6	12.3	0.62
Ti	5.48	5.34	0.27
O	14.8	43.3	2.18
N	5.86	19.6	0.98

This yields a compound of stoichiometry $Ca_{0.5}Sr_{0.48}Ta_{0.62}Ti_{0.27}O_{2.18}N_{0.98}$. There are several points of interest that arise from these results. Firstly, calcium from the halide mineralisers has occupied the A site of the perovskite in *ca.* a 1:1 ratio with strontium. This could have occurred on account of size constraints, calcium has a smaller crystal radius than strontium (140 pm *cf.* 158 pm), thus replacing strontium with calcium can reduce the strain within the structure in accordance with Goldschmidt's tolerance factors.[19] Secondly, the values obtained for the occupancies on the central metal atom position are similar to the stoichiometry of the reactants, when considering experimental errors for EDAX are around 10%. These errors also allow for the fact that the given stoichiometry, $Ca_{0.5}Sr_{0.48}Ta_{0.62}Ti_{0.27}O_{2.18}N_{0.98}$, is not electrochemically neutral.

The series goes from bright yellow ($SrTaO_2N$) through green for mixed tantalum titanium systems to blue for $SrTi(O,N,\square)_{3-\delta}$. UV-Vis. spectroscopy was carried out on the series of

compounds, see *fig. 6.4.* and colour measurements for the solid solution series are collated in *Table 6.3.* From these spectra, it is possible to see the shift in absorption edge to longer wavelengths with increasing tantalum content suggesting a reduction in band gap energy. The absorption edges are generally shallow unlike that of $SrTaO_2N$, with the steepest edges representing the samples of highest tantalum content; a steep absorption edge is an indication of colour purity.

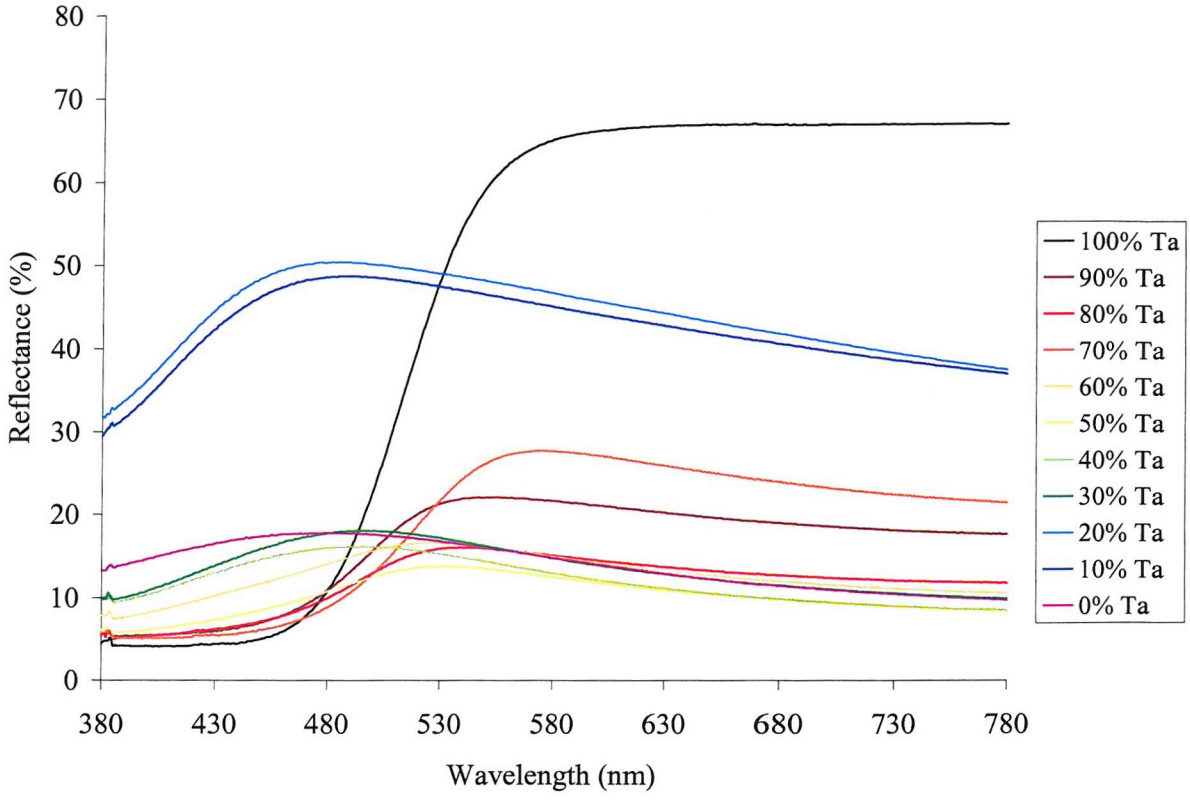

fig. 6.4: *UV-Visible spectra of $SrTa_xTi_{(1-x)}O_{(3-x)}N_x$, where $0 \leq x \leq 1$ from 100% Ta in ($SrTaO_2N$) to 0 % Ta in ($SrTi(O,N,\square)_{3-\delta}$)*

For the green and blue pigments there is also a reduction in reflectance at longer wavelengths, *i.e.* red light is absorbed by these samples, hence the profile of the spectra are altered from other spectra shown previously in this work. For the blue pigments, especially at 10 and 20% Ti doping, the reflectance band is continued into the ultraviolet.

In *Chapter 5* it is reported that the replacement of tantalum by a more electronegative element leads to a reduction in the band gap and thus a shift in the absorption edge to longer wavelengths. The converse seems to be true in this work, even though the electronegativity of

titanium is 1.54 *cf.* 1.5 for tantalum (Pauling scale), the band gap is actually increasing. This is because the valency of titanium is less, resulting in a reduction in the nitrogen content across the series. Therefore the presence of more oxygen increases the band gap, shifting the absorption edge towards the ultraviolet, which may explain the pale colours observed at high titanium doping.

Table 6.3: Colour measurements of the solid solution series $SrTa_xTi_{(1-x)}O_{(3-x)}N_x$, where $0 \leq x \leq 1$.

Target Sample	*L**	*a**	*b**	Observed Colour
$SrTaO_2N$	76.63	4.81	77.31	Yellow
$SrTa_{0.9}Ti_{0.1}O_{2.1}N_{0.9}$	51.45	-6.10	30.52	Yellow Green
$SrTa_{0.8}Ti_{0.2}O_{2.2}N_{0.8}$	44.90	-7.06	19.86	Green
$SrTa_{0.7}Ti_{0.3}O_{2.3}N_{0.7}$	54.50	0.63	39.73	Yellow Green
$SrTa_{0.6}Ti_{0.4}O_{2.4}N_{0.6}$	45.96	-7.35	8.56	Green
$SrTa_{0.5}Ti_{0.5}O_{2.5}N_{0.5}$	41.97	-7.52	11.18	Green
$SrTa_{0.4}Ti_{0.6}O_{2.6}N_{0.4}$	44.32	-7.19	-0.87	Blue Green
$SrTa_{0.3}Ti_{0.7}O_{2.7}N_{0.3}$	46.84	-7.44	0.44	Blue Green
$SrTa_{0.2}Ti_{0.8}O_{2.8}N_{0.2}$	74.71	-3.96	0.20	Pale Blue
$SrTa_{0.1}Ti_{0.9}O_{2.9}N_{0.1}$	73.68	-4.21	0.69	Pale Blue
$SrTi(O,N,\square)_{3-\delta}$	41.46	-4.02	-7.14	Steel Blue

It must be noted that values obtained from samples with a TaON impurity are not true to the colour of the compound. TaON has been described as yellow (high Ta purity) and green (Nb impurity, from ore source)[20] hence this affects the overall observed colour. This may suggest why the samples at 20% Ti doping are green but for the single phase product formed at 30% Ti doping the colour reverts to the yellow-green colour observed at 10% Ti doping. Alternatively this colour anomaly for $SrTa_{0.7}Ti_{0.3}O_{2.3}N_{0.3}$ may arise from the presence of calcium in the sample, deduced from EDAX data.

The *a** value is mainly negative across the series, this is expected as it represents a green hue within the pigment. If this number is positive it represents a redness value but this only occurs for $x = 1$ and 0.7. As it is impossible to see red hues of green and vice versa, it could suggest that a small experimental error is observed for $x = 0.7$ as this has an observable green hue.

From this data it can be seen that the best pigments are those with high tantalum content. As more titanium is added the pigment becomes duller with the synthesis of blue-green compounds. This trend is then reversed as high titanium doping levels are reached, for $x = 0.1$ and 0.2, a light blue coloured powder results. The blue colour is much paler than $x = 0$. As both these compounds show no notable mass increase it is likely that oxynitride phases have not formed, thus suggesting the band gap has not drastically altered. Therefore, the TGA data suggests minimal nitrogen content at high titanium doping. The origin of the steel blue colour may not be an effect caused by anionic substitutions and consequent narrowing of the band gap energy but by the presence of Ti^{3+} cations, as ordinarily $SrTi^{IV}O_3$ is white. The partial reduction of Ti^{4+} to Ti^{3+} may arise due to the reductive atmosphere of ammonia, with the Ti^{3+} ions imparting a blue colour on the ceramic route synthesis; the compound $SrTiO_{2.72}$ is reported to be dark blue-violet.[21]

6.3.1.2 ALKOXIDE PRECURSOR

A strontium titanium oxynitride was also synthesised by an alkoxide route adapting a preparation from the literature.[12] It has been reported that it is possible to use more reactive starting materials such as xerogels[13,22] to target oxynitrides phases. This has arisen as a cause of the unreactiveness of some metal oxides at low temperatures.

A sol-gel process was employed to make active oxide precursors, which used a mixture of acetic acid and acetic anhydride as a solvent in a 9:1 ratio. This route allows for a slow gelation process, ensuring optimal distribution of metal atoms in the precursor. The solvent keeps the amount of water at a low and constant concentration to permit a slow controlled condensation as the water promotes a condensation reaction of metal alkoxides. This concentration is maintained by the acetic anhydride buffer, which binds the water produced by esterification. In addition to this, acetic acid acts as a chelating agent suppressing premature coagulation of the evolving sol particles.

Stoichiometric amounts of titanium ethoxide (Aldrich, Technical grade) and a 70% solution of strontium isopropoxide (Strem, min 97%) in isopropanol (BDH) were added to the solvent, a 90% acetic acid (absolute) and 10% acetic anhydride mix. The resulting solution was kept at 50 °C for 48 hours. When the alkoxides were added to the solution, ligand exchange and esterification took place, producing enough water *in-situ* to hydrolyse the alkoxide monomers until gel formation occurred. The gel obtained was dried under vacuum

at 100 °C and heated under argon to 250 °C to remove all traces of solvent. Calcining the gels in an oxygen atmosphere at 600 °C burned out the organic residues. The precursor was still amorphous but was a homogeneous distribution of metal atoms, more reactive to ammonolysis treatment than just simple metal oxides. The resultant powder was fired at 900 °C under flowing ammonia for *ca.* 20 hours, ground, fired again and analysed.

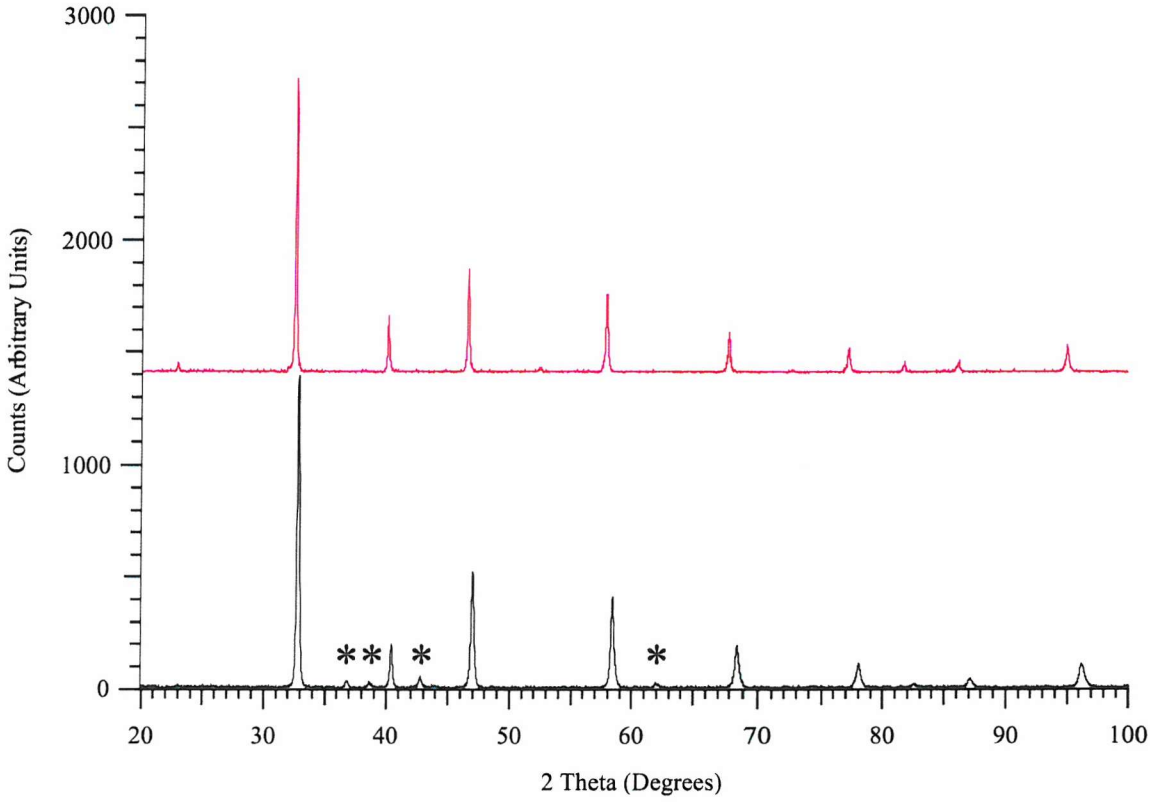

fig. 6.5: *Powder X-ray diffraction data for $SrTi(O,N,\square)_{3-\delta}$ (upper) synthesised via an alkoxide route and (lower) synthesised via direct ammonolysis at 850 °C with halide salts. The * represents a $CaTiO_3$ impurity as stated in discussion.*

Both compounds yield PXD profiles similar to $SrTiO_3$,[18] a cubic perovskite crystallising in the space group *Pm-3m*. In the ceramic route sample profile there are minor reflections, resolved from the background, which are not found in the literature for $SrTiO_3$. They do however provide a match with $CaTiO_3$.[23] As $CaCl_2$ is present as a mineraliser it is possible that $CaTiO_3$ or a mixed composition $(Ca,Sr)TiO_3$ phase has also formed.

Estimated lattice parameters, found in *Table 6.4*, were obtained using the program *CELREF*[24] and from this data cell volumes were calculated.

This data shows that the ceramic route yields a perovskite with a smaller unit cell size compared with the alkoxide route synthesis. This difference could be a direct result of the inhomogeneity of the sample, as discussed earlier.

Table 6.4: Estimated lattice parameters for $SrTi(O,N,\square)_{3-\delta}$.

Sample	*a* [Å]	*V* [Å^3]
Ceramic	3.886 (1)	58.68 (5)
Alkoxide	3.905 (8)	59.55 (37)
Literature[18]	3.907 (1)	59.64 (5)

There is a clear difference in hue for these two samples, the alkoxide route yields a green powder and the direct ammonolysis a blue powder. *Chapter 7* presents a more in depth discussion on colour versus synthetic route for the perovskite $SrTaO_2N$.

The spectra in *fig. 6.6* display similar broad reflectance bands, though the wavelength range at which these bands occur differs. This is probably due to the particle size of the reactants, with the alkoxide route yielding a precursor with a smaller particle size distribution than the ceramic reactants.

This reduction in particle size is often linked to an increase in reactivity. In turn, this allows for a greater nitrogen uptake and therefore a compound with a smaller band gap. Hence for the alkoxide route, the reflectance maximum occurs at longer wavelengths (*ca.* 540 nm) than the corresponding ceramic route (*ca.* 480 nm). This can explain the colour difference between the two samples detailed above. There may be little nitrogen incorporation within the anionic framework of the ceramic route compound, with the colour change from the white $SrTiO_3$ occurring due to the reduction of titanium.

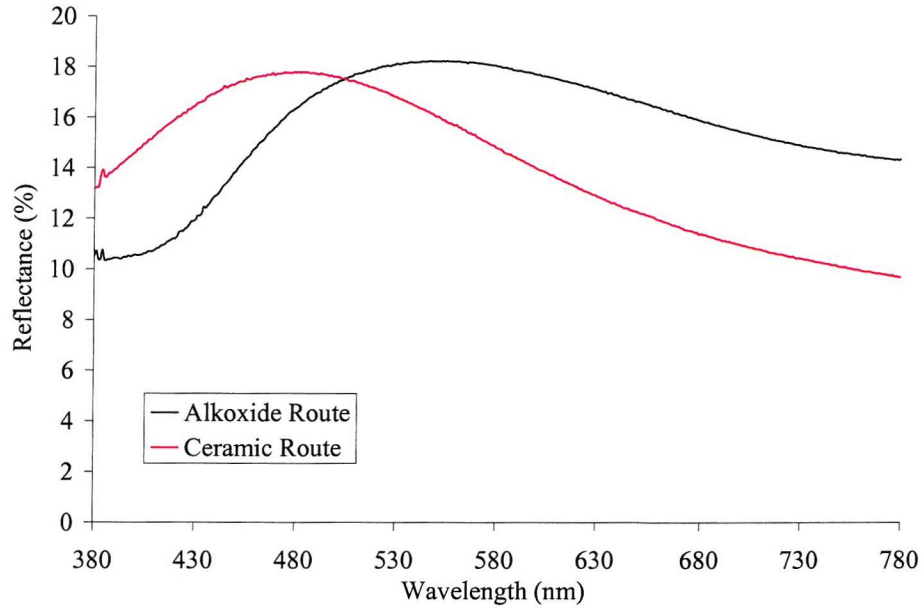

fig. 6.6: *UV-Visible spectra of $SrTi(O,N,\square)_{3-\delta}$ where the black spectrum represents the synthesis using metal alkoxides and the red spectrum a synthesis using metal oxides.*

Colour measurements were taken for the alkoxide synthesis of $SrTi(O,N,\square)_{3-\delta}$, and were found to be $L^* = 49.09$, $a^* = -3.87$, $b^* = 8.33$. The only major difference between these values and those of the ceramic route found in *Table 6.3* is for b^*. This takes a positive value, *i.e.* a yellowness value for the alkoxide route but a negative number for the ceramic route. As the ceramic powder is blue and $-b^*$ represents blueness, this is expected.

6.3.1.3 Mixed Metal Oxide Precursor

$SrTa_{0.3}Ti_{0.7}O_{2.7}N_{0.3}$ was also synthesised via a mixed metal oxide precursor. Stoichiometric amounts of $SrCO_3$ (99%), Ta_2O_5 (Aldrich, 99%) and TiO_2 (Alfa, 99.8%) were fired for 7 days at 1250 °C in air before treatment with ammonia at 950 °C. In this case mineralisers were not used but a more crystalline phase is formed, see *fig. 6.7*. This suggests that higher reaction temperatures allow for phases such as $SrTa_xTi_{(1-x)}O_{(3-x)}N_x$ to form more readily.

The PXD profiles show the same pattern in terms of the peak splitting, though the more crystalline sample has one perovskite phase dominating over the other. As the upper trace shifts to lower 2θ, it is an indication that the sample synthesised via an oxide precursor has larger lattice parameters.

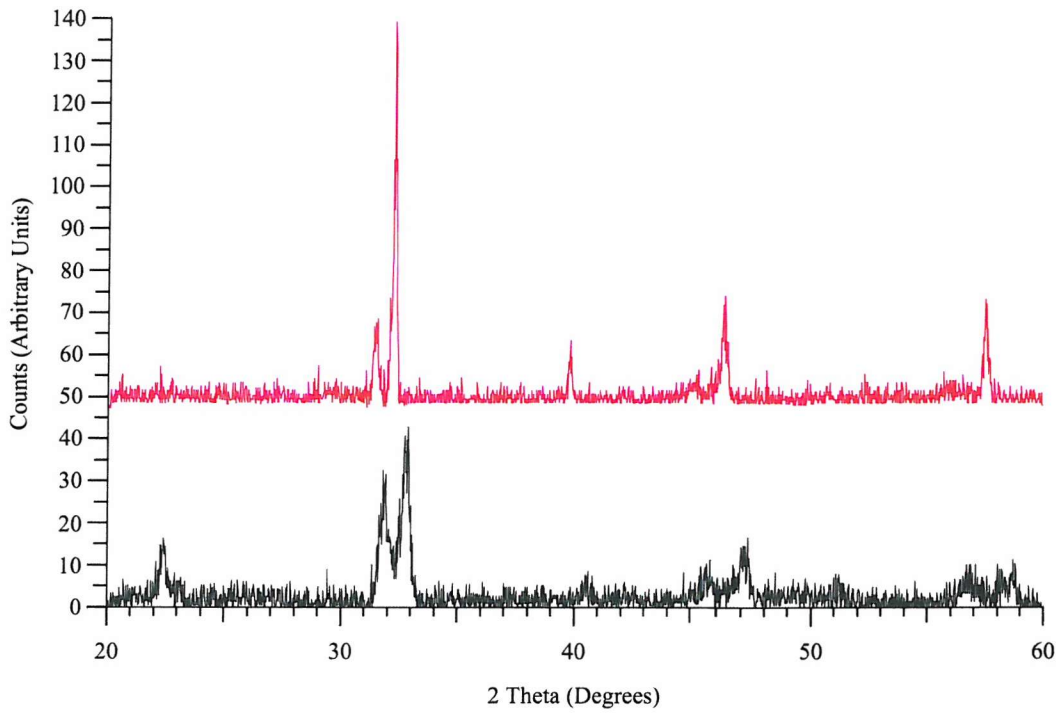

fig. 6.7: *Powder X-ray diffraction data for $SrTa_{0.3}Ti_{0.7}O_{2.7}N_{0.3}$, (upper) synthesised via an oxide precursor and (lower) synthesised via direct ammonolysis at 850 °C with halide salts.*

Both samples have a green colour but what is of note with these two samples is the slight difference in hue. Colour measurements were collected and for the oxide precursor synthesis were found to be L^* = 47.99, a^* = -6.95, b^* = 16.94, with the direct ammonolysis results reported in *Table 6.3*. This implies that the use of mineralisers actually impairs the quality of the pigment as the yellowness number is substantially improved (0.44 *cf.* 16.94). Unfortunately this method requires the use of high temperatures, which makes this technique redundant as the goal is to achieve successful syntheses on mica via low temperature routes thus facilitating the production of oxynitride coated mica pigments.

6.3.2 *SYNTHESIS AND CHARACTERISATION OF $ATa_{0.7}Ti_{0.3}O_{2.3}N_{0.7}$, A = Ca, Sr, Ba*

The substitution of alkaline earth metals in $SrTa_xTi_{(1-x)}(O,N)_3$ was attempted for x = 0.7 as no pyrochlore impurities are present in the PXD profile of $SrTa_{0.7}Ti_{0.3}O_{2.3}N_{0.7}$. The two compounds targeted were $CaTa_{0.7}Ti_{0.3}O_{2.3}N_{0.7}$ and $BaTa_{0.7}Ti_{0.3}O_{2.3}N_{0.7}$ with the strontium analogue reported in *Section 6.3.1*. PXD profiles are found in *fig. 6.8, vide infra*.

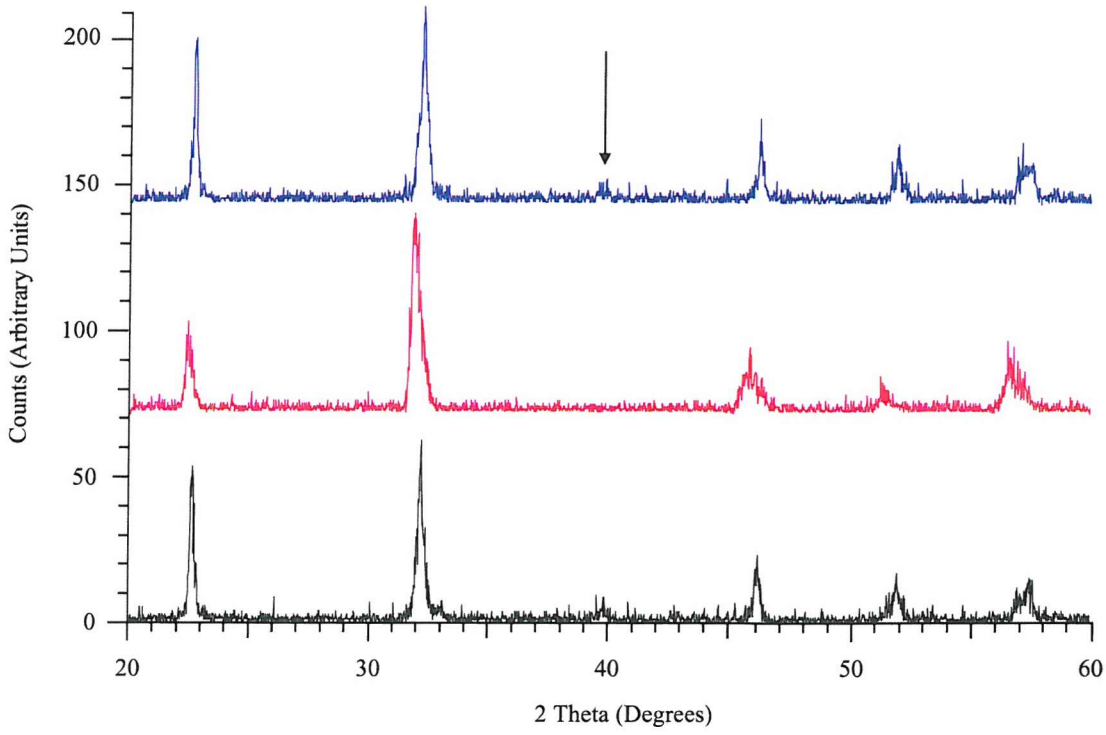

fig. 6.8: *Powder X-ray diffraction data for $ATa_{0.7}Ti_{0.3}O_{2.3}N_{0.7}$, A = Ca (black), Sr (red), Ba (blue). The arrow represents the 2 2 0 / 0 2 2 reflections allowed for the orthorhombic space group Pnma.*

The profiles suggest the compounds are isostructural with $CaTaO_2N$ found in the literature.[17] It is possible that due to the peak splitting, and thus distortions displayed in the materials synthesised in this work, that the compounds have formed in different crystal symmetries. The arrow in *fig. 6.8* points to the location of the 2 2 0 / 0 2 2 reflections in the orthorhombic $CaTaO_2N$. These are clearly present in both calcium and barium samples but in the strontium sample they could have the same magnitude of intensity as the background counts, and are therefore not distinguished.

Colour measurements have been acquired for the alkaline earth substitutions and are tabulated below. The colours of the calcium and barium samples are similar to the strontium sample after one heating cycle though have undergone further firing. Subsequent heating cycles improve the crystallinity of the product, though with this comes a darkening of the product yielding deep green powders. This additional ammonolysis explains the difference in greenness values ($-a^*$) and also the decrease in yellowness number ($+b^*$) as all samples have a green-yellow hue after the first ammonolysis.

Table 6.5: Colour measurements of $ATa_{0.7}Ti_{0.3}O_{2.3}N_{0.7}$, A = Ca, Sr, Ba.

Target Sample	*L**	*a**	*b**
$CaTa_{0.7}Ti_{0.3}O_{2.3}N_{0.7}$	33.89	-9.02	8.94
$SrTa_{0.7}Ti_{0.3}O_{2.3}N_{0.7}$	54.50	0.63	39.73
$BaTa_{0.7}Ti_{0.3}O_{2.3}N_{0.7}$	34.92	-9.41	10.00

6.3.3 SYNTHESIS OF $CaTi_{0.7}Nb_{0.3}O_{2.7}N_{0.3}$

As a point of interest, the perovskite phase $CaTi_{0.7}Nb_{0.3}O_{2.7}N_{0.3}$ was also targeted. A dark green perovskite is obtained. This suggests the 6 co-ordinate cation in the perovskite plays a vital role in the colour of the compound as like the strontium analogue, the quaternary phase $CaTi(O,N)_{3-\delta}$ is a steel blue. The replacement of titanium by niobium in the calcium phase and tantalum in the strontium phase $SrTi(O,N)_{3-\delta}$ results in the compound acquiring a greenish tinge, where the quaternary phases are both blue. As with the niobium substituitions in *Chapter 5* there is a darkening of the material with the observation that $CaTi_{0.7}Nb_{0.3}O_{2.7}N_{0.3}$ is darker than $SrTi_{0.7}Ta_{0.3}O_{2.7}N_{0.3}$.

6.4 TUNGSTEN

6.4.1 SYNTHESIS AND CHARACTERISATION OF $Ba_{0.12}Sr_{0.88}WON_2$

A perovskite phase $BaWON_2$ was targeted via the ammonolysis of $BaCO_3$ (Aldrich, 99%) and WO_3 (Alfa, 99.7%) at 650 °C, with $SrBr_2$ added as a mineraliser. This was followed by a further ammonolysis at 750 °C after washing thoroughly with deionised water. The PXD profile is found in *fig. 6.9.*

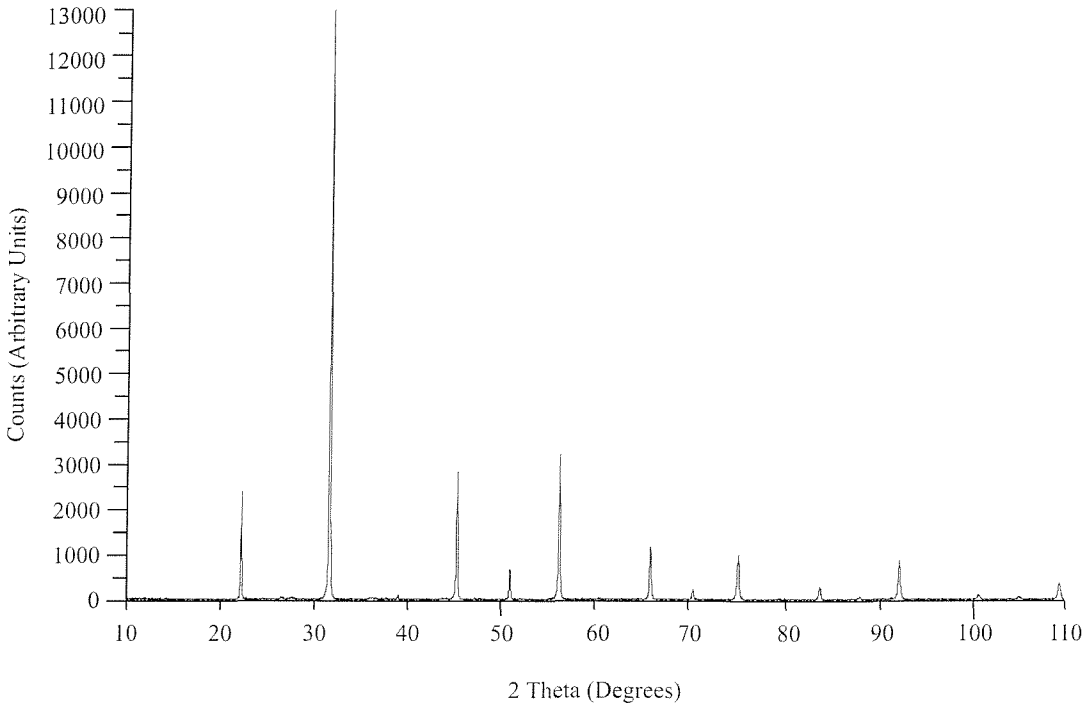

fig. 6.9: *Powder X-ray diffraction data for perovskite target phase $BaWON_2$.*

Powder neutron diffraction (PND) studies were carried out at the ISIS facility at the Rutherford Appleton Laboratory. A time of flight (TOF) data set was collected at 298 K on *POLARIS*, a medium resolution, high intensity powder diffractometer.

Structural characterisation of the perovskite was accomplished, using the *GSAS* suite of programs[25] to perform a combined Rietveld refinement[26,27] of the data sets from PXD and TOF neutron diffraction. The data sets were refined using a starting model of the cubic compound, $SrWO_2N$, published in the literature.[28]

Structure refinement shows that the sample is cubic and contains a high proportion of strontium on the A site of the perovskite as detailed in *Tables 6.6* and *6.7*. This strontium content has come from the mineraliser flux present during the reaction. As Sr^{2+} has a much smaller crystal radius than Ba^{2+} (158 pm *cf.* 175 pm) it explains why the compound adopts a cubic structure. Using Goldschmidt's tolerance factors,[19] it can be calculated that at 100% Ba occupancy, t is on the limit at which the co-ordination requirements for a perovskite can be met (t = 0.85-1.06). When barium is exchanged for strontium the tolerance factor falls to *ca.* unity, which is within the range at which a cubic perovskite structure is normally adopted. It must be noted that an average anionic radius is used as the radius of O^{2-} is smaller than N^{3-}.

Table 6.6: Crystallographic data for $Ba_{0.12}Sr_{0.88}WON_2$.

Compound	$Ba_{0.12}Sr_{0.88}WON_2$
Crystal System	Cubic
Space Group	*Pm-3m* (no. 221)
Cell Parameters	a = 4.002 (2) Å
Cell Volume	64.096 (1) $Å^3$
χ^2	0.8827
R_{wp}(PXD)	0.1719
R_{wp}(PND)	0.0260

Final refined occupancies are summarised in *Table 6.7* and the final profile fits achieved for the neutron data and X-ray data sets are shown in *figs. 6.10a* and *6.10b*.

Table 6.7: Refined atomic positions for $Ba_{0.12}Sr_{0.88}WON_2$. E.s.ds are given in parentheses.

Atom	x	y	z	Occupancy	$U_{(iso)}$ [$Å^2$]
Ba	0.5	0.5	0.5	0.123 (16)	0.0104 (3)
Sr	0.5	0.5	0.5	0.877 (16)	0.0104 (3)
W	0	0	0	1.0	0.0149 (3)
O	0.5	0	0	0.33	0.0083 (1)
N	0.5	0	0	0.66	0.0083 (1)

The average cation anion bond lengths are generated from a Rietveld refinement and are found to be W-(O/N) = 2.0010 (1) Å x6 and (Ba/Sr)-(O/N) = 2.8299 (1) Å x12, the W-(O/N)-W bond angle is 180° as all the atoms are on special positions within a cubic space group. Literature values for $SrWO_2N$ are a = 3.97951 (9) Å, W-(O/N) = 1.990 Å and Sr-(O/N) = 2.814 Å.[28] The Rietveld refinement shows that $Ba_{0.12}Sr_{0.88}WON_2$ has a larger unit cell and a longer A-(O/N) bond distance, which is explained by the increase in size of cation, Ba^{2+} *cf.* Sr^{2+}.

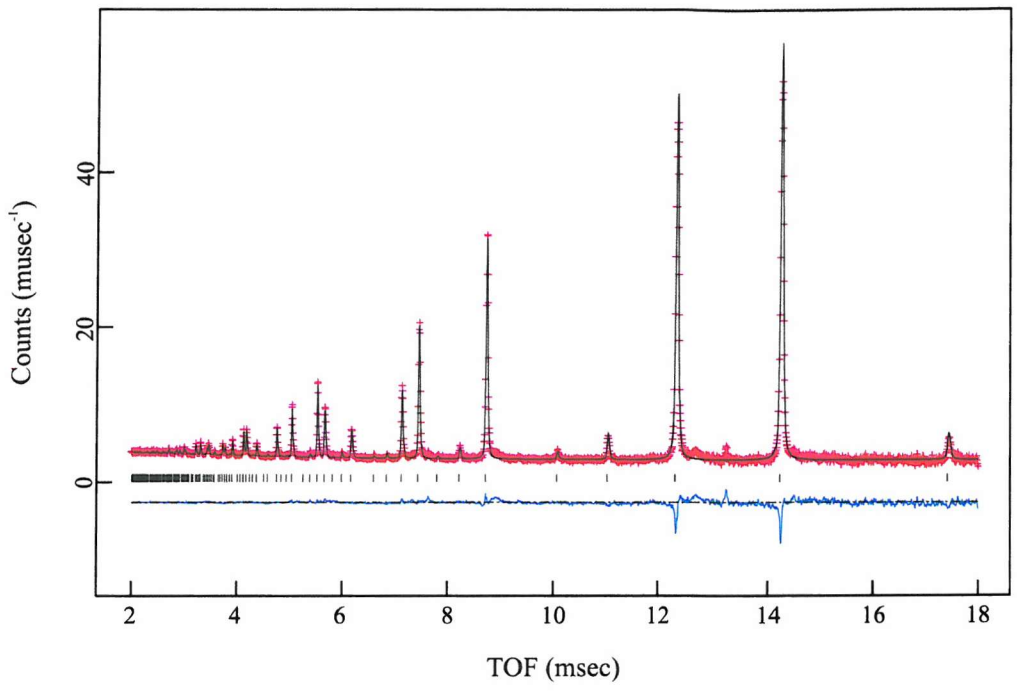

fig. 6.10a: *Rietveld refinement fit for $Ba_{0.12}Sr_{0.88}WON_2$; obtained from PND data collected on the POLARIS diffractometer backscattering bank at the Rutherford Appleton Laboratory (UK). The cross marks are the observed intensities, the upper trace the calculated profile, the black tick marks the calculated peak positions and the lower line the difference.*

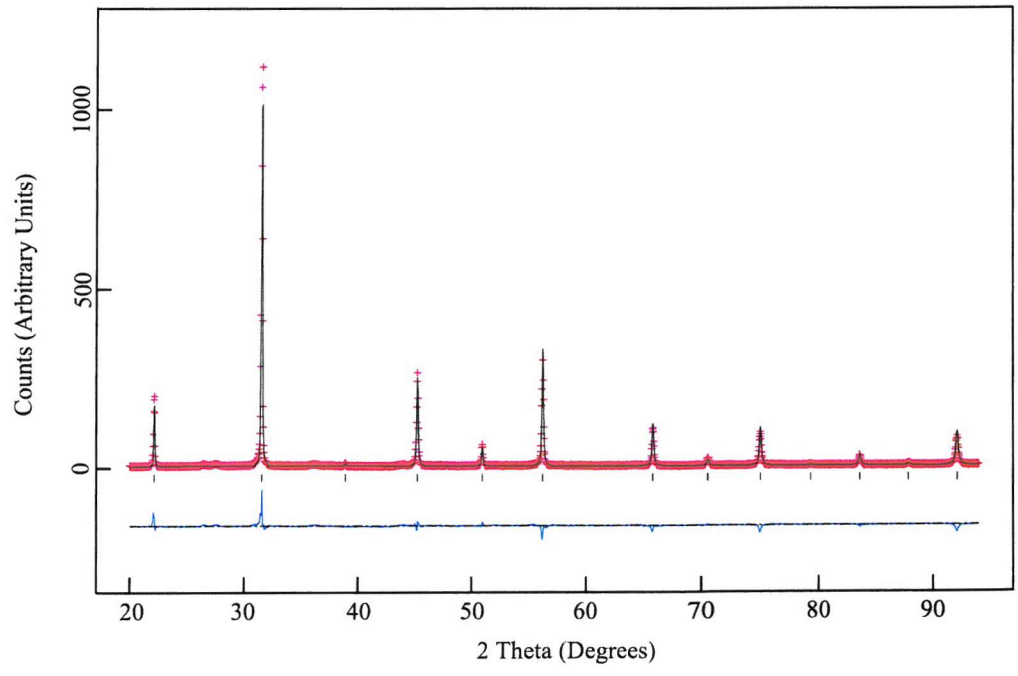

fig. 6.10b: *Rietveld refinement fit for $Ba_{0.12}Sr_{0.88}WON_2$; obtained from PXD data collected on a Siemens D5000. The cross marks are the observed intensities, the upper trace the calculated profile, the black tick marks the calculated peak positions and the lower line the difference.*

A small peak, present only in the PND refinement is attributed to the vanadium can the sample is contained within during data collection.

The anionic occupancies were refined and tended towards a two thirds occupancy for nitrogen. Thus they were fixed in a 1:2 oxygen to nitrogen ratio, such that neutrality is maintained. As there is more nitrogen than oxygen it can be assumed that tungsten remains as W (VI) on account of charge balance. The Sr analogue reported in the literature has a stoichiometry of $SrWO_2N$.[28] A refinement that allowed for bromine (from $SrBr_2$) on the anionic position resulted in negative temperature factors and very low bromine occupancy and thus it is deemed that only oxygen and nitrogen occupy the anionic framework.

The compound is a dark grey powder and thus no colour measurements were obtained as this compound would be of no commercial use as a pigment.

6.4.2 SYNTHESIS AND CHARACTERISATION OF $ATi_{0.7}W_{0.3}(O,N)_3$, A = Ca and Sr

Initially reactants were fired at 650 °C to target the perovskite $CaTi_{0.7}W_{0.3}(O,N)_3$. As electroneutrality is dependent on both Ti and W valency it is possible that anionic vacancies exist within the structure such that the total occupancy is not equal to 3, representing full anionic occupancy. If no vacancies are present the expected oxygen to nitrogen ratio yields a target stoichiometry of $CaTi_{0.7}W_{0.3}O_{2.4}N_{0.6}$. The PXD profiles in *fig. 6.11* highlight the two competing phases that exist after firing at 650 °C; a scheelite type phase which is assumed to be tungsten rich following $CaWO_4$[29] and a titanium rich perovskite type phase following $CaTiO_3$.[23]

After heating the sample at 750 °C, only peaks corresponding to a perovskite phase remain. However, there is noticeable segregation of the phases detectable via the two distinct peaks around $2\theta = 32°$ suggesting an inhomogeneous sample. Potentially a W rich and a Ti rich perovskite phase co-exist within the sample.

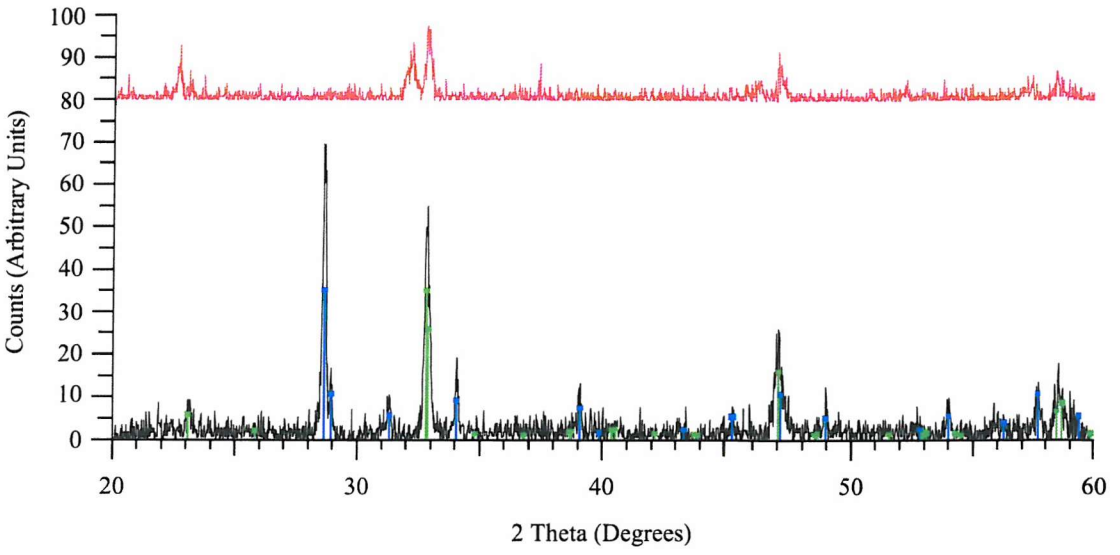

fig. 6.11: *Powder X-ray diffraction data for perovskite target phase $CaTi_{0.7}W_{0.3}(O,N)_3$. (lower) PXD profile after first firing at 650 °C where the blue lines represent a scheelite ($CaWO_4$) type phase and the green lines a perovskite ($CaTiO_3$) type phase. (upper) PXD profile after second firing at 750 °C.*

This separation of perovskite phases is repeated in $SrTi_{0.7}W_{0.3}(O,N)_3$ where the subsequent firing temperature was reduced to 700 °C. In this case the competing phase is $SrWO_4$,[30] which is similar to the mineral scheelite, though the reflections are shifted to lower 2θ values indicating a larger unit cell. This is expected when considering the increase in ionic radii from Ca^{2+} to Sr^{2+}. A titanium oxide impurity is present after both firings, which does not occur for the calcium analogue.

Cross-substitution in $CaWO_4$ has lead to an isostructural oxynitride series $LnWO_3N$, where Ln = Nd, Sm, Gd or Dy. The competition between scheelite and perovskite phases has been reported[31] for the synthesis of the $LnWO_3N$ series, with a perovskite phase being favoured at higher temperatures and longer firing times. Single phase oxynitride scheelites have been isolated through the ammonolysis of binary metal oxides of stoichiometry $Ln_2W_2O_9$[6] and could potentially be a route to mixed titanium tungsten oxynitrides.

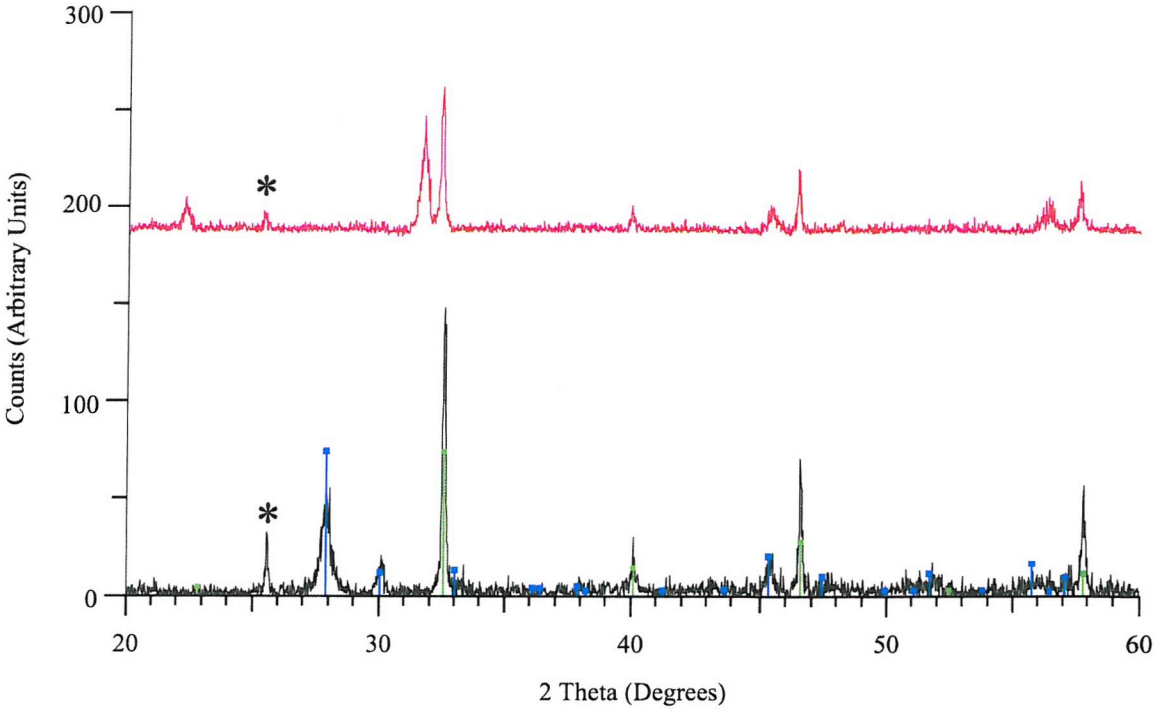

fig. 6.12: *Powder X-ray diffraction data for perovskite target phase $SrTi_{0.7}W_{0.3}(O,N)_3$. (lower) PXD profile after first firing at 650 °C where the blue lines represent a $SrWO_4$ type phase and the green lines a $SrTiO_3$ type phase. The * represents a Ti_3O_5 impurity phase. (upper) PXD profile after second firing at 750 °C.*

These compounds are blue, which may arise from the partial reduction of Ti (IV) to Ti (III) thus realising cation to cation intervalence charge transfers within the structures. However the colour is much brighter than the $SrTi(O,N)_3$ samples mentioned previously. Colour measurements have been calculated and are found in *Table 6.8*.

Table 6.8: Colour measurements of $ATi_{0.7}W_{0.3}(O,N)_3$, A = Ca and Sr

Target Sample	*L**	*a**	*b**
$CaTi_{0.7}W_{0.3}(O,N)_3$	48.18	-2.53	-17.30
$SrTi_{0.7}W_{0.3}(O,N)_3$	57.10	-4.15	-12.20

From this data it can be seen that there is little difference between the two samples, with the calcium sample possessing a higher blueness number indicating a better blue hue. The

lightness value of the strontium sample is higher, suggesting a more intense colour as more photons reach the eye, *i.e.* greater reflection.

6.4.3 SYNTHESIS AND CHARACTERISATION OF VARIOUS TUNGSTEN OXYNITRIDES

Tungsten oxynitride phases were targeted via direct ammonolysis of metal oxides, such as the scheelite phase $LaWO_3N$ and several perovskite phases including $CaTa_{0.7}W_{0.3}O_{1.7}N_{1.3}$ and $Ca_{0.5}La_{0.5}WO_{0.5}N_{2.5}$. The PXD profiles highlight the multiphase nature of the powders produced suggesting unsuccessful syntheses. No single phase oxynitride samples are formed. This is also the case when scheelite, $CaWO_4$, is heated at high temperatures under ammonia.

It is reported that a reduction of W(VI) occurs in combination with larger rare earth elements like lanthanum and neodymium. This occurs when the nitridation is carried out above 900 °C. The problem is accentuated when the nitrogen content is high and is explained by the incompatibility of the La^{3+} and Nd^{3+} cations in the eight-fold co-ordination site resulting from increased vacancy positions.[6]

A perovskite has been synthesised for a target stoichiometry of $SrTa_{0.5}W_{0.5}O_{0.5}N_{2.5}$ with $SrBr_2$ salts used as mineralisers. The PXD profile can be seen in *fig. 6.13*.

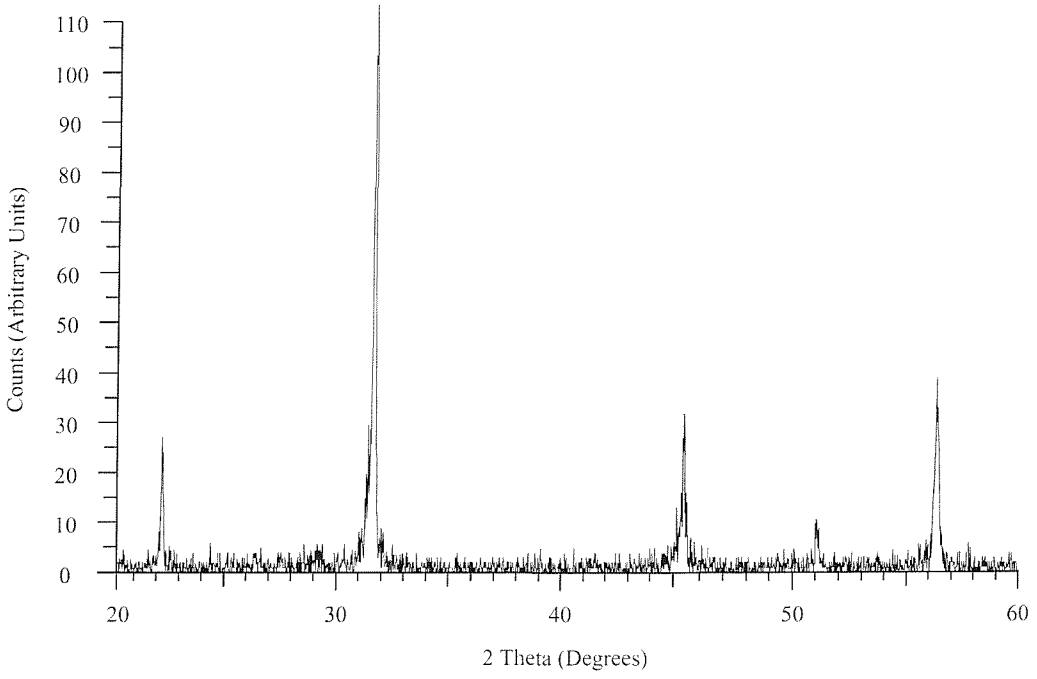

fig. 6.13: Powder X-ray diffraction data for perovskite target phase $SrTa_{0.5}W_{0.5}O_{0.5}N_{2.5}$.

Lattice parameters, $a = b = 5.660(2)$ Å and $c = 7.973$ (2) Å, were obtained using *CELREF*. The tetragonal space group *I4/mcm* is adopted as splitting within the PXD profile reveals distortions from cubic symmetry and also the profile is similar to that of $SrTaO_2N$ published in the literature.[17] A better understanding of the symmetry can be ascertained from Rietveld analysis, however this was not performed due to the similar scattering powers of Ta and W, thus no reliable information can be elucidated about the Ta and W atomic positions and composition. The reduction in cell size from literature values can be justified by the doping of W (VI) onto the B site where the crystal radius of W^{6+} is smaller than Ta^{5+} on account of charge density, (74 pm *cf.* 78 pm).

There is a probable reduction of W (VI) to W (V) and W (VI), thus a mixed valence tungsten compound is produced allowing intervalence transitions. This compound is black with $L^*a^*b^*$ values of 18.50, -0.62, -3.87 respectively. Whilst the values associated with colour are low there are still photons reflected from the sample resulting in a fairly high L^* value. For high grade black pigments, with uses such as optical instruments, this should ideally be as close to 0 as possible. Thus this material is not of use as a pigment.

6.5 ZIRCONIUM

The lanthanum zirconium oxynitride perovskite, $LaZrO_2N$, has been reported in the literature[4] therefore it is reasoned zirconium can be partially exchanged for tantalum in $CaTaO_2N$ and other known tantalum oxynitride perovskites.

Here a zirconium tantalum perovskite of target stoichiometry $CaTa_{0.7}Zr_{0.3}O_{2.3}N_{0.7}$ was synthesised at 850 °C. Further heating at 950 °C sees an improvement in crystallinity but an onset of an impurity phase represented by an asterisk in *fig. 6.14*.

The impurity could be one of several phases as they have similar PXD profiles. The potential candidates are $CaZr_4O_9$, ZrO_2 and $Zr_7O_{11}N_2$ suggesting that the perovskite phase is tantalum rich and may contain no zirconium at all.

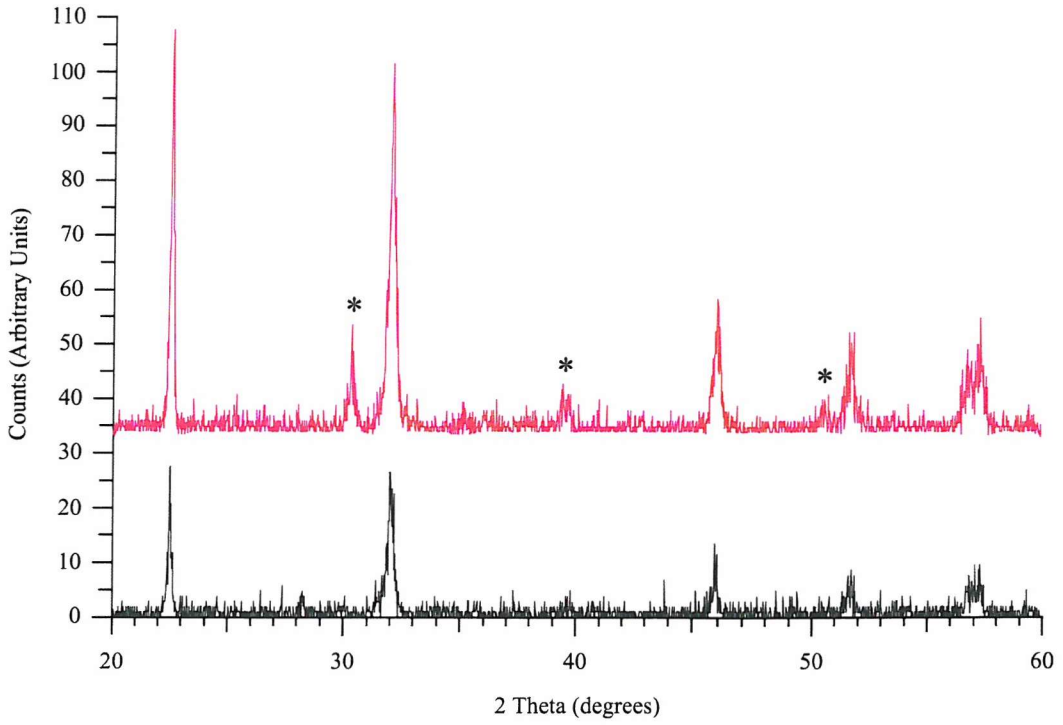

fig. 6.14: *Powder X-ray diffraction data for perovskite target phase $CaTa_{0.7}Zr_{0.3}O_{2.3}N_{0.7}$, where * represents an impurity phase.*

The compound is a yellow powder with $L^*a^*b^*$ values of 61.66, -1.43, 43.48 respectively. Although this has a high yellowness number, it is not as good as the values for $CaTaO_2N$ published in the literature, hence the addition of zirconium, if indeed it is incorporated within the unit cell, has an adverse affect on pigment quality.

6.6 DISCUSSION AND CONCLUSIONS

Several attempts at synthesising oxynitride compounds containing elements such as molybdenum, hafnium and tungsten have resulted in the reduction of the transition metal therefore mixed site compounds were targeted containing either tantalum or titanium as well as other transition metals within the system.

The partial substitution of tantalum for early transition metals in tantalum oxynitride perovskites has been achieved with some degree of success. The nominal solid solution, $SrTa_xTi_{(1-x)}O_{(3-x)}N_x$, where $0 \leq x \leq 1$ has shown a range of colours from yellow, high Ta content, through green to blue for high Ti content. A perovskite phase has been synthesised

for all x, though differences arise in the PXD profiles highlighting changes in crystal symmetry with composition.

Samples of high titanium content are generally pale blue powders resulting from an increase in the band gap towards higher energies, although a deep steel blue colour is obtained for 100% titanium doping. In contrast to other oxynitrides the colour may arise not from nitrogen incorporation but from a direct result of the reduction of Ti^{4+} to Ti^{3+}. Even a slight reduction in TiO_2 to $TiO_{2-\delta}$, turns the white pigment an intense blue black. This is a noticeable effect in the compound $TiO_{1.9993}$ corresponding to just 7 oxygen vacancies in 20,000 anionic sites.[32]

This statement is consolidated by TGA data on the solid solution series. There is a minimal increase in mass for samples of high titanium content. The mass increase is indicative of the replacement of nitrogen by the heavier element oxygen on a one for one basis, thus compounds in the series with high nitrogen content such as $SrTaO_2N$ have the greatest increase in mass.

It has been possible to synthesise an oxynitride perovskite containing strontium and titanium by an alkoxide route. This synthesis results in a green (as opposed to blue *cf.* ceramic route) single phase compound. EDAX results have shown characteristic X-ray emissions from nitrogen and yield a stoichiometry of $Sr_{0.84}Ti_{0.68}O_{2.35}N_{0.65}$. As errors are quite large for EDAX, it is likely that the cationic vacancies are not as great as implied by the elemental percentage analysis provided. Further studies on compound colour *vs.* synthetic route are documented in *Chapter 7*, with the synthesis of $SrTaO_2N$ via three different approaches.

The synthesis of tungsten oxynitrides has been more difficult, with several multiphase samples being produced. A reduction in the synthesis temperature has facilitated the production of a single phase perovskite, $Ba_{0.12}Sr_{0.88}WON_2$ though it has proved easier to synthesise mixed B site perovkites such as the titanium and tantalum containing compounds reported here.

In analogy with the pyrochlore competition reported in previous chapters there has been a problem with competing phases in tungsten syntheses here as well. This time however a

scheelite phase is in competition with the perovskite phase $ATi_{0.3}W_{0.3}(O,N)_3$, where A = Ca and Sr.

Several oxynitrides containing transition metals such as molybdenum, chromium and tungsten[1-3,6-10] have been reported in the literature. Thus it was hoped that compounds with intense hues may be synthesised containing early transition metals. Unfortunately the compounds synthesised in this chapter, primarily the blue and green compounds of the titanium and tungsten substituted perovskites, do not provide the same depth of colour as pigments already on the market today.

6.7 REFERENCES

[1] Li Y., Gao L.; *Mater. Lett.*, **57**, 1062 (2003)

[2] Veith G. M., Greenblatt M., Croft M., Goodenough J. B.; *Mat. Res. Bull.*, **36**, 1521 (2001)

[3] Liu G., Zhao X., Eick H. A.; *J. Alloy. Compd.*, **187**, 145 (1992)

[4] Clarke S. J., Guinot B. P., Michie C. W., Calmont M. J. C., Rosseinsky M. J.; *Chem. Mater.*, **14**, 288 (2002)

[5] Clarke S. J., Michie C. W., Rosseinsky M. J.; *Chem. Mater.*, **12**, 863 (2000)

[6] Antoine P., Marchand R., Laurent Y.; *Rev. Int. Hautes Tempér. Réfract. Fr.*, **24**, 43 (1987)

[7] Weller M. T., Skinner S. J.; *Int. J. Inorg. Mater.*, **2**, 463 (2000)

[8] Diot N., Larcher O., Marchand R., Kempf J. Y., Macaudière P.; *J. Alloy. Compd.*, **323-324**, 45 (2001)

[9] Marchand R., Antoine P., Laurent Y.; *J. Solid State Chem.*, **107**, 34 (1993)

[10] Elder S. H., DiSalvo F. J., Parise J. B., Hriljac J. A., Richardson Jr. J. W.; *J. Solid State Chem.*, **108**, 73 (1994)

[11] Clarke S. J., Chalker P. R., Holman J., Michie C. W., Puyet M., Rosseinsky M. J.; *J. Am. Chem. Soc.*, **124**, 3337 (2002)

[12] Günther E., Jansen M.; *Mat. Res. Bull.*, **36**, 1399 (2001)

[13] Grins J., Käll P., Svensson G.; *J. Mater. Chem.*, **4(8)**, 1293 (1994)

[14] Clarke S. J., Michie C. W., Rosseinsky M. J.; *J. Solid State Chem.*, **146**, 399 (1999)

[15] Marchand R., Pors F., Laurent Y.; *Rev. Int. Hautes Tempér. Réfract. Fr.*, **23**, 11 (1986)

[16] Jansen M., Letschert H.; *Nature*, **404**, 980 (2000)

[17] Günther E., Hagenmayer R., Jansen M.; *Z. Anorg. Allg. Chem.*, **626**, 1519 (2000)

[18] Brous J., Fankuchen I., Banks E.; *Acta Crystallogr.*, **6**, 67 (1953)

[19] Goldschmidt V. M.; *Skr. Nor. Vidensk. Akad. Kl 1: Mat. Naturvidensh. Kl* (1926)

[20] Lumey M., Dronskowski R.; *Z. Anorg. Allg. Chem.*, **629**, 2173 (2003)

[21] Gong W. H., Yun H., Ning Y. B., Greedan J. E., Datars W. R., Stager C. V.; *J. Solid State Chem.*, **90**, 320 (1991)

[22] Grins J., Svensson G.; *Mat. Res. Bull.*, **29(7)**, 801 (1994)

[23] Sasaki S., Prewitt C. T., Bass J. D.; *Acta Crystallogr. C*, **43**, 1668 (1987)

[24] Laugier J., Bochu B.; *CELREF*, Laboratoire des Matériaux et du Génie Physique, Ecole Nationale Supérieure de Physique de Grenoble INPG (France) (2000)

[25] Larson A. C., Von Dreele R. B.; *General Structure Analysis System*, MS-H805, Los Alamos National Laboratory, (USA) N M 87545 (1990)

[26] Rietveld H. M.; *Acta Crystallogr.*, **22**, 151 (1967)

[27] Rietveld H. M.; *J. Appl. Crystallogr.*, **2**, 65 (1969)

[28] Fawcett I. D., Ramanujachary K. V., Greenblatt M.; *Mat. Res. Bull.*, **32(11)**, 1565 (1997)

[29] Dickinson R. G.; *J. Am. Chem. Soc.*, **42**, 85 (1920)

[30] Guermen E., Daniels E., King J. S.; *J. Chem. Phys.*, **55**, 1093 (1971)

[31] Tessier F., Marchand R.; *J. Solid State Chem.*, **171**, 143 (2003)

[32] Tilley R.; *Colour and the Optical Properties of Materials*, Wiley (UK), First Edition (2000)

CHAPTER SEVEN

DEPOSITION OF OXYNITRIDE AND NITRIDE PHASES ON MICA

7 OXYNITRIDE COATED MICA PIGMENTS

7.1 INTRODUCTION

Various pigments commercially available today exploit angle-dependent optical effects.[1] These effects can have functional purposes when used in security printing and optical filters and decorative applications such as car paints and cosmetics. Whereas traditional pigments interact with light by either absorption or diffuse scattering, lustre pigments produce colour effects by specular reflection. There are several ways in which this can occur, examples include metal platelets acting as tiny mirrors, natural interference effects from pearls and shells and coated mica pigments.

This chapter ties in the work on new oxynitride pigments with work on novel lustre pigments. In this study, attempts were made to deposit oxynitride phases and Ta_3N_5 onto mica. At present there is a need to provide a broader range of lustre pigment colours to the market, focusing on red pigments in particular. Due to tougher legislation it is desirable that these pigments comprise non-toxic elements, unlike their predecessors which have contained metals such as cadmium, lead and mercury.[2] For example, an EU directive[3] prohibits the use of cadmium as a pigment, dye or stabiliser in specific polymers and its use as plating on metallic surfaces,[3] whilst a further directive restricts cadmium pigments in packaging.[4]

Reaction pathways to oxynitrides within this work so far concentrate on a traditional solid state approach. This is not a suitable method with which to directly coat mica for reasons discussed in this chapter. Therefore, several solution chemistry routes have been targeted to see which, if any, result in the successful synthesis of an oxynitride lustre pigment. The precursors were deposited onto mica using various techniques and the resultant powders were ammonolysised to synthesise oxynitrides. The products were analysed primarily by scanning electron microscopy imaging and by UV-Vis. spectroscopy, from which colour measurements were ascertained. Powder X-ray diffraction was also carried out to examine phases present within the lustre pigment powders.

7.2 DEPOSITION TECHNIQUES

7.2.1 LIMITATIONS OF CERAMIC ROUTE

High temperature ceramic reactions yield thermodynamically stable products but such reaction temperatures are unsuitable to form a pigment layer on mica. Mica decomposes at 850 °C and hence the ammonolysis of a deposited precursor must occur at temperatures lower than this. Unfortunately, the ceramic route discussed in earlier chapters is of little use here; the favourable temperature for a ceramic reaction to proceed with any successful syntheses of oxynitrides is ≥ 850 °C.[5-8] In order to lower the reaction temperature several wet chemistry techniques are studied along with more traditional ceramic and sealed ampoule syntheses. Wet chemistry techniques are advantageous as they form more reactive precursors that can then go on to form oxynitrides at lower temperatures during ammonolysis. These are also convenient procedures to deposit a precursor onto the mica surface.

Another concern is the use of mineralisers. Halide salts can attack mica and thus its pearlescent nature but it is the mineralisers that enhance the colour of the compounds. The mechanisms by which mineralisers work is poorly understood and there is much conjecture about their benefits but their presence as catalysts aids the formation of an extremely stable crystal structure and concurrently reduces the temperature of the reaction. Firing at greatly elevated temperatures can be one way to avoid the use of mineralisers but it is not beneficial here, as at such temperatures mica would decompose.

7.2.2 OVERVIEW OF WET CHEMISTRY METHODS

A wet chemistry approach towards homogeneous ceramic materials can encompass many techniques, *viz.* sol-gel and co-precipitation methods. Such approaches produce more reactive precursors that can be fired at lower temperatures in order to synthesise the target materials.

In summary, the sol-gel process involves the formation of a *sol*, the dissolution of metal salts or alkoxides forming a suspension in a suitable solvent. The sol is then heated slowly to form an amorphous gel and then further heating results in the evaporation of the solvent used.[9] This amorphous precursor is then annealed to yield a crystalline powder.

Like the sol-gel method, co-precipitation techniques require the complete solvation of metal ions in an appropriate solvent. This results in intimate mixing of the reagents on the atomic

level before firing (in contrast to this, traditional solid state routes rely on diffusion to obtain component mixing). The heterogeneous mix of metal ions are precipitated out of solution with the addition of a solvent in which they are insoluble, or potentially via an acid-base reaction. The solvent can then either be evaporated off with the assistance of heat or filtered and the precipitate retained. One drawback to this approach is that it may not be possible to fully precipitate the components out of solution, thus altering the stoichiometry.

7.2.3 SOLUTION METHOD (I)

This method[10] was adopted to synthesise the following phases on mica: Ta_3N_5, $CaTaO_2N$, $SrTaO_2N$ and $LaTaON_2$. Stoichiometric amounts of metal chlorides {$TaCl_5$ (Aldrich, 99.9%,)} and nitrates {$Ca(NO_3)_2{\cdot}4H_2O$ (Aldrich, 99%), $Sr(NO_3)_2$ (Aldrich, 99.995%), $La(NO_3){\cdot}6H_2O$ (Aldrich, 99.99%)} were added to HNO_3 (50 cm^3, 2 M) and ethanol (100 cm^3, 99.86% v/v). Mica ($KAl_3Si_3O_{11}$; dehydroxylated muscovite, supplied by Merck) was added after dissolution of metal salts in a 1:1 ratio by mass. Ammonia (*ca.* 20 cm^3, S.G = 0.880) was added slowly until a precipitate formed (*ca.* pH 11) and the resulting liquor was heated till dry and then decomposed at 350 °C overnight. Finally, the powder was annealed under flowing ammonia at 800 °C for *ca.* 20 hours.

7.2.4 SOLUTION METHOD (II)[11]

This method was implemented to deposit the following on mica: Ta_3N_5 and a calcium titanium oxynitride phase. Stoichiometric amounts of metal salts, *i*) $TaCl_5$ (Aldrich, 99.9%) or *ii*) $TiCl_4$ (Aldrich, 99.9%) and $CaCl_2$ (BDH, fused granular), were dissolved in water to a concentration of *ca.* 2 mol dm^{-3}. Mica ($KAl_3Si_3O_{11}$; dehydroxylated muscovite, supplied by Merck) in a 1:1 ratio mica : reagents by mass was added to 20 cm^3 water with constant stirring. The resulting slurry was heated to 70 °C and the pH adjusted to 2 with the addition of dilute HCl (50 cm^3 maximum volume used, 2 M). The metal chloride solution was added to the slurry. Dilute NaOH (50 cm^3 maximum volume used, 2 M) was added slowly to precipitate the metal ions onto the mica flakes. The slurry was then filtered, the resulting solid was washed with distilled water to remove any by-products and dried for 16 hours at *ca.* 110 °C. The resultant precursor was fired under flowing ammonia for *ca.* 20 hours at 850 °C.

7.2.5 MISCELLANEOUS DEPOSITION TECHNIQUES ATTEMPTED

Various other techniques were employed to try and deposit pigment onto mica. Firstly an intercalation of $TaCl_5$ with mica was achieved by firing a 1:1 ratio of $TaCl_5$ (Aldrich, 99.9%) and mica ($KAl_3Si_3O_{11}$; dehydroxylated muscovite, supplied by Merck) in a sealed ampoule at 250 °C. This was above the melting point of $TaCl_5$ (216 °C). The resulting powder was then fired under ammonia at 750 °C for 20 hours to form Ta_3N_5, a bright red pigment.

Also, Ta_2O_5 (Aldrich, 99%) was ground with mica (1:1 wt. ratio) and fired for *ca.* 60 hours under fast flowing ammonia at 800 °C.

Finally, the synthesis of $SrTaO_2N$ with mica was carried out. Stoichiometric amounts of Ta_2O_5 (Aldrich, 99%) and $SrCO_3$ (Aldrich, 99.9%) were fired with mica and halide salt mineralisers (NaCl, KCl, $CaCl_2$) in a 1:1:1 ratio under flowing ammonia at 800 °C, the halide salts were then leached from the mixture with excess deionised water. This latter technique was identical to the traditional ceramic route[5,6] and was carried out in order to see the effects mineralisers played on the lustrous properties of mica.

7.3 Ta_3N_5 ON MICA

7.3.1 DIFFERENT APPROACHES EMPLOYED IN DEPOSITION OF Ta_3N_5 ON MICA

Ta_3N_5 and TaON are known to be bright red and yellow powders respectively,[12,13] hence they were selected as candidate phases to deposit onto mica. They were chosen not only for their suitability as pigments due to their stability and non-toxic components but also because they are deemed good starting points to investigate deposition and ammonolysis techniques as only one metal ion is involved. This removed the problem of forming a homogeneous compound from a heterogeneous mix of metal ions. Ta_3N_5 was chosen as it is much easier to form. The ammonolysis stage often goes to completion, thus making the successful synthesis of a single phase TaON sample difficult. The difficulty with forming the oxynitride phase results from problems obtaining a steady and optimum NH_3 flow rate. A careful balance of furnace temperature and duration of firing is also required.

For ease of reference, the codes in *Table 7.1* are adopted throughout *Section 7.3*. They correspond to the different synthetic methods adopted in preparing the interference pigment Ta_3N_5 on mica.

Table 7.1: Synthetic methods for targeting Ta_3N_5 on mica.

Sample	Approach Adopted
A	Ceramic Method
B	Solution Method (I)
C	Solution Method (II)
D	Sealed Ampoule

7.3.2 POWDER X-RAY DIFFRACTION

Short scan powder X-ray diffraction (PXD) data sets were collected on a Siemens D5000 using Cu $K_{\alpha 1}$ radiation (λ=1.5406 Å). The data sets show both mica and Ta_3N_5 pigment phases, with the mica dominating the pattern as it is far more crystalline than the Ta_3N_5 phase.

From *fig. 7.1* it can be seen that the 0 0 6 reflection at *ca.* $2\theta = 26.5°$ is due to the crystal structure of mica ($KAl_3Si_3O_{11}$)[14] as it is not present in the PXD pattern of Ta_3N_5, reported in the literature.[15] Likewise the peak at *ca.* $2\theta = 24.5°$ can be attributed to the 1 1 0 reflection of Ta_3N_5 and is not present in the PXD pattern of mica. The 1 1 0 reflection of Ta_3N_5 is present in all deposition products and several other peaks also provide a match for the pigment. This suggests Ta_3N_5 has formed in every case. Although Ta_3N_5 has formed through these wet chemistry techniques, it can be seen that the crystallinity is poor in comparison to the pattern obtained from the sample synthesised via a ceramic route (displayed in red).

As the mica is more crystalline than Ta_3N_5, it dominates the PXD data sets of the coated mica powders. Several pigment peaks are masked by these mica peaks and are in fact the combination of reflections from both pigment and mica. On considering the mole ratios there is less pigment than mica within the sample, this too affects the number of counts detected with the mica peaks being more intense as there are more moles of mica *cf.* Ta_3N_5. However as tantalum is a heavy element it has a greater X-ray scattering power, thus the pigment peaks

will be more intense than mica peaks when present in equimolar quantities. Furthermore, as mica is a layered structure it can have preferred orientation effects. Preferred orientation is the tendency for crystallites, due to their morphology, to be ordered in a particular way or set of ways. Systematic distortions of the reflection intensities are an outcome of preferred orientation.

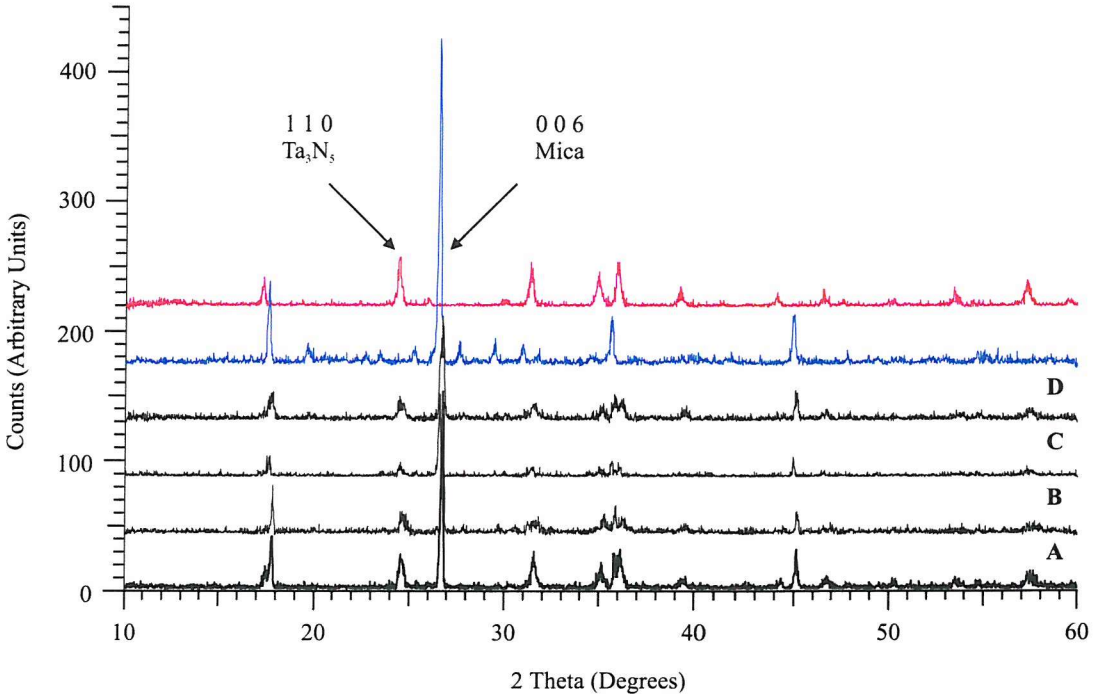

fig. 7.1: *PXD patterns of Ta_3N_5 on mica scaled to the 0 2 0 reflection of Ta_3N_5 for different deposition techniques where (A) is the ceramic route, (B) solution method* (I), *(C) solution method* (II) *and (D) the intercalation route. The blue PXD pattern is for mica ($KAl_3Si_3O_{11}$) and the red pattern, Ta_3N_5.*

Profile analysis[16,17] of Ta_3N_5 (synthesised via the ceramic route) was perfomed and the lattice parameters tabulated. The starting model was obtained from published literature values for Ta_3N_5.[15] They were compared to values obtained from *CELREF*[18] for the Ta_3N_5 coated mica powders to highlight any differences present. Results can be found in *Table 7.2* and *7.3*. The cell volumes have been calculated from the lattice parameters and are shown in *Table 7.3*. An OCD plot is located in *Appendix IV*.

The lattice parameters are similar and thus considering errors there is no marked difference between the *chimie douce* approaches and the more traditional solid state approach. Overall

from this data it could be said that there is no correlation between the size of the unit cell and the method employed for synthesis.

Table 7.2: Crystallographic data for Ta_3N_5.

Compound	Ta_3N_5
Crystal System	Orthorhombic
Space Group	*Cmcm* (no. 63)
Cell Parameters	a = 3.889 (3) Å
	b = 10.223 (7) Å
	c = 10.271 (8) Å
Cell Volume	408.41 (8) Å^3
χ^2	2.690
R_{wp}	0.1551

Table 7.3: Comparison of lattice parameters.

Sample	a [Å]	b [Å]	c [Å]	V [Å^3]
A	3.887 (3)	10.233 (1)	10.277 (1)	408.8 (4)
B	3.913 (1)	10.198 (2)	10.174 (3)	406.0 (3)
C	3.895 (4)	10.283 (1)	10.198 (2)	408.5 (5)
D	3.886 (5)	10.238 (2)	10.217 (2)	406.5 (7)

7.3.3 SCANNING ELECTRON MICROSCOPY IMAGING

Scanning electron microscopy (SEM) is a surface technique and can be used to identify different morphologies within a sample. In this work SEM is employed to identify how well the pigment coatings adhere to the surface of mica. SEM images for Ta_3N_5, synthesised in a manner of ways are shown in *figs. 7.2 - 7.5*. The magnification, spot size and accelerating voltages vary in each case, as they have been optimised to acquire the best possible image for each sample.

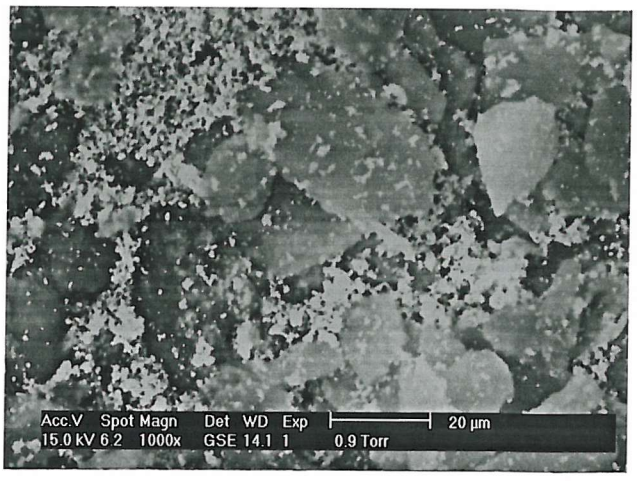

fig. 7.2: *SEM image sample A, Ta_3N_5 with mica synthesised via a ceramic route.*

fig. 7.3: *SEM image sample B, Ta_3N_5 with mica synthesised via solution method (I).*

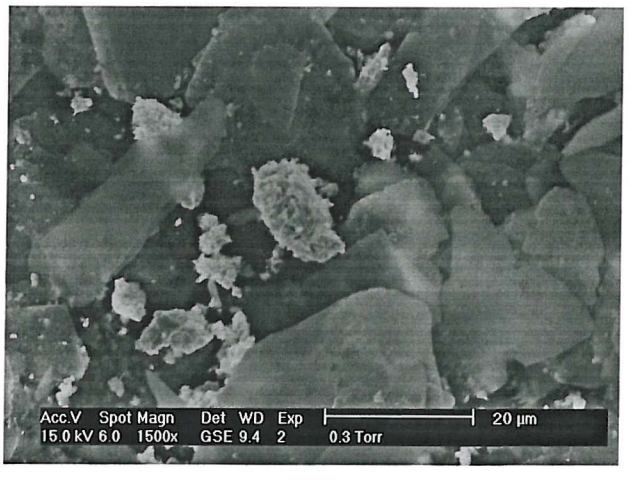

fig. 7.4: *SEM image sample C, Ta_3N_5 with mica synthesised via solution method (II).*

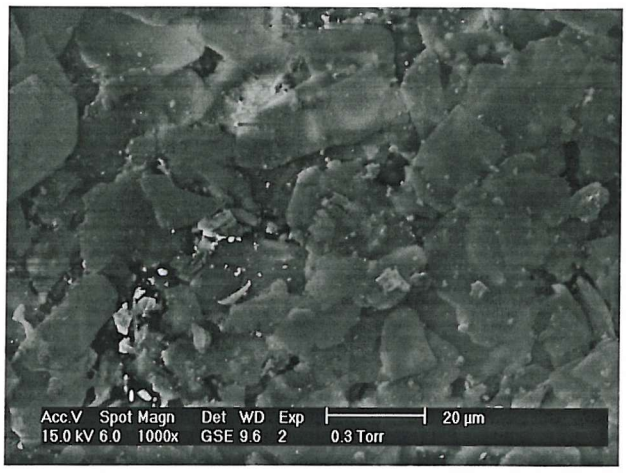

fig. 7.5: SEM image sample D, Ta_3N_5 with mica synthesised via an intercalation route.

In each case both the mica (dehydrated muscovite) and Ta_3N_5 can readily be distinguished. The mica laminae are identified as the big flakes whereas the pigment particles are much smaller. The pigments take on a lighter shade due to the unevenness of the coating on the carbon disc. When the surface is not flat, particles sticking out of the plane will pick up more signal and thus appear lighter. As they can be identified as two separate phases, uncoated mica and pigment, no route is successful in uniformly coating the mica flakes with tantalum nitride.

Sample (A), the ceramic route, is not expected to be successful for it is unlikely that Ta_2O_5 would adsorb to the surface of the mica during ammonolysis to form Ta_3N_5 coated mica. For samples (B) and (C), synthesised using wet chemistry techniques problems arise due to the insolubility of most tantalum salts. The $TaCl_5$ cannot remain in solution long enough before taking up water from the atmosphere and precipitating out as the hydrated oxide of Ta_2O_5. It may be possible to carry out this stage under an inert atmosphere, such as nitrogen, with dry reagents to avoid the precipitation of tantalum salts.

Finally, the intercalation route, sample (D), seems a possible alternative. An atmosphere of $TaCl_5$ is created in a sealed tube by heating above the volatility point of $TaCl_5$. Although it is difficult to differentiate the Ta_3N_5 phase from the mica laminae due to the brightness of the image, they do exist as two separate phases, pigment and mica.

7.3.4 *UV-VISIBLE SPECTROSCOPY*

UV-Visible spectroscopy was carried out and from this data colour measurements were obtained to ascertain differences between pigment and pigment with mica. This is mainly to observe dilution effects on the pigment, as when coated on mica it is only a percentage of the bulk sample. In these examples, the pigment and mica ratio is 1:1. However, the amount of pigment is usually minimised for industrial purposes as this is attributed to the bulk of the cost compared to the relatively inexpensive substrate. The amount of pigment present will affect the overall colour measurements, as mica dilutes the colour concentration, thus a careful balance of mica and pigment is eventually required to yield an optimised thickness of coating. Commercial oxide coated mica particles have a pigment coating typically in the region of 50 - 100 nm.

The reflectance spectrum of mica is characteristic of a transparent material, whereby light is reflected across the whole of the visible region and little is absorbed. Hence, the overall reflectances of the coated mica pigments are augmented as they all contain a high proportion of mica.

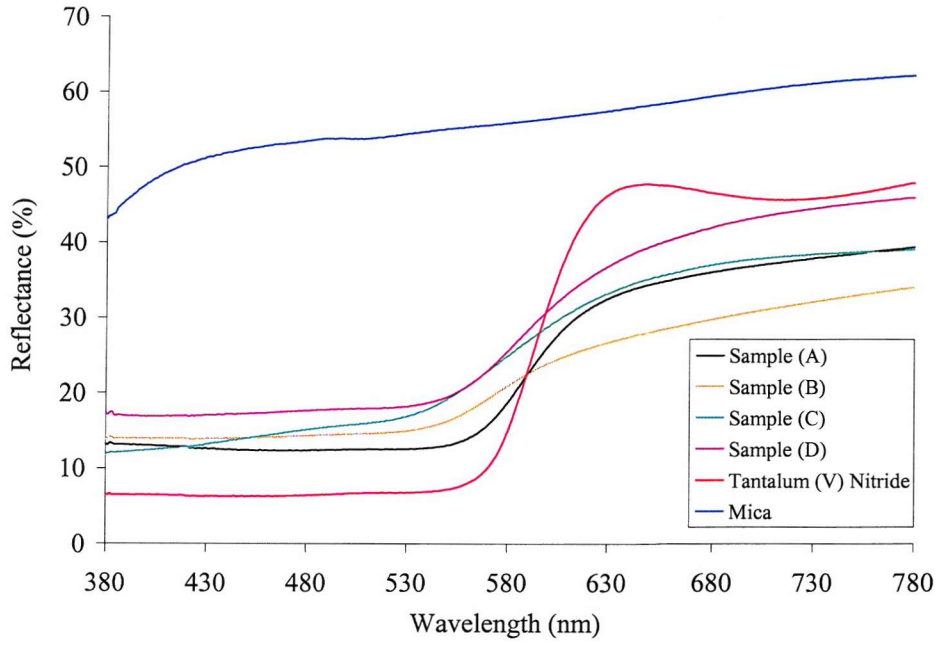

fig. 7.6: *UV-Visible spectroscopy data for samples A – D and also for Ta_3N_5 and mica alone.*

The absorption edges in each spectrum all occur over the 530–630 nm region. However the absorption edges of the coated mica pigments are much shallower than the steep gradient displayed in the Ta_3N_5 spectrum. These absorption edges are similar to the edges of the tantalum oxynitride phases found in the literature.[5]

The spectra of samples A - D all follow the characteristic pattern of the reflectance spectrum of Ta_3N_5. The coated mica pigments show more reflectance at the blue wavelengths of the spectrum *cf.* Ta_3N_5. This is due to the presence of mica raising the overall light reflectance from the samples across the entire visible region. The reflectance of red wavelengths of light is greater for Ta_3N_5 than for any of the coated mica pigment samples. This is expected as the samples do not possess the same intensity of colour as the Ta_3N_5 pigment alone. They are not a vibrant red but a rust colour. $L^*a^*b^*$ measurements can explain the differences in colour between these powders and are detailed in the next section.

7.3.5 COLOUR MEASUREMENTS

Colour measurements were acquired from the spectroscopic data and were contrasted to the values obtained for Ta_3N_5 and for mica. The measurements are collated in *Table 7.4*.

The $L^*a^*b^*$ values are in some respect similar for both the coated mica pigments and Ta_3N_5. The lightness values are on average mid-way between white and black. However the values which represent the colour of a compound are much lower for the mica coated pigments. The important value to contrast is + a^*, or the redness value. For all coated mica pigments, it is around half the value that is obtained for pigment alone. In terms of colour, in particular redness value, ceramic reaction pathways yield the optimum shade of pigment. As discussed earlier this is not a good method for pigment adsorption onto mica. There is not much difference in $L^*a^*b^*$ values for all the other compounds, thus, in terms of colour there is not one synthetic route that is favoured over another.

Table 7.4: Colour measurements for Ta_3N_5 and Ta_3N_5 coated mica.

Sample	*L**	*a**	*b**
A	48.22	19.80	10.72
B	52.12	14.28	12.19
C	53.17	13.27	15.44
D	54.75	15.18	10.63
Ta_3N_5 (Ta_2O_5)	44.64	38.84	25.02
Ta_3N_5 ($TaCl_5$)	38.15	34.33	22.18
Mica	79.11	0.87	2.87

One reason for the differences in colour between a solution preparation and a ceramic route is the size of the crystallites that are synthesised. In general, the particle size is smaller using a wet chemistry route than with the traditional solid state route. The bigger the particle size the more intense the colour, hence the solution route powders are much duller than those synthesised using the ceramic route.

Finally, the values for mica are as expected. There is little contribution to the colour represented by a^* and b^* values close to zero. The L^* value is high as anticipated for mica, which is a golden beige powder that is almost transparent when distributed in a thin layer.

7.4 ALKALINE EARTH AND RARE EARTH TANTALUM OXYNITRIDES ON MICA

7.4.1 EXPERIMENTAL METHOD

Solution method (I) was employed throughout this section to synthesise the known oxynitride phases $CaTaO_2N$,[6,19] $SrTaO_2N$[6,19] and $LaTaON_2$.[6,20] Also $SrTaO_2N$ was synthesised under ammonia using the traditional solid state route in the presence of mica and mineralisers. The objective of this was to examine the effects of mineralisers and ammonia upon mica, aided by separate heating cycles of just mica and mica with halide salts under ammonia.

7.4.2 POWDER X-RAY DIFFRACTION

PXD patterns were collected on a Siemens D5000 (2θ = 10-60°, step size 0.02°) and the data compared to the patterns collected for mica alone and also for the individual pigment phases.

The data sets show both mica and oxynitride pigment phases and as with the tantalum (V) nitride data sets, mica dominates the pattern, as it is far more crystalline, *see fig 7.7.*

The pigment is present in all three compounds but is hard to identify due to the low intensity of peaks. The broadening of peaks at 22-23° and 31-33° represent overlapping of both the perovskite and mica peaks whereas the sharp more intense peaks indicate only mica. This broadening of the peaks is most clearly seen in the $CaTaO_2N$ and $LaTaON_2$ profiles, the $SrTaO_2N$ is more amorphous. The PXD profile shows the presence of Ta_3N_5 as a competing phase. This is foreseen as the addition of mica in a 1:1 ratio decreases the likelihood of contact between crystal faces of the two reactants, thus increasing the migration pathways of the cations during synthesis.

Finally the formation of $SrTaO_2N$ with mineralisers and mica resulted in a powder that is not very crystalline.

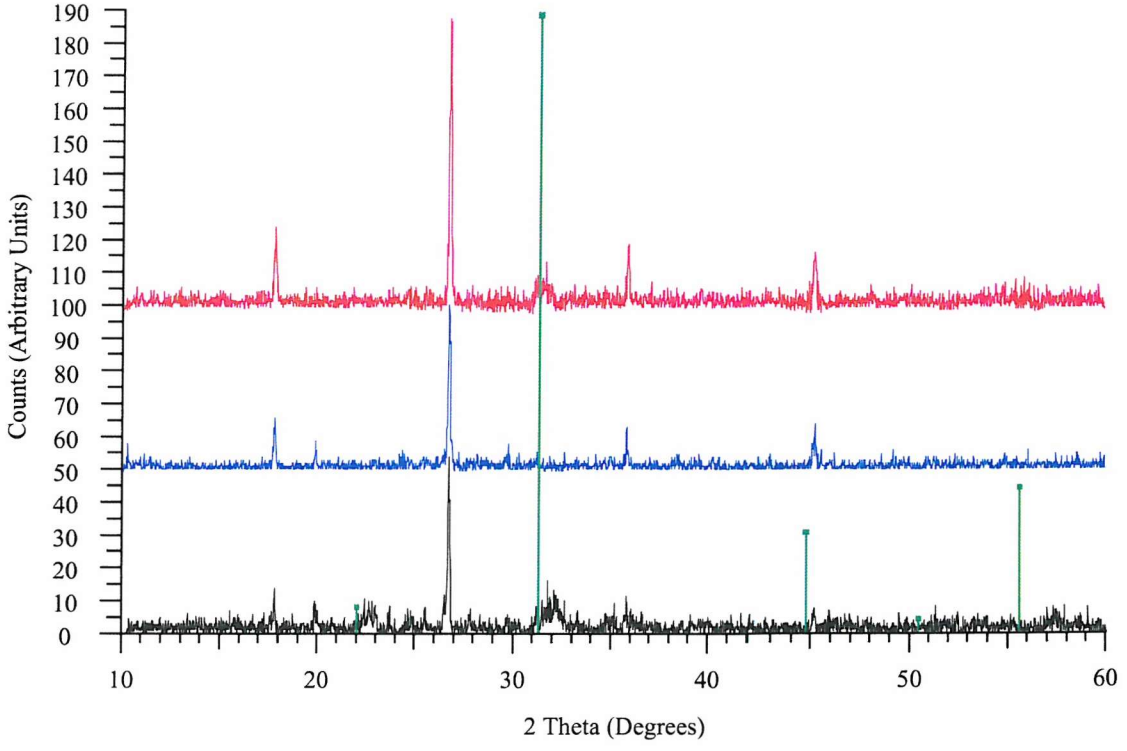

fig. 7.7: *PXD patterns of various oxynitride phases on mica. $CaTaO_2N$ is shown in black, $SrTaO_2N$ in blue and $LaTaON_2$ in red. The green lines indicate average positions of peaks attributed to the oxynitride perovskites all other peaks are attributed to mica.*

7.4.3 SCANNING ELECTRON MICROSCOPY IMAGING

SEM images were obtained for the target oxynitride phases $LaTaON_2$, $SrTaO_2N$ and $CaTaO_2N$ on mica and are shown in *figs. 7.8-7.12*.

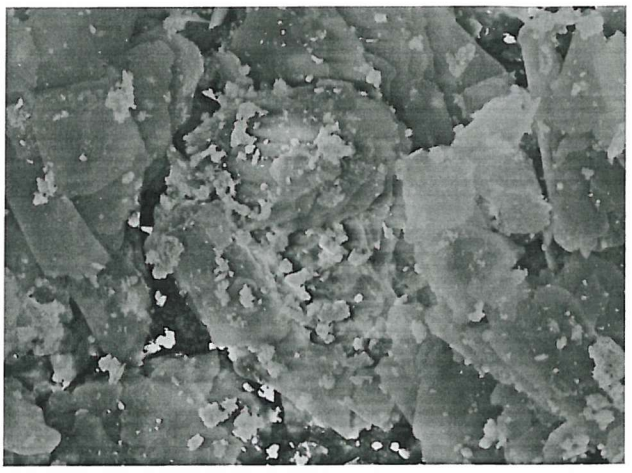

fig. 7.8 a: SEM image of an $LaTaON_2$ sample synthesised via solution method (I).

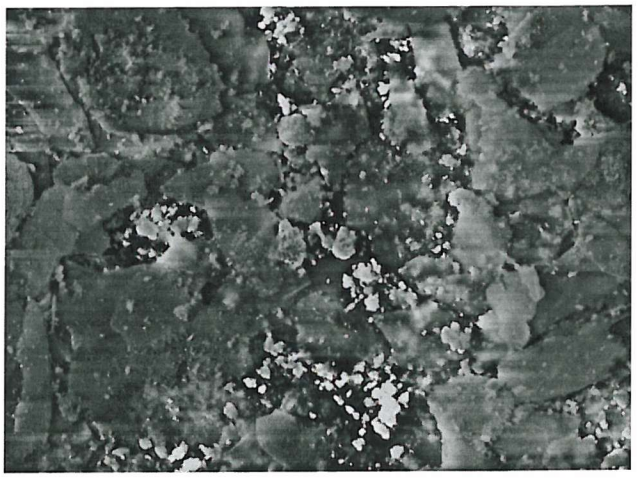

fig. 7.8 b: SEM image of an $LaTaON_2$ sample synthesised via solution method (I).

The two images in *fig. 7.8* were acquired from samples of $LaTaO_2N$, the sample shown in the lower image was synthesised under a fast flow of NH_3. This alters the colour slightly as it allows a greater uptake of nitrogen, due in part to the fast removal of waste gases such as CO_2 from the carbonate and H_2O (produced during the reaction). These gases are replaced with the more reactive ammonia.

Both these images show two separate phases, platelets of mica and small particles of pigment which appear to agglomerate in lumps and are scattered throughout the sample. The pigment does not form a thin film on the surface of the mica as required for a lustre pigment.

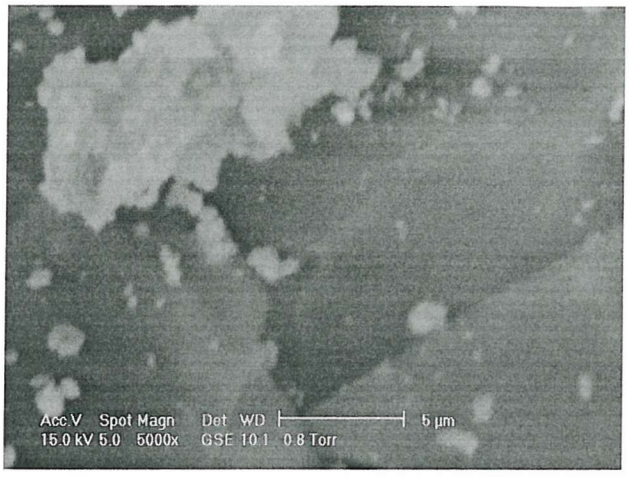

fig. 7.9: *SEM image of a $SrTaO_2N$ sample synthesised via solution method (I).*

The image in *fig. 7.9* is very grainy. It proved difficult to acquire a sharp focussed image of this sample of $SrTaO_2N$ but careful examination of the image reveals the characteristic mica platelets and agglomerated pigment particles. Grinding the sample can reduce the size of pigment particle but in mica deposition, grinding is kept to a minimum to avoid destroying the laminar crystal structure of mica. It is possible to acquire a uniform particle size distribution by sieving the products through a fine mesh.

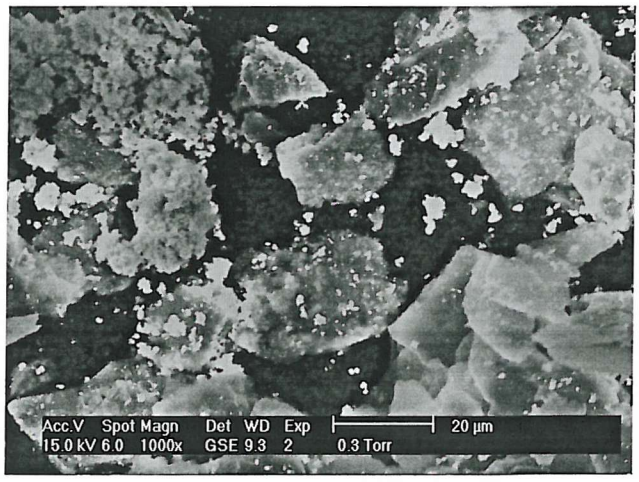

fig. 7.10: *SEM image of a $SrTaO_2N$ sample synthesised via ceramic route (halide salts).*

In *fig. 7.10* is an image of $SrTaO_2N$ synthesised using a solid state route. Again, the coating process is unsuccessful. On visual inspection of the sample there appears to be no nacreous effect from the mica showing the adverse effect halide salts have on mica. One possible explanation is that there may be ion exchange occurring between the aluminosilicate layers, where the potassium ions are replaced with smaller calcium ions. This in turn can cause the layers to break up thus removing the regular interlayer spacing, which ultimately affects the optical properties by changing the interference effects.

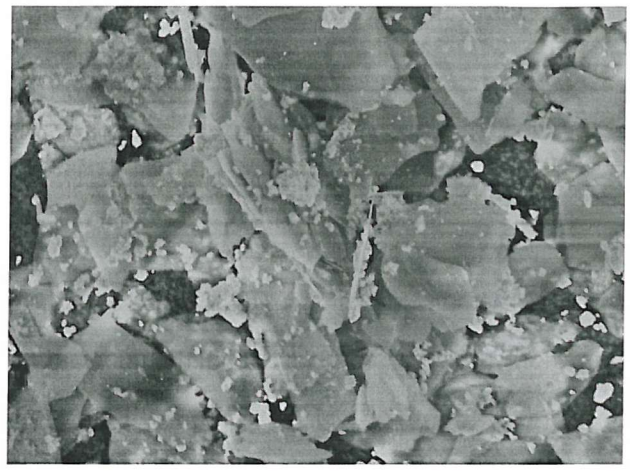

fig. 7.11: SEM image of a $CaTaO_2N$ sample synthesised via solution method (I).

The image in *fig. 7.11* of $CaTaO_2N$ on mica also displays separate pigment and mica phases and no coating of the mica substrate. These images highlight a major problem of segregation. This is a direct result of the insolubility of tantalum salts. On contact with aqueous solutions the $TaCl_5$ forms a hydrous tantalum oxide (Ta_2O_5) precipitate, thus a homogeneous solution of ions is not possible. However the co-precipitation techniques are still of use as they provide a more reactive tantalum starting material which in turn means a reduction in ammonolysis temperature. An adaptation to method (I) was attempted for $CaTaO_2N$ whereby the solutions of metal ions in EtOH and HNO_3 were added dropwise to a swirling solution of mica in NH_3. This was then collected and fired under ammonia as usual.

The results of this adaptation are shown in *fig. 7.12*. The pigment has not coated the mica platelets and thus two separate morphologies can be seen, grey platelets and white particles. As the grey platelets are of similar magnitude in *figs. 7.11* and *7.12*, both images must be of similar magnification and thus the two images can be compared. The pigment particles are

more agglomerated in the slow addition, *fig. 7.12*, whereas in *fig. 7.11* the pigment particles are, in general, much smaller.

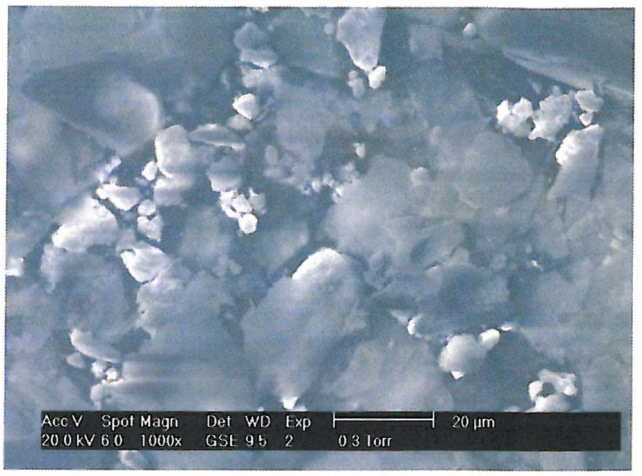

fig. 7.12: *SEM image of a $CaTaO_2N$ sample synthesised via a dropwise addition.*

7.4.4 UV-VISIBLE SPECTROSCOPY

UV-Visible spectroscopy was carried out on all coated mica pigments and then contrasted to spectra obtained for the pigment phase alone synthesised by the traditional solid state route, which is already known to yield vibrant coloured pigments as discussed in the previous chapters. The spectra obtained are displayed in *figs. 7.13-7.15* for $LaTaON_2$, $SrTaO_2N$ and $CaTaO_2N$ respectively.

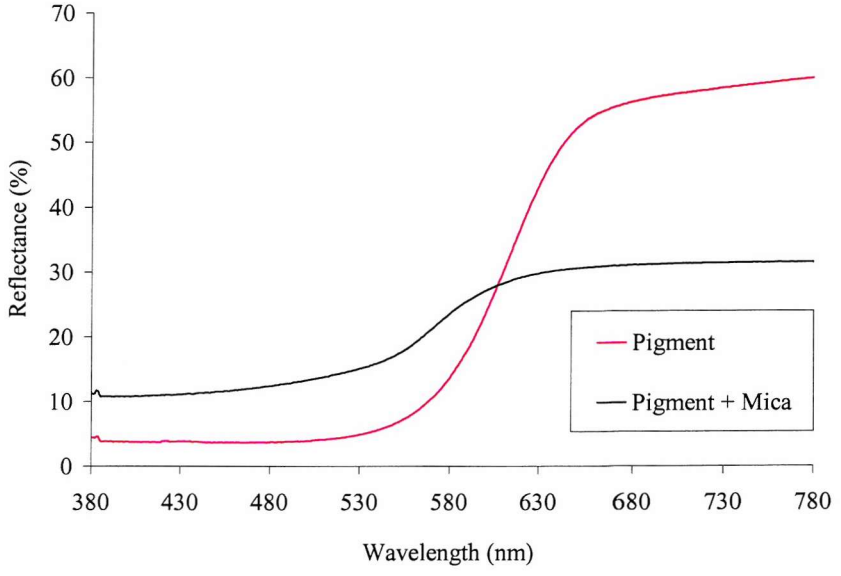

fig. 7.13: *UV-Visible spectroscopy data for $LaTaON_2$ with and without mica.*

The differences in the spectra between the oxynitride pigment on mica and pigment alone can clearly be seen. This is similar to the tantalum (V) nitride results, the quality of the pigment deteriorates with mica resulting in a golden beige colour. $LaTaO_2N$ is itself brick red.

The pigment reflects *ca.* 50 % more light in the red wavelengths of the spectrum than the coated mica sample. The combination of red light being reflected and blue light being absorbed gives $LaTaON_2$ its desirable colour. This data shows that the coated mica pigment in fact absorbs a fair proportion of red light and indeed it reflects some of the blue light. In terms of colour alone and disregarding any surface adsorption considerations, this results in an unsuitable candidate for lustre pigment applications.

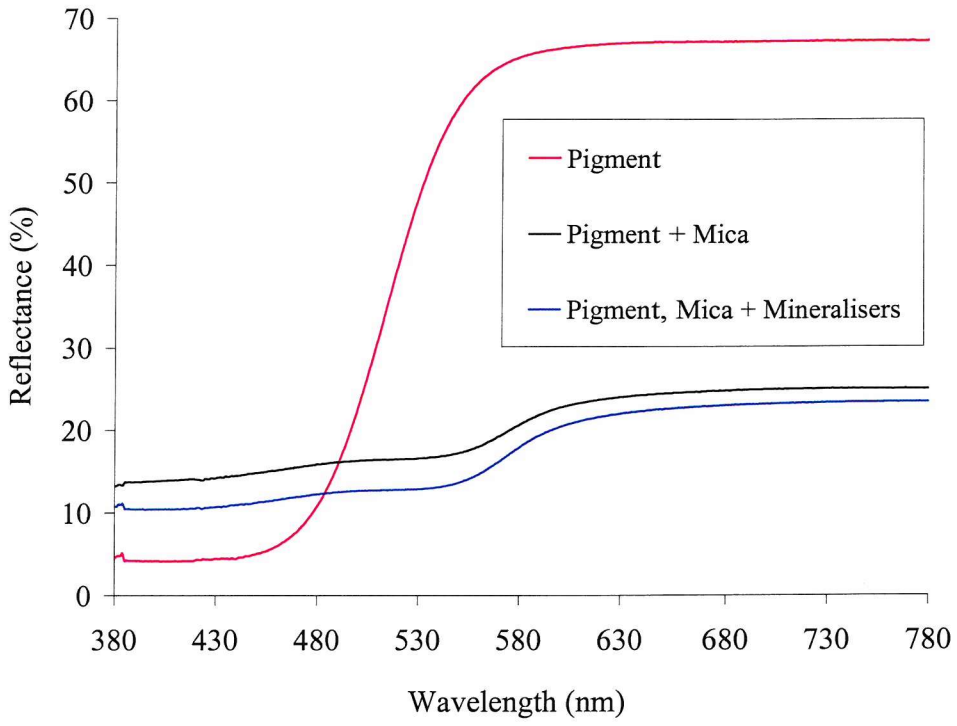

fig. 7.14: UV-Visible spectroscopy data for $SrTaO_2N$ with and without mica.

The absorption edge for $SrTaO_2N$ is at higher energy for the pigment alone. $SrTaO_2N$, when synthesised using a traditional solid state route with halide salts, is a yellow compound. This means that some shorter wavelengths of light, corresponding to yellow light, must also be reflected compared to the pigment on mica, a bronze beige colour, resulting in the shift towards the left in *fig. 7.14*. The difference in absorption edge may indicate the presence of another phase in the mica sample, such as Ta_3N_5. As this nitride is red it would absorb more

of the higher energy wavelengths than $SrTaO_2N$. It could also indicate a difference in stoichiometry, with the mica sample containing more nitrogen. This would result in a reduction in the band gap and a shift in the absorption edge to longer wavelengths.

The spectroscopic data yields no details on the differences between the coated mica pigment synthesised with mineralisers and the sample synthesised via solution method (I). Hence it is by observation alone that one can observe the degradation of lustrous effects by halide salts.

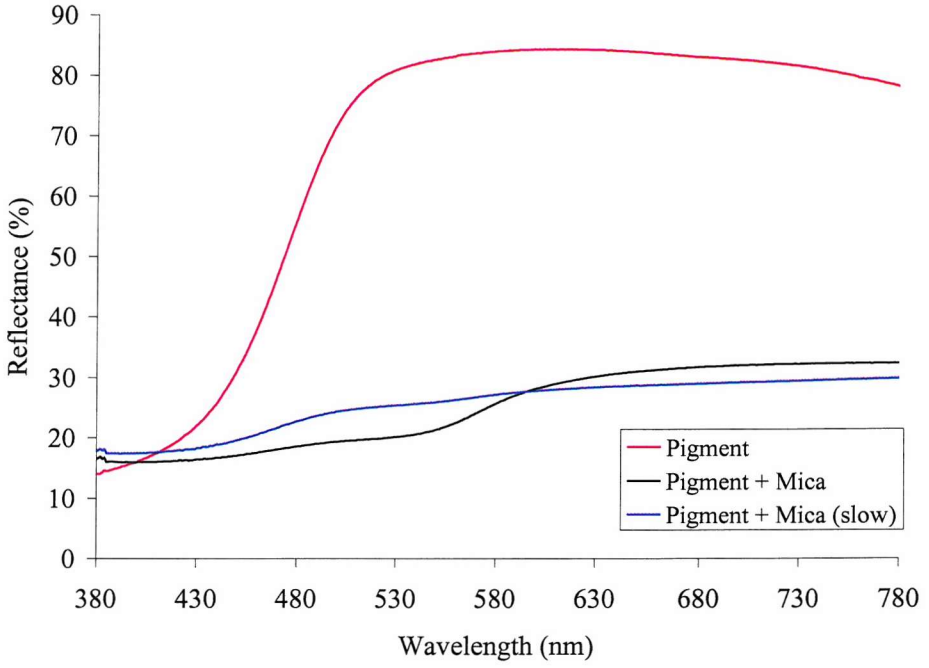

fig. 7.15: UV-Visible spectroscopy data for $CaTaO_2N$ with and without mica.

Again the visible spectroscopy data for the pigment $CaTaO_2N$ in *fig. 7.15*, shows a shift towards the shorter wavelengths compared to pigment on mica. This is expected as the colours observed are bright yellow for the pigment but brown beige for the pigment on mica. In analogy with $SrTaO_2N$, this difference could be attributed to impurity phases or a difference in nitrogen stoichiometry between pigment and pigment with mica. The coated mica pigments do not display the same steep absorption edge as oxynitrides but a much shallower increase in reflected light across the whole visible region towards longer wavelengths. The shallow absorption edges indicate a low level of colour purity. The slow dropwise additions of metal ions results in an absorption edge close to that of $CaTaO_2N$ itself at *ca.* 430 nm. This in turn could mean that a better homogeneous deposition of metal ions

has occurred on the surface of the mica flakes leading to a more facile synthetic pathway. Though SEM results show that both phases, mica and $CaTaO_2N$, exist independently.

7.4.5 COLOUR MEASUREMENTS

Colour measurements were acquired from the spectroscopic data and were contrasted to the values obtained for the pigment by itself. The measurements are given in *Table 7.5*.

In all cases the $L^*a^*b^*$ values for the pigments are not replicated in their coated mica counterparts. For $LaTaON_2$ on mica the redness value, a^*, is only a third of the true value for the pigment. The vibrant red colour has been lost. This too is the case for both $SrTaO_2N$ and $CaTaO_2N$ on mica whereby the yellowness value, b^*, is only a fraction of the value it takes for the respective pigment alone. Hence, the desired yellow colour of these pigments has been lost when synthesised via wet chemistry techniques.

Table 7.5: Colour measurements for pigment and pigment coated mica.

Sample	L^*	a^*	b^*
$LaTaON_2$ pigment only	41.39	39.10	31.47
$LaTaON_2$ with mica	50.95	13.34	17.49
$SrTaO_2N$ pigment only	76.63	4.81	77.31
$SrTaO_2N$ with mica	50.29	6.63	8.08
$SrTaO_2N$ with mica and mineralisers	46.20	9.53	10.49
$CaTaO_2N$ pigment only	90.72	-8.29	58.17
$CaTaO_2N$ with mica	54.97	7.55	10.86
$CaTaO_2N$ with mica (slow addition)	57.94	-0.12	10.27

It can be concluded that mineralisers play an important part in the overall colour of the compound formed, as does the actual synthetic route employed. This is discussed in *Section 7.6* where different routes to the same target compound, $SrTaO_2N$ are investigated.

7.5 CALCIUM TITANIUM OXYNITRIDE ON MICA

7.5.1 EXPERIMENTAL METHOD[11]

Metal chlorides, $CaCl_2$ (BDH, fused granular) and $TiCl_4$ (Aldrich, 99%), were dissolved in water in equimolar quantities and HCl (2 M) was added slowly to acidify the solution to pH 2. Mica was slurried into the water in a 1:1 ratio, mica to reagent, before chloride addition took place. After dissolution NaOH (2 M) was added to precipitate the metal ions out of solution and onto the surface of the mica. Due to the presence of a mica slurry it was impossible to detect when precipitation had taken place so further additions of NaOH were carried out until *ca.* pH 11 was obtained and thus OH^- ions were present in excess. The precipitate was then filtered and dried before firing under flowing ammonia overnight at temperatures between 700 and 750 °C.

A ceramic alternative, without mica, was synthesised in order that colour measurements and PXD plots could be compared. $CaCO_3$ (99%) and TiO_2 (BDH, 98%) were ground in acetone media in an equimolar ratio. Halide salt mineralisers were added in a 50% wt. ratio and the resultant homogeneous powder was fired under flowing ammonia for *ca.* 20 hours at 850 °C.

7.5.2 POWDER X-RAY DIFFRACTION

PXD patterns were collected on a Siemens D5000 and the data compared to the patterns collected for mica alone and also for the individual pigment phases, see *fig. 7.16.* The traditional solid state route yields a pattern with similar reflections to the orthorhombic perovskite $CaTiO_3$.[21] No such phase is detectable when synthesised via a solution method in the presence of mica. The reflections that are present in the red pattern correspond to the literature patterns for the dehydrated muscovite used in this experiment.[14]

Although there is no detectable crystalline pigment phase in the coated mica sample it is a similar colour to the calcium titanium oxynitride. The reflections attributed to mica may be dominating the profile and thereby making it difficult to distinguish the less crystalline pigment phase from the background.

As $CaTiO_3$ is not intensely coloured it could suggest that some oxygen has been replaced by nitrogen forming a perovskite-type oxynitride phase, $CaTiO_{3-\delta}(N,\square)_\delta$. In order to maintain

electroneutrality there could also be defects within the anionic sub-lattice due to the extra charge on N^{3-} *cf.* O^{2-}. Introduction of nitrogen into the unit cell would narrow the band gap of the material as discussed previously thus permitting selective absorption within the visible region resulting in a coloured compound.

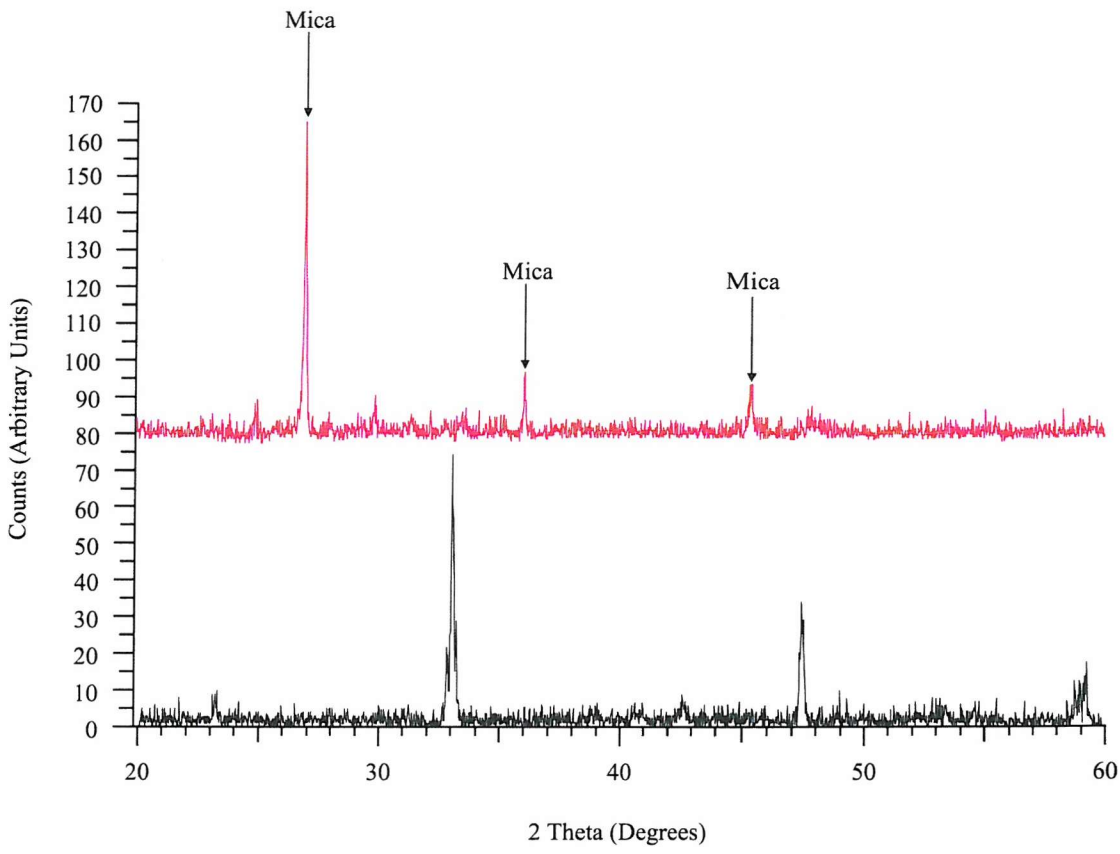

fig. 7.16: *PXD patterns of a calcium titanium oxynitride phase, where the black pattern is for a pigment synthesised via a ceramic route and the red pattern is for a pigment on mica.*

Alternatively there may be a partial reduction of Ti^{4+} to Ti^{3+} due to the reductive atmosphere of ammonia. It would only take a small fraction of titanium ions to change oxidation states for a drastic colour change to occur.[22] So with only a few anionic vacancies the compound can remain neutral overall.

The crystallinity of the pigment is in fact secondary to the colour. If the colour of a compound is suitable and repeatable when synthesised in bulk then the material may still be an ideal candidate for commercial applications as long as the compound has the desired

pigment properties, such as stability to heat and light. Hence, this material was analysed further using UV-Vis. spectroscopy, colour measurements and SEM.

One important factor is the actual thickness of the film coating on the mica substrate. The penetration depth of the X-ray beam is typically about 1000 Å thus the technique is not surface sensitive but probes the bulk of the sample. Commercial oxide coated mica particles have a pigment coating typically in the region of 50 - 100 nm, which is on the limit of detection meaning that the pigment film must be above a certain thickness in order that its structure be determined by PXD. The calcium titanium sample discussed here may only have a thin coating and thus be undetected in a PXD profile.

7.5.3 SCANNING ELECTRON MICROSCOPY IMAGING

SEM was carried out and an image obtained representing the composition of the calcium titanium phase on mica, see *fig. 7.17.*

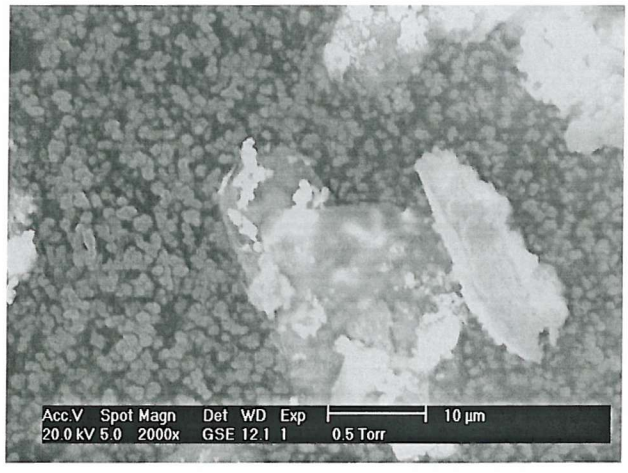

fig. 7.17: SEM image of a calcium titanium oxynitride phase on mica.

The bright regions in this picture are a direct result of charging. As time progresses more electrons are held on the surface of the sample than are dispersed away, the rate at which electrons hit the surface being greater than the rate at which they leave. This results in a build up of negative charge on the sample surface. Further incoming primary electrons are thus repelled and deviated from the normal path, adversely resulting in a distorted and blurry image.[23] However flakes of mica can be identified and the whiter regions are pigment

particles agglomerated on the surface of the mica. The small grey particles are in fact characteristic of the carbon disc the sample is adhered to.

7.5.4 ENERGY DISPERSIVE ANALYSIS OF X-RAYS

Energy Dispersive Analysis of X-rays (EDAX) was carried out on the calcium titanium oxynitride sample without mica to ascertain what percentage of calcium and titanium was present within the phase produced. Although an equimolar ratio of calcium and titanium ions are present in the solid state reaction there may be slight discrepancies in order to maintain electroneutrality. The results from the EDAX analysis are given in *Table 7.6.*

Table 7.6: Percentage analysis of elements present in the $CaTiO_{3-\delta}(N,\square)_{\delta}$ sample.

Element	Weight %	Atomic %	Ratio
C	13.45	27.26	1.54
O	25.84	39.32	2.23
Ca	25.99	15.78	0.89
Ti	34.72	17.64	1.00

The values for carbon have come from the carbon disc mount the sample is adhered to and is not a constituent element of the compound. Thus the overall stoichiometry of the compound, according to the EDAX data is $Ca_{0.89}TiO_{2.2}$. When considering an experimental error of ~10% for EDAX, then this is a similar stoichiometry to $CaTiO_3$. It must be noted that as no calcium titanate phase is present in the PXD profile it is equally likely that CaO and TiO_2 are deposited onto the substrate. If no reaction has occurred, the colour could arise from TiO_2 with the partial reduction of titanium cations as discussed earlier.

The EDAX analysis of this compound detected no nitrogen within the sample. This suggests that the colour may well arise due to the reduction of the titanium cation from an oxidation state of IV to III. The change in oxidation states from Ti^{4+} to Ti^{3+} means that the titanium is no longer a d^0 cation but a d^1 cation. Intervalence charge transfer may occur between two titanium cations causing the powder to be coloured. However, EDAX data is more unreliable for lighter elements and there could still be the possibility of trace amounts of nitrogen within

the sample. As the stoichiometry displays anionic vacancies, this results in an overall positive charge. If some of the vacancies were actually nitrogen this would not be the case.

7.5.5 UV-VISIBLE SPECTROSCOPY

UV-Visible spectroscopy was carried out on the calcium titanium oxynitride coated mica sample and compared to data collected for the perovskite.

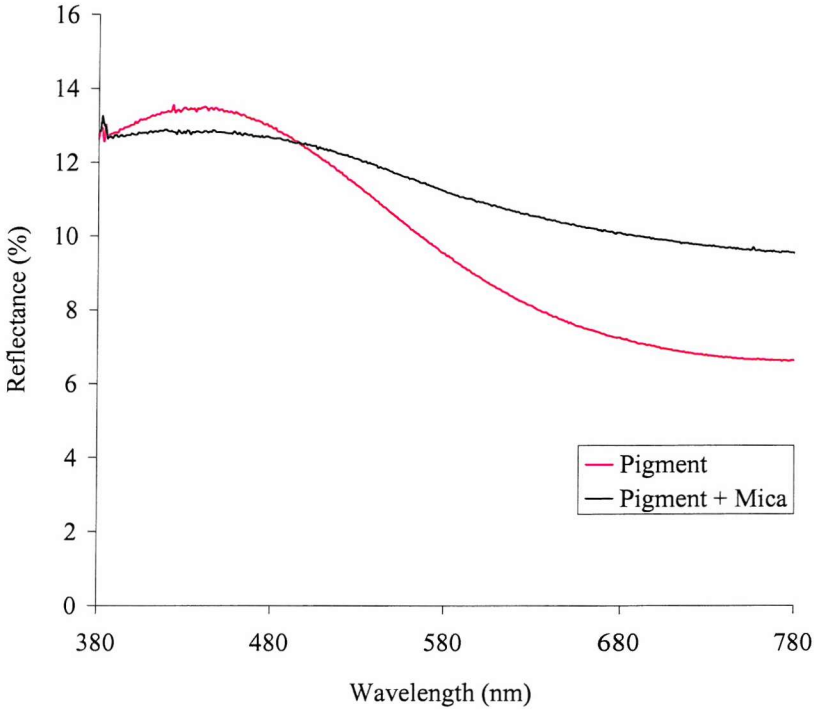

fig. 7.18: UV-Visible spectroscopy data for a calcium titanium oxynitride with and without mica.

These samples both had a blue hue, hence the spectra are reversed, *i.e.* a portion of blue light is now reflected whilst most light at the red end is absorbed. The spectra are similar in that they do not possess the steep absorption edge that is detected in the visible spectra of the tantalum pigments.

Overall it can be seen that little light is reflected which is expected, as the powders obtained are not intensely coloured. More light is reflected from the lustre sample due to the contribution of reflected light from mica itself. This is different to the tantalum samples, which themselves yield more intensely coloured powders.

7.5.6 COLOUR MEASUREMENTS

Colour measurements were acquired from the spectroscopic data and were contrasted to the values obtained for the pigment by itself. The measurements were collated in *Table 7.7*.

Table 7.7: Colour measurements for pigment and pigment coated mica.

Sample	*L**	*a**	*b**
Ceramic Route, no mica	38.87	-3.94	-7.43
Pigment and mica 700 °C	40.73	-1.84	-2.90
Pigment and mica 750 °C	31.50	-1.26	-0.92

The ceramic route sample has both the greatest blueness value and greenness value but there is not a remarkable difference between this sample and the sample synthesised via wet techniques with mica. $CaTi(O,N)_3$ does not yield an intensely coloured compound so $L^*a^*b^*$ values are expected to be much closer to zero than the tantalum pigments.

7.6 THE EFFECT OF SYNTHETIC ROUTE ON COLOUR

7.6.1 EXPERIMENTAL METHOD

Three different approaches were adopted to target the known material $SrTaO_2N$,[6,19] a traditional ceramic route, an alkoxide route[24] and a co-precipitation route (co-ppt), *viz.* samples 1, 2 and 3 respectively.

Sample 1 was synthesised by firing $SrCO_3$ (Aldrich, 99.9%) and Ta_2O_5 (Aldrich, 99%) with halide salt mineralisers at 850 °C under an atmosphere of flowing ammonia for *ca.* 20 hours, a route used extensively in previous chapters.

Sample 2 was synthesised by adapting a preparation from the literature using metal alkoxides.[24] It has been reported that it is possible to use more reactive starting materials such as xerogels[25,26] to target oxynitrides phases. This has arisen as a cause of the unreactiveness of some oxides at low temperatures. This alkoxide route was previously used

in the synthesis of $SrTi(O,N)_3$ in *Chapter 6*. In this synthesis, titanium ethoxide is exchanged for tantalum pentaethoxide (Aldrich, 99.8%), other reactants remain the same.

Sample 3 was synthesised by a method similar to solution method (I). Stoichiometric amounts of $TaCl_5$ (Aldrich, 99.9%) and $SrCl_2$ (Aldrich, 99%) were added to HNO_3 (50 cm^3, 2 M) and ethanol (100 cm^3, 99.86% v/v). After dissolution of the metal ions, ammonia (*ca.* 20 cm^3, S.G = 0.880) was added slowly until a precipitate formed and the resulting liquor was heated till dry and then decomposed at 350 °C overnight. Finally, the powder was annealed under flowing ammonia at 850 °C for *ca.* 20 hours. This experiment was repeated using a 5% excess of $SrCl_2$ to ensure full occupancy on the A site of the perovskite.

7.6.2 POWDER X-RAY DIFFRACTION

PXD patterns were collected on a Siemens D5000 diffractometer and a Bruker D8 diffractometer (alkoxide route) and the data sets compared to literature models.[6,19] The data sets collected are shown in *fig. 7.19*.

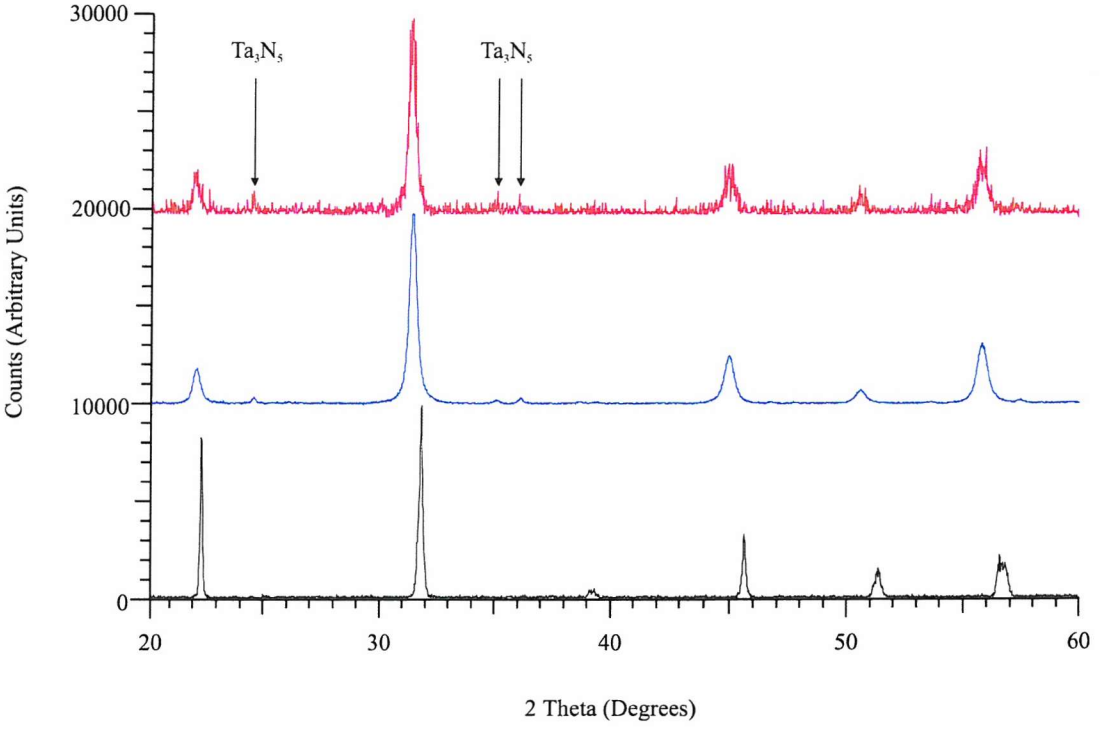

fig. 7.19: *PXD patterns of $SrTaO_2N$, where the black pattern is sample 1 (ceramic), the blue pattern is sample 2 (alkoxide) and the red pattern is sample 3 (co-ppt, 5 % excess $SrCl_2$).*

A perovskite has formed for each synthetic route with the same reflections as the literature data.[6] Samples 2 and 3, synthesised via wet chemistry techniques have broader peaks than that of the ceramic route. This arises due to differences in particle size, the broader the peak the smaller the particle size. In general, the bigger the particle size the more intense the colour becomes, hence the brightest pigment is the yellow sample $SrTaO_2N$, synthesised via a traditional solid state route. The alkoxide route yields a brown sample whereas the co-ppt route yields an orange powder. This is a direct result of a Ta_3N_5 impurity, marked on the upper pattern of *fig. 7.19*. Ta_3N_5 is a bright red compound, which is darkening the yellow compound $SrTaO_2N$, resulting in the orange and brown powders.

Adding an excess of the strontium salt in the case of the co-ppt route, sample 3, would ideally result in a SrO impurity in the product. As this is white it could enhance the pigment making it brighter. It is difficult to tell whether SrO has formed as the reflections overlap some of the Ta_3N_5 peaks. As sample 3 was much more amorphous, Rietveld analysis of the structure does not reveal sufficient information about the impurity phases.

The cell parameters of the three compounds were calculated using *CELREF*[18] to highlight differences in the sizes of the unit cell. The results are found in *Table 7.8*. They were compared to a literature model of $SrTaO_2N$ crystallising in the tetrahedral space group *I4/mcm*.[6]

Table 7.8: Lattice parameters for $SrTaO_2N$ synthesised via different routes.

Sample	*a* [Å]	*b* [Å]	*c* [Å]
$SrTaO_2N$ (Ceramic)	5.618 (3)	5.618 (3)	7.944 (5)
$SrTaO_2N$ (Alkoxide)	5.714 (4)	5.714 (4)	8.044 (8)
$SrTaO_2N$ (co-ppt 5% XS $SrCl_2$)	5.712 (3)	5.712 (3)	8.039 (4)
Literature data[6]	5.7049 (3)	5.7049 (3)	8.0499 (5)

From the lattice parameter data it can be seen that a smaller unit cell size is generated when $SrTaO_2N$ is formed using a ceramic route, ($V \approx 250$ Å^3 *cf.* ≈ 262 Å^3). Both wet chemistry techniques yield bigger cell parameters of similar magnitudes. This difference could be due to nitrogen uptake. As the ionic radius of nitrogen is larger than oxygen, the compounds with

nitrogen are likely to have a larger unit cell than those with less nitrogen. This would be consistent with the colour changes of the different routes. More nitrogen within the compound narrows the band gap shifting the interband transition to the lower energy wavelengths, *i.e.* from yellow to orange and red.

Another feature of note is the splitting of the peaks in the PXD patterns. Both sample 2 and the sample 3 yield perovskites that maybe of lower symmetry than the ceramic route, sample 1. The PXD patterns for the latter compound show less splitting of the reflections, this in turn implies less distortion from a cubic geometry. Obtaining good quality data, suitable for Rietveld analysis, would have determined the space groups of each compound, as weaker reflections can be resolved from the background.

7.6.3 UV-VISIBLE SPECTROSCOPY

UV-Visible spectroscopy data sets were collected on the three samples of $SrTaO_2N$ in order to contrast the differences in colour dependant on synthetic route adopted. The data can be seen in *fig. 7.20*. This data and the *L*a*b** measurements that can be obtained from the spectra will go some way to explaining the differences in colour, though particle size analysis would have been a useful aid.

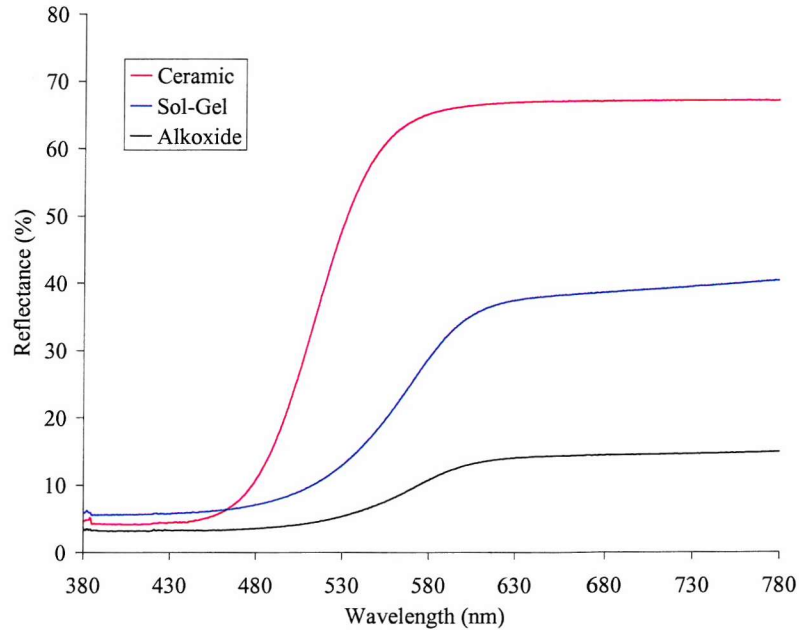

fig. 7.20: UV-Visible spectroscopy data for $SrTaO_2N$ synthesised via a ceramic route (red), co-ppt route (blue) and an alkoxide route (black).

The absorption edge of sample 1 (ceramic) lies at a shorter wavelength than the co-ppt compound (3) which in turn is at a shorter wavelength than that of the alkoxide (2). This is in direct relation to the colours the compounds adopt, with the $SrTaO_2N$ (ceramic) being yellow, $SrTaO_2N$ (co-ppt) orange and $SrTaO_2N$ (alkoxide) brown. In order to appear yellow rather than orange a compound must reflect the yellow wavelengths of light, which are higher in energy than the energy of red light. This accounts for the absorption edge being higher in energy for the ceramic compound than the other compounds. The band gaps of these three compounds all lie in the visible region. The compounds absorb all photons with energies greater than the band gap but not those with energies smaller than the band gap. Hence the ceramic compound has a larger band gap energy than the other compounds as this is absorbing only the higher energy photons at the blue end of the visible region. As the substitution of oxygen for nitrogen within the crystal structure leads to a reduction in the band gap energy it could suggest that less nitrogen is present within the ceramic $SrTaO_2N$ than for the other compounds, assuming negligible effect from particle size on resultant colour.

7.6.4 COLOUR MEASUREMENTS

Colour measurements were acquired from the spectroscopic data and the measurements were collated in *Table 7.9*, thus enabling contrasts to be made.

The alkoxide route may appear brown due to the formation of tantalum nitride as well as the $SrTaO_2N$ perovskite. As Ta_3N_5 is red, its presence may darken the overall appearance of sample 2 thus making the powder duller.

Table 7.9: Colour measurements for $SrTaO_2N$.

Sample	*L**	*a**	*b**
$SrTaO_2N$ (Ceramic)	76.63	4.81	77.31
$SrTaO_2N$ (co-ppt 5% XS $SrCl_2$)	52.33	21.40	37.99
$SrTaO_2N$ (Alkoxide)	33.92	14.47	21.35

Every sample takes a positive *a** value and a positive *b** value thus suggesting the powders to be red-yellow in colour. The yellowness value is substantially higher for the ceramic

sample *cf.* the other samples, as expected for a bright yellow compound. The other compounds, which are in fact orange (co-ppt) and brown (alkoxide), have higher redness values. Hence the $L^*a^*b^*$ measurements are indicative of the observed colours.

7.7 DISCUSSION AND CONCLUSIONS

A major problem for this work is that tantalum salts are insoluble in most media. $TaCl_5$ is soluble in ethanol and thus the best route appears to involve dissolving $TaCl_5$ in ethanol. However, this method is not perfect in producing a homogeneous solution of cations. The $TaCl_5$ is difficult to manage in air and as the ethanol is not dry, hydrous tantalum oxide precipitates out of the ethanolic solution. When mica is incorporated forming a slurry, the solutions become opaque and hence it is impossible to identify if the cations are in solution or have formed a precipitate. Therefore an excess of base, NH_3 (method I) or NaOH (method II) is always required.

This is not the only problem associated with the routes involving mica. At temperatures greater than 850 °C mica will decompose. This is one reason why the ceramic route cannot be used to any success in the synthesis of a lustrous oxynitride material. It is however not the only reason that invalidates this route. This route is reliant on the use of halide salt mineralisers. Such compounds destroy mica and its pearlescent characteristics.

Unfortunately the ceramic route provides the better product in bulk pigment alone. In work completed during the earlier stages of this project the use of mineralisers was investigated. Samples of $Ca_{0.5}La_{0.5}TaO_{1.5}N_{1.5}$ were targeted. One set of conditions included the use of halide salts whereas the other did not. The results indicate the necessity of mineralisers. The resultant powder of the synthesis without mineralisers is a pale peach colour whereas the addition of mineralisers results in a bright yellow-orange coloured powder. Not only do mineralisers affect the colour of the powder but also its crystallinity. The PXD pattern of the yellow orange compound is consistent with a crystalline perovskite-type phase adopting the same symmetry as $CaTaO_2N$.[6] The other powder is quite amorphous and a multiphase combination of mixed metal oxides, which have undergone nitrogen substitution due to the observed peach hue of the powder.

Several trials were carried out to test the effect mineralisers had on mica. The halide salts are shown to cause the degradation of mica as opposed to the flow of reactive gas. Mica although transparent can take on a golden beige colour when the layers are built up, this is due to iron impurities within the mica. After firing mica and halide salts together with flowing ammonia the resultant powder becomes silver-grey. If the mineralisers are omitted but the mica subjected to the same reaction conditions the golden beige colour is retained.

The colour of an oxynitride phase alters drastically depending on the synthetic approach. From the $L^*a^*b^*$ values for $SrTaO_2N$, the best pathway for oxynitride synthesis lies with the ceramic route, closely followed by the co-ppt route. This again comes back to the question of mineralisers. Of the three routes taken only the ceramic route contains added mineralisers. These salts cannot be added to the solution chemistry routes adopted as the presence of the chlorides would destroy the characteristic nacreous effects of mica exploited in lustre pigments.

Particle size plays an important role in reactivity. Finely divided powders have a high surface area providing more crystal faces on which the migration of ions can take place in order to form a stable product. As solution techniques often result in precursors with small particle sizes, it may suggest that these techniques provide pathways that are more reactive than the ceramic routes. An increase in reactivity may lead to a greater uptake of nitrogen within the target compound that in turn leads to a narrowing of the band gap as the compound would display a greater degree of covalency. This ultimately changes the observed colour, therefore explaining why Ta_3N_5 goes from bright red when formed from Ta_2O_5 to a rust colour when formed via a solution method.

The size of the crystallites also plays a part in the final colour of the product. In general particle size is smaller when synthesis involves a solution pathway instead of the traditional solid state route. This is seen in the broadening of the reflections in the PXD data sets, a broader peak denoting smaller crystallites. As a general rule, bigger particle sizes result in more intense colours hence the ceramic route yields the brightest pigments. This makes the deposition of a bright oxynitride pigment onto the surface of mica much more difficult. The adsorption of pigment onto mica occurs *in-situ* as the pigment phase is synthesised. This does not usually occur if mica is included with metal oxides in a traditional solid state reaction as the reaction takes place at the interface between the binary oxides. The synthesis of

oxynitride phases via wet chemistry techniques that use the mica surface as a nucleation site is paramount to producing a lustre pigment that displays the same colour effect as the oxynitride alone.

Although the samples appear to have a lustrous effect, this is not due to the light reflections from the pigment coating and the mica together but instead the lustrous effect of mica is independently providing the shimmer and the pigment providing the colour of the sample. SEM images highlight the difficulty in achieving any coating on mica. They display the two different morphologies, the laminar flakes of mica and the pigment agglomerates. Where there is a little binding to the surface it is clustered and not the desired thin uniform coating. This is another issue that would need to be addressed if a suitable synthetic approach is found. In order to harness the refractive effects of mica the optical thickness of the pigment film on the substrate is carefully controlled.[22]

One promising outcome however is that all the powders synthesised without mineralisers still display the same optical effects that mica possesses. The lustrous properties are not ruined during ammonolysis techniques. However in comparison to commercial lustre pigments it is easy to see by eye alone the difference between oxide coated mica pigments and the oxynitride pigment and mica mixtures that have been synthesised in this work.

Possible areas for further work and improvements to the syntheses do exist, especially in relation to scaling up the production of oxynitrides. Certain routes are not viable for bulk synthesis; such is the case in the intercalation of $TaCl_5$ on mica. This was carried out in a sealed ampoule, a process not suited for industrial manufacture.

The industrial process to oxide coated mica pigments provides more control than the routes adopted in the laboratory allow. Suitable equipment is employed to carefully control the pH of the reaction vessel. This aids the slow precipitation of a reactive precursor onto the mica surface ready for annealing. Two reagents can be added gradually and simultaneously allowing a continuous precipitation at the required pH level. In the laboratory, the pH is crudely regulated by pipetting acid or base into the solution when the reading on a hand held meter fluctuates. Hence with the appropriate control measures it is possible to deposit tantalum onto mica in order to synthesise tantalum nitride and oxynitride coated mica pigments.[27] A patent describes how a suspension of mica muscovite in distilled water is

heated to 75 °C and a $TaCl_5$ solution (solvent dilute HCl) is slowly added to the reactor with the pH maintained at 9 via further additions of HCl. The preparation is filtered off and washed with distilled water and dried. The precursor is put in a fluidised bed reactor and calcined at 1000 °C for 48 hours under flowing ammonia.

The colour measurements in this work are diffuse reflectance measurements. In fact diffuse reflectance measurements are only suited to the oxynitride pigments themselves. Lustre pigments achieve their optical effects via the specular reflectance of light and thus there are better ways in which colour data can be collected and analysed for such optical effect pigments.

7.8 REFERENCES

[1] Pfaff G., Reynders P.; *Chem. Rev.*, **99**, 1963 (1999)

[2] Buxbaum G.; *Industrial Inorganic Pigments*, Wiley-VCH (Germany), Second Edition (1998)

[3] European Economic Community Guideline No. 91 / 338 / EWG (1991)

[4] European Union Directive 94/62/EC

[5] Jansen M., Letschert H.; *Nature*, **404**, 980 (2000)

[6] Günther E., Hagenmayer R., Jansen M.; *Z. Anorg. Allg. Chem.*, **626**, 1519 (2000)

[7] Marchand R., Laurent Y., Guyader J., L'Haridon P., Verdier P.; *J. Eur. Ceram. Soc.*, **8**, 197 (1991)

[8] Clarke S. J., Guinot B. P., Michie C. W., Calmont M. J. C., Rosseinsky M. J.; *Chem. Mater.*, **14**, 288 (2002)

[9] Wright J. D., Sommerdijk N. A. J. M.; *Sol-Gel Materials: Chemistry and Applications*, Taylor and Francis (UK), First Edition (2001)

[10] Henry P. F., Hughes R. W., Ward S. C., Weller M. T.; *Chem. Commun.*, **19**, 1959 (2000)

[11] Eskelinen P., Ritala M., Leskela M.; *J. Solid State Chem.*, **103**, 160 (1993)

[12] Brese N. E., O'Keefe M.; *Struct. Bonding (Berlin)*, **79**, 307 (1992)

[13] Orhan E., Tessier F., Marchand R.; *Solid State Sci.*, **4**, 1071 (2002)

[14] Keppler H.; *Am. Mineral.*, **75**, 529 (1990)

[15] Straehle J.; *Z. Anorg. Allg. Chem.*, **402**, 47 (1973)

[16] Rietveld H. M.; *Acta Crystallogr.*, **22**, 151 (1967)

[17] Rietveld H. M.; *J. Appl. Crystallogr.*, **2**, 65 (1969)

[18] Laugier J., Bochu B.; *CELREF*, Laboratoire des Matériaux et du Génie Physique, Ecole Nationale Supérieure de Physique de Grenoble INPG (France) (2000)

[19] Marchand R., Pors F., Laurent Y.; *Rev. Int. Hautes Tempér. Réfract. Fr.*, **23**, 11 (1986)

[20] Marchand R., Pors F., Laurent Y.; *Ann. Chim. Fr.*, **16**, 553 (1991)

[21] Sasaki S., Prewitt C. T., Bass J. D.; *Acta Crystallogr. C*, **43**, 1668 (1987)

[22] Tilley R.; *Colour and the Optical Properties of Materials*, Wiley (UK), First Edition (2000)

[23] Goodhew P., Humphreys J., Beanland R.; *Electron Microscopy and Analysis*, Taylor & Francis (UK), Third Edition (2001)

[24] Günther E., Jansen M.; *Mat. Res. Bull.*, **36**, 1399 (2001)

[25] Grins J., Käll P., Svensson G.; *J. Mat. Chem.*, **4(8)**, 1293 (1994)

[26] Grins J., Svensson G.; *Mat. Res. Bull.*, **29(7)**, 801 (1994)

[27] Bertaux S., Reynders P., Wichmann J-U., Schweda E.; *Pearlescent pigments, preparation and use.*, (Merck) Patent Number US2003147820

CHAPTER EIGHT

CONCLUSIONS

8 CONCLUSIONS

8.1 INORGANIC PIGMENTS

Inorganic pigments are used to enhance the appearance of an object. Inorganic pigments are favoured over typically brighter organic pigments as they are stable to high temperatures unlike their organic counterparts. Inorganic pigments have not only high thermal stabilities but are resistant to light, the weather, pollution and chemical attack in acidic and alkaline environments. The properties they possess encompass brilliance, tinting strength, opacity and dispersability.[1] In recent years, the toxicity of a compound has also been an issue when considering suitability for an application. In former times the desire for bright colours led to the use of dangerous compounds. In the 19th century wallpaper coloured with Scheele's green, a bright green compound precipitated from arsenious acid with copper sulfate solution ($HCuAsO_3$), and Paris green, a mixed copper arsenic acetate ($3Cu(AsO_2)_2 \cdot Cu(CH_3COO)_2$) was widely sought after. However, these compounds are unstable and in contact with moist air release toxic vapours containing arsenic. Such pigments are believed to have brought about many deaths from arsenic poisoning, most notoriously was the death of Napoleon.[2]

In recent times, concern about the use of heavy metals such as cadmium, chromium and lead in materials has resulted in tighter health and safety regulations.[3] Many pigment systems in use contain such metals, *i.e.* cadmium sulfoselenide ($CdS_{1-x}Se_x$), chromium oxide (Cr_2O_3) and lead chromate ($PbCrO_4$), thus an increased effort to industrially synthesise inorganic pigments with less toxic elements has begun. Unfortunately, the replacement of certain colour systems has been difficult to achieve thus far.

8.2 OXYNITRIDES

One radical approach to the synthesis of novel pigments has focused on mixed anion compounds such as oxysulfides and oxynitrides. The introduction of different anions alters the band gap which in turn allows absorption in the visible region of the electromagnetic spectrum giving rise to coloured compounds. This project has focussed on oxynitrides as suitable replacements to cadmium and chromium based pigments as several systems have proved to be red through to green in colour. Recently Jansen *et al.* found that $CaTaO_2N$ and $LaTaON_2$ are bright yellow and red compounds respectively with rivalling properties to

cadmium pigments.[4] This work has systematically varied the components of the basic tantalum oxynitride perovskite to target optimum pigment systems. By varying parameters such as the cation composition and ratio whilst retaining the perovskite structure, the anionic stoichiometry also alters. This enables fine-tuning of the band gap to vary the pigment colour.

It has been found that it is possible to substitute many divalent and trivalent cations onto the A site of a perovskite. The perovskite structure tolerates large strains through defects and distortions to lower symmetry but certain radius ratio rules must be considered. From the Goldschmidt tolerance factors[5] it can be calculated that ions such as $Mg^{2+}$and Y^{3+} are often too small whereas a bigger ion such as Ba^{2+} is almost at the limit of radius size that can occupy the 12 co-ordinate site within the perovskite structure. This has lead to increased amounts of competing pyrochlore phase, *viz.* $Ln_2Ta_2O_5N_2$ where Ln is a smaller lanthanide ion, in certain target reactions.

The colours of alkaline earth and rare earth substitutions into $CaTaO_2N$ and $LaTaON_2$ modify the colour from yellow through orange to red. However by replacing tantalum with niobium on a one for one basis results in modifications to the brightness of these quaternary phases. This alters the colour from the bright yellows and reds towards browner and more dull compounds. It is possible to alter the colour of the compound completely by doping other transition metals onto the B cation site, such as the green and blue titanium doped compounds and the blue tungsten doped compounds also reported here. However, these colours do not rival the same intense colours of current green and blue pigment systems.

8.3 LUSTRE PIGMENTS

It is possible to manufacture compounds with special effects, as is the case with lustre pigments.[6] This category of pigment can embrace many different types, including the metal oxide coated mica pigments whose lustre properties arise from interference effects. The current range of lustre pigments is very limited, typical coatings include TiO_2 and Fe_2O_3. It is reasoned that the deposition of oxynitride pigments onto the surface of mica flakes may lead to novel metal oxynitride coated mica pigments. The low solubility of tantalum salts has made the deposition of oxynitride phases onto mica difficult. Small scale reactions and the use of crude equipment has hindered the successful deposition of tantalum salts as well. In

industry, it is possible to have more control over the deposition techniques, as appropriate equipment is available. However, this study of oxynitride pigments may provide a basis to discover which metal oxynitride coated mica pigments are worth targeting.

8.4 LIMITATIONS AND FURTHER WORK

Homogenity of the sample is often a problem in ammonolysis, with a gradient of colour being observed along the alumina reaction boat, as well as within the bulk of the sample underneath the surface. This arises due to the mobility of ions and thus the diffusion of reactants in the solid state, with the trivalent N^{3-} ion being slower than O^{2-} on account of charge density. There is also a problem with fugacity[7] *i.e.* the tendency of a gas to expand or escape, meaning the flow rate of the reactive gas is critical. A low flow rate results in poor nitridation whereas a very high flow rate can result in nitride impurities such as Ta_3N_5.

There is also an unresolved issue that this work generates, and that is one of nitrogen uptake by the forming phase during ammonolysis. From powder X-ray diffraction it is impossible to ascertain nitrogen content as both anions O^{2-} and N^{3-} are isoelectronic. Powder neutron diffraction is a costly approach towards the better understanding of anionic distribution and is therefore not the most appropriate technique to use. A few methods to highlight are firstly the Kjeldahl technique, a method for determining nitrogen in inorganic compounds.[8] In this method a sample is decomposed to ammonium hydrogen sulfate by excess hot conc. H_2SO_4. The resulting solution is made strongly alkaline to convert the ammonium ion to ammonia, distilled and absorbed in a large quantity of boric acid liberating a borate ion for each molecule of ammonia. This solution is then titrated against a standard HCl solution to calculate the amount of nitrogen present. This is an extremely long technique as the decomposition step can take upwards of 10 hours and is therefore not ideal. If suitable equipment is available, it is possible to carry out elemental analysis by combustion to determine the content of oxygen and nitrogen in ceramic materials.

More rigorous calculations can be employed to estimate the band gap of the semiconductors synthesised. For instance electrochemical photocurrent spectroscopy has been used to calculate band gap energies in the solid solution series $In_xGa_{1-x}N$, $0 \leq x \leq 0.140$.[9] Also

electronic structures can be computed within the Density Functional Theory (DFT), a technique used to calculate band gap energies in TaON and Ta_3N_5.[10,11] Although beyond the scope of this study it is of note that accurate calculations can be made which may give a better working knowledge of how material composition can be altered in order to fine-tune the band gap.

There have also been studies into the oxidation state of tantalum in oxynitride compounds.[7] X-ray photoelectron spectroscopy (XPS) has been employed to find the binding energy and thus the oxidation state of tantalum in $BaTaO_2N$. This technique would be useful to ascertain the formal oxidation states of titanium and tungsten in the compounds synthesised in this work. It is surprising that oxynitrides exist that contain the highest oxidation state of a transition metal *i.e.* Ti^{4+} and W^{6+} after exposure to a reductive atmosphere during ammonolysis as the corresponding binary nitrides do not exist.[12]

Finally the subject of particle size is an important issue that could be addressed in subsequent work. Particle size affects the tinting strength (depth) of colour of a solid. This tinting strength can be observed by mixing pigment with linseed oil or white emulsion paint. Particle size is reduced by grinding the sample and then sieving with a fine mesh, say 50 microns, to remove impurities as these affect the pigment quality. Hence finer pigment particles are more expensive but as they produce a high tinting strength, less is required. SEM can be employed to give an estimation of grain size though a technique that measures the scattering of laser light is more commonly used. At large angles, small particles scatter light more intensely whereas the converse is true for larger particles, which scatter more intensely at smaller angles. Mie's theory can be employed to convert the intensity of light scattered over a range of different angles into a particle size distribution within a sample.

8.5 REFERENCES

[1] Buxbaum G.; *Industrial Inorganic Pigments*, Wiley-VCH (Germany), Second Edition (1998)

[2] Tilley R.; *Colour and the Optical Properties of Materials*, Wiley (UK), First Edition (2000)

[3] European Economic Community Guideline No. 91 / 338 / EWG (1991)

[4] Jansen M., Letschert H.; *Nature*, **404**, 980 (2000)

[5] Goldschmidt V. M.; *Skr. Nor. Vidensk. Akad. Kl 1: Mat. Naturvidensh. Kl* (1926)

[6] Pfaff G., Reynders P.; *Chem. Rev.*, **99**, 1963 (1999)

[7] Hellwig A., Hendry A.; *J. Mat. Sci.*, **29**, 4686 (1994)

[8] Vogel A. I.; *Textbook of Quantitative Inorganic Analysis*, Longman (UK), Fourth Edition (1981)

[9] Beach J. D., Al-Thani H., McCray S., Collins R. T., Turner J. A.; *J. Appl. Phys.*, **91**, 5190 (2002)

[10] Fang C. M., Orhan E., de Wijs G. A., Hintzen H. T., de Groot R. A., Marchand R., Saillard J. Y., de With G.; *J. Mat. Chem.*, **11**, 1248 (2001)

[11] Orhan E., Tessier F., Marchand R.; *Solid State Sci.*, **4**, 1071 (2002)

[12] Tessier F., Marchand R.; *J. Solid State Chem.*, **171**, 143 (2003)

APPENDICES

APPENDICES

Appendix I: Lanthanide and trivalent ion sources and purities.

Ln	Source	Purity
Sc_2O_3	Aldrich	99.999%
Y_2O_3	Aldrich	99.999%
La_2O_3	Aldrich	99.9%
CeO_2	Aldrich	99.9%
Pr_6O_{11}	Aldrich	99.99%
Nd_2O_3	Merck	99.9%
Sm_2O_3	Strem	99.9%
Eu_2O_3	Aldrich	99.9%
Gd_2O_3	Pierce Inorganics	99.9%
Tb_4O_7	Pierce Inorganics	99.9%
Dy_2O_3	Pierce Inorganics	99.9%
Ho_2O_3	Aldrich	99.9%
Er_2O_3	Pierce Inorganics	99.9%
Tm_2O_3	Aldrich	99.9%
Yb_2O_3	Pierce Inorganics	99.9%
Lu_2O_3	Aldrich	99.99%
In_2O_3	Aldrich	99.99%

Appendix II: Powder X-ray diffraction data for target sample $Ca_{0.5}In_{0.5}TaO_{1.5}N_{1.5}$ (black) compared to $CaTaO_2N$ (red).

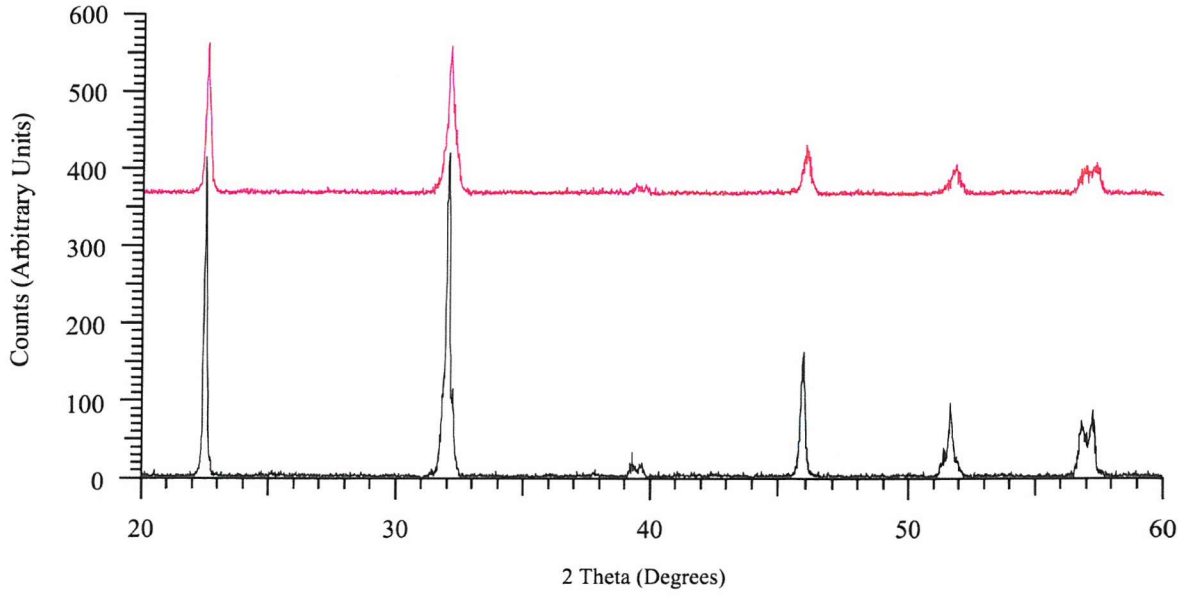

Appendix III: Observed calculated distance plots for various samples in Chapter 4.

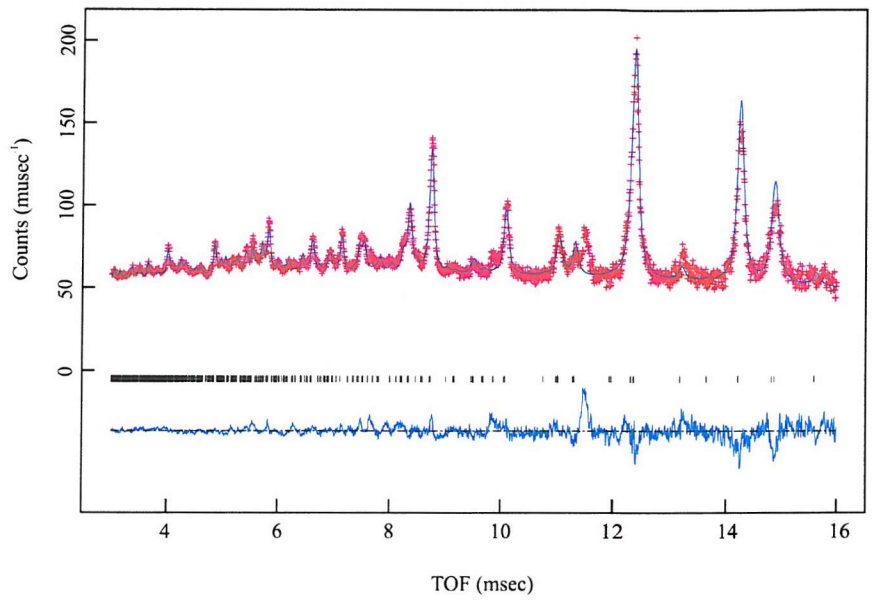

Rietveld refinement fit for $Ca_{0.61}La_{0.39}TaO_{1.61}N_{1.39}$; obtained from PND data collected on the POLARIS diffractometer backscattering bank at the Rutherford Appleton Laboratory (UK). The cross marks are the observed intensities, the upper trace the calculated profile, the black tick marks the calculated peak positions and the lower line the difference.

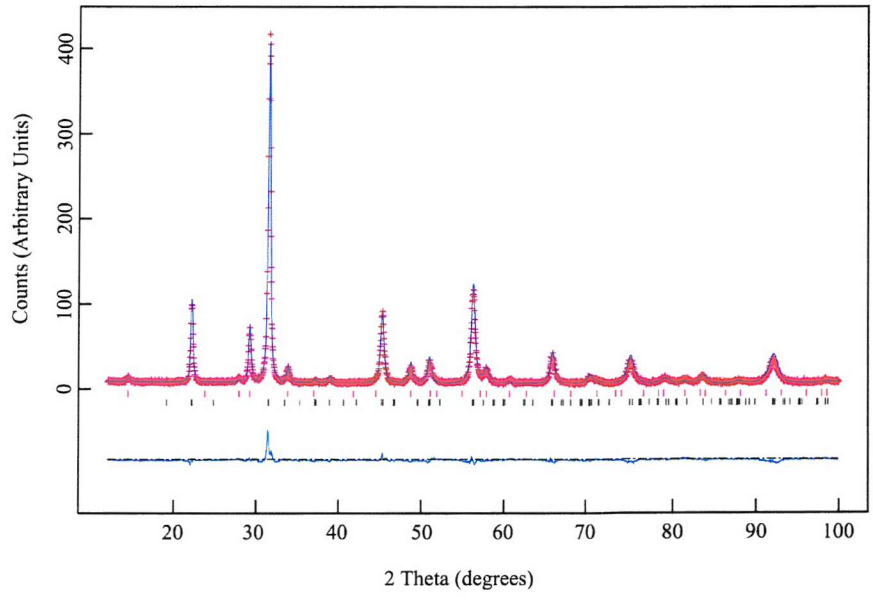

Rietveld refinement fit for $Ca_{0.61}La_{0.39}TaO_{1.61}N_{1.39}$; obtained from PXD data collected on a Siemens D5000. The cross marks are the observed intensities, the upper trace the calculated profile, the black tick marks the calculated perovskite peak positions, the red tick marks the calculated pyrochlore peak positions and the lower line the difference.

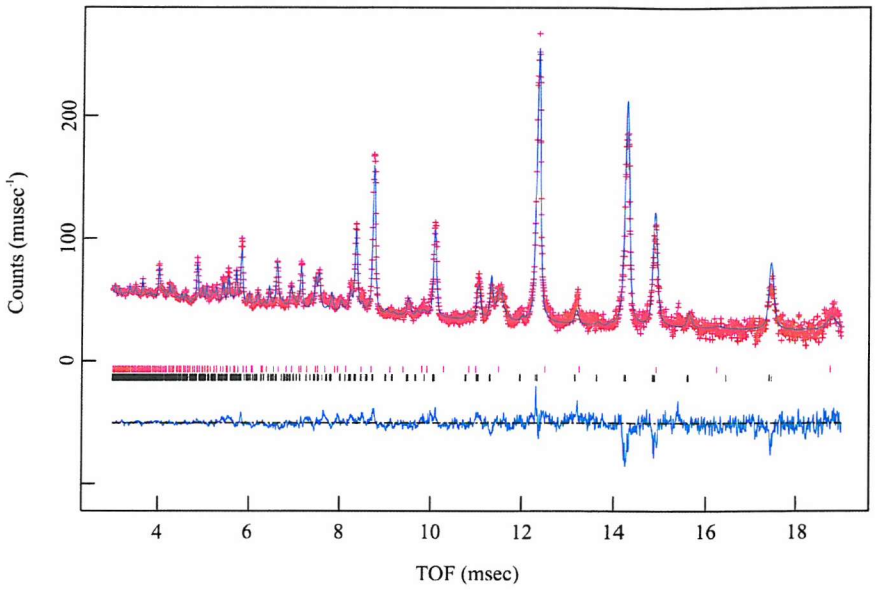

Rietveld refinement fit for $Ba_{0.24}La_{0.76}TaO_{1.24}N_{1.76}$; obtained from PND data collected on the POLARIS diffractometer backscattering bank at the Rutherford Appleton Laboratory (UK). The cross marks are the observed intensities, the upper trace the calculated profile, the black tick marks the calculated perovskite peak positions, the red tick marks the calculated pyrochlore peak positions and the lower line the difference.

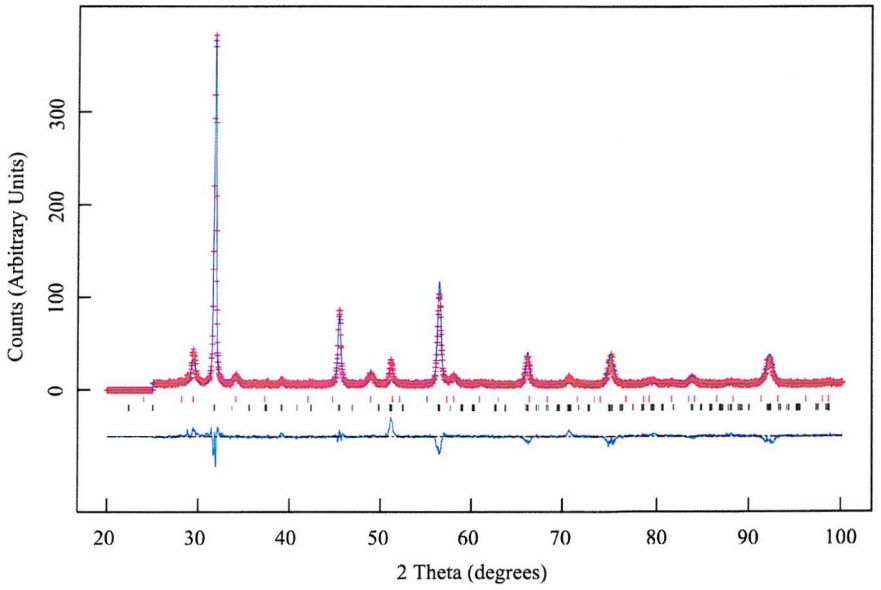

Rietveld refinement fit for $Ba_{0.24}La_{0.76}TaO_{1.24}N_{1.76}$; obtained from PXD data collected on a Siemens D5000. The cross marks are the observed intensities, the upper trace the calculated profile, the black tick marks the calculated perovskite peak positions, the red tick marks the calculated pyrochlore peak positions and the lower line the difference.

Appendix IV: Observed calculated distance plots for Ta_3N_5 in Chapter 7.

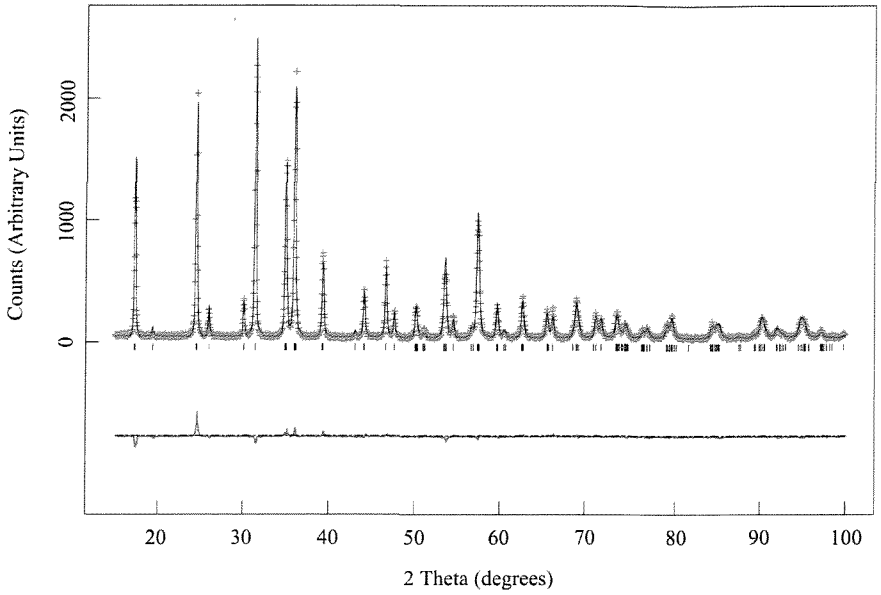

Rietveld refinement fit for Ta_3N_5; obtained from PXD data collected on a Siemens D5000. The cross marks are the observed intensities, the upper trace the calculated profile, the black tick marks the calculated peak positions and the lower line the difference.